

2022

The co-evolution of molecular clumps and high-mass stars

<https://hdl.handle.net/2144/44800>

Boston University

BOSTON UNIVERSITY
GRADUATE SCHOOL OF ARTS AND SCIENCES

Dissertation

**THE CO-EVOLUTION OF MOLECULAR CLUMPS
AND HIGH-MASS STARS**

by

TAYLOR GRAHAM HOGGE

B.A., University of Virginia, 2013
M.A., Boston University, 2016

Submitted in partial fulfillment of the
requirements for the degree of
Doctor of Philosophy
2022

© 2022 by
TAYLOR GRAHAM HOGGE
All rights reserved

Approved by

First Reader

James M. Jackson, PhD
Adjunct Professor of Astronomy

Second Reader

Dan Clemens, PhD
Professor of Astronomy

Acknowledgments

I want to thank my advisor, Prof. Jim Jackson, for being a great mentor and imparting some of his vast knowledge on me through our frequent discussions. Even when he was on the other side of the Earth, he made himself available to discuss any science problems I was working through and offer advice. He was always willing to push me to give talks and write observing proposals, which helped me grow as an astronomer. Lastly, he gave me the opportunity to experience new places around the world like Sydney, Tokyo, and Hawaii, all of which were amazing adventures.

Next, I want to thank Scott Whitaker, who has been like a second advisor to me. Scott's knowledge of statistics has been particularly helpful in my research, which involved statistical analyses of large data sets. My discussions with him at our group meetings have given me a much stronger understanding of error analysis and how to approach and answer scientific questions.

I also want to thank Ian Stephens and Jonathan Foster, who were postdoctoral researchers involved with the RAMPS project. Ian has been an excellent mentor and was integral in helping me survive my first year at BU as I tried to manage classes and the RAMPS observations and data reduction. Ian is an incredibly hard worker and was truly an inspiration. Although Jonathan was at Yale while I was at BU, he was also very helpful with RAMPS data reduction. His coding examples in particular gave me a great example of how to code well and gave me the impetus to begin learning Python, for which I am immensely grateful.

I thank my second reader, Prof. Dan Clemens, for his thorough readings and comments on my dissertation. Although the extensive edits were not my idea of a

fun time, the document is certainly in a much better state than it would have been without him.

I am also grateful for my other committee members, Prof. Tom Bania, Prof. Wen Li, and Prof. Cara Battersby, for taking time out of their busy schedules to help see me across the finish line.

I want to thank the other grad students, particularly those in my class and the classes one year above and below me, for helping me get through grad school with my good humor intact. Although we all worked hard, it was the moments having fun together that made the whole process survivable.

I am grateful for the support of my family, particularly my parents and parent-in-laws, whose constant encouragement has been much appreciated.

Last, but certainly not least, I want to thank my wife, Kara, for her support, patience, and love. She has stuck with me throughout this long process and I couldn't have made it through without her. Her unconditional love, along with that of our cat, Suki, and our dog, Moose, has always given me a reason to get out of bed and keep pursuing this goal. Her own hard work getting her doctorate in psychology was also a huge inspiration to me. Kara, I love you and am forever thankful.

**THE CO-EVOLUTION OF MOLECULAR CLUMPS
AND HIGH-MASS STARS**

TAYLOR GRAHAM HOGGE

Boston University Graduate School of Arts and Sciences, 2022

Major Professor: James M. Jackson,
Adjunct Professor of Astronomy

ABSTRACT

Since high-mass stars form deeply embedded within dense molecular clumps, the evolution of young stars and of dense clumps is inextricably linked. Previous datasets, however, lack the information necessary to test the prevailing theories. Definitive tests require a sufficiently large sample of molecular clumps and maps of their gas temperatures, column densities, velocity dispersions, and velocities at a spatial resolution comparable to, or smaller than, the clump scale (~ 1 pc). The Radio Ammonia Mid-Plane Survey (RAMPS), a new molecular line survey of thermal NH₃ and H₂O masers, provides the necessary data. In this dissertation, I used RAMPS data and archival datasets to test several theories of high-mass star formation and to investigate the co-evolution of molecular clumps and high-mass stars.

All theories of high-mass star formation make testable predictions regarding clump kinematics and gravitational stability. Analyses of RAMPS kinematic data revealed that the majority of molecular clumps, particularly those in early evolutionary stages, are unstable to gravitational collapse. Further, they display infall motions, a key prediction of the theory of competitive accretion. I also investigated

the kinematics of molecular filaments by comparing their measured velocity gradients to those predicted by hydrodynamical simulations. The measured spatial distributions of velocity gradients are inconsistent with existing models.

Feedback from protostars and stars is predicted to alter the properties of surrounding clumps. I investigated feedback size scales and found that high-mass protostellar and stellar feedback significantly changes the temperatures, chemical abundances, and velocity dispersions of clumps on scales of ~ 0.3 to 3 pc.

Finally, I observed a massive molecular cloud filament undergoing an interaction with a supernova shock, which is accelerating, heating, and injecting turbulence into the filament's gas. Although the molecular cores hosted by the filament may remain gravitationally bound, the filament is gravitationally unbound and likely being dispersed. Given that the shock is removing a reservoir of gas that could have been accreted by the cores, these data suggest that the supernova is inhibiting star formation.

Contents

1	Introduction	1
1.1	Theories of High-Mass Star Formation	1
1.2	Observations of High-Mass Star-Forming Clumps	8
1.2.1	Infrared	8
1.2.2	Radio	10
1.3	Open Questions	12
1.4	Data Required to Answer Open Questions	13
1.5	Introduction to RAMPS	13
1.6	Dissertation Outline	14
2	The Radio Ammonia Mid-Plane Survey	15
2.1	Introduction	15
2.2	Observations	17
2.2.1	Line Selection	17
2.2.2	Instrumentation	20
2.2.3	Observing Strategy	20
2.3	Data Reduction and Processing	25
2.4	Results	28
2.5	Analysis	30
2.5.1	Clump Analysis	31
2.5.2	H ₂ O Maser Analysis	66

2.6	Comparison with Previous Surveys	76
2.6.1	Comparison with HOPS	78
2.6.2	Comparisons of RAMPS with BGPS and ATLASGAL	80
2.6.3	Comparison with Targeted NH ₃ Surveys	83
2.7	Conclusion	88
3	The Early Dynamical Evolution of Molecular Clumps and Filaments	90
3.1	Introduction	90
3.1.1	Molecular Clump Kinematics	90
3.1.2	Molecular Filament Kinematics	97
3.2	Gravitational Stability	98
3.2.1	Virial Analysis	99
3.2.2	The Virial Analysis Subsample	99
3.2.3	Calculating Virial Masses	100
3.2.4	Virial Parameters	102
3.2.5	Blue Asymmetric Line Analysis	111
3.3	Filament Kinematics	127
3.3.1	Filament Analysis Sample	127
3.3.2	Filament Spines	130
3.3.3	Filament Velocity Gradients	134
3.3.4	Comparison with Simulations	137
3.4	Conclusions	145
4	Protostellar and Stellar Feedback in Massive Molecular Clumps	147
4.1	Introduction	147
4.2	The First Protostars in Massive Clumps	151
4.2.1	Evolutionary States Associated with H ₂ O Masers	151

4.2.2	H ₂ O Masers Associated with Quiescent Clumps	153
4.2.3	Observational Challenges	156
4.3	Feedback from High-Mass Protostars and Stars	158
4.3.1	High-Mass Protostellar Feedback	158
4.3.2	High-Mass Stellar Feedback	167
4.4	Conclusions	174
5	External Feedback from the W41 Supernova Remnant	177
5.1	Introduction	177
5.1.1	A Possible SNR-MC Interaction in G23.33-0.30	178
5.2	Observations and Data Reduction	186
5.2.1	VLA Observations	188
5.2.2	ACA Observations	188
5.2.3	SMA Observations	189
5.3	Results	190
5.4	Analysis	196
5.4.1	NH ₃ (3,3) Maser Emission	196
5.4.2	Thermal NH ₃ Emission	198
5.4.3	Virial Analysis	200
5.5	Discussion	203
5.5.1	Evidence of a Large-Scale Shock	203
5.5.2	W41's SNR-MC Interaction with GMC G23.0-0.4	208
5.5.3	W41's Potential Impact Geometry	216
5.5.4	Possible Negative Feedback from SNR W41	220
5.6	Conclusion	223
6	Summary and Conclusions	226

6.1	Chapter Summaries	226
6.1.1	Chapter 1 Summary	226
6.1.2	Chapter 2 Summary	227
6.1.3	Chapter 3 Summary	228
6.1.4	Chapter 4 Summary	228
6.1.5	Chapter 5 Summary	229
6.2	Open Questions	229
6.2.1	What are the dynamical states of the youngest clumps?	229
6.2.2	How does feedback begin and does it regulate the evolution of molecular clumps?	230
6.2.3	Can external feedback from SNe influence the evolution of nearby molecular clumps?	231
6.3	Conclusions	232
	Appendices	233
A	NH ₃ Physics	233
B	Baseline Fitting	235
C	Noise Maps	241
D	Integrated Intensity Maps	241
E	First Velocity Moment Maps	252
F	NH ₃ Line Modeling	252
	References	271
	Curriculum Vitae	286

List of Tables

2.1	RAMPS molecular lines	19
2.2	FIR Data Characteristics	48
2.3	RAMPS Molecular Clump Catalog	65
2.4	RAMPS H ₂ O Maser Catalog	77
3.1	Virial Analysis Results	104
3.2	Fraction of Collapsing Clumps	105
3.3	Blue Asymmetry Comparison	126
3.4	Filament Analysis Sample	129
5.1	Known NH ₃ (3,3) Masers	181
5.2	Observations	187
5.3	Archival Data	187
5.4	VLA NH ₃ (3,3) Maser Properties	197
5.5	Molecular Core Properties	202

List of Figures

2.1	KFPA beam pattern	21
2.2	Map of integration time	23
2.3	Histograms of rms noise	28
2.4	NH ₃ (1,1) rms noise map for fields L10 through L13	29
2.5	NH ₃ (1,1) integrated intensity map for fields L10 through L13	30
2.6	NH ₃ (1,1) first moment map for fields L10 through L13	31
2.7	Histograms of clump coordinates	34
2.8	Clump angular sizes	35
2.9	RAMPS clump detection completeness	37
2.10	Example NH ₃ fits	39
2.11	NH ₃ fit parameter values and errors	42
2.12	Clump distances	45
2.13	Galactic distribution of clumps	46
2.14	Clump physical sizes	47
2.15	Clump dust properties	53
2.16	Gas temperature vs. dust temperature	54
2.17	NH ₃ abundances	55
2.18	Clumps masses and luminosities	57
2.19	Clump evolution examples	60
2.20	Gas property histograms by evolutionary state	62
2.21	Histograms of H ₂ O maser brightness temperatures	71

2.22	Histograms of H ₂ O maser velocities	73
2.23	Histograms of H ₂ O maser velocity spreads	75
2.24	RAMPS and HOPS NH ₃ (1,1) integrated intensity comparison	79
2.25	RAMPS and HOPS NH ₃ (1,1) and (2,2) (<i>l, v</i>)-diagram comparison	80
2.26	RAMPS and HOPS H ₂ O maser detection comparison	81
2.27	RAMPS non-detections of ATLASGAL/BGPS sources	83
2.28	ATLASGAL/BGPS non-detections of RAMPS sources	84
2.29	Comparison with Svoboda et al. (2016) results	86
2.30	Comparison with Wienen et al. (2012) results	87
3.1	Blue asymmetry cartoon	95
3.2	Histogram of virial masses	102
3.3	Virial parameters separated by evolutionary state	106
3.4	RADEX ¹³ CO(1-0) optical depths	113
3.5	Velocity errors for ¹³ CO(1-0) and NH ₃ (1,1) fits	115
3.6	¹³ CO(1-0) optical depth-weighted velocity vs. intensity-weighted velocity	116
3.7	Example ¹³ CO(1-0) and NH ₃ (1,1) fits	117
3.8	V_{diff} values and errors	119
3.9	Histogram of V_{diff}	120
3.10	Histograms of V_{diff} separated by evolutionary state	121
3.11	Asymmetry parameter for synthetic ¹³ CO(1-0) lines	125
3.12	Medial axis example	131
3.13	Filament spine example	133
3.14	<i>p-v</i> distribution example	134
3.15	Monte Carlo method to derive errors on ∇V_{LSR}	136
3.16	The <i>p-v</i> and <i>p-∇v</i> distributions of G11.056-0.100	137

3.17	Velocity and density structure of the filament G26.942+0.180	141
3.18	Velocity and density structure of the filament G28.517-0.145	142
3.19	∇V_{peak} vs. ∇V_{off} and ∇V_{min}	144
4.1	MIR emission toward G31.464+0.185	155
4.2	T_{kin} , $\chi(\text{NH}_3)$, and σ distributions for the protostellar clump G23.606-0.011	162
4.3	Feedback zone amplitude vs. physical size for protostellar clumps . .	164
4.4	Feedback zone physical size vs. number density for protostellar clumps	166
4.5	T_{kin} , $\chi(\text{NH}_3)$, and σ distributions for the H II region clump G21.382-0.246	170
4.6	Feedback zone amplitude vs. physical size for H II region clumps . .	172
5.1	RAMPS NH ₃ (1,1) through (4,4) spectra toward G23.33-0.30	179
5.2	Continuum, maser, and high energy emission toward W41	182
5.3	MIR emission toward W41	184
5.4	GRS ¹³ CO emission toward W41	185
5.5	8 μm , NH ₃ (2,2), and (3,3) emission toward G23.33-0.30	191
5.6	NH ₃ (2,2), CS(5-4), and SiO(5-4) emission toward G23.33-0.30	192
5.7	NH ₃ (1,1) through (6,6) emission toward G23.33-0.30	193
5.8	¹³ CO, C ¹⁸ O, and dust continuum emission toward G23.33-0.30	194
5.9	G23.33-0.30 $p - v$ distribution	196
5.10	G23.33-0.30 T_{rot} , σ , and V_{LSR} maps	200
5.11	T_{rot} and σ vs. V_{LSR}	204
5.12	Shock interaction cartoon	205
5.13	RADEX NH ₃ (3,3) optical depths and brightness temperatures	207
5.14	RADEX NH ₃ (4,4), (5,5), and (6,6) brightness temperature ratios	209
5.15	GRS ¹³ CO(1-0) integrated intensity toward W41	211

5.16 RGB image of GRS ^{13}CO integrated intensity over different velocity ranges	213
5.17 Correlation between GRS ^{13}CO emission at $59 - 61 \text{ km s}^{-1}$ and at $76 - 78 \text{ km s}^{-1}$	214
5.18 MIR emission toward W41 cap and <i>WISE</i> HII Region sources	217
5.19 Illustration 1 of potential W41 impact geometry	220
5.20 Illustration 2 of potential W41 impact geometry	221
A.1 NH_3 rotational energy level diagram	234
B.1 Histograms of R	237
B.2 R for spectra with synthetic spectral lines	239
B.3 Example RAMPS $\text{NH}_3(1,1)$ spectra and associated values of R	241
B.4 Histograms of R	242
C.1 $\text{NH}_3(1,1)$ rms noise map for fields L14 through L17.	242
C.2 $\text{NH}_3(1,1)$ rms noise map for fields L18 through L21.	242
C.3 $\text{NH}_3(1,1)$ rms noise map for fields L22 through L25.	243
C.4 $\text{NH}_3(1,1)$ rms noise map for fields L26 through L29.	243
C.5 $\text{NH}_3(1,1)$ rms noise map for fields L30 through L33.	243
C.6 $\text{NH}_3(1,1)$ rms noise map for fields L34 through L37.	243
C.7 $\text{NH}_3(1,1)$ rms noise map for fields L38 through L41.	244
C.8 $\text{NH}_3(1,1)$ rms noise map for field L43.	244
C.9 $\text{NH}_3(1,1)$ rms noise map for field L45.	244
C.10 $\text{NH}_3(1,1)$ rms noise map for field L47.	245
C.11 $\text{NH}_3(2,2)$ rms noise map for fields L10 through L13.	245
C.12 $\text{NH}_3(2,2)$ rms noise map for fields L14 through L17.	245
C.13 $\text{NH}_3(2,2)$ rms noise map for fields L18 through L21.	246
C.14 $\text{NH}_3(2,2)$ rms noise map for fields L22 through L25.	246

C.15 NH ₃ (2,2) rms noise map for fields L26 through L29.	246
C.16 NH ₃ (2,2) rms noise map for fields L30 through L33.	246
C.17 NH ₃ (2,2) rms noise map for fields L34 through L37.	247
C.18 NH ₃ (2,2) rms noise map for fields L38 through L41.	247
C.19 NH ₃ (2,2) rms noise map for field L43.	247
C.20 NH ₃ (2,2) rms noise map for field L45.	248
C.21 NH ₃ (2,2) rms noise map for field L47.	248
C.22 H ₂ O rms noise map for fields L10 through L13.	249
C.23 H ₂ O rms noise map for fields L14 through L17.	249
C.24 H ₂ O rms noise map for fields L18 through L21.	249
C.25 H ₂ O rms noise map for fields L22 through L25.	249
C.26 H ₂ O rms noise map for fields L26 through L29.	250
C.27 H ₂ O rms noise map for fields L30 through L33.	250
C.28 H ₂ O rms noise map for fields L34 through L37.	250
C.29 H ₂ O rms noise map for fields L38 through L40.	250
C.30 H ₂ O rms noise map for field L45.	251
C.31 H ₂ O rms noise map for field L47.	251
D.1 NH ₃ (1,1) integrated intensity map for fields L14 through L17	252
D.2 NH ₃ (1,1) integrated intensity map for fields L18 through L21	252
D.3 NH ₃ (1,1) integrated intensity map for fields L22 through L25	253
D.4 NH ₃ (1,1) integrated intensity map for fields L26 through L29	253
D.5 NH ₃ (1,1) integrated intensity map for fields L30 through L33	253
D.6 NH ₃ (1,1) integrated intensity map for fields L34 through L37	254
D.7 NH ₃ (1,1) integrated intensity map for fields L38 through L41	254
D.8 NH ₃ (1,1) integrated intensity map for field L43	254
D.9 NH ₃ (1,1) integrated intensity map for field L45	255

D.10 NH ₃ (1,1) integrated intensity map for field L47	255
D.11 NH ₃ (2,2) integrated intensity map for fields L10 through L13	256
D.12 NH ₃ (2,2) integrated intensity map for fields L14 through L17	256
D.13 NH ₃ (2,2) integrated intensity map for fields L18 through L21	256
D.14 NH ₃ (2,2) integrated intensity map for fields L22 through L25	257
D.15 NH ₃ (2,2) integrated intensity map for fields L26 through L29	257
D.16 NH ₃ (2,2) integrated intensity map for fields L30 through L33	257
D.17 NH ₃ (2,2) integrated intensity map for fields L34 through L37	258
D.18 NH ₃ (2,2) integrated intensity map for fields L38 through L41	258
D.19 NH ₃ (2,2) integrated intensity map for field L43	258
D.20 NH ₃ (2,2) integrated intensity map for field L45	259
E.1 NH ₃ (1,1) first moment map for fields L14 through L17	259
E.2 NH ₃ (1,1) first moment map for fields L18 through L21	259
E.3 NH ₃ (1,1) first moment map for fields L22 through L25	260
E.4 NH ₃ (1,1) first moment map for fields L26 through L29	260
E.5 NH ₃ (1,1) first moment map for fields L30 through L33	260
E.6 NH ₃ (1,1) first moment map for fields L34 through L37	261
E.7 NH ₃ (1,1) first moment map for fields L38 through L41	261
E.8 NH ₃ (1,1) first moment map for field L43	261
E.9 NH ₃ (1,1) first moment map for field L45	262
E.10 NH ₃ (1,1) first moment map for field L47	262
F.1 Example NH ₃ (1,1) line model with different line widths	263
F.2 Difference between quadrupole and measured optical depth ratios . .	265

Chapter 1

Introduction

1.1 Theories of High-Mass Star Formation

Although high-mass stars are rare, due to their short main sequence (MS) lifetimes ($t_{MS} \approx 10^{10} (\frac{M}{M_\odot})^{-2.5}$ yr) and the shape of the stellar initial mass function (IMF) (e.g., Salpeter 1955; Kroupa 2001; Chabrier 2003), they nevertheless dominate the chemical and kinematic evolution of the interstellar medium (ISM) in galaxies (e.g., Kennicutt 1998, 2005). Because the formation and early evolution of high-mass stars occurs within dense ($n \sim 10^4$ cm $^{-3}$) molecular clumps ($M \sim 250 - 2000$ M $_\odot$, $R \sim 1$ pc), investigating the evolution of these clumps (hereafter I will use “clump” to refer to a molecular clump) is essential to understand the formation and evolution of high-mass stars and the stellar clusters in which they reside (Zinnecker & Yorke 2007; Motte et al. 2018).

Although there is no clear observational prestellar evolutionary sequence for high-mass stars like there is for low-mass stars, observations and theory provide a broad outline (Motte et al. 2018). Clumps start in a cold, quiescent stage, prior to the formation of high-mass protostars (HMPs), and fragment into pre-stellar molecular cores ($M \gtrsim 1$ M $_\odot$, $R \sim 0.05$ pc). The protostellar stage of clump evolution begins once a core (hereafter I will use “core” to refer to a molecular core) forms a HMP. As protostars accrete from the surrounding core material, they launch powerful outflows and heat the surrounding gas with their radiation. HMPs eventually reach the main sequence, when their strong ultraviolet (UV) radiation fields form bubbles of ionized

gas called H II regions. The H II region stage of clump evolution is characterized by the expansion of the H II region into the surrounding gas. Feedback (I use “feedback” to refer to mechanisms that transfer energy from protostars and MS stars back to the surrounding gas) from massive stars may disrupt or even trigger star formation in the surrounding clump through the addition of thermal and kinetic energy. Turbulence added by massive stellar feedback may provide support against further collapse and eventually disperse clumps, while bulk flows from stellar winds and the resulting shocks may compress gas, promoting further gravitational collapse within the clump. Finally, high-mass stars end their lives with energetic supernovae (SNe) explosions, creating shock waves that can travel tens of parsecs.

The thermal and kinematic evolution of clumps may play an important role in the early evolution of high-mass stars. If the precursors to high-mass stars accrete an appreciable amount of their final masses from their surrounding clumps, then changes to the clump properties as a result of feedback could affect star formation rates. I refer to this potential link between the evolution of clumps and high-mass stars as co-evolution. Consequently, testing and characterizing the co-evolution of molecular clumps and high-mass stars is important.

Despite the general theoretical expectations, the co-evolution of molecular clumps and high-mass stars has not been well tested. This is in part because it is difficult to observe thousands of high-mass star-forming clumps (HMSFCs) at the clump scale (~ 1 pc). Given their rarity, the distances to many HMSFCs are large compared to clumps that only form low-mass stars. Furthermore, the formation of stars is obscured by dense gas and dust, which absorbs light at visual and near-infrared wavelengths (λ). Although observations at far-infrared, submillimeter, millimeter, and radio wavelengths mitigate the issue of extinction, the angular resolution for a diffraction limited telescope of diameter D is proportional to the wavelength observed

$(\theta \propto \frac{\lambda}{D})$, resulting in poorer angular resolution at longer wavelengths. Thus, massive clumps often contain substructures that are unresolved by single-dish telescopes.

The early evolution of molecular clumps is particularly uncertain, since cold, quiescent molecular clumps are fainter at submillimeter and millimeter wavelengths than those hosting HMPs and H II regions. Because quiescent clumps are more difficult to observe, observations have not yet sufficiently tested the mechanisms by which the precursors to HMPs fragment and accrete.

Although all theories of high-mass star formation agree that the kinematics of quiescent molecular clumps are important, theories differ on how the kinematic evolution of clumps affects protostellar evolution. While the theory of turbulent core accretion (McKee & Tan 2003) predicts that turbulence within clumps prevents the gravitational collapse of massive cores, the theory of competitive accretion (Bonnell et al. 2001, 2004) predicts fragmentation into low-mass cores that later acquire significant mass from clump material via high accretion rates ($\sim 10^{-4} M_{\odot} \text{ yr}^{-1}$; Bonnell & Bate 2006). To produce such high accretion rates, competitive accretion requires that HMSFCs undergo gravitational collapse, which feeds the cores near the clump center most. If HMPs accrete most of their final masses from massive cores, as predicted by turbulent core accretion, then changes to clump properties would have a limited impact on the evolution of HMPs. If HMPs are instead clump-fed, as predicted by competitive accretion, then changes to the gas properties of clumps may alter star formation rates and result in co-evolution between molecular clumps and high-mass stars.

Previous targeted molecular line surveys have tested whether molecular clumps are unstable to collapse by comparing clump virial masses, the mass that can be supported against collapse by a clump's turbulence, to their gas masses (Wienen et al. 2012; Svoboda et al. 2016). Although these surveys have provided evidence that

the average clump is collapsing, the derived clump masses assumed thermal coupling between the gas and dust, which is often a poor assumption (Merello et al. 2019). Given that the derivation of gas masses from dust masses is strongly dependent on temperature, this assumption adds substantial uncertainty to the virial analysis (up to a factor of ~ 2). In addition, single-pointing surveys can only measure turbulent molecular line widths in a single beam. By only measuring the velocity dispersion in a single beam centered on the peak of the dust emission, the results of these single-pointing surveys will be biased toward the levels of turbulence along the direction of peak dust emission, which may be more likely to have sources of kinematic feedback nearby. If kinematic feedback can raise the velocity dispersion in a localized region by $\sim 40\%$ above the clump-averaged value, then virial parameters would be overestimated by a factor of ~ 2 . Consequently, the virial states of HMSFCs may be more accurately determined by including turbulent line widths measured across the full sky-projected faces of clumps and employing masses derived using the dust temperatures.

Filamentary structures, which are ubiquitous in the ISM (e.g., André et al. 2010; Men’shchikov et al. 2010; Molinari et al. 2010a; Henning et al. 2010), likely play a significant role in star formation (there is an informative review by André et al. 2014). A major open question concerning filaments is whether gas flows along filament spines feed accreting cores. One signature of an accelerating gas flow is a gradient in the velocity field along the spine of a filament. Although observations have detected velocity gradients in filaments (Kirk et al. 2013; Zernickel et al. 2013; Yuan et al. 2020), analysis of general trends is made more difficult by small sample sizes and unknown inclination angles relative to the observer. In addition, velocity gradients do not uniquely identify gravitational flows, since shear motion can also produce velocity gradients (Duarte-Cabral & Dobbs 2016; Meidt et al. 2018).

Simulations are useful to help understand these data, since the simulated filament inclination angles and their three-dimensional velocity fields are known. Gómez & Vázquez-Semadeni (2014) and Smith et al. (2016) have made specific predictions about the relationship between filament velocity gradients and density peaks that are unique to gas flows that accrete onto cores. Simulations by Gómez & Vázquez-Semadeni (2014) produced filaments that featured the largest velocity gradients at the sites of highest column density, indicative of strong inflow motions onto molecular cores. On the other hand, simulations by Smith et al. (2016) produced filaments that featured sub-parsec oscillations in the flow velocity related to the turbulent velocity field, but a more ordered flow on parsec scales. Smith et al. (2016) found that these flows tended to concentrate gas where the parsec-scale velocity gradient was the least, since the larger, oppositely signed gradients on either side were indicative of flow toward this point. Given that observed filaments have unknown inclination angles, it is crucial to observe the velocity fields of a large sample of filaments to test both theories.

In addition to observational challenges, HMSFCs eventually host sources of feedback that affect molecular clump evolution. As protostars and MS stars accrete from their natal clumps, they release outflows, winds, and radiation back into the clump. Such feedback mechanisms can change the thermal, chemical, and kinematic properties of the surrounding clump, which in turn affects further fragmentation and accretion near the sources of feedback. This feedback, which causes protostars and MS stars to alter their own evolution as well as the evolution of neighboring cores, protostars, and MS stars, is difficult to model analytically.

In lieu of analytical solutions, simulations are necessary to make progress. To investigate the impact of kinematic feedback from protostars, Wang et al. (2010) performed simulations of protostars hosting outflows within a massive, collapsing

clump. This study found that outflows can significantly reduce protostellar accretion by breaking up accretion flows and increasing the turbulent support of the clump. On the other hand, simulations by Peters et al. (2010) suggest that radiative feedback from massive stars heats the surrounding gas, increasing the Jeans mass required for fragmentation (Jeans 1902). Accretion flows that are unable to fragment can more efficiently accrete onto a central source (Krumholz et al. 2007). Chemical modeling shows that radiative feedback can also alter chemical abundances by orders of magnitude (Busquet et al. 2011). The larger the region influenced by such feedback, the greater the subsequent effect on clump and core evolution; thus, the size of such feedback zones is an important quantity since it determines the extent over which the gas properties of the clump can be affected. Theoretical work by Gaches & Offner (2018) predicts that protoclusters embedded in dense gas ($n \sim 10^4 \text{ cm}^{-3}$) can heat only a small region ($R \sim 0.05 - 0.2 \text{ pc}$), but similar predictions about the extent of enhanced turbulence and chemical abundances are lacking.

Given the potential importance of feedback to high-mass star formation, it is essential to provide an observational test of the size of these feedback zones, which is lacking to date. Consequently, mapping observations that can help provide the temperature, kinematic, and chemical structure of clumps hosting HMPs and H II regions are necessary.

In addition, some theories predict that early protostellar feedback is crucial to the formation of massive stars. For example, turbulent core accretion may require radiative feedback from an early generation of low-mass protostars to prevent the fragmentation of high-mass cores (Krumholz & McKee 2008), but the low luminosities of low-mass protostars make them impractical to detect in distant HMSFCs. Collisionally excited masers offer a potential solution, since they are triggered by actively accreting low- and high-mass protostars (Codella et al. 1996; Moscadelli et al.

2005; Goddi & Moscadelli 2006; Ao et al. 2018) and are luminous enough to be detected over large distances (Furuya et al. 2001). The presence of such maser emission associated with a quiescent clump would suggest the existence of a low-mass protostar prior to the formation of an HMP, consistent with the predictions of Krumholz & McKee (2008). The isotropic H₂O maser luminosity is given by the following relation (Anglada et al. 1996),

$$\frac{L_{\text{H}_2\text{O}}}{L_{\odot}} = 2.30 \times 10^{-8} \left[\frac{\int I_{\nu} dv}{\text{Jy km s}^{-1}} \right] \left[\frac{d}{\text{kpc}} \right]^2, \quad (1.1)$$

where $\int I_{\nu} dv$ is the line flux integrated over velocity and d is the distance. Previous observations of such masers (Walsh et al. 2011) have the point source sensitivity to detect maser emission from low-mass protostars, which have $L_{\text{H}_2\text{O}} \sim 10^{-8} L_{\odot}$ (Furuya et al. 2003), out to distances of only ~ 1 kpc. Thus, a survey with at least an order of magnitude better point source sensitivity is necessary to detect these masers out to the typical distances of high-mass star-forming clumps ($d \gtrsim 3$ kpc) and place strong limits on the existence of an early generation of low-mass protostars in massive clumps.

Star formation within a clump may also be affected by sources outside of that clump, such as nearby SNe. Given that shocks from SNe can travel tens of parsecs, they may influence the star formation process in nearby ($\lesssim 20$ pc) clumps. Simulations of shocks impacting dense clumps provide conflicting results. Some simulations imply that SNe inhibit star formation (Pittard & Parkin 2016; Smith et al. 2020), some imply that such shocks stimulate the collapse of cores (Orlando et al. 2005), and others imply that supernovae-driven turbulence is relatively short-lived and has no significant effect on star formation (Seifried et al. 2018). Because previous observations of such interactions have been unable to probe gas temperature, velocity dispersion, and velocity variations below the clump scale (Maxted et al. 2016), these

observations cannot help distinguish among these predictions. On the other hand, these observations suggest that such interactions are associated with broad molecular line widths (Reach et al. 2005) and shock-excited maser emission in the NH₃(3,3) inversion transition (McEwen et al. 2016). Consequently, a large mapping survey of NH₃ lines would provide the molecular line widths and NH₃(3,3) data necessary to identify candidate SNe interaction sites, which could then be observed at higher spatial resolution to investigate sub-clump scale gas temperature, velocity dispersion, and velocity variations.

1.2 Observations of High-Mass Star-Forming Clumps

Given the open questions concerning theories of high-mass star formation, as well as the rarity of HMSFCs, observations of a large sample of molecular clumps are necessary to progress our understanding. In this section, I describe several recent surveys of HMSFCs from infrared to radio wavelengths to provide context and to identify gaps that need to be filled.

1.2.1 Infrared

Although young stellar clusters embedded within molecular clumps can be detected by their near-infrared (NIR; $\sim 1 - 5\mu\text{m}$) radiation (Megeath et al. 2005), the earlier stages of high-mass star formation are obscured at these wavelengths by dust (Draine 1989). Consequently, infrared surveys designed to investigate the formation of high-mass stars and clusters tend to observe at mid-infrared (MIR; $\sim 5 - 40\mu\text{m}$) and far-infrared (FIR; $\sim 40 - 500\mu\text{m}$) wavelengths. Although cold, quiescent clumps are opaque even at MIR wavelengths (Sridharan et al. 2005; Rathborne et al. 2006), dust heated by embedded HMPs emits strongly near $\lambda \sim 24\mu\text{m}$ (Chambers et al. 2009). Once HMPs transition onto the MS, the H II regions they form are luminous

at $\lambda \sim 8 \mu\text{m}$ as well as at $\lambda \sim 24 \mu\text{m}$ (Watson et al. 2008; Kerton et al. 2015). Thus, MIR emission is a useful probe of molecular clump evolutionary states (e.g., Jackson et al. 2013). The dust associated with cool molecular clumps is bright in the FIR, where its spectral energy distribution (SED) is well-described by a graybody dust model (Lagache et al. 1998). Dust modeling of a clump’s FIR SED allows the inference of the dust temperature and column density (e.g., Guzmán et al. 2015), provided assumptions about the dust abundance, composition, and size distribution are made (Ossenkopf & Henning 1994). Furthermore, the mass of a clump can be determined if the distance is known and a dust-to-gas mass ratio is assumed (Hildebrand 1983).

Given the advantages offered by MIR and FIR emission, observations at these wavelengths are important. Although the Earth’s atmosphere is opaque to most of the infrared spectrum, infrared satellite observatories like *Spitzer* and *Herschel* allow observations at these wavelengths. Several IR continuum surveys observed large portions of the Galactic plane using these observatories: the Galactic Legacy Infrared Mid-Plane Survey Extraordinaire (GLIMPSE; Benjamin et al. 2003; Churchwell et al. 2009), MIPS Galactic Plane Survey (MIPSGAL; Carey et al. 2009), and the Herschel infrared Galactic Plane Survey (Hi-GAL; Molinari et al. 2010b). These surveys observed thousands of high-mass star-forming clumps (Peretto & Fuller 2009; Molinari et al. 2016), and provide the key MIR and FIR continuum data necessary to estimate their dust properties and evolutionary states.

Although these data are crucial, the main shortcomings of dust continuum observations are their lack of kinematic information and their inability to provide distance estimates. Given that kinematic data and distances are necessary to test most theories of high-mass star formation, MIR and FIR observations alone cannot answer many of the open questions on high-mass star formation.

1.2.2 Radio

Cold dust emits strongly at millimeter (mm) and submillimeter (submm) wavelengths. Thus, mm and submm dust continuum emission is an excellent tracer of molecular clumps and valuable for SED modeling of cold clumps. The 870 μm APEX Telescope Large Area Survey of the Galaxy (ATLASGAL; Schuller et al. 2009) and the 1.1 mm Bolocam Galactic Plane Survey (BGPS; Aguirre et al. 2011) are dust continuum surveys that include large regions of overlap with the complementary MIR and FIR Galactic plane surveys.

Although these longer submm and mm wavelength observations are more sensitive to cold dust than those at shorter FIR wavelengths, dust emission's dependence on temperature is exponential unless $\lambda \gg \frac{hc}{k_B T}$ (where h is Planck's constant, c is the speed of light, and k_B is Boltzmann's constant), in which case it is linear. For cold clumps ($T_{dust} < 15$ K), $\lambda = \frac{hc}{k_B T}$ corresponds to $\lambda \sim 1$ mm. Thus, the large clump catalogs produced by the 870 μm ATLASGAL observations (Csengeri et al. 2014) and the 1.1 mm BGPS observations (Rosolowsky et al. 2010) may be biased toward warmer, more evolved clumps.

Radio molecular line data have several advantages over dust continuum data. Along with providing velocity dispersions and detecting velocity gradients, the kinematic data from molecular line observations are used to estimate kinematic distances (e.g., Schmidt 1957; Clemens et al. 1988; Whitaker et al. 2017), which can be refined by maser parallax data (Reid et al. 2016). Distances are essential to determine the dynamical states of clumps and filaments, as well as to measure the extent of protostellar and stellar mechanical feedback.

In addition, the brightness temperatures of low frequency ($\nu_0 < 30$ GHz, $\lambda > 1$ cm) spectral lines have a linear dependence on temperature, rather than the exponential dependence of the shorter wavelength dust emission. Consequently, such

observations are less biased toward hotter clumps. Molecular transitions with larger critical densities are particularly advantageous. While CO and its isotopologues (^{13}CO , C^{18}O , C^{17}O) are sensitive to lower density gas ($n \sim 10^3 \text{ cm}^{-3}$) typical of giant molecular clouds (GMCs; Scoville & Solomon 1975; Solomon et al. 1979; Dame et al. 2001), the NH_3 inversion lines at 23 GHz are most sensitive to the denser gas ($n \sim 10^4 \text{ cm}^{-3}$) often associated with molecular clumps (Cheung et al. 1968; Sweitzer 1978). Because the NH_3 inversion transitions allow the inference of gas temperature and NH_3 column density (Walmsley & Ungerechts 1983), they can reveal the thermal and chemical effects of the radiative feedback from HMPs and massive MS stars (Evans 1999).

The H_2O maser line at 22.235 GHz is another useful tool for studying HMSFCs (Elitzur et al. 1989). Observations suggest that H_2O masers trace actively accreting protostars, since they are excited by protostellar outflows and disk wind shocks (Moscadelli et al. 2020). Because H_2O masers have large isotropic line luminosities ($L_{\text{H}_2\text{O}} = 10^{-10} - 1 \text{ L}_\odot$; Palagi et al. 1993; Furuya et al. 2001, 2003; Cyganowski et al. 2013), they can even signal the presence of deeply embedded and low luminosity protostars (Healy et al. 2004).

Although several clump surveys have observed these valuable NH_3 and H_2O transitions (Dunham et al. 2011; Walsh et al. 2011; Purcell et al. 2012; Wienen et al. 2012; Urquhart et al. 2015; Svoboda et al. 2016; Wienen et al. 2018), the analysis of these data were limited by their respective instrumentation and source selection methods. While single pointing surveys (Dunham et al. 2011; Wienen et al. 2012; Svoboda et al. 2016; Wienen et al. 2018) provide a measure of a clump's properties, they cannot reveal the spatial variations required to detect velocity gradients and measure the size of regions affected by feedback. The NH_3 and H_2O mapping survey by Walsh et al. (2011) observed a considerable area (100 deg^2), but achieved

a spatial resolution (~ 2 pc at $d = 3$ kpc) that is insufficient to resolve typical clump sizes (~ 1 pc) at typical distances to HMSFCs ($d \gtrsim 3$ kpc). Mapping surveys that employed larger telescopes had smaller sample sizes biased toward later evolutionary states (Urquhart et al. 2015). No datasets currently available provide spatially resolved maps of gas properties for a large ($\sim 1,000$), representative sample of clumps. Consequently, there are still many open questions concerning high-mass star formation.

1.3 Open Questions

The evolution of high-mass stars is made more complex by their potential connection to the evolution of molecular clumps. If high-mass stars accrete from outside their natal cores, then changes to the clump gas properties can alter protostellar accretion and evolution. Consequently, the degree to which feedback from protostars, stars, or SNe can significantly change the gas properties within clumps is important. To help test and characterize the co-evolution of molecular clumps and high-mass stars, this dissertation will focus on the following open questions:

1. *What are the dynamical states of the youngest clumps?* 1.1 Are quiescent clumps in a state of gravitational collapse or are they supported by turbulence? 1.2 Are the velocity gradients observed in molecular filaments reproduced by simulations of gas flowing to dense cores?
2. *How does feedback begin and does it regulate the evolution of molecular clumps?* 2.1 Does protostellar feedback begin with low-mass protostars, prior to the formation of HMPs? 2.2 Does radiative and kinematic feedback from HMPs and massive MS stars change the thermal, chemical, and kinematic properties of their host clumps? 2.3 What are the physical sizes of the regions affected by such feedback?

3. *Can external feedback from SNe influence the evolution of nearby molecular clumps?* 3.1 Can supernova shocks inject turbulence into dense molecular filaments and their embedded cores? 3.2 Can interactions between SNe and dense filaments stimulate or inhibit the future formation of stars?

1.4 Data Required to Answer Open Questions

To answer these open questions, I require temperature, column density, and kinematic data for a sample of at least 1,000 clumps that contain adequately large subsamples of quiescent, protostellar, and H II region clumps. The NH₃ inversion lines provide these data most efficiently, but such observations must have the sensitivity to detect NH₃(1,1) lines with typical brightness temperatures of $T_B \sim 1$ K (Purcell et al. 2012). Progress on the internal structure of clumps and filaments necessitates sufficient angular resolution to at least partially resolve the ~ 1 pc clump scale and sufficient velocity resolution to accurately measure velocities and velocity dispersions. Consequently, I require molecular line maps with sub-pc spatial resolution and ~ 0.2 km s⁻¹ spectral resolution, sufficient to resolve typical molecular clump line widths. Finally, more sensitive H₂O data are needed to test whether low-mass protostars form prior to HMPs within HMSFCs. Low-mass ($M \sim 1 M_\odot$) protostars have isotropic H₂O maser luminosities of $L_{\text{H}_2\text{O}} \sim 10^{-8} L_\odot$, which corresponds to a flux of ~ 0.5 Jy at a distance of 3 kpc (Brand et al. 2003; Furuya et al. 2003). Thus, a flux sensitivity of ~ 0.15 Jy is required to detect the H₂O maser emission from low-mass protostars at typical distances to HMSFCs.

1.5 Introduction to RAMPS

The Radio Ammonia Mid-Plane Survey (RAMPS; Hogge et al. 2018) takes advantage of the Green Bank Telescope's (GBT) excellent 22-25 GHz sensitivity and

mapping speed to survey molecular clumps in six NH_3 inversion lines and the H_2O maser line. RAMPS has sufficient sensitivity, areal coverage, angular resolution, and spectral resolution to identify the requisite number of clumps and to map the kinematic, thermal, chemical, and physical structure of clumps and filaments. RAMPS improves on previous NH_3 surveys by mapping thousands of molecular clumps at $\theta \sim 30''$ angular resolution, which corresponds to ~ 0.5 pc at a distance of 3 kpc. In addition, RAMPS has a spectral resolution of $\sim 0.2 \text{ km s}^{-1}$ and achieves a sensitivity of $\sigma_{T_B} \sim 0.13 \text{ K}$ per channel, sufficient to detect all molecular clumps in the survey region with $M \geq 260 \text{ M}_\odot$ within 8 kpc. Thus, RAMPS provides maps, usually spatially resolved, of gas temperature, NH_3 column density, velocity, and velocity dispersion toward sufficiently large samples of molecular clumps in various evolutionary stages. In addition, the H_2O masers detected by RAMPS locate actively accreting protostars within the clumps. Consequently, RAMPS provides the data types, quantity, and clump samples necessary to answer the open questions described above.

1.6 Dissertation Outline

In Chapter 2, I describe RAMPS and present global properties of the clump sample; in Chapter 3, I explore the early dynamical evolution of clumps to determine whether high-mass stars might be clump-fed; in Chapter 4, I examine the effect of protostellar and stellar feedback on the gas properties of clumps to test whether such feedback can alter the evolution of clumps; in Chapter 5, I investigate external feedback on a molecular filament from an interaction with a supernova remnant to determine whether SNe can alter the evolution of clumps; and in Chapter 6, I summarize my work.

Chapter 2

The Radio Ammonia Mid-Plane Survey

2.1 Introduction

Because high-mass stellar feedback can significantly alter the gas properties of the molecular clumps from which they accrete, the evolution of high-mass stars is inextricably linked to the evolution of molecular clumps. Consequently, it is difficult to analytically model the co-evolution of high-mass stars and molecular clumps (e.g., Larson & Starrfield 1971; Bonnell et al. 2001; McKee & Tan 2003; Peters et al. 2010; Wang et al. 2010; Arthur et al. 2011; Klassen et al. 2017). Furthermore, such molecular clumps are challenging to probe observationally because their typical distances are large ($d > 1$ kpc).

In Chapter 1, I described some of the current observational efforts needed to advance our understanding of high-mass star formation. These include Galactic plane dust surveys, targeted molecular line surveys, and unbiased molecular line surveys. Although the large area dust continuum surveys like Hi-GAL, ATLASGAL, and BGPS have provided crucial information about the dust properties of clumps, these data cannot provide clump masses and luminosities without distance estimates.

Follow-up single-pointing NH₃ observations targeted samples of ATLASGAL (Wienen et al. 2012, 2018) and BGPS (Dunham et al. 2011; Svoboda et al. 2016) clumps, providing the kinematic distances necessary to estimate their masses and luminosities. While this information is indeed crucial, single-pointing surveys cannot provide spatial information about the gas properties of clumps. Furthermore,

for cold clumps ($T_{dust} \sim 10$ K), the 1.3 cm NH₃ emission is linearly dependent on temperature ($\lambda \gg \frac{hc}{k_B T}$), while the submm and mm dust emission has an exponential dependence on temperature ($\lambda \sim \frac{hc}{k_B T}$). Consequently, molecular line surveys that target sources detected from the dust continuum may detect fewer cold, quiescent clumps than molecular line mapping surveys. Given that the open questions described in Section 1.3 require observations of clumps in early evolution states and evidence of spatial variations in gas properties, mapping surveys are necessary.

The H₂O Southern Galactic Plane Survey (HOPS; Walsh et al. 2011; Purcell et al. 2012) mapped a 100 deg² region of the Galactic plane in NH₃ using the 22 m Mopra telescope. Although the HOPS maps provided spatial information on the gas properties of clumps, Mopra’s angular resolution ($\sim 2'$) could only resolve the ~ 1 pc clump scale for the nearest ($d < 2$ kpc) sources. Furthermore, HOPS could not detect particularly cold, diffuse clumps due to significant beam dilution and the limited telescope collecting area. Dust continuum and molecular line surveys have characterized the properties of large samples of clumps. Yet, theoretical predictions concerning the gravitational collapse of clumps, gas flows within filaments, and the physical extent of the thermal, kinematic, and chemical effects of feedback remain inadequately tested by existing datasets.

A new, modern mapping survey in NH₃ was required to provide the data necessary to test theoretical predictions about the evolution of high-mass stars and molecular clumps. We designed RAMPS to provide the necessary maps of gas properties that are spatially resolved at the clump scale (~ 1 pc) for more distant sources ($d < 6$ kpc) than in previous surveys. Consequently, the RAMPS data, in conjunction with the complementary dust survey data, can help answer many of the open questions on the evolution of high-mass stars and molecular clumps.

In Section 2.2, I begin by discussing the survey design of RAMPS and the GBT observations. Subsequently, I present the data results of the RAMPS survey in Section 2.4. In Section 2.5, I analyze data from RAMPS and archival datasets to estimate clump gas properties, dust properties, distances, evolutionary states and H₂O maser properties. In Section 2.6, I compare the gas and dust properties of the RAMPS clump sample to the clump properties derived from previous molecular line and dust continuum surveys. Finally, I summarize my conclusions in Section 2.7.

2.2 Observations

This section describes RAMPS observations and details the reduction of the data. Section 2.2.1 describes the lines we selected for the survey, Section 2.2.2 describes the instrumentation, and Section 2.2.3 describes the observing strategy.

2.2.1 Line Selection

We used RAMPS observations to target 13 molecular lines, which are listed in Table 2.1. This dissertation will address the NH₃(1,1), NH₃(2,2), and H₂O (6_{1,6}–5_{2,3}) lines, since these are the most frequently detected and the most useful for determining the physical properties of molecular clumps.

2.2.1.1 NH₃ Inversion Line Emission

The NH₃ inversion transitions near 23 GHz have long been used as an important tool for estimating gas properties in molecular clumps (Cheung et al. 1968; Barrett et al. 1977; Ho et al. 1977). Unlike tracers of more diffuse gas such as CO, the NH₃ inversion transitions have higher critical densities ($n_{\text{crit}} \gtrsim 4 \times 10^3 \text{ cm}^{-3}$; Ho & Townes 1983), so they primarily trace the dense gas associated with molecular clumps, rather than the less dense gas associated with giant molecular clouds (GMCs).

In addition, the energy spacing of these NH₃ transitions (Appendix A) allow estimation of the NH₃ rotational temperature (T_{rot}) from line amplitude ratios. Thus, NH₃ observations can help directly estimate the gas temperature within dense molecular clumps. Furthermore, the hyperfine splitting (Appendix A) allows estimation of optical depths (τ) and NH₃ column densities (N_{tot}). These data can also provide the NH₃ fractional abundance via the ratio of N_{tot} and H₂ column density.

NH₃ also provides kinematic information, such as the velocity dispersion (σ) and the local standard of rest (LSR) velocity (V_{LSR}). The velocity dispersion provides a measure of the turbulence in molecular clumps, which can be used to determine the degree to which molecular clumps are unstable to gravitational collapse. Maps of σ can also reveal the physical extent of feedback from high-mass stars and protostars. Furthermore, the measured V_{LSR} of a molecular clump can be used to estimate its kinematic distance by comparison with a Galactic rotation curve (Reid et al. 2014). Distance is one of the most important derived parameters, since it is necessary to infer mass, size, and luminosity.

2.2.1.2 The 22.235 GHz H₂O Maser Line

The collisionally pumped H₂O maser line at 22.235 GHz (Cheung et al. 1969b) is another useful line for the study of molecular clumps, because it is known to trace active star formation. Although the exact evolutionary stage or stages probed by H₂O masers in star-forming clumps remain uncertain (Voronkov et al. 2010), H₂O masers are frequently found in high-mass SFRs, signaling the presence of shocks associated with the star formation process. They are, however, also seen toward low-mass SFRs, and could potentially indicate the existence of low-mass protostars in massive molecular clumps that do not yet harbor an HMP (Healy et al. 2004). H₂O masers are also associated with asymptotic giant branch (AGB) stars (Schwartz & Barrett 1971; Schwartz et al. 1974), which can be observed using VLBI techniques to study

Table 2.1. RAMPS molecular lines.

Molecule	Transition	Frequency (MHz)	E_{upper}/k (K)	Number of Receivers
NH ₃	(J, K) = (1,1)	23694.47	23	7
NH ₃	(J, K) = (2,2)	23722.60	64	7
NH ₃	(J, K) = (3,3)	23870.08	124	7
NH ₃	(J, K) = (4,4)	24139.35	201	7
NH ₃	(J, K) = (5,5)	24532.92	295	7
CH ₃ OH	$J_{K_p} = 10_1 - 9_2 A^-$	23444.78	143	7
HC ₅ N	$J = 9 - 8$	23963.90	6	7
HC ₅ N	$J = 8 - 7$	21301.26	5	1
HC ₇ N	$J = 19 - 18$	21431.93	10	1
CH ₃ OH	$J_{K_p} = 12_2 - 11_1 A^-$	21550.34	479	1
HNCO	$J_{K_p, K_o} = 1_{0,1} - 0_{0,0}$	21981.57	1	1
H ₂ O	$J_{K_p, K_o} = 6_{1,6} - 5_{2,3}$	22235.08	644	1
CCS	$J = 2 - 1$	22344.03	2	1

Note. — The quantum numbers given in the “Transition” column are J , the rotational quantum number, K , the projection of J along the molecular axis of symmetry, K_p , the value of K in the limiting case of a prolate spheroid molecule, and K_o , the value of K in the limiting case of an oblate spheroid molecule. CH₃OH 12₂ – 11₁ A^- is a rotational transition within the first vibrationally excited state, i.e., $v = 1$.

the dynamics of their atmospheres and winds (Spencer et al. 1979). Furthermore, masers are well suited for parallax measurements (Reid et al. 2014) since they are extremely luminous compact sources. Consequently, H₂O masers are particularly useful for measuring Galactic SFR distances, many of which are accurate to ~ 0.2 kpc at 5 kpc (Hachisuka et al. 2009; Honma et al. 2007).

2.2.2 Instrumentation

We utilized the Green Bank Observatory’s 100 m diameter Robert C. Byrd Green Bank Telescope (GBT; Prestage et al. 2009) for RAMPS observations. The GBT’s dish is large and fully steerable, which allows us to observe a large area with high angular resolution. We used the *K*-band Focal Plane Array (KFPA; Morgan et al. 2008), a seven-element receiver array that operates in the *K*-band frequency range of 18-27.5 GHz. Due to the GBT’s offset feed arm, each receiver has a beam pattern that is well represented by a Gaussian with minimal gain in the sidelobes, on the order of $\sim 10^{-3}$ times the gain at beam center. Each beam has a 35'' full width at half maximum (FWHM) at the rest frequency of NH₃(1,1) and a beam-to-beam distance of approximately 95'' (Figure 2.1). The receivers feed into the VErsatile GBT Astronomical Spectrometer (VEGAS; Anish Roshi et al. 2012), a spectrometer equipped for use with focal plane arrays. VEGAS is capable of processing up to 1.25 GHz bandwidth from eight spectrometer banks, each with eight dual polarized sub-bands.

2.2.3 Observing Strategy

One of the main advantages RAMPS offers is the utilization of a new observing mode available for use with the KFPA and VEGAS. While the KFPA has seven available receivers, the VEGAS back end supports eight spectrometer banks. Hence, six of the seven KFPA receivers can each feed into individual spectrometer banks, while the central receiver can feed into two spectrometer banks. With this spectral setup we used all seven of the KFPA’s receivers, with 13 dual polarized sub-bands and 23 MHz bandwidth per sub-band. The sub-bands were initially centered at $V_{LSR} = 0$ km s⁻¹, but were later shifted to $V_{LSR} = 30$ km s⁻¹ to fully capture emission at higher V_{LSR} . We observed with the “medium” spectral resolution, providing a channel width

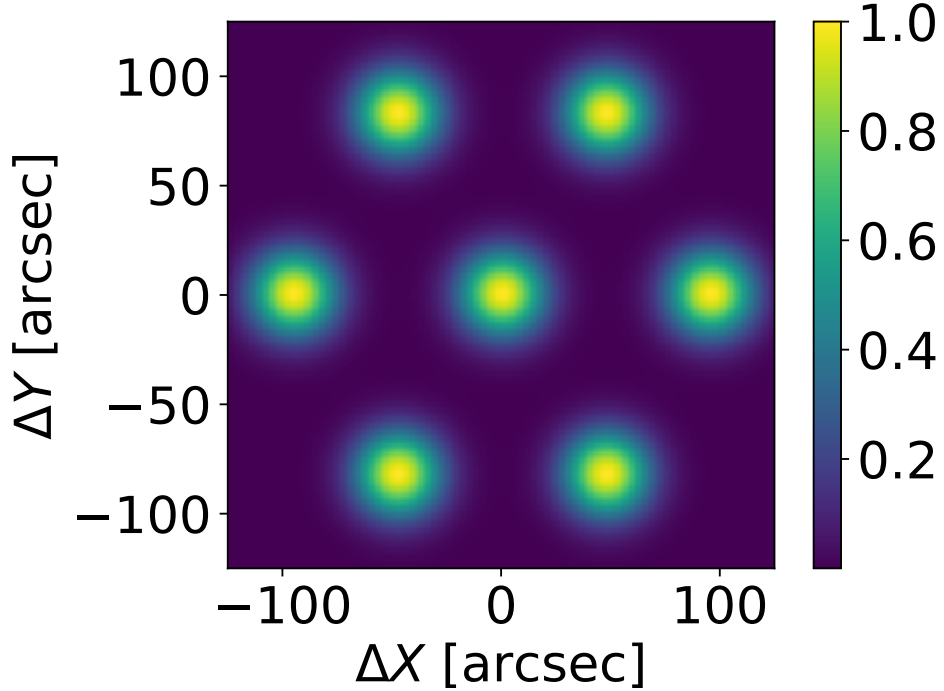


Fig. 2.1 Beam pattern of the KFPA. The color represents the sensitivity as a function of angle relative to the sensitivity at beam center. Each receiver has a Gaussian beam shape with an FWHM of $\sim 35''$ at the rest frequency of $\text{NH}_3(1,1)$, and the beam-to-beam distance is $\sim 95''$.

of 1.4 kHz ($\sim 0.018 \text{ km s}^{-1}$). We performed Doppler tracking using the $\text{NH}_3(1,1)$ rest frequency.

This unique setup allowed simultaneous observations of two spectral setups. The first spectral setup included the targeted lines with rest frequencies above 23 GHz, which were observed using all seven receivers. The second spectral setup included the targeted lines with rest frequencies below 23 GHz, which were observed using the central receiver. The list of targeted lines and the number of receivers used for each line is shown in Table 2.1. We observed the NH_3 inversion transitions using all seven receivers to achieve better sensitivity for the NH_3 data. Although the use of a single receiver rather than seven receivers for the H_2O observations resulted in less

sensitivity, H₂O masers are typically bright, and thus the GBT frequently detected this line. RAMPS also observed several other lines, and the number of receivers used for each line is shown in Table 2.1.

RAMPS observations covered 21.6 deg² of the Galactic mid-plane in the Galactic longitude (l) range $l = 9^{\circ}5 - 40^{\circ}5$, with additional observations at $l = 41^{\circ}, 43^{\circ}, 45^{\circ}, 47^{\circ}$, and $49^{\circ}5$. The maximum range in Galactic latitude (b) was $|b| \leq 0^{\circ}4$, with an excursion down to $b \sim -0^{\circ}6$ at $l = 25^{\circ}$. The survey region was broken up into $1^{\circ} \times 0^{\circ}8$ “fields” centered on integer-valued Galactic longitudes and 0° Galactic latitude.

RAMPS was initially awarded 210 hrs on the GBT for a pilot survey for the purpose of testing the feasibility of the project and helping commission VEGAS. Pilot survey observations were performed between 2014 March 16 and 2015 January 22. At the start of the pilot survey, we tested two different mapping schemes at fields centered at $l = 10^{\circ}$ and 30° . The first of these schemes divided fields into rectangular “tiles” of size $0^{\circ}25 \times 0^{\circ}20$, and the second divided fields into “strips” of size $1^{\circ} \times 0^{\circ}058$. The two schemes differed considerably in the quality of the resulting maps, mainly due to gain variations caused by differing elevations and weather conditions. Due to the long, thin shape of the strips, clumps were often too large to fit completely within the width of a single strip. A clump that was observed in two separate strips was thus observed in different weather conditions and at different elevations, which resulted in different noise conditions for different parts of the clump. Once the separate observations were combined to create a larger map, this resulted in “striping” artifacts in the mapping direction. Given that clumps usually fit completely within tiles, noise variations at map edges were less problematic for the tile division scheme. Although no mapping scheme can eliminate noise variations between maps that were observed in different conditions, we chose to map the rest of the survey region with tiles to reduce this effect. After the initial tests of the tiling

scheme, we adjusted the parameters for the size and position of the tiles to provide greater overlap between adjacent tiles and fields. Specifically, we increased the tile size to $0^{\circ}26 \times 0^{\circ}208$ and performed additional observations at the overlap regions between the fields already observed.

Tiles were observed in on-the-fly mapping mode, scanning in Galactic longitude, with 4 integrations beam $^{-1}$, 1 s integrations, and $0^{\circ}008$ between rows. Due to these mapping parameters, the sampling of a tile was uneven perpendicular to the scan direction. In addition, the angle of the KFPA with respect to the Galactic plane, which could not be designated by the observer, affected the sampling pattern. The uneven sampling pattern and its dependence on the array angle are displayed in Figure 2.2, which shows the expected integration time for each spectrum in a data cube assuming the KFPA configuration displayed in the lower left corner of each map. The angle of the array depends on the target's position in the sky; thus, different tiles were mapped with the array at different angles.

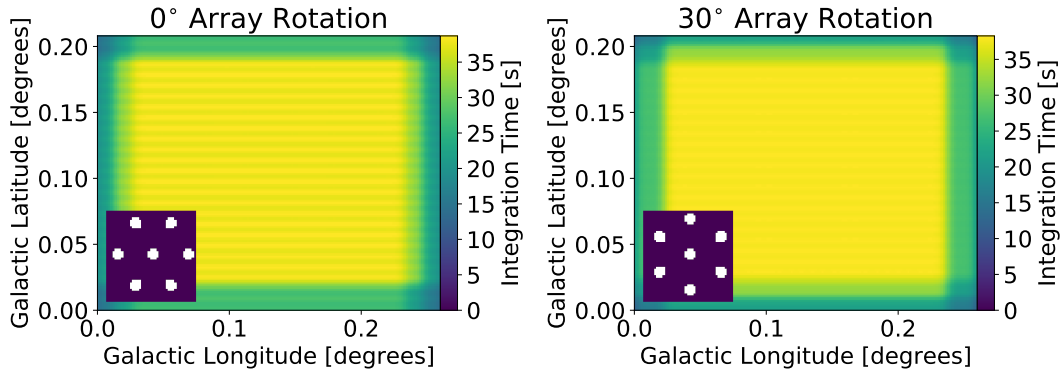


Fig. 2.2 The color shows the expected integration time for each spectrum in a data cube assuming the use of all seven beams and the KFPA configuration shown in the box at the lower left of each tile. An array rotation of 0° provided the least uniform sampling.

Observing an individual tile took approximately 1 hr. Before mapping a tile, we adjusted the pointing and focus of the telescope by observing a known calibrator with flux greater than 3 Jy at K band. This met the standard pointing calibration frequency of once per hour and provided a typical r.m.s. pointing error of $\sim 3''$ for a typical wind speed of 5 m s^{-1} . Before observing a new field, we also performed a single pointed observation (“on/off”) toward one of the brightest BGPS 1.1 mm sources in the field. These observations served as a test to ensure that the receiver and back end were configured correctly, as well as a way to evaluate system performance and repeatability over the observing season. A reference “off” observation was taken at an offset of 1° in Galactic latitude from the tile center immediately before and after mapping in order to subtract atmospheric emission. Although CO-emitting clumps can be found at $b > 1^\circ$ (Dame et al. 2001), observations of $^{13}\text{CO}(1\text{-}0)$ emission, a tracer of higher column densities than CO(1-0), imply that dense clumps are rarer at $b \sim 1^\circ$ (Jackson et al. 2006). Indeed, my inspection of the data showed only one tile had evidence of a persistent contaminating NH_3 signal in the “off” position. In this case, the contaminating signal was far enough away in velocity from any emission so as not to affect the analysis.

After completing the pilot survey, we were awarded additional time to map the remaining survey region. These observations were performed between 2015 December 5 and 2019 January 31. Although originally awarded 690 hr to complete the survey, the GBT’s divestment by the National Science Foundation drastically reduced the telescope time available for public use. Consequently, we were unable to execute a fully blind survey, so we adjusted our approach to account for the reduced observing time. Hogge et al. (2018) showed that the RAMPS $\text{NH}_3(1,1)$ emission matches the BGPS emission relatively well. Thus, we used BGPS maps to prioritize regions with obvious 1.1 mm continuum emission from multiple molecular clumps. Although this

biased the survey towards clumps that are brighter in dust emission, most of the clumps that were near the detection limit of BGPS were also near the detection limit of RAMPS. Because I could perform only limited analysis on such faint clumps, their absence should not significantly alter my analysis of the ensemble of RAMPS clumps. Prioritizing regions with significant BGPS emission allowed RAMPS to observe the largest sample of molecular clumps possible in the allotted time; hence, we chose this observing strategy for the remainder of the survey.

2.3 Data Reduction and Processing

I reduced RAMPS data cubes using the GBT Mapping Pipeline (Masters et al. 2011) and the `gbtgridder`¹. The reduction process calibrated and gridded the KFPA data to produce l,b,v data cubes (i.e., an array of data with two spatial axes in Galactic coordinates (l, b) and one velocity axis (v)). The mapping pipeline calibrated and processed the raw data into FITS files for each array receiver, sub-band, and polarization, and the `gbtgridder` gridded the data using a Gaussian kernel. The data cubes were gridded with a pixel size of $6''$ ($\sim 1/6$ FWHM beam width) and a channel width of 1.43 kHz ($\sim 0.018 \text{ km s}^{-1}$). For each spectrum, the `gbtgridder` determined a zeroth-order baseline from the average of a group of channels near the edges of the band. It then generated a baseline-subtracted data cube that I used for further analysis.

Before combining adjacent tiles, I cropped the data cubes along their spatial axes in order to remove pixels with no spectral data. I performed the spatial cropping using PySpecKit (Ginsburg & Mirocha 2011), a Python spectral analysis and reduction toolkit, utilizing the `subcube` function of the `Cube` class. I also cropped the data cubes along their spectral axis. The purpose of the spectral cropping was two-fold:

¹<https://github.com/nrao/gbtgridder>

to remove artifacts due to low gain at the edges of the bandpass, and to remove a portion of the NH₃ spectra at large negative velocities. Because the spectrometer sub-bands are bandpass filters, they have lower sensitivity at the band edges than at their centers. In addition, significant weather variations that occurred on timescales shorter than an hour could not be accounted for by the “off” observations taken before and after mapping a tile. The resulting spectra featured a steep cusp shape at the sub-band edges. Consequently, I cropped all spectra at their edges by $\sim 3\%$ of the total 1.25 MHz bandwidth. I performed additional cropping on the NH₃ spectra to remove unnecessary channels at large negative velocities. At the Galactic longitudes that RAMPS observes ($l = 10^\circ - 50^\circ$), CO emission occurs solely within the range $V_{LSR} = -60$ to 160 km s^{-1} (Dame et al. 2001). My inspection of the RAMPS NH₃(1,1) data revealed no significant emission at $V_{LSR} < -10 \text{ km s}^{-1}$, so I cropped the portion of the NH₃ spectra at $V_{LSR} < -30 \text{ km s}^{-1}$.

After cropping the edge channels, I regredded and combined adjacent data cube tiles within each field using the MIRIAD (Sault et al. 1995) tasks **REGRID** (version 1.17) and **IMCOMB** (version 1.11), respectively. In order to include the region of overlap between fields, I also combined adjacent fields and subsequently cropped each of these cubes to a width of $1^\circ 1$ in Galactic longitude to limit the file size. This process produced data cubes for each field centered at integer values of l with a $0^\circ 05$ region of overlap with the adjacent fields on either side. Next, I applied a median filter to the spectra to increase the signal-to-noise ratio (S/N), as well as to remove any anomalously large channel-to-channel variations. The original channel width of the RAMPS data cubes was 0.018 km s^{-1} . I smoothed the NH₃ data cubes along their spectral axis using a median filter with a width of 11 channels and resampled to produce a new channel width of 0.2 km s^{-1} . I chose this channel width to resolve, in at least five spectral channels, the FWHM line widths ($\Delta V \gtrsim 1 \text{ km s}^{-1}$) typically

observed in high-mass SFRs (Rathborne et al. 2016) and in infrared dark clouds (Sanhueza et al. 2012). I smoothed the H₂O data cubes using a median filter with a width of seven channels and resampled to produce a new channel width of 0.12 km s⁻¹. I chose a narrower channel width for the H₂O data to avoid blending the multiple narrow velocity components typical of H₂O masers. Because H₂O maser lines often have larger S/Ns than typical NH₃ lines, the narrower channel width did not significantly affect maser detections.

Next, I subtracted polynomial baselines from the spectra to remove any remaining bandpass shapes. Before fitting for a baseline, I masked any spectral lines that were present in the spectra, since these would influence the baseline fit if left unmasked. In principle, it is possible to utilize archival molecular line data to inform where to mask NH₃ emission in the RAMPS spectra. In practice, the large CO (Dame et al. 2001) and ¹³CO (Jackson et al. 2006) surveys exhibit multiple velocity components with broad line widths along many lines of sight. Given that NH₃(1,1) emission features strong hyperfine lines, further masking outside of the velocities with significant CO or ¹³CO emission would be required to mask the hyperfine emission. Thus, using the CO or ¹³CO emission to mask the RAMPS NH₃ spectra would severely limit the number of unmasked channels. Consequently, I chose to use the spectra to determine the channels with significant emission. I describe the details of the masking procedure in Appendix B.

After masking, I fit the spectra with zeroth, first, and second order polynomials and accepted the result with the smallest reduced χ^2 as the best-fit baseline. Finally, I subtracted the best-fit baselines from their respective spectra to produce baseline-subtracted spectra that were suitable for further analysis. I provide further details on the method and reliability of the baseline fitting in Appendix B.

2.4 Results

To estimate the noise in each spectrum, I masked spectral lines using the methods described in Appendix B and calculated the rms noise (σ_{rms}) of the masked spectra. This estimate includes a contribution from Gaussian noise, as well as from any residual baseline. Figure 2.3 shows histograms of σ_{rms} values for each spectrum in the RAMPS dataset. Because the NH₃ lines were observed using seven receivers, the median noise values are much lower than for the H₂O spectra. The exception are a small group of NH₃(1,1) and (2,2) spectra that have much larger errors than any of the H₂O spectra. This was caused by an instrumentation issue with one of the VEGAS banks, which added extra noise to small portions of the maps. Fortunately, these regions did not overlap with any signal, and so did not affect my analysis. Although later RAMPS observations no longer made use of the problematic bank, simultaneous observation of H₂O were no longer possible. Consequently, we did not observe the H₂O maser line for the last ten observing sessions of the survey.

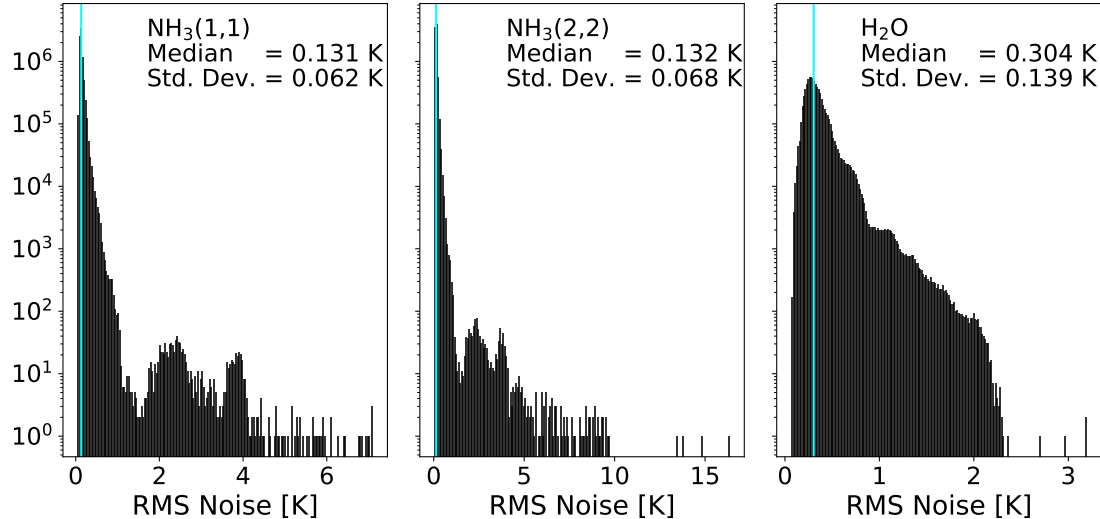


Fig. 2.3 Histograms of the rms noise for all RAMPS NH₃(1,1), (2,2), and H₂O spectra. The cyan lines show the median σ_{rms} values for each transition.

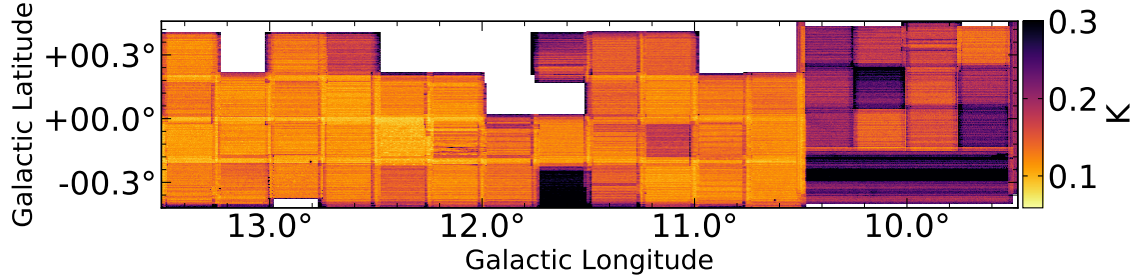


Fig. 2.4 Map of the rms noise in the $\text{NH}_3(1,1)$ spectra for fields L10 through L13.

Figure 2.4 shows an example $\text{NH}_3(1,1)$ noise map for the fields centered at $l = 10^\circ, 11^\circ, 12^\circ$, and 13° . The $\text{NH}_3(1,1)$ noise maps for the fields centered at $l \geq 14^\circ$, as well as the $\text{NH}_3(2,2)$ and H_2O noise maps for the full survey, are shown in Appendix C. Since spectra from tiles observed in poor weather or at low elevations have much higher noise, the noise can vary significantly from tile to tile. There is also evidence for noise variations within tiles due to the nonuniform integration time across a tile (Fig. 2.2). This effect is most significant in the H_2O data, since these maps are not fully sampled along the Galactic latitude axis by the single receiver.

Next, I determined the integrated intensity and first velocity moment of each spectrum. I masked each channel exhibiting a value less than $3\sigma_{rms}$ and additionally required each unmasked channel be contiguous with two other unmasked channels. The additional requirement of consecutive significant channels is meant to exclude channels with significant intensity that are purely a result of Gaussian noise. I then summed over the unmasked channels to obtain the integrated intensity in units of K km s^{-1} . Figure 2.5 shows an example $\text{NH}_3(1,1)$ integrated intensity map for the fields centered at $l = 10^\circ, 11^\circ, 12^\circ$, and 13° . The $\text{NH}_3(1,1)$ integrated intensity maps for the fields centered at $l \geq 14^\circ$, as well as the $\text{NH}_3(2,2)$ integrated intensity maps for the full survey, are shown in Appendix D. The integrated intensity maps reveal molecular clumps of various shapes and angular sizes. While a portion of the

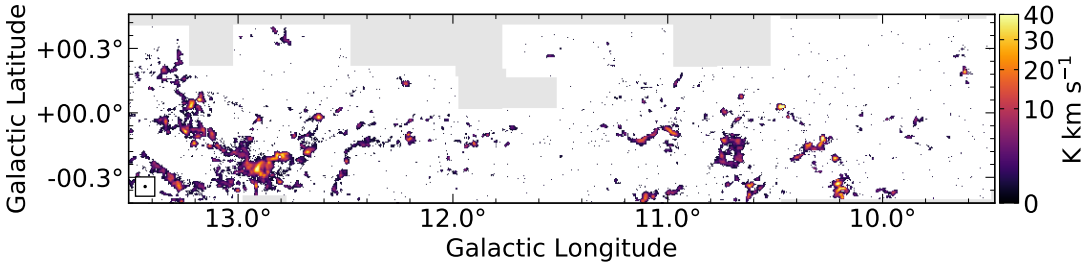


Fig. 2.5 Map of the $\text{NH}_3(1,1)$ integrated intensity for fields L10 through L13. The color mapping is on a logarithmic scale from 0 K km s^{-1} to 40 K km s^{-1} , where white represents a non-detection. The GBT beam size is shown in the lower left.

detected clumps seem to be grouped together in large complexes, many clumps are spread more uniformly across the surveyed area.

I used the same spectral mask employed for the integrated intensity calculation to determine the first velocity moment. The first moment of a spectrum is given by

$$\langle v \rangle = \frac{\sum v_i T_i}{\sum T_i}, \quad (2.1)$$

where T_i and v_i are the intensity and velocity of the i^{th} channel, respectively. Figure 2.6 shows an example $\text{NH}_3(1,1)$ first moment map for the fields centered at $l = 10^\circ, 11^\circ, 12^\circ$, and 13° . The $\text{NH}_3(1,1)$ first moment maps for the fields centered at $l \geq 14^\circ$ are shown in Appendix D. These maps show clumps with velocities in the range $V_{LSR} = -10$ to 140 km s^{-1} . In addition, the maps reveal groupings of clumps with similar velocities that signify large velocity-coherent structures.

2.5 Analysis

In this section, I present my analysis of data from both RAMPS and archival datasets. Section 2.5.1 describes my analysis of the molecular clumps and Section 2.5.2 describes my analysis of the H_2O masers.

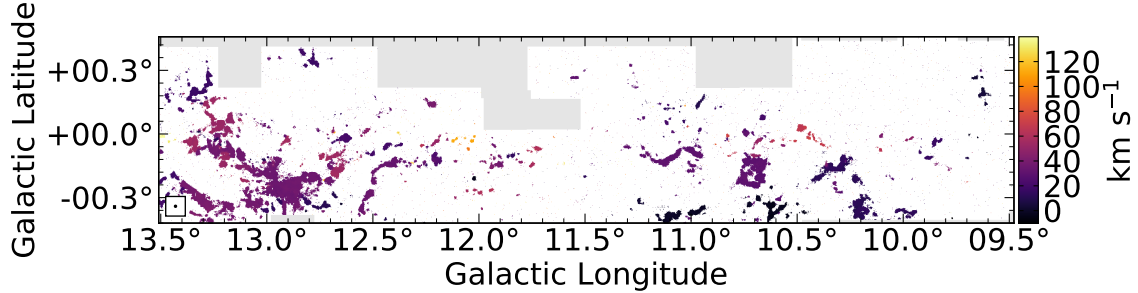


Fig. 2.6 Map of the $\text{NH}_3(1,1)$ first moment for fields L10 through L13. The color mapping is on a linear scale from -10 km s^{-1} to 135 km s^{-1} , where white represents a non-detection. The GBT beam size is shown in the lower left.

2.5.1 Clump Analysis

This section describes my analysis of the molecular clumps detected by RAMPS using NH_3 data and archival datasets. Section 2.5.1.1 details my custom clump-finding algorithm, Section 2.5.1.2 describes my analysis of the $\text{NH}_3(1,1)$ and $(2,2)$ data to estimate gas properties, Section 2.5.1.3 describes the adopted distance algorithm, and Section 2.5.1.4 details my analysis of FIR dust continuum data to estimate clump masses and luminosities.

2.5.1.1 The Sample of Molecular Clumps

Previous clump surveys have utilized various clump-finding algorithms to determine clump positions and sizes. Schuller et al. (2009) fit two-dimensional (2D) Gaussian profiles to the ATLASGAL $870 \mu\text{m}$ dust continuum emission. Although this analysis works well for compact sources, Figure 2.6 shows that many of the velocity-coherent structures detected by RAMPS are not well represented by 2D elliptical Gaussians. Molecular line mapping surveys have often utilized nonparametric clump-finding algorithms, such as Clumpfind (Williams et al. 1994), that search for emission connected in position-position-velocity (*ppv*) space. A similar analysis on $\text{NH}_3(1,1)$ data is complicated by the transition's bright satellite lines, which would

be recognized as additional clumps by most clump-finding algorithms. To overcome this, I designed a clump-finding algorithm that searched for signals displaying all five NH₃(1,1) nuclear quadrupole lines.

First, I increased the signal-to-noise in each spectrum using a rolling sum with a 1 km s⁻¹ window. For each channel in a spectrum, I summed those channels within the 1 km s⁻¹ window that had $T_B > \sigma_{rms}$. Next, I calculated the error on the summed channels as $\sigma_{sum} = \sigma_{rms}\sqrt{N_{chan}}$, where N_{chan} is the number of channels used to calculate the sum. I then located the channels with significant summed values ($> 3\sigma_{sum}$). Finally, I excluded significant channels that were not accompanied by significant channels at the velocity offsets of the NH₃(1,1) satellite lines ($-19.4, -7.7, +7.7, +19.4$ km s⁻¹). I undertook his step to isolate the channels associated with the main NH₃(1,1) line.

Although this method successfully identifies the NH₃(1,1) main line for emission with bright satellite lines, it fails when confronted with faint satellite line emission. Consequently, if there was no significant emission at the channels that matched the five line hyperfine pattern, I relaxed the criteria. Given that the inner pair of satellite lines are brighter than the outer pair, I excluded significant channels that were not accompanied by significant channels at the velocity offsets of the inner NH₃(1,1) satellite lines.

If there was also no significant emission from the inner satellite lines, then I did not exclude any significant channels and assumed that all channels with significant emission were associated with the main NH₃(1,1) line. This method is advantageous because it uses the satellite lines to differentiate emission from multiple sources, but is not limited to sources with strong satellite emission. I performed this analysis on each spectrum in each data cube and then searched for islands of contiguous emission in ppv space.

After identifying these islands of contiguous emission, I labeled their associated channels with unique identifiers to differentiate emission from separate clumps. This process produced three-dimensional (3D) “label cubes.” The channels in the label cubes were assigned either a value of zero, indicating that the channel was not associated with any clumps, or a nonzero integer value, which served as a unique clump identification number. I also collapsed the 3D labels along their velocity axes to produce 2D “label maps” for each clump. The purpose of this step was to easily identify the spectra that contained emission associated with a particular clump.

Although this process was successful at picking out emission from molecular clumps, it also found some spurious sources. This may be due in part to the non-Gaussian noise introduced by the masking process. To mitigate these false sources, I rejected sources with 3D label sizes less than 100 voxels and 2D label sizes less than 25 pixels. From a visual inspection of the remaining sources, the removal of the spurious detections was successful. The limiting size employed corresponded to an angularly unresolved source with a velocity dispersion of $\sigma \lesssim 0.3 \text{ km s}^{-1}$. Thus, this limitation has likely excluded only a small number of real sources.

I applied this clump-finding method to the entire RAMPS NH₃(1,1) dataset. Doing so yielded 2,680 molecular clumps. I determined the Galactic coordinates of each of the clumps using the corresponding 3D label cubes and data cubes to calculate their intensity weighted positions. Figure 2.7 shows histograms of l and b for the clumps. The distribution of l shows that most of the detected clumps have Galactic longitudes in the range $l = 23^\circ - 33^\circ$, which corresponds to the direction of the 5 kpc molecular ring that hosts most of the molecular gas within the solar circle (Scoville & Solomon 1975; Solomon et al. 1979). The b distribution appears more symmetric, but shows a clear offset from $b = 0^\circ$ with a mean of $\langle b \rangle = -0^\circ.041 \pm 0^\circ.004$. Given

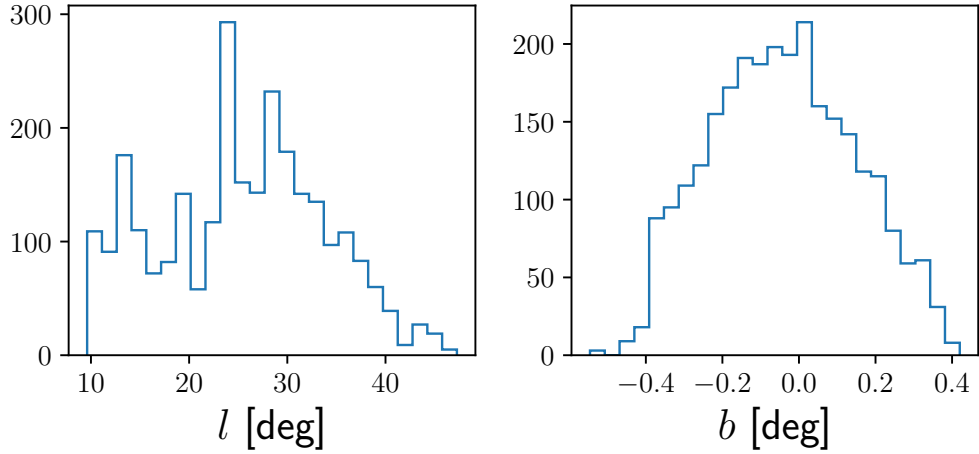


Fig. 2.7 Galactic coordinate histograms of the detected clumps. Left: Histogram of clump longitudes. Right: Histogram of latitudes.

that previous surveys have also detected more sources toward negative latitudes (e.g., Rosolowsky et al. 2010; Csengeri et al. 2014), this offset is likely genuine.

Next, I employed the 2D label maps to determine the angular sizes of the clumps. I defined the major axis diameter (θ_{maj}) as the angular distance between the two labeled pixels farthest apart, with the major axis defined as the axis connecting these pixels. I defined the minor axis diameter (θ_{min}) as the angular distance between the two pixels that formed an orthogonal line to the major axis and were farthest from each other at the midpoint of the major axis.

I also calculated the effective angular radius $\theta_{R,eff} = \sqrt{\frac{\Omega}{\pi}}$, where Ω is a clump's angular area. Figure 2.8 shows a histogram of $\theta_{R,eff}$ and a plot of θ_{maj} vs. θ_{min} . The $\theta_{R,eff}$ distribution exhibits a sharp cutoff near $\theta_{R,eff} \sim 17''$, which corresponds to the angular radius of a source unresolved by the GBT beam, and a tail that extends to a few hundred arcseconds.

The plot of θ_{maj} vs. θ_{min} displays colored symbol markers that indicate the density of points, which I estimated using the Gaussian kernel density estimator (KDE)

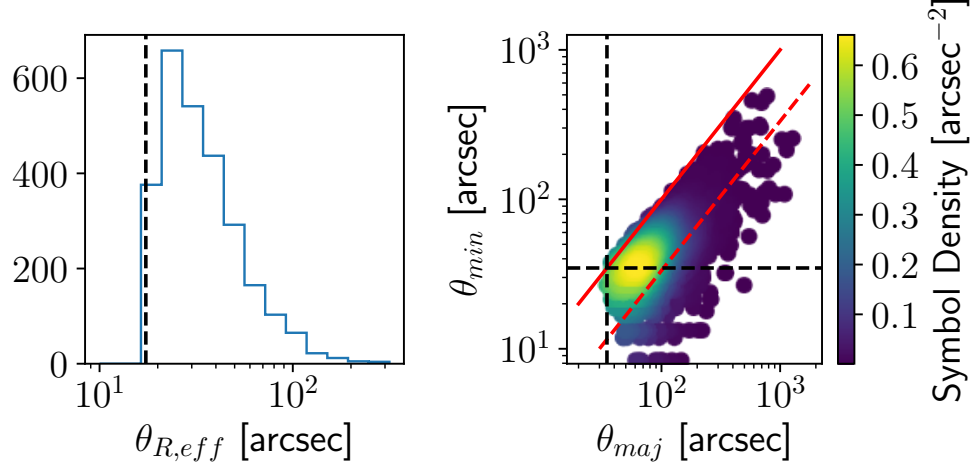


Fig. 2.8 Clump sizes in arcsecs. Left: Histogram of the angular radius $\theta_{R,eff}$. The black dashed line indicates the angular radius resolution limit. Right: Plot of the major and minor axis angular diameters θ_{min} vs. θ_{maj} , where the color represents the density of points determined from the Gaussian KDE on the linearly spaced data, the solid red line marks $\theta_{maj} = \theta_{min}$, and the dashed red line marks $\theta_{maj} = 3\theta_{min}$. The black dashed lines indicate the angular diameter resolution limits.

given by the `scipy.stats.gaussian_kde` function. The `gaussian_kde` function utilizes a Gaussian kernel with a size determined by the multivariate covariance matrix of the data multiplied by a scaling factor. The scaling factor depends on the number of data points and the number of dimensions in the dataset. I used the default kernel, which is given by Scott's Rule (Scott 1992). The result of the Gaussian KDE is a multidimensional probability density function. The density of points is obtained by multiplying the probability density function by the total number of points.

The plot of θ_{maj} vs. θ_{min} shows that most clumps are at least partially resolved by the GBT beam and many display a filamentary morphology ($\theta_{maj} > \theta_{min}$). The plot also shows that a sub-population of clumps display θ_{min} values below the angular resolution limit. This is an effect of the signal-to-noise cutoff, which excluded pixels with intensities below the noise threshold.

In order to test the completeness of the RAMPS clump sample, as well as the capabilities of my clump-finding algorithm, I created data cubes with synthetic clump emission and performed my clump-finding analysis on these data. To create the synthetic data, I first constructed a noise cube and a source cube separately. I emulated the spatial noise variations found in the real data by using as a template the $\text{NH}_3(1,1)$ σ_{rms} map from a field with an average noise equal to the RAMPS average. Next, I created the synthetic clumps using a spherically symmetric clump model with a constant volume density as a function of radius. I assumed typical clump properties: a radius of 1 pc, a velocity dispersion of $\sigma = 0.7 \text{ km s}^{-1}$, a temperature of $T_{rot} = 15 \text{ K}$, and a fractional NH_3 abundance of $\chi(\text{NH}_3) = 2 \times 10^{-8}$.

To test the completeness for different column density thresholds, I created synthetic clumps with three different masses: 100, 260, and 1600 M_\odot ², which correspond to average mass surface densities (Σ) of 6.7×10^{-3} , 1.7×10^{-2} , and $1.1 \times 10^{-1} \text{ g cm}^{-2}$, respectively. For each mass, I created 11,400 clumps that had random velocities and were evenly distributed among integer-valued distances in the range $d = 1 - 20 \text{ kpc}$. I accounted for beam dilution by convolving the synthetic emission with the GBT beam before adding it to the synthetic noise data cube.

Figure 2.9 shows the results of this analysis. RAMPS is 95% complete out to 15 kpc for 1600 M_\odot clumps and out to 8 kpc for 260 M_\odot clumps; thus, RAMPS should be sensitive to almost all high-mass star-forming clumps within 8 kpc. Although the detection of 100 M_\odot clumps in this analysis is severely noise-limited, such sources can be detected at farther distances if they have a higher column density than I have modeled while still remaining angularly resolved.

²Assuming a 30% star formation efficiency and a Kroupa (2001) initial mass function, the most massive stars produced by 100, 260, and 1600 M_\odot clumps are 4, 8, and 30 M_\odot , respectively (Sanhueza et al. 2017).

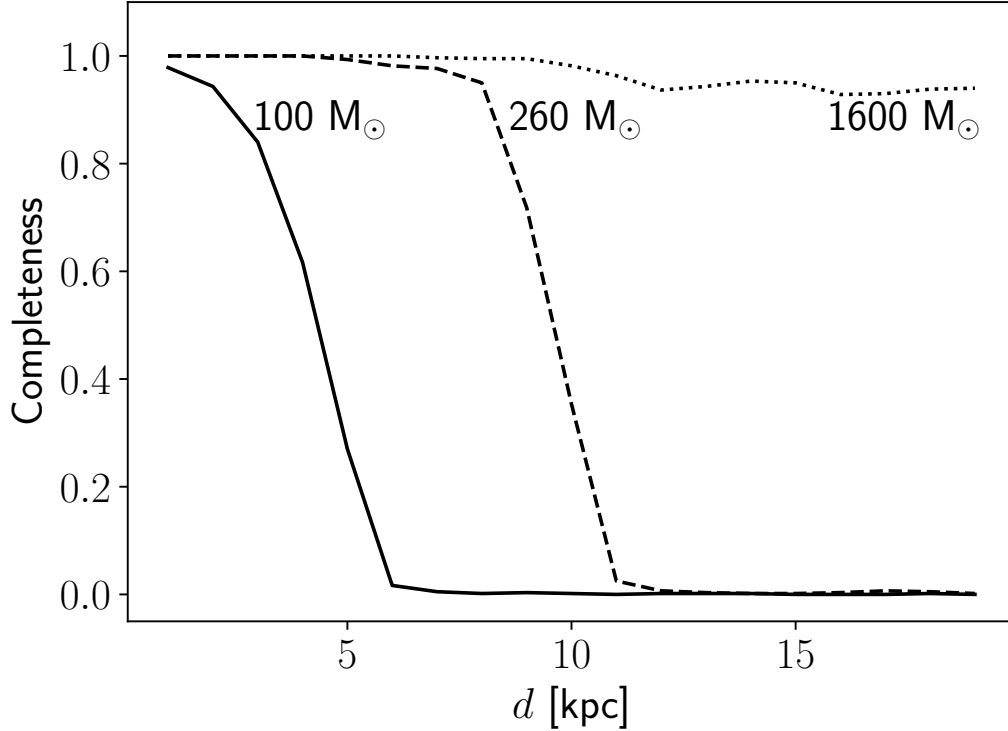


Fig. 2.9 Completeness as a function of distance for synthetic clumps with $T_{rot} = 15$ K, $R = 1$ pc, $\sigma = 0.7$ km s $^{-1}$, uniform density distributions, and masses of $M_{clump} = 100$ (solid), 260 (dashed), and $1600 M_\odot$ (dotted).

2.5.1.2 Gas Properties

The primary purpose of the NH₃ analysis was to use the NH₃(1,1) and (2,2) spectra to estimate the gas properties of molecular clumps, such as T_{rot} , N_{tot} , $\tau(1, 1)_0$, σ , and V_{LSR} . To calculate T_{rot} and N_{tot} , I used a PySpecKit NH₃ inversion line model and fitting routine.

As a preliminary step, I fit the NH₃(1,1) spectra to determine accurate σ and V_{LSR} values in order to initialize the PySpecKit fit routine near sensible values. This step allowed the PySpecKit fit routine to converge rapidly on the best-fit parameter values, rather than getting lost in a spurious local minimum in parameter space.

The preliminary fits of the NH₃(1,1) spectra have also provided measured values of σ , V_{LSR} , and $\tau(1,1)_0$ for all positions that display significant NH₃(1,1) emission, rather than only those that display significant NH₃(1,1) and (2,2) emission.

I used the 2D label map produced by the clump-finding algorithm to guide the NH₃(1,1) fitting procedure, such that I only attempted to fit a spectrum if it contained channels assigned to a clump. I detail the NH₃(1,1) line modeling in Appendix F. I ran the fit routine first with a single-component model. Some of the RAMPS spectra contain two sets of lines at different velocities, which represent two different molecular clumps along the line of sight. After the initial fit, I attempted a two-component fit on the spectrum. If either of the two-component fit amplitudes were less than three times the noise, or if their velocities did not correspond to that of a detected clump, I used the single-component fit as the best-fit model of the spectrum. Otherwise, I determined the more favorable model using the Bayesian Information Criterion (BIC; Schwarz 1978), which is given by $BIC = k \log(N) + \log(2\pi) + 2\log(\sigma_{rms}) + \chi^2$, where k is the number of free parameters and N is the number of independent data points. I adopted the two-component model (BIC₂) over the single-component model (BIC₁) if $BIC_2 < BIC_1 - 5$.

After the initial fit of the NH₃(1,1) spectra, I employed the PySpecKit NH₃ fitting routine. I utilized the `fiteach` function of the `cubes` class to fit the RAMPS NH₃(1,1) and (2,2) data cubes. This function takes in NH₃ inversion transition data cubes and fits them with an NH₃ model. I detail the simultaneous line modeling of the NH₃(1,1) and (2,2) lines in Appendix F. To ensure that I fit only pixels containing significant signal, I modified my clump-finding algorithm to search for contiguous NH₃(2,2) emission. I masked pixels that did not have significant NH₃(2,2) emission and a successful NH₃(1,1) fit. I used the initial fit of the NH₃(1,1) data to determine

whether to attempt a two-component fit and determined the more favorable model as with the NH₃(1,1) fits. Figure 2.10 shows a few examples of typical fit results.

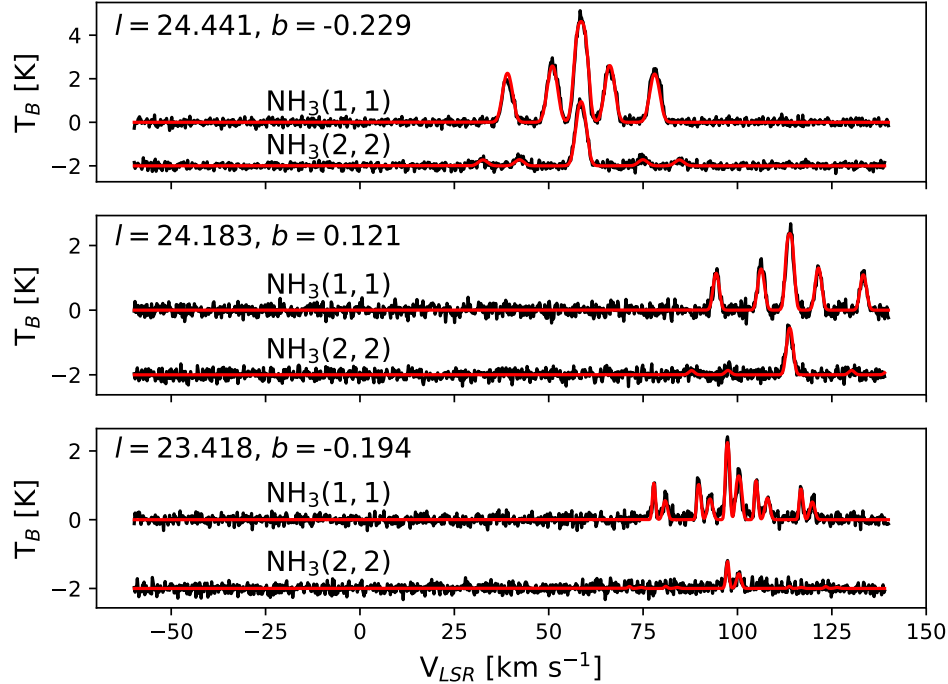


Fig. 2.10 Example fit results for three typical spectra. NH₃(1,1) and (2,2) spectra are shown in black and the fits are overplotted in red. The Galactic coordinates at the upper left in each panel indicate the positions of the spectra.

To help determine the reliability of the fit results, I plotted the 1σ error on the parameters against the parameter values in Figure 2.11. The top row shows T_{rot} and the Bouhafs et al. (2017) gas kinetic temperature (T_{kin}) given by

$$T_{kin} = T_{rot} \left[1 - \frac{T_{rot}}{T_0} \ln[1 + 1.608e^{-25.25/T_{rot}}] \right]^{-1}, \quad (2.2)$$

where $T_0 = 41.18$ K is the energy difference between NH₃(1,1) and (2,2). Because this relation only accounts for the NH₃(1,1), (2,1), and (2,2) states, it is only valid for $T_{kin} < 40$ K where the population in the higher K states is negligible.

Figure 2.11 shows that typical statistical errors on T_{rot} and T_{kin} are $\lesssim 1$ K, though they are larger at low ($T_{rot}, T_{kin} < 10$ K) and high ($T_{rot} > 25$ K, $T_{kin} > 35$ K) temperatures. Because $T_0 \sim 40$ K, the $\text{NH}_3(1,1)$ -to-(2,2) amplitude ratio is insensitive at $T_{rot} \gtrsim 40$ K. Consequently, high temperatures have large associated errors, while fits with low temperatures have larger errors due to the reduced signal-to-noise on the $\text{NH}_3(2,2)$ line. Overall, the T_{rot} and T_{kin} fit values are accurately determined, with 99% of both values exhibiting $S/N > 3$.

The second row of Figure 2.11 displays the errors on N_{tot} and the beam-averaged column density $N_{tot,ba} = \phi N_{tot}$. The N_{tot} plot shows a separation into two groups at $N_{tot} = 10^{15} \text{ cm}^{-2}$, which is the result of a degeneracy between ϕ and N_{tot} . Equations 3 and 6 in Appendix F show that at low optical depths the line brightness is linearly dependent on both ϕ and N_{tot} , resulting in lower errors on N_{tot} and higher errors on ϕ . Consequently, I have also reported $N_{tot,ba}$, which does not suffer from this degeneracy. The N_{tot} and $N_{tot,ba}$ fit values exhibit $S/N > 3$ for 90% and 85% of their respective values.

The third row of Figure 2.11 shows σ and V_{LSR} . These kinematic quantities are measured accurately, with typical errors of $\sim 0.03 \text{ km s}^{-1}$ for both σ and V_{LSR} . The σ estimates are very accurate, with 99% of the fit values exhibiting $S/N > 3$. The V_{LSR} values are accurate compared to the channel width ($\sim 0.2 \text{ km s}^{-1}$), with 96% of the fit values having an error $< 0.1 \text{ km s}^{-1}$.

The last row of Figure 2.11 shows the errors on ϕ and $\tau(1,1)_0$. Although the degeneracy between ϕ and N_{tot} is evident in the fits with very large errors on ϕ and very small errors on $\tau(1,1)_0$ at low optical depths, most of the errors are small compared to the parameter values. Indeed, the ϕ and $\tau(1,1)_0$ fit values exhibit $S/N > 3$ for 92% and 89% of their respective values. Given that a large percentage

of the parameter fit values are well determined, RAMPS data are a valuable tool to precisely estimate the physical properties of the detected molecular clumps.

2.5.1.3 Distances

Reliable distances (d) are crucial to infer many clump properties of interest (e.g., mass, luminosity, physical size), but distances are difficult to determine accurately. The two main methods of estimating clump distances are the kinematic distance method (Oort et al. 1958) and the maser parallax method (Reid et al. 2009). The kinematic distance method compares a clump’s LSR velocity to a Galactic rotation curve to determine the distance to the clump. The major limitation to this method is that within the Solar circle a given velocity corresponds to two distances, causing the so-called kinematic distance ambiguity (KDA). Previous studies have broken this degeneracy by searching for the presence or absence of 21 cm H I absorption or self-absorption lines (Wilson 1972). While these analyses are valuable, the results depend sensitively on the H I absorption detection threshold and the assumptions about the Galactic rotation curve (e.g., Wienen et al. 2015; Whitaker et al. 2017). Maser parallax observations allow an alternative method to determine clump distances. Although such observations provide the most accurate distances available, these data are more sparse since they require very long baseline interferometry (VLBI) observations and are limited to sources with strong maser emission.

Reid et al. (2016) introduced a method to estimate distances that incorporated kinematic distance information and maser parallax data. Parallax data from the Bar and Spiral Structure Legacy (BeSSeL) survey (Xu et al. 2013) and the Japanese VLBI Exploration of Radio Astrometry (VERA; Honma et al. 2012) projects have been used to model the Milky Way’s spiral arm structure (Reid et al. 2014). Reid et al. (2016) constructed a parallax-based distance calculator that takes into account spiral arm structure, kinematic distance, Galactic latitude, and location near a GMC

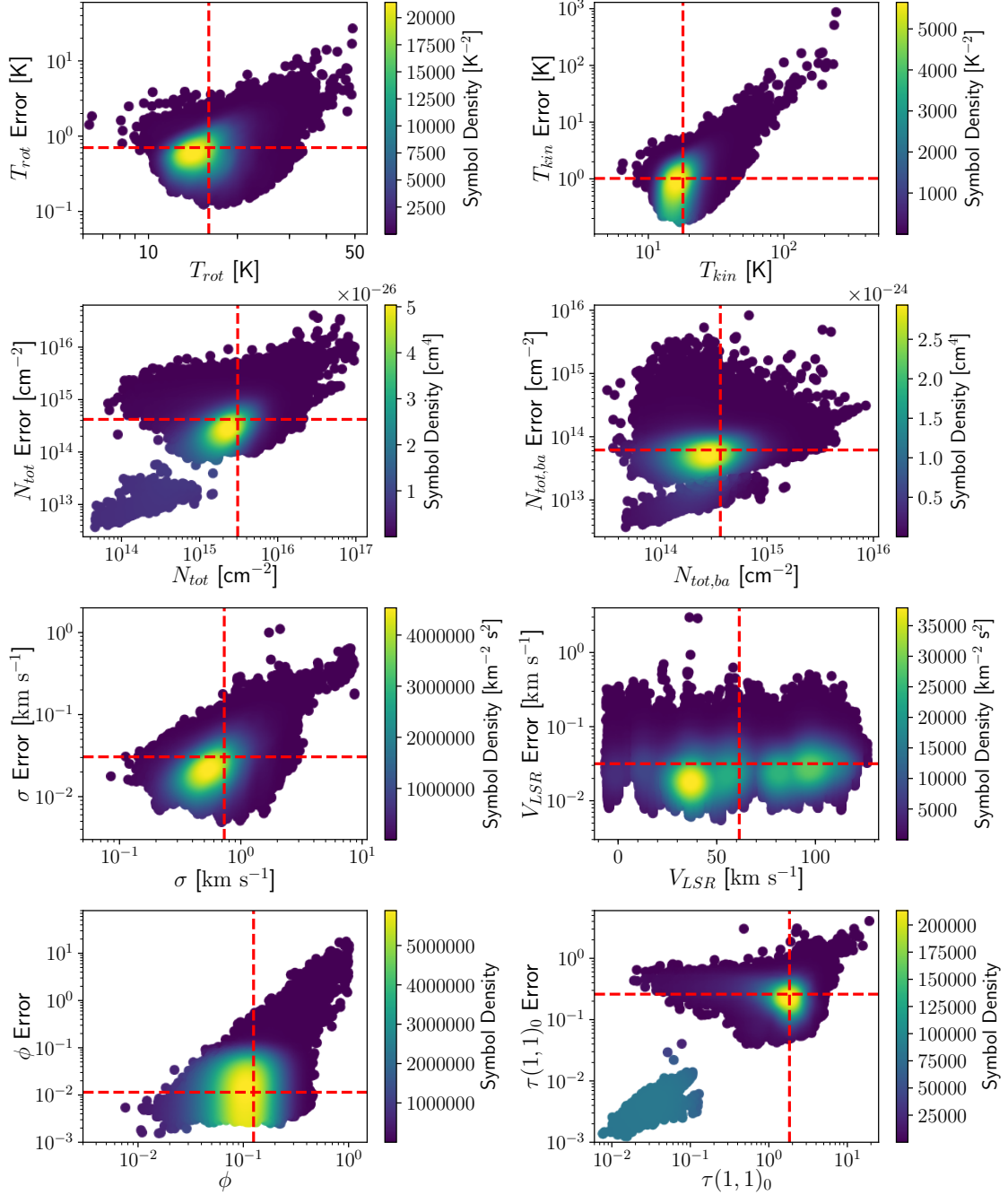


Fig. 2.11 Plot of parameter errors vs. parameter values for each free parameter, as well as T_{kin} , $N_{tot,ba}$, and $\tau(1,1)_0$, which are determined by free parameters. The color corresponds to the density of data points determined from the Gaussian KDE on the linearly spaced data. The median of the parameter value and the error on the parameter are shown by the dashed lines. From top left to bottom right the plots show errors for T_{rot} , T_{kin} , N_{tot} , $N_{tot,ba}$, σ , V_{LSR} , ϕ and $\tau(1,1)_0$.

with a known parallax measurement. Reid et al. (2016) employed a Bayesian statistical approach, which used the probability density functions (PDFs) of each of these distance estimators to create a total distance PDF. This approach provided the most probable distance and error, as well as the probability that a source was associated with a particular spiral arm.

To test this method, Reid et al. (2016) compared their distance estimates to distances determined by Anderson et al. (2012). Anderson et al. (2012) resolved the KDA for most of their sample of 149 H II regions using the H I absorption technique. Reid et al. (2016) tested their Bayesian method on a subset of 62 sources that Anderson et al. (2012) confidently assigned to the far kinematic distance. With no prior information about the near/far distance assignment, Reid et al. (2016) was able to assign distances with $> 90\%$ probability for 34 of the 62 sources. Of these 34 sources, the Reid et al. (2016) distance assignment matched the Anderson et al. (2012) assignment for all but six sources.

For three of these six sources, Reid et al. (2016) found that their most probable distances were near the end of the Galactic bar. Barred galaxies often feature non-circular streaming motions near their bars (Sellwood & Sánchez 2010), which can confuse the assignment of kinematic distances. For the remaining three sources, Reid et al. (2016) found an association with the near portion of the Sagittarius arm at ~ 2.1 kpc, rather than at the far kinematic distance of ~ 12 kpc. These sources have a Galactic longitude near $l = 34^\circ$, which would place them near the supernova remnant W44. The expansion motions associated with SNe can also create anomalous velocities that add systematic error to the resolution of the near/far KDA. Thus, the use of maser parallax data is a useful tool for resolving the KDA, particularly in the presence of non-circular motions.

Although this method only works for sources associated with spiral arms, high-mass star formation is strongly correlated with molecular gas in spiral galaxies (e.g., Loren et al. 1973; Wong & Blitz 2002; Bigiel et al. 2008). This correspondence suggests that the dense molecular clumps in which high-mass stars form and evolve are located in spiral arms, where the molecular gas densities are high. Since approximately half of the RAMPS clumps are expected to form at least one massive star ($M_{clump} \geq 260 M_{\odot}$), this is a valid assumption for many of the clumps in the RAMPS sample.

The Reid et al. (2016) distance algorithm uses a clump's Galactic coordinates, its V_{LSR} , and the error on its V_{LSR} to estimate its distance. I used the $\text{NH}_3(1,1)$ intensity weighted position, the average V_{LSR} , and half of the V_{LSR} range ($\frac{V_{max}-V_{min}}{2}$) of each clump as a conservative estimate of the velocity error. Figure 2.12 shows histograms of the two most probable distances (d_1, d_2), the errors on those distances ($d_{1,err}, d_{2,err}$), and the probabilities for each distance given by the distance PDF (p_1, p_2). Half of the clumps in the sample have moderately reliable distances ($p_1 > 75\%$) and a quarter have no probable alternative distances ($p_1 > 95\%$). The probabilities averaged over the ensemble of clumps are $\langle p_1 \rangle = 71\%$ and $\langle p_2 \rangle = 21\%$. Thus, the most probable distances are on average significantly more likely than the second most probable distances.

The main feature of the d_1 histogram is an excess of clumps at $3.5 - 5$ kpc, which corresponds to a region where the Aquila Spur and the end of the Galactic bar border the Scutum arm (Reid et al. 2014, and references therein). The rest of the clumps have distances in the range of $\sim 1 - 15$ kpc.

Figure 2.13 shows a face-on view of the clump sample's spatial distribution using the adopted distances. Given that the distance algorithm uses the spiral arm model to determine distances, it is no surprise that the clump positions follow the spiral

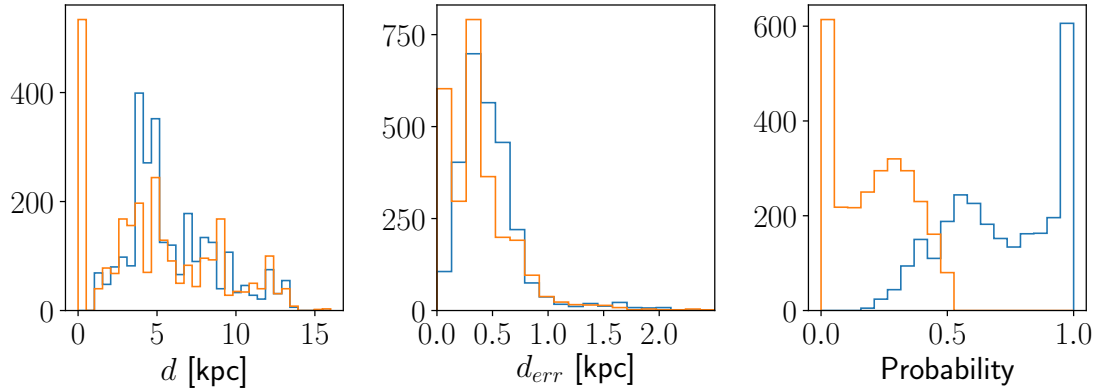


Fig. 2.12 Results of the distance calculation, where the first and second most probable distances are shown in blue and orange, respectively. Left: Histogram of clump distances, d_1 and d_2 . Middle: Histogram of the error on clump distances, $d_{1,err}$ and $d_{2,err}$. Right: Histogram of the probability of an accurate spiral arm association, p_1 and p_2 .

pattern displayed in Reid et al. (2016). On the other hand, the small errors (~ 0.3 kpc) and high probabilities for the distance estimates imply a strong correspondence between the locations of spiral arms and the kinematic distances for most of the clumps in the sample.

Accurate distances to clumps also allow the calculation of their physical sizes ($D_{maj} = d \times \tan(\theta_{maj})$, $R_{eff} = d \times \tan(\theta_{R,eff})$). Figure 2.14 displays clump sizes in parsecs. As expected from previous mapping surveys, the majority of clumps exhibit size scales of ~ 1 pc. The dearth of core-scale objects (~ 0.1 pc) reflects the RAMPS angular resolution, which corresponds to 0.8 pc at the median distance of 5 kpc. The largest sources in the sample, many of which show a filamentary morphology, often feature several sites of massive star formation. Determining the physical sizes and morphologies of clumps and filaments is essential to make progress on the many open questions about their dynamical, thermal, and chemical evolution.

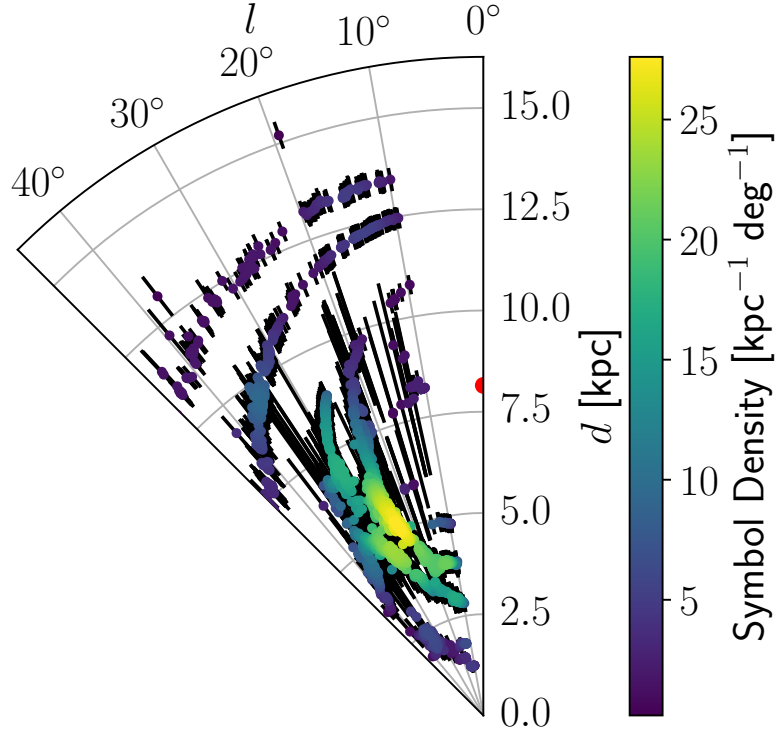


Fig. 2.13 North Galactic polar view of the clump spatial distribution using the adopted distances. The colors of the data points represent the density of clumps determined from the Gaussian KDE and the error on the distances are shown in black. The position of the Galactic center is shown with a red symbol marker.

2.5.1.4 Dust Properties

Dust continuum emission allows the inference of dust temperatures (T_{dust}), mass surface densities (Σ), clump masses (M_{clump}), and luminosities (L_{clump}), which are crucial to understanding the high-mass star formation process. In this section, I describe the construction and analysis of dust SEDs for the RAMPS sample of molecular clumps. Section 2.5.1.4.1 describes the construction of dust SEDs, Section 2.5.1.4.2 details the SED modeling, Section 2.5.1.4.3 describes the estimation of NH_3 abundances, and Section 2.5.1.4.4 describes the estimation of clump masses and luminosities.

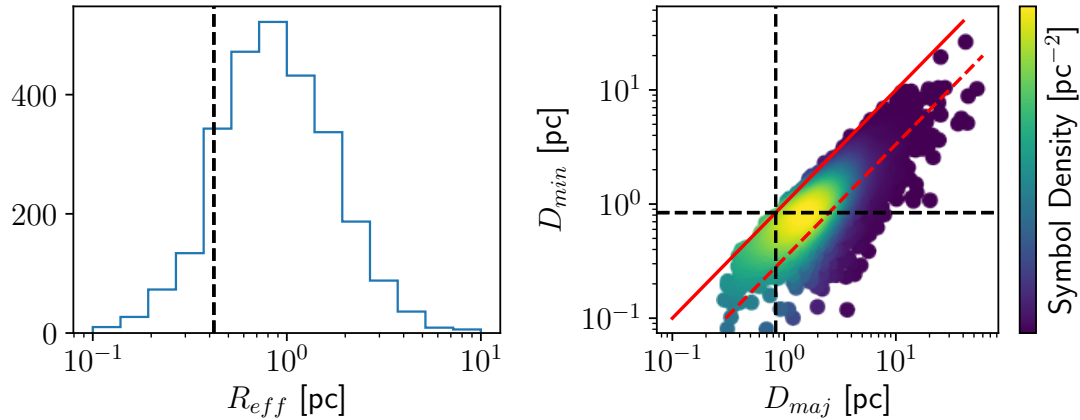


Fig. 2.14 Clump sizes in parsecs. Left: Histogram of R_{eff} . The black dashed line indicates the physical radius resolution limit for the median distance of $d = 5$ kpc. Right: Plot of D_{min} vs. D_{maj} with colors and lines as in Figure 2.8. The black dashed lines indicate the physical diameter resolution limit for the median distance of $d = 5$ kpc.

2.5.1.4.1 Dust SEDs

To construct and analyze dust SEDs, I followed the methodology described by Guzmán et al. (2015), who modeled the dust properties of the clumps targeted by the Millimeter Astronomy Legacy Team 90 GHz Survey (MALT90; Jackson et al. 2013). Guzmán et al. (2015) used Hi-GAL and ATLASGAL data to fit a single-temperature greybody dust SED model, which produced results consistent with previous SED modeling of molecular clumps. Because the densest molecular clumps can be opaque at $70 \mu\text{m}$, I did not use the Photometric Array Camera and Spectrometer (PACS; Poglitsch et al. 2010) $70 \mu\text{m}$ continuum data. To create the dust SEDs, I utilized the other Hi-GAL continuum bands: the PACS $160 \mu\text{m}$ continuum data and the Spectral and Photometric Imaging Receiver (SPIRE; Griffin et al. 2010) $250, 350$, and $500 \mu\text{m}$ continuum data. I also included the ATLASGAL $870 \mu\text{m}$ continuum data observed with the Large APEX Bolometer Camera (LABOCA; Siringo et al. 2009) on the

Table 2.2. FIR Data Characteristics

Survey	Instrument	Band (μm)	θ_{beam} (arcsec)	σ_{noise} (MJy sr $^{-1}$)
Hi-Gal	PACS	160	12.0	1.5
Hi-Gal	SPIRE	250	17.0	0.7
Hi-Gal	SPIRE	350	24.0	0.7
Hi-Gal	SPIRE	500	35.0	0.7
ATLASGAL	LABOCA	500	19.2	0.7

APEX telescope. Table 2.2 lists characteristic information about these datasets. In addition to the statistical error quoted in Table 2.2, I assumed a 10% error when comparing data in different bands, such as during SED modeling, to account for the calibration uncertainty of the SPIRE photometers ($\sim 5.5\%$) and the beam solid angle ($\sim 4\%$, Section 5.2.13 of the SPIRE Handbook).

I retrieved the Hi-GAL data using the Herschel Science Archive and generated 160, 250, 350, and 500 μm maps using the Herschel Interactive Processing Environment (HIPE). Given the extended emission detected from most RAMPS clumps, I applied the extended source calibration procedure (Section 5.2.5 from the SPIRE Handbook³) to the SPIRE maps. I downloaded the fully reduced and calibrated ATLASGAL 870 μm data from the ATLASGAL archive. Combining these data to create SEDs required further processing. Because each band has a different beam size, I first convolved the maps to a common resolution. I convolved the 160, 250, 350, and 870 μm maps to $35''$, the angular resolution of the 500 μm data, which is comparable to the resolution of the RAMPS NH₃ data. I performed the convolution on the Hi-GAL data using the Aniano et al. (2011) convolution kernels and I used a 2D Gaussian with FWHM = $\sqrt{35''0^2 - 19''2^2} \approx 29''.3$ for the ATLASGAL data.

³http://hereschel.esac.esa.int/Docs/SPIRE/spire_handbook.pdf

Next, I regridded the maps to place them all on the same spatial grid. The last step prior to constructing the dust SEDs is background subtraction of the Hi-GAL data. Although spatial filtering removes large-scale Galactic cirrus emission from the ATLASGAL data (Siringo et al. 2009), it nevertheless remains in the Hi-GAL data and must be removed (e.g., Battersby et al. 2011). The ATLASGAL spatial filtering removes uniform emission on scales greater than $\sim 2.5'$, so I performed a similar background subtraction on the Hi-GAL data.

I constructed the background maps using an iterative smoothing approach in order to create a background with flux variations less than 10% over angular scales less than $2.5'$. For the first iteration, I smoothed each image with a $30''$ Gaussian kernel. If a pixel in the smoothed map was $2\sigma_{noise}$ greater than the corresponding pixel in the original map, then I replaced the background pixel value with the pixel value in the original map. The smoothed map resulting from this first iteration then became the input map for the next iteration and the process was repeated. There were two criteria that end this procedure: (1) when the difference between successive iterations for each pixel was $< 5\%$ or (2) once 170 iterations were completed. Multiple convolutions with the same smoothing kernel increase the effective smoothing kernel to $\theta_{eff} = \sqrt{N}\theta$, where N is the number of iterations and θ is the size of the smoothing kernel. To create background images with flux variations less than 10% over angular scales less than $2.5'$, the effective smoothing kernel should have a width of $\sim 2.5'$ at 90% of the maximum, which corresponds to $FWHM \approx 6.5'$. The number of iterations required to reach this effective smoothing scale is $N = \left(\frac{6.5}{0.5}\right)^2 \approx 170$; thus, once the procedure reaches 170 iterations, the effective smoothing kernel will ensure that the background image features flux variations less than 10% over angular scales less than $2.5'$. If the procedure stops prior to completing 170 iterations due to pixel differences $< 5\%$ between successive rounds, the background estimation has already

recovered most of the significant large-scale emission. I estimated the large-scale background emission in this manner for each of the Hi-GAL bands and subtracted these backgrounds from the original data. Finally, I concatenated the convolved and background-subtracted Hi-GAL 160, 250, 350, and 500 bands and the convolved ATLASGAL 870 μm band to create dust SED data cubes of the entire RAMPS region.

2.5.1.4.2 Dust SED Modeling

The dust SED model is determined by only two free parameters: T_{dust} and Σ . Σ is proportional to the H₂ column density ($N(\text{H}_2)$), which is given by $N(\text{H}_2) = \frac{\Sigma}{\mu m_p} = 2.14 \times 10^{23} \frac{\Sigma}{[\text{g cm}^{-2}]}$, where $\mu = 2.8$ is the adopted mean molecular weight and m_p is the proton mass. The monochromatic intensity at a frequency ν is

$$I_\nu(T_{dust}, \Sigma) = B_\nu(T_{dust})(1 - e^{-\kappa_\nu \Sigma \mathbb{R}}), \quad (2.3)$$

where $B_\nu(T_{dust})$ is the Planck function at T_{dust} , \mathbb{R} is the gas-to-dust mass ratio, and κ_ν is the dust absorption coefficient. I assumed a typical gas-to-dust mass ratio of $\mathbb{R} = 100$ and that $\kappa_\nu = \kappa_0(\nu/\nu_0)^\beta$, where β is the dust spectral index (Hildebrand 1983). Combining the equation for κ_ν with Equation 2.3 results in

$$I_{\nu_1}/I_{\nu_2} = (\nu_1/\nu_2)^{\beta+2}, \quad (2.4)$$

which provides a method for estimating β . Guzmán et al. (2015) used Equation 2.4 to estimate β for 14 sources and found a mean of $\beta = 1.6$ with a dispersion of 0.5. Although the dispersion is large, it is consistent with a 15% flux uncertainty, which is comparable to the assumed 10% flux uncertainty. The measured β agrees with the Ormel et al. (2011) dust coefficient model for silicate-graphite grains with 3×10^4

years of coagulation and no ice mantles. In principle, it is possible to fit T_{dust} , Σ , and β simultaneously, but it requires better spectral sampling below 500 GHz to break the degeneracy between T_{dust} and β (Shetty et al. 2009a,b; Juvela & Ysard 2012). Consequently, I adopted $\beta = 1.6$ for the SED modeling.

To fit the SEDs, I minimized the χ^2 , which is given by

$$\chi^2(T_{dust}, \Sigma) = \sum_{\nu} \frac{(I_{\nu,obs} - I_{\nu,mod})^2}{\sigma_{noise,\nu}^2}, \quad (2.5)$$

where the sum is taken over the utilized bands, $I_{\nu,obs}$ is the observed flux, and $I_{\nu,mod}$ is the model flux after weighting by the respective bandpass. Although I used all five bands for most of the SED fits, in some cases the background-subtracted 160 μ m data were negative where there were valid data for the other bands. Pixels without significant 160 μ m data tended to be associated with colder clumps, whose temperatures and surface densities can be estimated solely from the longer wavelength data. Consequently, I fit pixels with negative 160 μ m fluxes by excluding this band from the minimization.

Next, I estimated the error on T_{dust} and Σ . I started by calculating the function $\Delta\chi^2 = \chi^2 - \chi^2_{min}$. The projection of the $\Delta\chi^2 = 2.3$ contour onto the T_{dust} and Σ axes provides an estimate of the 1σ uncertainty on these parameters (Lampton et al. 1976). These errors are sufficiently characterized by the following equations

$$\begin{aligned} \sigma_{T_{dust}}^- &= \eta_{10}(0.3 - 0.4T_{10} + 0.4T_{10}^2), \\ \sigma_{T_{dust}}^+ &= \eta_{10}(1.1 - 1.3T_{10} + 0.7T_{10}^2), \\ \sigma_{\log(\Sigma)} &= \eta_{10}(0.03 - 0.03\log(\Sigma)), \end{aligned} \quad (2.6)$$

where $T_{10} = T_{dust}/(10 \text{ K})$ and η_{10} is the adopted calibration error in units of 10%. Finally, I regridded the T_{dust} and Σ parameter maps to match the RAMPS grid.

The clump-averaged and peak values of T_{dust} and Σ for the RAMPS sample of molecular clumps are shown in Figure 2.15. The inferred clump-averaged dust temperatures are similar to previous studies, but the RAMPS clumps have lower column densities on average than the MALT90 sources analyzed by Guzmán et al. (2015). This discrepancy is likely a result of their ATLASGAL flux-limited sample, which excluded very diffuse clumps.

Next, I compared the T_{kin} values derived from NH₃ and the T_{dust} values derived from the dust SEDs. Figure 2.16 displays T_{kin} vs. T_{dust} for each pixel with valid values for both properties. It is often assumed that collisions maintain thermal coupling between the gas and dust at the densities typical of molecular clumps ($\sim 10^4 \text{ cm}^{-3}$), but these data demonstrate that this assumption is inaccurate for certain temperature regimes. Although the plot of T_{kin} and T_{dust} exhibits significant scatter, the data show a clear trend with a slope less than unity. At $T_{dust} < 12 \text{ K}$, the majority of the data show $T_{kin} > T_{dust}$ and at $T_{dust} > 20 \text{ K}$ the data show $T_{kin} < T_{dust}$. Merello et al. (2019) compared the gas and dust temperatures from several targeted NH₃ surveys and observed a similar trend.

Two processes may be responsible for this behavior: the depletion of coolant molecules at low temperatures and the stochastic heating of small dust grains at high temperatures. Cooling calculations by Goldsmith (2001) predicted that in cold ($T_{dust} \sim 10 \text{ K}$) molecular gas, the freeze out of molecules onto dust grains would significantly limit radiative gas cooling. If the gas was also diffuse ($n \leq 10^4 \text{ cm}^{-3}$), poor gas-dust coupling would result in $T_{kin} > T_{dust}$.

Stochastic heating of dust grains at higher temperatures can produce the opposite effect (Draine & Li 2001). When a small grain absorbs a photon, its energy can increase above kT_{kin} . Because dust emission is strongly dependent on temperature, most of this energy is emitted at $E > kT_{kin}$, skewing T_{dust} toward higher values when

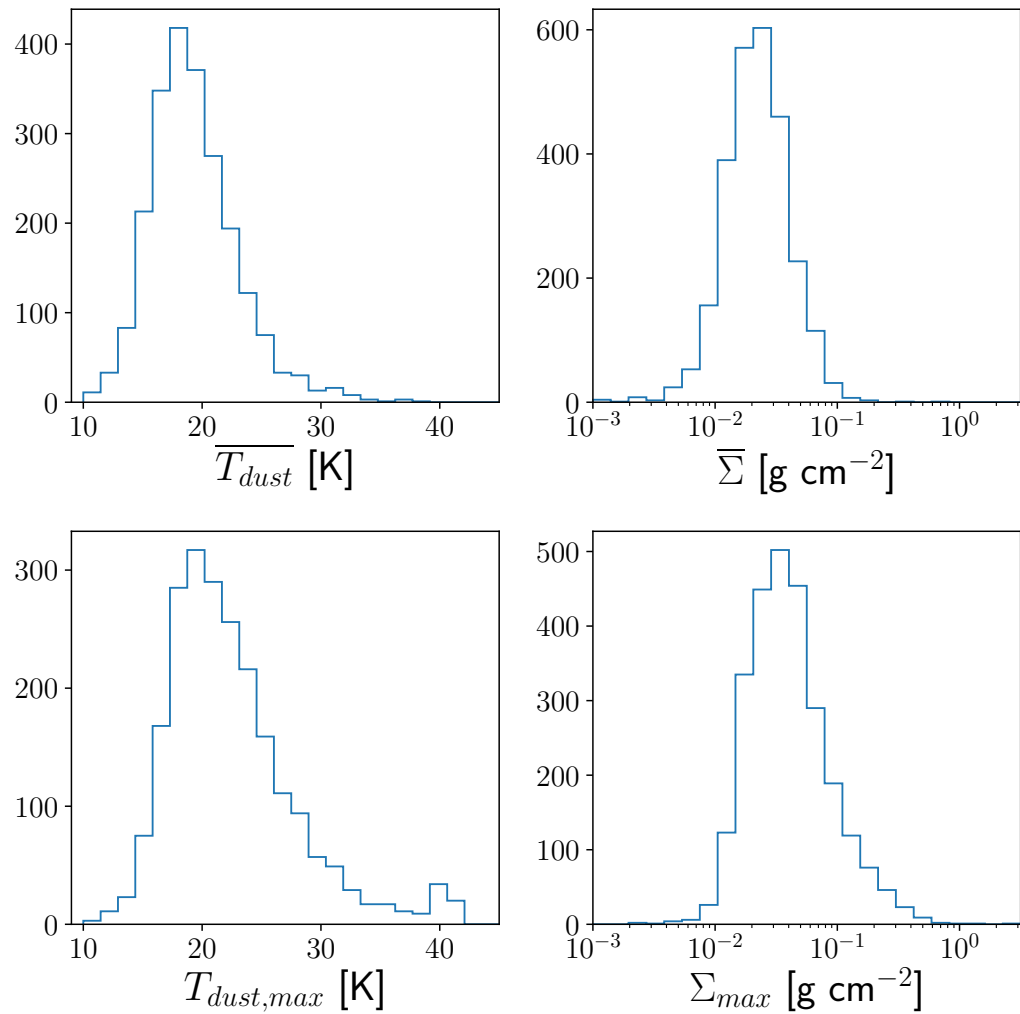


Fig. 2.15 Histograms of the clump-averaged T_{dust} (top left), the clump-averaged Σ (top right), the maximum T_{dust} (bottom left), and the maximum Σ (bottom right) for the RAMPS sample of clumps.

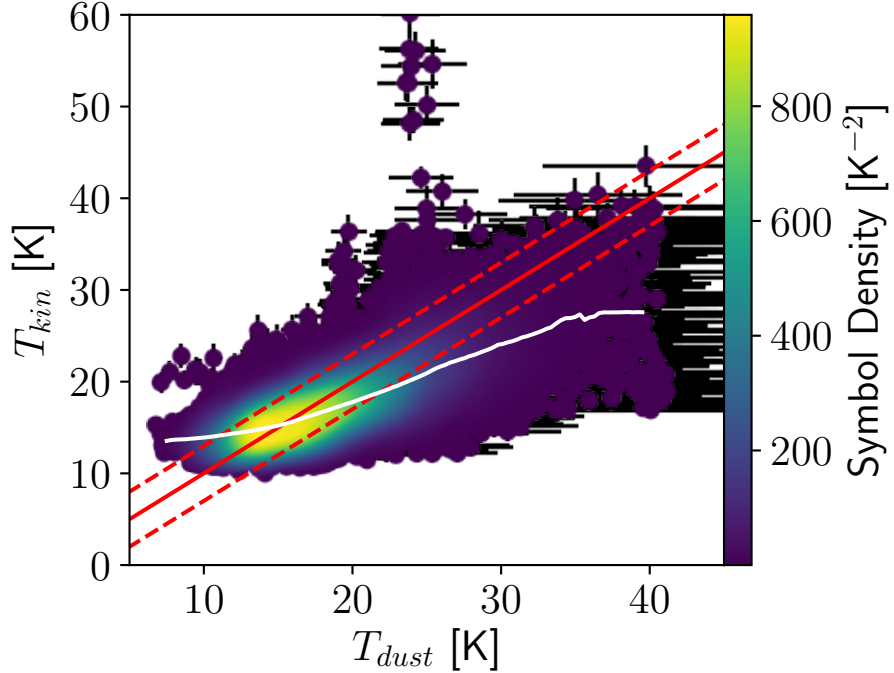


Fig. 2.16 Plot of T_{kin} vs. T_{dust} , where each point represents an individual pixel. Symbol color represents the density of points, the solid red line indicates $T_{dust} = T_{kin}$, the dashed red lines indicate $T_{dust} = T_{kin} \pm 3$ K, and the white line shows a rolling median with a 5 K window width.

radiative heating is important. This effect would be enhanced in gas heated by a (proto)stellar source, resulting in $T_{kin} < T_{dust}$ for warmer dust ($T_{dust} > 20$ K).

2.5.1.4.3 NH₃ Fractional Abundance

I also calculated the NH₃ fractional abundance $\chi(\text{NH}_3) = N(\text{NH}_3)/N(\text{H}_2) = (N_{tot,bu}\mu m_p)/\Sigma$, where $\mu = 2.8$ is the mean molecular weight and m_p is the proton mass. The gas chemistry in molecular clumps is affected by the freeze out of molecules onto dust, the release of these molecules back to the gas phase as HMPs heat their surroundings, and chemical reactions with other species. Figure 2.17 displays the

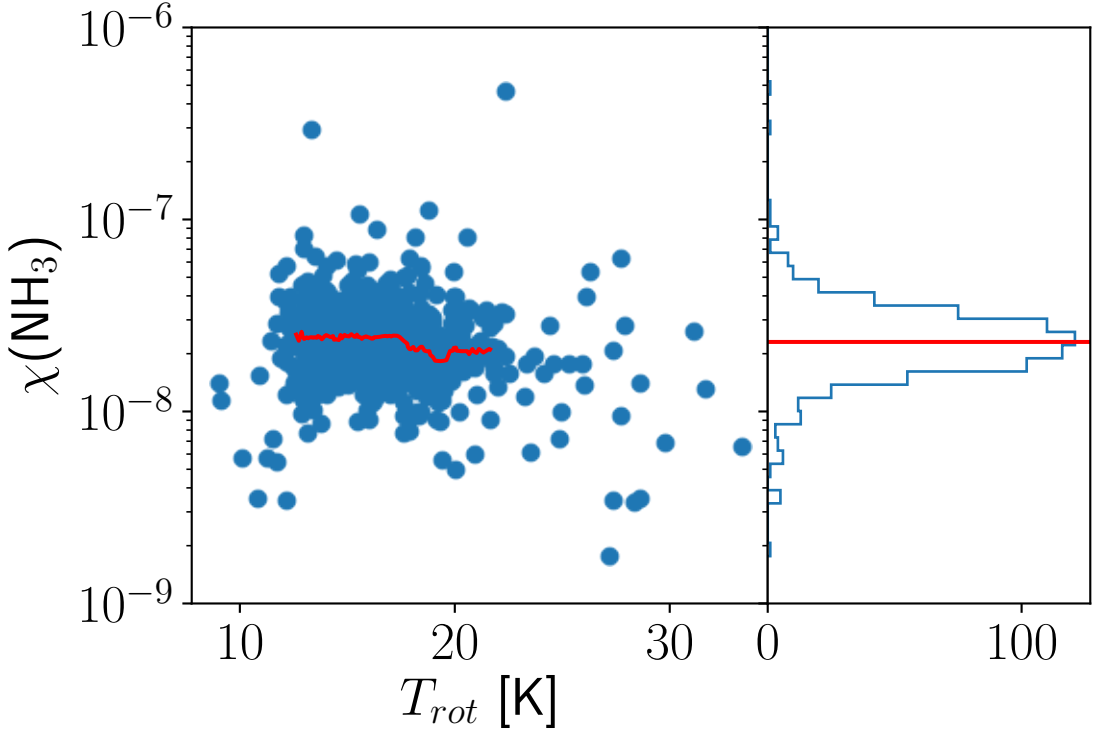


Fig. 2.17 Left: Plot of $\chi(\text{NH}_3)$ vs. T_{rot} , where the red line shows a rolling median with 1 K width. Right: Histogram of $\chi(\text{NH}_3)$, where the red line shows the median value of $\chi(\text{NH}_3) = 2.30 \times 10^{-8}$.

clump-averaged values of $\chi(\text{NH}_3)$ vs. T_{rot} and a histogram of $\chi(\text{NH}_3)$. The rolling median overlaid on the $\chi(\text{NH}_3)$ data shows no significant trend with T_{rot} , implying that if HMPs and massive MS stars are significantly changing the chemistry of their clumps, it is not sufficiently widespread to change the clump-averaged values. In Chapter 4, I further investigate the relationship between radiative feedback and NH_3 chemistry by comparing radial profiles of T_{rot} and $\chi(\text{NH}_3)$ for the protostellar and H II region clumps. The histogram of clump-averaged $\chi(\text{NH}_3)$ shows values in the range 2×10^{-9} to 5×10^{-7} with a linear median of 2.3×10^{-8} . These values are consistent with Merello et al. (2019), who found a comparable range and a median value of $\chi(\text{NH}_3) = 1.46 \times 10^{-8}$.

2.5.1.4.4 Clump Masses and Luminosities

Next, I used the distances estimated in the previous section to calculate M_{clump} and L_{clump} . To calculate M_{clump} , I summed the Σ values over the extent of each clump and used the distances to translate surface densities to masses. The calculation of L_{clump} requires an additional assumption that all stellar radiation is reprocessed by the dust and emitted at longer wavelengths. Given that dense molecular clumps have large visual extinctions, this is a reasonable assumption. I used the Contreras et al. (2017) formula for luminosity given by

$$L_{clump} = 40L_\odot \left(\frac{T_{dust}}{10 \text{ K}} \right)^{5.7} \left(\frac{d}{\text{kpc}} \right)^2 \left(\frac{\Omega_S}{\text{arcmin}^2} \right) \left(\frac{\Sigma}{\text{g cm}^{-2}} \right) C(T_{dust}, \Sigma), \quad (2.7)$$

where Ω_S is the source solid angle and $C(T_{dust}, \Sigma) = (1 + 1.6 \times 10^{-3} \Sigma T_{dust}^{1.7})^{-1}$ is a factor that corrects for opacity and dust temperature effects. The derivation of Equation 2.7 is described in Appendix A of Contreras et al. (2017).

Figure 2.18 shows the distributions of M_{clump} and L_{clump} for clumps with moderately reliable distances ($p_1 > 0.75$). The distributions for this subset of the RAMPS sample contain more low mass, low luminosity sources than the Contreras et al. (2017) sample. This is likely a consequence of comparing the results of the flux-limited, targeted MALT90 survey to those of a large area survey like RAMPS. In the following chapters I will use the dust-derived properties to test theories of the thermal, chemical, and kinematic evolution of molecular clumps.

2.5.1.5 Evolutionary Classification

To investigate the evolution of molecular clumps, I first classified them based on the presence or absence of HMPs and H II regions. Previous work has shown that MIR emission is a useful probe of a clump's evolutionary state (e.g., Jackson et al.

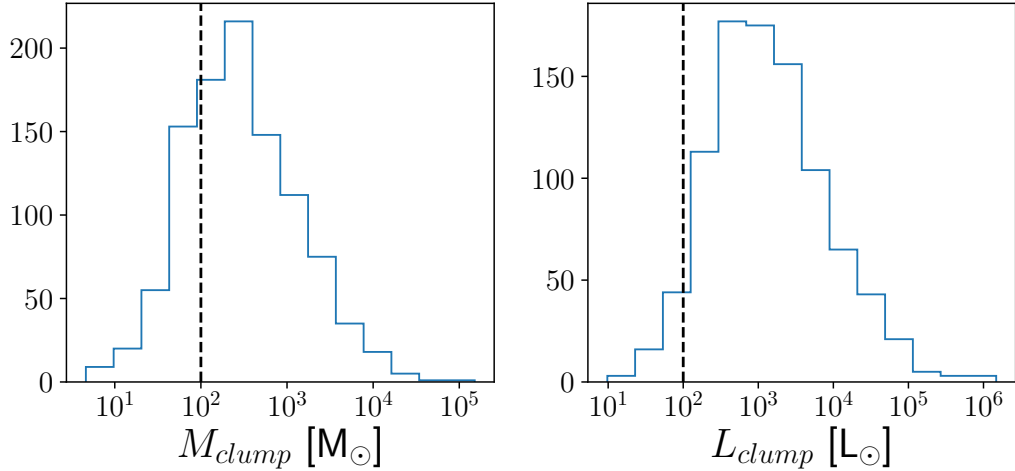


Fig. 2.18 Histogram of M_{clump} and L_{clump} for clumps with reliable distances ($p_1 > 0.75$). Left: The black dashed line indicates the 85% mass completeness limit for a spherical, uniform density clump with a radius of $R = 1$ pc at a distance of $d = 3$ kpc. Right: The black dashed line indicates the corresponding luminosity of a $M = 100 M_\odot$ clump with a radius of $R = 1$ pc and an average dust temperature of $T_{dust} = 15$ K.

2013; Guzmán et al. 2015). Cold, dense molecular clumps, the precursors to massive stars and stellar clusters, are opaque at MIR wavelengths and so are referred to as infrared dark clouds (IRDC; Rathborne et al. 2006). Once HMPs form, they warm the surrounding gas and dust, resulting in bright 24 μm emission. HMPs eventually head toward the MS in HR diagrams. High-mass MS stars emit significant UV emission and form H II regions. The UV radiation field emitted by massive stars also causes the fluorescent excitation of polycyclic aromatic hydrocarbons (PAHs), which exhibit strong emission features near 8 μm (Puget & Leger 1989).

Following the procedure outlined in Jackson et al. (2013), I used GLIMPSE 3.6 and 8 μm data and MIPSGAL 24 μm data to classify RAMPS clumps into five categories: quiescent, protostellar, H II region, photodissociation region (PDR), and unknown. I classified clumps as quiescent if they were MIR dark and did not host sources of MIR emission. I classified clumps as protostellar if they were mostly MIR

dark, but featured compact 24 μm emission. I classified clumps that featured bright 8 and 24 μm emission with a “bubble” morphology as H II region clumps. Although I did not confirm whether these sources were indeed H II regions, Anderson et al. (2011) performed follow-up radio recombination line observations of candidate H II regions and concluded that nearly all MIR “bubble” sources were likely H II regions. I classified clumps within 8 μm -bright PDR shells surrounding H II regions as PDR clumps. Although the PDR classification pertains more to environment than to evolution, the differing dust properties of PDR clumps (Guzmán et al. 2015) suggest that they belong to a separate class of clumps. Finally, I classified any clumps that did not fit into these categories as unknown clumps. This was the broadest category, since it included 24 μm -dark, 8 μm -translucent clumps that did not fit in the quiescent class, as well as clumps whose evolutionary state was ambiguous due to multiple clumps or MIR sources along the line of sight.

Although it is difficult to estimate the uncertainty associated with this classification scheme, I reassessed the classifications over different days to reduce this uncertainty. I changed the classifications of only a handful of clumps that were originally classified as quiescent, protostellar, or H II region clumps. On the other hand, it was sometimes difficult to determine whether 8 μm PAH emission was associated with clumps in the PDR class or whether this emission was in the foreground. Consequently, ~ 100 clumps that I originally classified as PDR clumps I later reclassified to the unknown category. My classification of the 2,680 clumps in the RAMPS sample resulted in 309 (12%) quiescent clumps, 383 (14%) protostellar clumps, 714 (27%) H II region clumps, 445 (17%) PDR clumps, and 829 (31%) unknown clumps.

The evolution of molecular clumps is influenced by their thermal and kinematic properties, their environment, and the formation and evolution of massive stars.

Embedded HMPs and MS stars add heat and turbulence, potentially altering their own evolution by altering the physical conditions of their surrounding clumps.

Figure 2.19 shows maps of T_{rot} , $N_{tot,ba}$, and σ for three example clumps chosen to highlight different evolutionary stages. The gas within the quiescent clump is cold, has a moderate column density, and has a small velocity dispersion that implies a low degree of turbulence. The protostellar clump hosts two 24 μm -bright protostars within the inner integrated intensity contour. The column density is larger near these sources, and the gas temperature and velocity dispersion are particularly enhanced surrounding the brighter source. The gas properties within the H II region clump show significant variation, with enhanced temperatures and velocity dispersions near where the H II is expanding into the clump. The column density peak within the clump is not coincident with the H II region. On the contrary, the center of the H II region appears near a column density minimum, suggesting that the H II region has cleared out a cavity with its expansion. At farther distances from the exciting sources in the protostellar and H II region clumps, the gas remains cool and less turbulent. These data clearly show the significant effect high-mass protostars and stars have on their natal clumps.

Next, I investigated the evolution of gas properties using the full subsamples of the different evolutionary states. Figure 2.20 shows the distributions of the median T_{rot} , $N_{rot,ba}$, and σ values for the evolutionary classification subsamples. The median values for these properties provide averages that are less susceptible to individual fit quality. I also used bootstrap resampling to calculate the median and the error on the median for each distribution. These values are reported in Table 2.5.1.5 and indicated by red lines in Figure 2.20. Although the distributions exhibit large spreads, there is evidence of significant evolutionary trends.

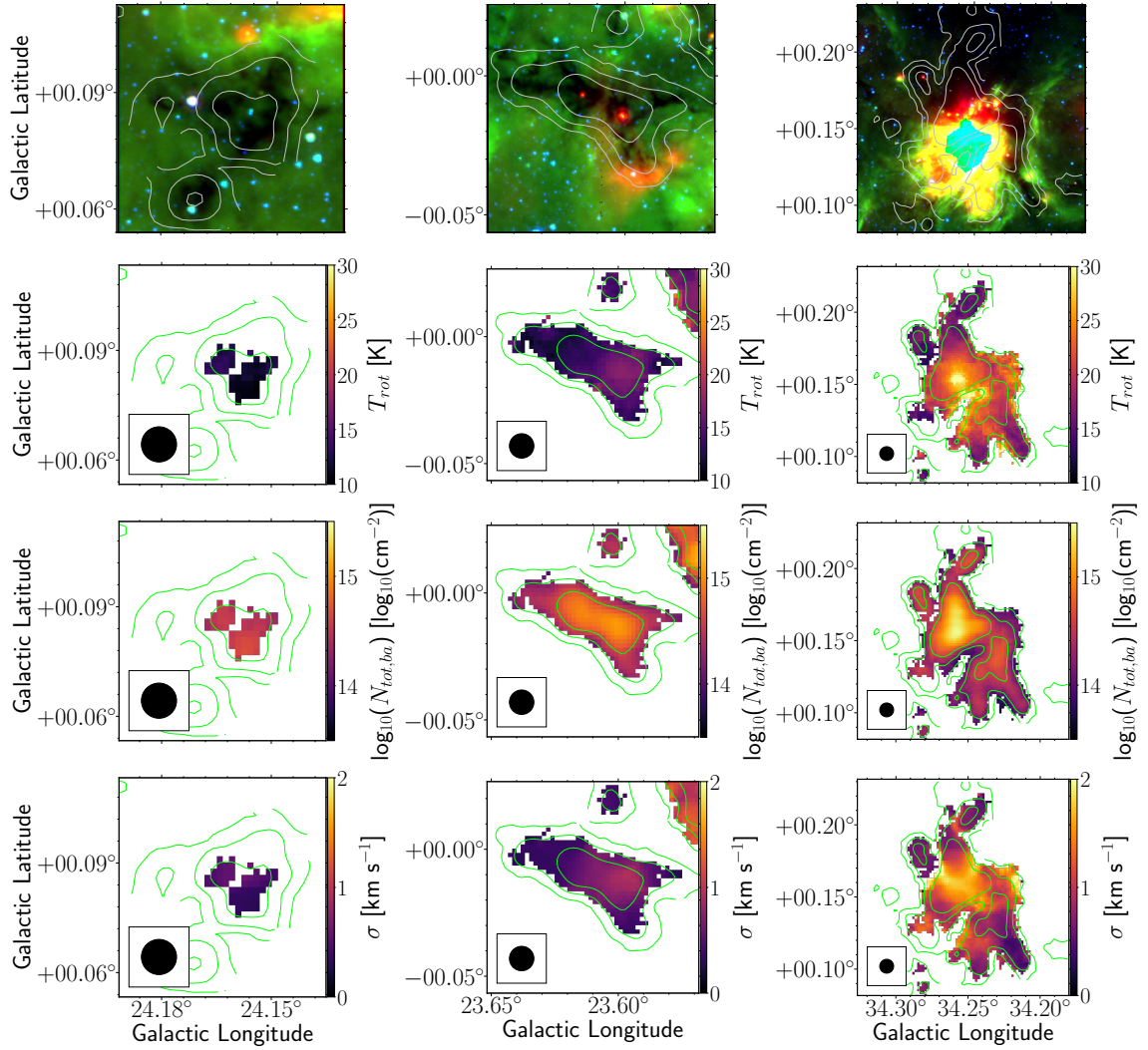


Fig. 2.19 Maps of three clumps at different evolutionary stages: quiescent (left), protostellar (middle), and H II region (right). The rows show the GLIMPSE/MIPSGAL 3.6 μm (blue), 8 μm (green), and 24 μm (red) MIR image (first row), T_{rot} (second row), $N_{tot,ba}$ (third row), and σ (fourth row). The contours show the 20th, 50th, and 80th percentile of the integrated intensity and the beam size is shown in the lower left.

The T_{rot} distributions indicate a significant evolutionary trend in T_{rot} between the quiescent, protostellar, and H II region clump subsamples. Although the median value for the protostellar T_{rot} distribution is only ~ 1 K larger than the median value for the quiescent T_{rot} distribution, this difference is statistically significant. Likewise, the median value for the H II region T_{rot} distribution is significantly larger than those of the quiescent and protostellar T_{rot} distributions. Thus, the RAMPS T_{rot} data show that protostars and H II regions significantly heat their surrounding clumps.

While the $N_{rot,ba}$ do show differences between evolutionary states, the differences between the quiescent, protostellar, and H II region clumps are not significant. The most significant differences between the $N_{rot,ba}$ distributions are between the PDR clump distribution and those of the quiescent, protostellar, and H II region clumps. This result is consistent with the results of Guzmán et al. (2015), who found that the PDR clump sample had lower mass surface densities on average than the quiescent, protostellar, and H II region clump samples.

Like the T_{rot} distributions, the σ distributions exhibit significant differences among evolutionary states. In particular, the σ distribution for the H II region clumps has a significantly higher median than for those of the quiescent and protostellar clumps. On the other hand, the median of the protostellar σ distribution is only marginally greater than that of the quiescent clump sample.

Median Clump Properties by Evolutionary State			
Evol.	T_{rot} [K]	$N_{rot,ba}$ [cm^{-2}]	σ [km s^{-1}]
Q	13.4 ± 0.2	$2.36 \pm 0.16 \times 10^{14}$	0.48 ± 0.03
P	14.3 ± 0.2	$2.44 \pm 0.09 \times 10^{14}$	0.53 ± 0.02
H	16.7 ± 0.2	$2.35 \pm 0.07 \times 10^{14}$	0.67 ± 0.01
PDR	16.0 ± 0.5	$1.56 \pm 0.10 \times 10^{14}$	0.63 ± 0.03
U	15.2 ± 0.5	$2.09 \pm 0.13 \times 10^{14}$	0.59 ± 0.03

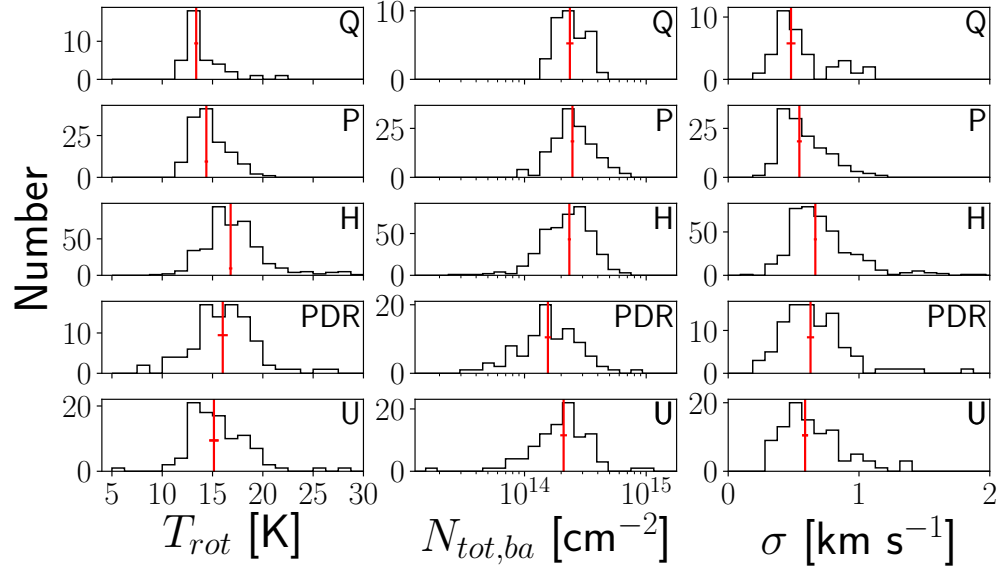


Fig. 2.20 Histograms show the mean T_{rot} , $N_{tot,ba}$, and σ for the clump sub-populations separated by evolutionary state. From top to bottom the clumps are separated into quiescent, protostellar, H II region, PDR, and unknown groups. The red vertical lines indicate the median of their respective distributions and the red horizontal lines at their midpoints indicate the error on the median determined from bootstrap resampling.

To further test whether the gas properties evolve significantly between the quiescent, protostellar, and H II region stages, I performed two-sample Kolmogorov-Smirnov (K-S) tests on these distributions. This analysis tests whether two samples have the same parent distribution. The test returns the K-S statistic and the p -value, where a small K-S statistic (< 0.2) or a large p -value ($p > 0.05$) indicates insufficient evidence that the parent distributions differ. Table 2.5.1.5 lists the results of the K-S tests for the quiescent, protostellar, and H II region clump samples.

The K-S tests for the T_{rot} distributions result in large K-S statistic values ($K - S > 0.3$) and very small p -values ($\ll 0.05$). These values imply with high confidence that the T_{rot} distributions for the quiescent, protostellar, and H II region sub-populations are not drawn from the same parent distribution. This result

suggests that massive protostars and MS stars both add significant heat to their surrounding clumps.

The K-S tests comparing the quiescent and protostellar σ distributions to the H II region σ distribution results in large K-S statistic values ($K - S \gtrsim 0.2$) and very small p -values ($\ll 0.05$). On the other hand, the K-S test comparing the quiescent and protostellar σ distributions results in a p -value greater than 0.05, signifying that the test cannot rule out the null hypothesis that the distributions are drawn from the same parent distribution. This is most likely a result of the limited sample size.

The σ values show in Figure 2.20 and used for this analysis are derived from the simultaneous fits to the NH₃(1,1) and (2,2) data. Given that significant NH₃(2,2) emission is rarer than significant NH₃(1,1) emission in the RAMPS data, the σ values derived solely from the NH₃(1,1) fits comprise a much larger sample. If only the σ values from the fits to the NH₃(1,1) data are considered, then the distributions are significantly different, with a K-S statistic of 0.19 and a p -value of 3.8×10^{-6} . This result implies that massive protostars and MS stars both add significant turbulence to their surrounding clumps.

Although it is no surprise that high-mass stars add heat and turbulence to their natal clumps, it is not clear whether the significant evolution of the clump-averaged T_{rot} and σ values corresponds to a change in the gas properties throughout clumps or whether the change is localized around the exciting sources. In Chapter 4, I investigate the spatial extent of radiative and kinematic feedback from HMPs and MS stars in more detail.

Unlike the K-S tests for the T_{rot} and σ distributions, the K-S tests for the $N_{rot,ba}$ distributions result in small K-S statistic values (< 0.2) and large p -values (> 0.05). Thus, these results cannot reject the null hypothesis that the quiescent, protostellar, and H II region $N_{rot,ba}$ distributions are drawn from the same parent distribution.

This lack of evolution may indicate tension with the competitive accretion theory of high-mass star formation, which predicts that the collapse of molecular clumps is essential to generate the high densities and accretion rates necessary to form HMPs (Bonnell et al. 2004). I investigate this further in Chapter 3, where I analyze the early dynamical evolution of molecular clumps and filaments to determine whether collapse motions and fluid flows present a viable method for gas to travel from the clump-scale to the core-scale.

K-S Tests of Clump Properties by Evolutionary State						
Median Clump Properties	Q vs. P		P vs. H		Q vs. H	
	K-S	p-value	K-S	p-value	K-S	p-value
T_{rot}	0.34	2.6×10^{-3}	0.49	1.4×10^{-21}	0.62	2.5×10^{-11}
$N_{rot,ba}$	0.12	8.2×10^{-1}	0.13	7.2×10^{-2}	0.18	2.2×10^{-1}
σ	0.22	1.1×10^{-1}	0.28	1.4×10^{-7}	0.45	1.6×10^{-6}

2.5.1.6 RAMPS Clump Catalog

In Section 2.5.1.1, I described the method I used to identify 2,680 clumps from the RAMPS NH₃(1,1) data. Table 2.3 lists the properties of the first 7 clumps in the catalog. I provide the full catalog of 2,680 clumps at OpenBU⁴. From left to right, the columns list the clump designations, which also indicate the intensity-weighted Galactic coordinates, the angular sizes ($\theta_{maj} \times \theta_{min}$), the clump-averaged T_{rot} , $N_{tot,ba}$, σ , V_{LSR} , and $\chi(\text{NH}_3)$ values, the distances (d_1) and distance probabilities (p_1), the masses (M_{clump}), the bolometric luminosities (L_{clump}), and the evolutionary states. The even table rows list the errors on the derived clump properties.

⁴<https://open.bu.edu/handle/2144/43142>

Table 2.3. RAMPS Molecular Clump Catalog

Clump Designation	$\theta_{maj} \times \theta_{min}$ ('x')	T_{rot} (K)	$N_{tot,ba}$ (cm $^{-2}$)	σ (km s $^{-1}$)	V_{LSR} (km s $^{-1}$)	$\chi(\text{NH}_3)$	d_1 (kpc)	p_1	M_{clump} (M $_{\odot}$)	L_{clump} (L $_{\odot}$)	Evol. State
G09.612+0.142	1.7×1.0	0.315	5.289	...	4.8	0.26	3.1×10^2	2.9×10^2	Q
		0.006	0.006	...	0.2		0.3×10^2	0.3×10^2	
G09.623+0.191	3.8×2.4	20.51	4.7×10^{14}	0.831	4.289	3.6×10^{-8}	4.8	0.27	2.9×10^3	1.4×10^5	H
		0.08	0.2×10^{14}	0.004	0.005	0.1×10^{-8}	0.2		0.3×10^3	0.1×10^5	
G09.629+0.266	1.1×0.8	0.33	2.709	...	3.9	0.35	1.0×10^2	1.1×10^2	P
		0.01	0.009	...	0.3		0.1×10^2	0.2×10^2	
G09.634+0.298	0.9×0.7	0.224	22.467	...	2.8	0.44	5.8×10^1	1.2×10^1	P
		0.007	0.007	...	0.2		0.9×10^1	0.2×10^1	
G09.649-0.017	1.3×0.7	0.32	-2.30	...	4.8	0.43	6.4×10^1	1.5×10^2	U
		0.01	0.01	...	0.2		0.6×10^1	0.2×10^2	
G09.662+0.264	2.3×0.9	0.331	3.697	...	3.9	0.33	3.2×10^2	3.1×10^2	P
		0.005	0.005	...	0.3		0.5×10^2	0.5×10^2	
G09.690-0.003	1.1×0.8	0.43	-1.51	...	4.8	0.43	1.1×10^2	...	P
		0.01	0.01	...	0.2		0.1×10^2	...	

Note. — The odd table rows list clump properties and the even table rows list the corresponding errors. Gas properties are clump-averaged values. The clumps with no T_{rot} or $N_{tot,ba}$ values did not display significant NH₃(2,2) emission, while the clumps with no L_{clump} values did not have a corresponding T_{dust} value.

2.5.2 H₂O Maser Analysis

In this section, I describe my analysis of the RAMPS H₂O data. In Section 2.5.2.1, I describe the detection of H₂O masers. In Section 2.5.2.2, I calculate maser positions. In Section 2.5.2.3, I classify masers by their associated environment to determine which masers are associated with star-forming regions (SFRs) and which are associated with AGB stars. In Section 2.5.2.4, I analyze brightness temperature distributions to determine whether the RAMPS H₂O data could be used to detect maser emission due to low-mass star formation and to test whether the flux distributions of the H₂O maser classes are significantly different. In Section 2.5.2.5, I analyze the maser V_{LSR} distributions to test whether the SFR maser velocities are consistent with rotation in the Galactic disk and whether the AGB maser velocities exhibit a significantly different velocity distribution. In Section 2.5.2.6, I analyze the maser velocity spread distributions to determine whether the different shock geometries associated with SFRs and AGB stars have resulted in different velocity spreads in their maser emission.

2.5.2.1 H₂O Maser Detection

The first step in my analysis of the RAMPS H₂O data was to detect significant H₂O maser emission. Since sites of H₂O maser emission are unresolved by single dish radio telescopes, the apparent angular extent of their emission is the size of the telescope beam. Maser sites often exhibit multiple velocity components (Claussen et al. 1996; Walsh et al. 2011). Sometimes different velocity components are physically associated with the same clump, while in other cases these components are associated with different clumps along the line-of-sight. For H₂O masers associated with molecular clumps, the brightest line components are usually found at velocities close to the clump velocities (Urquhart et al. 2011). Thus, like clumps whose emission

overlaps, overlapping maser sites can be separated by the velocities of their brightest line components.

To detect masers and separate overlapping masers sites, I created integrated intensity and first moment maps using the brightest maser line in each H₂O spectrum. For each H₂O spectrum with $T_{B,max} \geq 5\sigma_{rms}$, I masked all channels with $T_B < 3\sigma_{rms}$, as well as those channels that were not contiguous with at least two other unmasked channels. To isolate emission from the brightest line in each spectrum, I also masked channels outside of a 1 km s⁻¹ window surrounding the peak channel. I summed over the unmasked channels to calculate the integrated intensity and used Equation 2.1 to calculate the first moment.

I created a preliminary list of maser detections by searching for contiguous unmasked pixels. This method produced a few suspected false detections. These false detections generally showed significant signal in only one pixel or in a few pixels that were contiguous in the Galactic latitude direction. This is a result of the coarser sampling in the Galactic latitude direction of the maps, which also degrades the angular resolution of the H₂O maps in that direction. I suspected that these were false detections because they had low intensities and showed a relatively uniform velocity distribution, which are attributes expected from random noise. The suspected false detections did not usually exhibit a significant signal in two pixels that were contiguous in the Galactic longitude direction. To remove these spurious detections, I required that each unmasked pixel in the integrated intensity maps have an unmasked neighbor in the Galactic longitude direction.

Finally, I separated physically overlapping maser emission. Because single maser sites are unresolved, they display the same velocity over the entire angular extent of their emission. On the other hand, since overlapping maser sites are usually associated with sources that have different velocities, the emission from the brightest maser

lines in each site will exhibit a different velocity. To identify overlapping maser sites, I searched for contiguous H₂O emission that featured a spread in the first velocity moment values greater than 2 km s⁻¹. Next, I created separate integrated intensity maps at the velocities of the overlapping masers and performed further analysis using these maps. With this analysis, I detected 707 masers in total, providing the largest collection of H₂O masers from a single survey to date.

2.5.2.2 H₂O Maser Positions

Next, I determined the positions of the detected masers. I calculated the integrated intensity-weighted position of each maser using Equations 2.8 and 2.9. I estimated the error on the positions using

$$\sigma_l = \sqrt{\sum_i (l_i - l)^2 \left(\frac{\sigma_{I_i}}{\sum_i I_i}\right)^2 + \sigma_{\text{pointing}}^2} \quad (2.8)$$

$$\sigma_b = \sqrt{\sum_i (b_i - b)^2 \left(\frac{\sigma_{I_i}}{\sum_i I_i}\right)^2 + \sigma_{\text{pointing}}^2} \quad (2.9)$$

where σ_l is the error on the calculated Galactic longitude, σ_b is the error on the calculated Galactic latitude, σ_{I_i} is the error on the integrated intensity of the i^{th} pixel, and σ_{pointing} is the 1D error on the pointing of the telescope. The error on the integrated intensity (σ_{I_i}) is given by

$$\sigma_{I_i} = \sigma_{rms} \sqrt{N} \quad (2.10)$$

where N is the number of unmasked channels used to calculate I_i and σ_{rms} is the noise in a single channel. The error on the pointing of the telescope is estimated from the average wind speed during the observing period (GBT Dynamic Scheduling Project Note 18.1). A conservative estimate of a 5 m s⁻¹ wind speed during the daytime at a height of 10 m above the ground results in $\sigma_{\text{pointing}} \approx 3''$. The error on the telescope

pointing dominates the error on the maser positions, such that $\sigma_l \approx \sigma_b \approx \sigma_{\text{pointing}}$ for every source.

2.5.2.3 H₂O Maser Environments

The 22.235 GHz H₂O maser transition is associated with both SFRs and AGB stars (Reid & Moran 1981). As part of my H₂O maser analysis, I estimated the associated environment of all of the RAMPS H₂O masers using NH₃(1,1) and MIPSGAL (Carey et al. 2009) 24 μm data. Urquhart et al. (2011) performed follow-up NH₃ and H₂O maser observations of ~ 600 massive star-forming regions identified by the Red MSX Survey (Hoare et al. 2005; Mottram et al. 2007; Urquhart et al. 2008). They found that $\sim 95\%$ of the 308 detected masers displayed emission within 20 km s⁻¹ of the NH₃ V_{LSR} . They attributed the H₂O masers that fell outside of this range to chance alignments or maser variability (Breen et al. 2010). I used this result to inform my classification of the RAMPS H₂O maser environments. If an H₂O maser was spatially coincident with NH₃ emission and displayed emission within 20 km s⁻¹ of the NH₃ velocity, I inferred that the maser was associated with a SFR. For masers that were not associated with NH₃ emission, I checked the MIPSGAL data for the presence of a 24 μm -bright star coincident with the maser position. If that was the case, I concluded that the maser was associated with an AGB star. I assigned an unknown association to masers that were not associated with either SFRs or AGB stars. These masers may be associated with distant or low luminosity SFRs and AGB stars that are too faint to detect in NH₃ or at 24 μm . Out of 707 detected masers, I found that 351 ($50 \pm 2\%$) are associated with an SFR, 266 ($38 \pm 2\%$) are associated with an AGB star, and 90 ($13 \pm 1\%$) have an unknown association.

2.5.2.4 T_B Distribution

The brightness temperature of a point source, such as a maser, depends only on its luminosity and distance. Thus, the T_B distributions depend on both the maser luminosity and distance distributions. Figure 2.21 shows the T_B distributions for the maser samples separated by environment. The distributions are roughly of power-law form for $T_B > 2$ K. While the brightness temperature distributions of the various maser groups look roughly similar, the distribution of the SFR masers exhibits a shallower power-law slope than the distribution of the AGB star masers, resulting in many more SFR masers having $T_B > 100$ K.

The turnover at $\sim 1 - 2$ K in each distribution represents the completeness limit. This value is expected, since the typical σ_{rms} value for the H₂O spectra is ~ 0.3 K and I required that each detected maser have an intensity of at least five times the noise. The average detection limit of 1.5 K corresponds to an isotropic H₂O maser luminosity (Equation 1.1) of $4.7 \times 10^{-8} L_\odot$ at a distance of 3 kpc (Anglada et al. 1996). Thus, these data are suitable to detect H₂O maser emission from low-mass protostars with bolometric luminosities $\gtrsim 10 L_\odot$ (Furuya et al. 2003) at typical distances to high-mass star-forming clumps.

To compare these distributions in a quantitative manner, I performed a two-sample Kolmogorov–Smirnov (K-S) test. Table 2.5.2.4 displays the results of the K-S tests. The results suggest a high confidence ($p < 0.05$) that the SFR T_B distribution does not have the same parent distribution as the AGB or unknown T_B distributions. On the other hand, the K-S test of the AGB and unknown T_B distributions has a small K-S statistic (< 0.1) and a large p -value ($p \gg 0.05$). This result indicates that the test cannot reject the null hypothesis that the AGB and unknown T_B distributions are drawn from the same parent distribution.

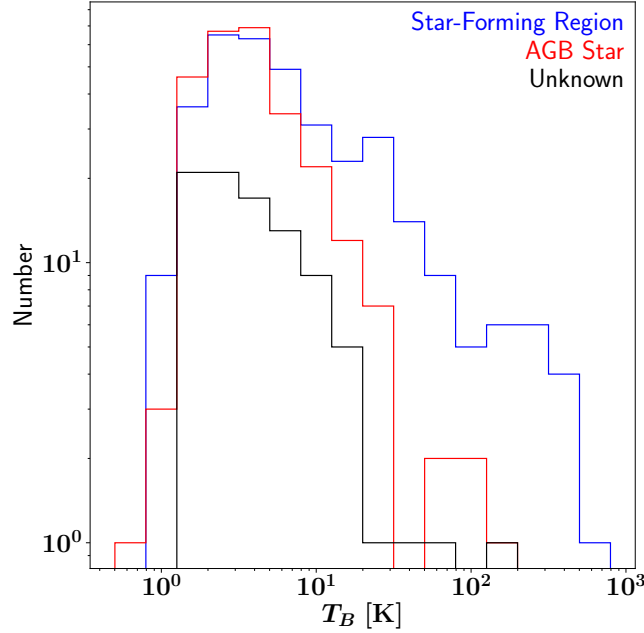


Fig. 2.21 Histograms of T_B for H_2O masers associated with star-forming regions (blue), AGB stars (red), and unknown environments (black).

K-S Test Results - T_B		
T_B Distributions	K-S	p -value
SFR-AGB	0.22	1.0×10^{-6}
SFR-U	0.22	1.7×10^{-3}
AGB-U	0.08	7.9×10^{-1}

In addition, I fit the T_B distributions for $T_B > 3$ K using a power-law function to determine whether the slopes of the distributions were significantly different. The power-law indices for the SFR, AGB, and unknown maser T_B distributions are -0.612 ± 0.002 , -1.247 ± 0.006 , and -1.030 ± 0.012 , respectively. The significant difference between these distributions could be a result of differing distance distributions, luminosity distributions, or a combination of the two.

Given that SFRs are typically found within the Galactic disk while AGB stars can be associated with the Galactic halo, I tested the difference in flux distributions between samples uniformly distributed in a disk and a sphere. A sample of sources with identical luminosities arranged in a uniform sphere resulted in a power-law flux distribution with an index of ~ -1.5 , while the same sample arranged in a uniform disk resulted in an index of ~ -1 . In reality, the distribution of isotropic maser luminosities exhibits a power-law form. Moscadelli et al. (2020) found a power-law index of 1.35 for their derived distribution of isotropic maser luminosities. Consequently, I also created a population of synthetic sources with a power-law luminosity distribution with an index of 1.35. These sources uniformly distributed in a disk resulted in a flux distribution with a power-law index of -0.56 , while the sources uniformly distributed in a sphere resulted in a flux distribution with a power-law index of -0.69 . Thus, it is likely that the shallower power-law distribution of the SFR maser T_B distribution is at least partially due to their location within the Galactic disk.

2.5.2.5 V_{LSR} Distribution

Although H₂O masers do not emit exactly at the V_{LSR} of their exciting sources, maser emission is usually close in velocity ($\lesssim 10 \text{ km s}^{-1}$) to the V_{LSR} of the associated source (e.g., Urquhart et al. 2011; Billington et al. 2020). Consequently, the V_{LSR} distributions for the SFR and AGB masers should be related to the V_{LSR} distributions of SFRs and AGB stars, respectively. Figure 2.22 displays histograms of the V_{LSR} of the brightest maser line, separated by environment. The masers associated with SFRs exhibit only a few sources at negative V_{LSR} , while the masers associated with AGB stars or with an unknown association show a broader spread in velocities with many sources at negative V_{LSR} . The difference between the V_{LSR} distributions is likely due to differing spatial distributions within the Galaxy. Masers associated with SFRs

are found only where there is molecular gas; thus, these masers are excited primarily within the midplane of the Galaxy and follow roughly circular orbits. Consequently, the SFRs that are in the first quadrant of the Galaxy with a Galactocentric radius $\lesssim 8$ kpc have positive velocities. On the other hand, AGB stars can be found in both the Galactic disk and the Galactic halo. Unlike in the Galactic disk, the V_{LSR} of stars in the Galactic halo do not correspond to their distances. Thus, AGB star masers with large negative velocities are expected.

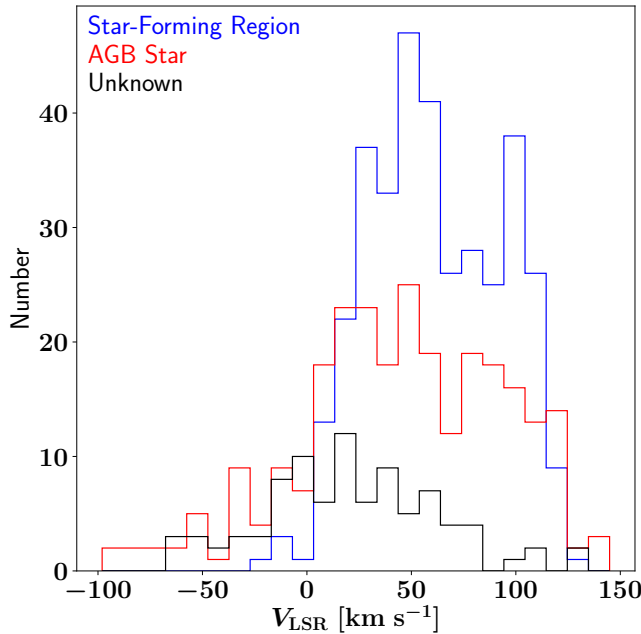


Fig. 2.22 Histograms of V_{LSR} for H_2O masers associated with star-forming regions (blue), AGB stars (red), and unknown environments (black).

Next, I compared the V_{LSR} distributions using the K-S test. Table 2.5.2.5 displays the results of these tests, all of which have large K-S statistics (> 0.2) and small p -values ($p \ll 0.05$). These results imply that the SFR, AGB, and unknown maser V_{LSR} distributions are not drawn from the same parent distribution. Thus, the masers with an unknown association likely have a different Galactic distribution

than both the AGB masers and the SFR masers. Considering that the unknown masers are not associated with significant NH₃ emission or an obvious 24 μm stellar source, these masers may be associated with more distant sources that are below the RAMPS and MIPSGAL detection thresholds, respectively.

K-S Test Results - V_{LSR}		
V_{LSR} Distributions	K-S	<i>p</i> -value
SFR-AGB	0.22	4.6×10^{-7}
SFR-U	0.45	1.4×10^{-13}
AGB-U	0.27	1.0×10^{-4}

2.5.2.6 Velocity Spread Distribution

H₂O maser spectra often feature multiple maser components at different velocities (e.g., Caswell & Breen 2010; Walsh et al. 2011). The spread of these velocity components provides information about the kinematics of the exciting source. For each maser with multiple velocity components, I calculated $V_{spread} = V_{max} - V_{min}$ for the significant ($> 5\sigma_{rms}$) maser lines. Figure 2.23 shows the V_{spread} distributions for the SFR, AGB, and unknown masers that feature multiple lines.

The SFR maser V_{spread} distribution extends to ~ 100 km s⁻¹, with peaks at ~ 10 km s⁻¹ and ~ 30 km s⁻¹. Masers in SFRs are often triggered by shocks associated with protostellar outflows, so the maser velocities roughly indicate outflow velocities modulo $\sin(i)$, where i is the outflow inclination angle. Such outflows have velocities of 10–100 km s⁻¹ (Arce et al. 2007), which are consistent with the observed distribution of V_{spread} .

The V_{spread} distribution for the AGB masers peaks at ~ 20 km s⁻¹, with a handful of masers exhibiting larger V_{spread} values of > 50 km s⁻¹. AGB masers are excited in the circumstellar envelopes of evolved stars and trace expansion motions (Larson

& Starrfield 1971). Most of the V_{spread} values are consistent with typical expansion velocities of $< 30 \text{ km s}^{-1}$ (e.g., Herwig 2005; Ramstedt et al. 2009). RAMPS also detected two AGB masers with $V_{spread} > 100 \text{ km s}^{-1}$, which likely arise from “water-fountain” post-AGB stars (Yung et al. 2017) that can excite H₂O maser emission with V_{spread} up to $\sim 400 \text{ km s}^{-1}$ (Walsh et al. 2009).

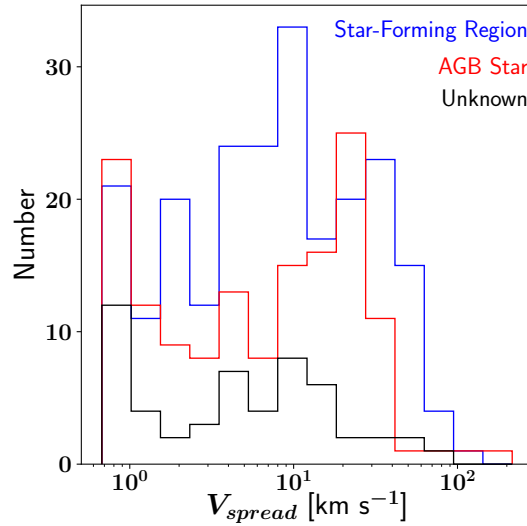


Fig. 2.23 Histograms of the V_{LSR} spread over which emission was detected for H₂O masers associated with star-forming regions (blue), AGB stars (red), and unknown environments (black).

Next, I compared each distribution using a K-S test, the results of which are shown in Table 2.5.2.6. The K-S tests produced small K-S statistics and large p -values. Although the SFR and AGB masers are presumably excited in environments with different shock geometries, the K-S tests cannot reject the null hypothesis that the SFR, AGB, and unknown V_{spread} distributions have been drawn from the same distribution.

K-S Test Results - V_{spread}		
V_{spread} Distributions	K-S	<i>p</i> -value
SFR-AGB	0.11	2.4×10^{-1}
SFR-U	0.17	1.3×10^{-1}
AGB-U	0.18	1.4×10^{-1}

2.5.2.7 RAMPS H₂O Maser Catalog

In Table 2.4, I present data for the first 7 sources in the RAMPS H₂O maser catalog. I present the full catalog of 707 masers at OpenBU⁵. The table columns list the derived positions (l, b), the best-fit brightness temperatures (T_B) and velocities (V_{LSR}) of the brightest lines, the minimum velocities (V_{min}), maximum velocities (V_{max}), and velocity spreads (V_{spread}) for H₂O masers with multiple lines, and the associated environments. The even table rows list the errors on these derived properties.

2.6 Comparison with Previous Surveys

RAMPS is one of a number of recent surveys of the Galactic plane. In this section, I compare RAMPS data to a few of these previous surveys. In Section 2.6.1, I compare RAMPS data to HOPS data to test whether RAMPS data can be used to spatially resolve, and provide the gas properties of, many more molecular clumps than HOPS data. In Section 2.6.2, I compare the gas and dust properties of clumps detected from the ATLASGAL and BGPS data to test whether quiescent clumps are more readily detected using RAMPS data. In Section 2.6.3, I compare the gas properties derived from RAMPS data to those derived from targeted single-pointing NH₃

⁵<https://open.bu.edu/handle/2144/43147>

Table 2.4. RAMPS H₂O Maser Catalog

l (deg)	b (deg)	T_B (K)	V_{LSR} (km s ⁻¹)	V_{min} (km s ⁻¹)	V_{max} (km s ⁻¹)	V_{spread} (km s ⁻¹)	Association
9.6207	0.1936	169	6.93963	-6.3287	8.6080	14.9367	SFR
		1	3×10^{-5}	1×10^{-4}	3×10^{-4}	3×10^{-4}	
9.6518	-0.0609	6.34	49.060	49.060	64.386	15.326	AGB
		0.08	1×10^{-3}	1×10^{-3}	3×10^{-3}	3×10^{-3}	
9.7310	-0.1423	2.05	-15.469	AGB
		0.04	3×10^{-3}	
9.9123	-0.3461	4.0	11.771	AGB
		0.1	1×10^{-3}	
9.9615	-0.3684	3.05	-13.340	U
		0.04	4×10^{-3}	
9.9855	-0.0287	9.65	48.4078	47.25	58.556	11.30	SFR
		0.07	2×10^{-4}	4×10^{-2}	6×10^{-3}	4×10^{-2}	
10.0033	-0.1933	3.8	-58.374	U
		0.1	5×10^{-3}	
10.0198	-0.3931	60	9.314	9.314	9.921	0.607	SFR
		30	2×10^{-3}	2×10^{-3}	9×10^{-3}	10×10^{-3}	
11.0222	-0.3792	1.00	26.5555	21.899	26.5555	4.657	AGB
		0.04	9×10^{-4}	2×10^{-3}	9×10^{-4}	2×10^{-3}	
10.2535	-0.1083	3.2	8.491	SFR
		0.1	1×10^{-3}	
10.2849	-0.1177	4.7	13.1008	SFR
		0.1	8×10^{-4}	

Note. — Odd rows list H₂O maser Galactic positions (l, b), brightness temperatures (T_B) and velocities (V_{LSR}) of the brightest line component, the minimum line velocity (V_{min}), the maximum line velocity (V_{max}), the spread in line velocities (V_{spread}), and the associated environment. The H₂O masers are classified as being associated with a star-forming region (SFR), an asymptotic giant branch (AGB) star, or an unknown environment (U). Even rows list the errors on the relevant quantities in the odd rows. The errors on l and b values are not listed, but they are dominated by the telescope pointing error of $\sim 3''$. Some masers show significant emission in only a single velocity component, so these sources have no entries in the V_{min} , V_{max} , and V_{spread} columns.

surveys to test whether my analysis of the RAMPS data has sufficiently reproduced the gas properties derived from the single-pointing surveys.

2.6.1 Comparison with HOPS

HOPS observed $\text{NH}_3(1,1)$ through $(3,3)$ and the 22 GHz H_2O maser line over 100 deg² of the Southern Galactic plane using the 22 m Mopra telescope. RAMPS and HOPS are easily comparable, since the surveys overlap over the Galactic longitude range $l = 10^\circ - 30^\circ$. Figure 2.24 shows the RAMPS and HOPS $\text{NH}_3(1,1)$ integrated intensity maps in the range $l = 22.5^\circ - 24.5^\circ$. Although the RAMPS $\text{NH}_3(1,1)$ sensitivity is comparable to that of HOPS (RAMPS $\sigma_{rms} \sim 0.13$ K vs. HOPS $\sigma_{rms} \sim 0.19$ K), the GBT's large diameter provides better angular resolution. Many clumps contain emission that is unresolved and beam diluted by the $\sim 2'$ Mopra beam. Consequently, such sources exhibit larger brightness temperatures when observed with the GBT.

Figure 2.25 displays (l, v) -diagrams of both RAMPS and HOPS $\text{NH}_3(1,1)$ and $(2,2)$ over a 5° portion of the overlapping region. The (l, v) -diagrams show that the $\text{NH}_3(1,1)$ satellite lines are detected for almost every source in the RAMPS data. Given that the satellite line are necessary to derive optical depths, RAMPS data can be used to derive the NH_3 column densities of many more clumps than HOPS data. The GBT's superior angular resolution has also resolved groups of clumps into their constituent members, revealed more filamentary structures, and allowed the analysis of RAMPS data to discern temperature, column density, and kinematic structure within clumps. Probing clumps at this scale is crucial for understanding how the onset of high-mass star formation affects the evolution of the surrounding clump.

RAMPS is the most sensitive large survey of H_2O masers to date; thus, it is important to compare the RAMPS H_2O maser detections to those of HOPS, the previous largest H_2O maser survey.

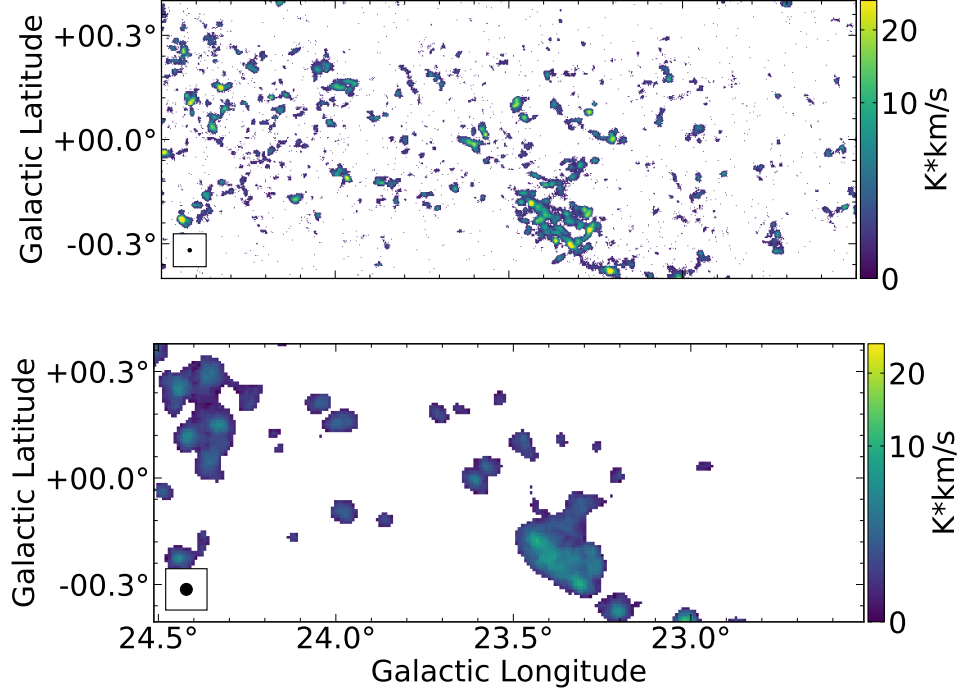


Fig. 2.24 Comparison between the RAMPS (top) and HOPS (bottom) $\text{NH}_3(1,1)$ integrated intensity maps for a sample region. The respective beam sizes are shown in the lower left of each map.

Walsh et al. (2011) detected 540 sites of maser emission in the 100 deg^2 HOPS survey region, or $5.4 \text{ masers}/\text{deg}^2$. I detected 707 masers in the 21.6 deg^2 RAMPS survey region, or $32.7 \text{ masers}/\text{deg}^2$. For a direct comparison, Figure 2.26 shows the masers detected in the range $l = 22.5^\circ - 24.5^\circ$ by each survey. While 15 masers were detected from the HOPS data, I detected 82 masers from RAMPS data. Thus, the maser detection rate from the analysis of the RAMPS H_2O data is significantly higher than the detection rate from the HOPS analysis.

I also note that two masers in this region were detected in the HOPS data, but were not detected in the RAMPS data. Considering that maser intensities can vary significantly (Elitzur 1992), it is possible that these masers were brighter during

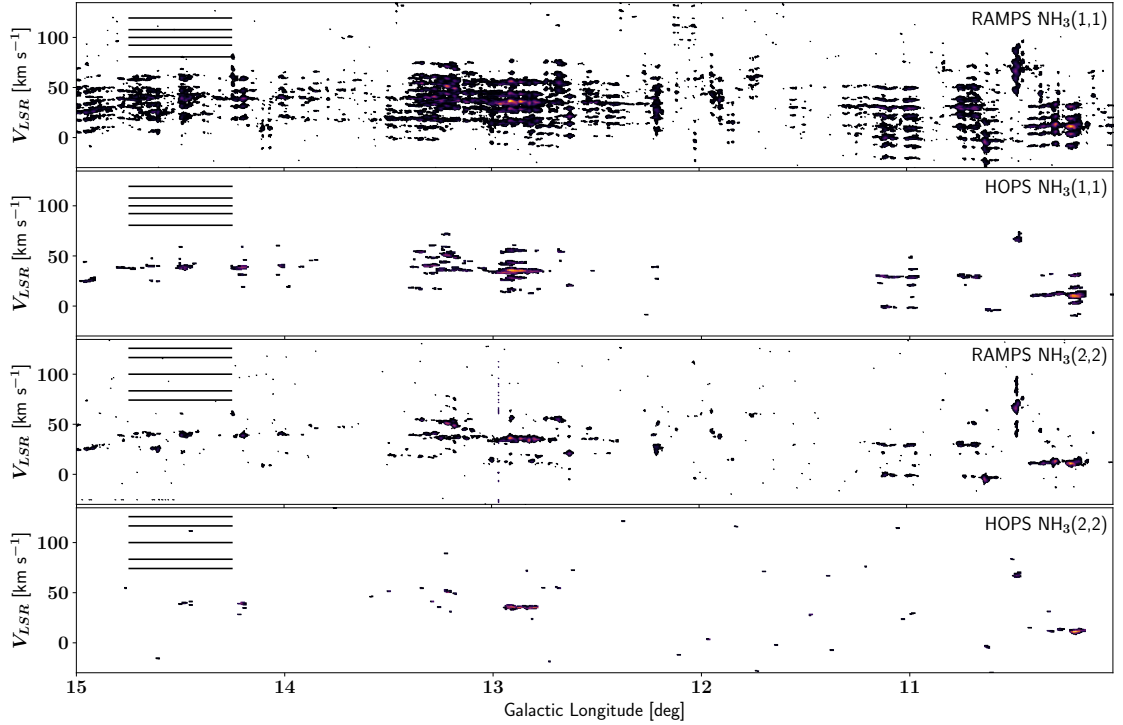


Fig. 2.25 Comparison between RAMPS and HOPS $\text{NH}_3(1,1)$ and $(2,2)$ (l, v)-diagrams in the range $l = 10^\circ - 15^\circ$. The horizontal lines at the upper left in each panel display the respective hyperfine patterns.

the HOPS observations but faded to intensities below the detection limit during the more sensitive RAMPS observations. Given that the GBT is $\sim 20\times$ more sensitive to point sources than Mopra, the variability would need to be large to explain the RAMPS non-detections.

2.6.2 Comparisons of RAMPS with BGPS and ATLASGAL

The BGPS 1.1 mm and ATLASGAL 870 μm dust continuum surveys both overlap the region of the Galactic plane observed by RAMPS. Due to spatial filtering, BGPS and ATLASGAL are biased toward more compact ($< 2.5'$), and presumably higher column density, sources. Consequently, they are appropriate continuum surveys to compare with RAMPS.

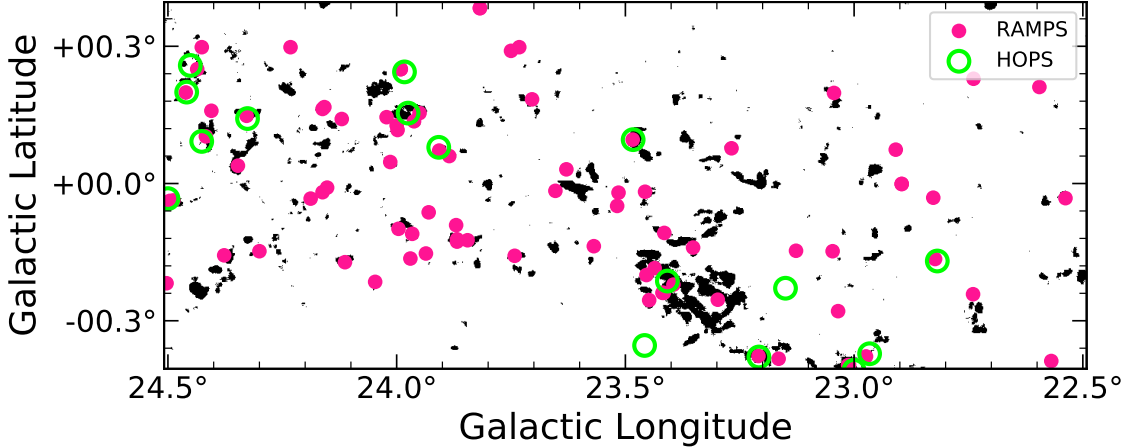


Fig. 2.26 Comparison between RAMPS and HOPS H_2O maser detections. RAMPS $\text{NH}_3(1,1)$ integrated intensity is in black for visibility and the maser positions are shown with magenta (RAMPS) and green (HOPS) symbol markers.

Of the 3,716 clumps detected from the BGPS data, 53% of these were also detected using RAMPS data. Of the 2,680 clumps detected from the RAMPS data, 55% of these were also detected using the BGPS data. Of the 2,104 ATLASGAL clumps within the RAMPS region, 86% were detected from the RAMPS data. Of the 2,680 clumps detected from the RAMPS data, 42% correspond to an ATLASGAL clump. To put these values in context, I also tested the correspondence between BGPS and ATLASGAL detections at Galactic longitudes $10^\circ \leq l \leq 40^\circ$ and Galactic latitudes $-0.4^\circ \leq b \leq 0.4^\circ$. The BGPS catalog contained a corresponding source within $30''$ for 70% of the ATLASGAL sources, while the ATLASGAL catalog contained a corresponding source within $30''$ for 38% of the BGPS sources. Thus, the RAMPS detection rate is similar to that of BGPS and better than ATLASGAL.

Given that the dust continuum data are 2D maps, while the molecular line data are 3D data cubes, ATLASGAL and BGPS data required different source extraction methods than the RAMPS data. BGPS source extraction method used a seeded watershed algorithm (Yoo 2004) and ATLASGAL source extraction method utilized

Gaussclumps (Stutzki & Guesten 1990; Kramer et al. 1998) on the multiscale filtered continuum data. Both extraction methods define clumps as compact structures. On the other hand, the RAMPS source extraction method searched for velocity-coherent structures, which can be compact or extended.

The properties of the extracted sources also depend on the observed tracers. Figure 2.27 shows the dust properties of the clumps common to each survey and those that RAMPS did not detect. Given that the submm and mm dust emission has an exponential dependence on temperature ($h\nu \sim k_B T_{dust}$), while the 23 GHz NH₃ emission has a linear dependence on temperature ($h\nu \ll k_B T_{dust}$), it is not surprising that BGPS and ATLASGAL are more sensitive to hotter clumps than RAMPS. In addition, the sources not detected by RAMPS have lower column densities, presumably because diffuse sources have lower optical depths, and therefore lower molecular line brightness temperatures.

Figure 2.28 shows the NH₃-derived source properties of the clumps common to each survey and of those only detected by RAMPS. The clumps detected solely by RAMPS typically have colder gas temperatures. These RAMPS-only clumps also have lower column densities than those detected in the continuum tracers. The RAMPS-only clumps also have small velocity dispersions compared to the clumps detected by RAMPS, ATLASGAL, and BGPS. Part of this difference could be due to hotter sources exhibiting larger velocity dispersions due to feedback.

Another cause for this difference may be explained by the change in the optical depth profile of a line as a function of σ . If the total optical depth for two clumps with the same $N_{tot,ba}$ and T_{kin} is the same, the clump with the smaller σ will have a larger line center optical depth and brightness temperature. Consequently, if all other parameters are equal, molecular line mapping surveys will be more sensitive to clumps with low σ than dust continuum surveys.

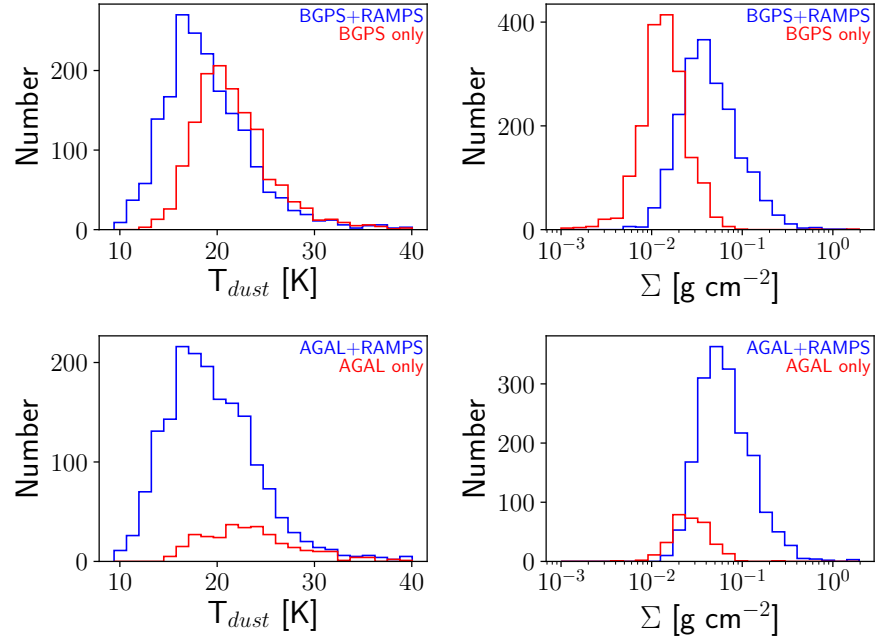


Fig. 2.27 Top row: Comparison of T_{dust} and Σ distributions for clumps detected by both BGPS and RAMPS and those detected solely by BGPS. Bottom row: Comparison of T_{dust} and Σ distributions for clumps detected by both ATLASGAL and RAMPS and those detected solely by ATLASGAL.

2.6.3 Comparison with Targeted NH₃ Surveys

In order to derive kinematic distances and gas properties for the ATLASGAL and BGPS clump samples, Svoboda et al. (2016) undertook targeted NH₃ observations toward the BGPS clumps using the GBT and Wienen et al. (2012) observed a subsample of the ATLASGAL clumps using the Effelsburg 100 m telescope. Svoboda et al. (2016) used the GBT NH₃ data to calculate T_{kin} , $\tau(1, 1)_{tot}$, and σ for the BGPS clump sample.

Figure 2.29 shows a comparison of the Svoboda et al. (2016) values with those derived using RAMPS data. I converted the Svoboda et al. (2016) T_{kin} values to T_{rot} using Equation 2 from Walmsley & Ungerechts (1983). There appears to be a discrepancy between the T_{rot} values, where RAMPS finds larger values by ~ 2 K.

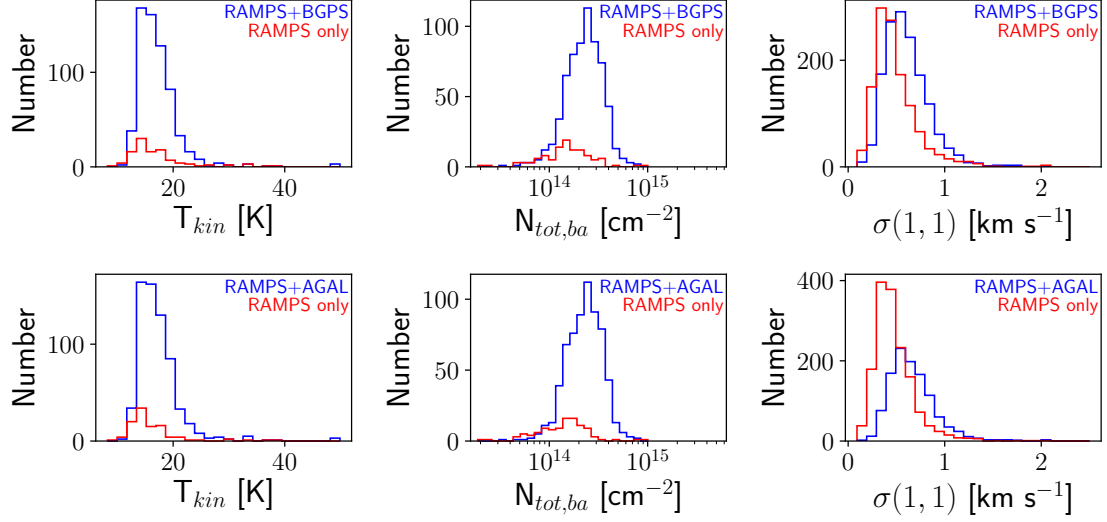


Fig. 2.28 Top row: Comparison of T_{kin} , $N_{tot,ba}$, and $\sigma(1, 1)$ distributions for clumps detected by both RAMPS and BGPS and those detected solely by RAMPS. Bottom row: Comparison of T_{kin} , $N_{tot,ba}$, and $\sigma(1, 1)$ distributions for clumps detected by both RAMPS and ATLASGAL and those detected solely by RAMPS.

This discrepancy is a result of different assumptions used to derive the rotational level populations. Svoboda et al. (2016) followed the analysis procedure of Dunham et al. (2011), who used T_{kin} to set the rotational level populations. These T_{kin} values were derived from T_{rot} using the relation in the Appendix of Swift et al. (2005), while T_{rot} was derived from the $\text{NH}_3(1,1)$ and $(2,2)$ amplitudes in the standard manner. On the other hand, the PySpecKit NH_3 model employed for RAMPS analysis assumed that T_{rot} , derived from the $\text{NH}_3(1,1)$ and $(2,2)$ amplitudes, sets the rotational levels. Consequently, the T_{kin} values derived using the NH_3 model employed by Dunham et al. (2011) have lower values than those derived using the PySpecKit NH_3 model employed by RAMPS.

Although the derived temperatures are different, the $\tau(1,1)_{tot}$ and σ values generally agree within their errors. Because the Svoboda et al. (2016) NH_3 analysis fit for a nonthermal excitation temperature ($T_{ex} \leq T_{kin}$), the derived $\tau(1,1)_{tot}$ values

were not affected by the discrepant temperatures. Likewise, the reported RAMPS $\tau(1, 1)_{tot}$ values were derived from the NH₃(1,1) fits using Equation 2 in Appendix F, with T_{ex} as a free parameter. Because the RAMPS and Svoboda et al. (2016) analyses both derived the $\tau(1, 1)_{tot}$ values using the same assumptions, the values generally agree within their errors.

Wienen et al. (2012) used the Effelsburg NH₃ data to calculate T_{rot} , N_{tot} , ϕ , and σ for the BGPS clump sample. I used N_{tot} and ϕ to calculate $N_{tot,ba}$, since N_{tot} and ϕ are degenerate at low optical depths but the product $N_{tot} \times \phi$ is robust. Figure 2.30 shows a comparison of these properties derived from the Wienen et al. (2012) data and from RAMPS data. The two surveys derive very similar T_{rot} values, which generally match within the errors. Aside from some outliers, the σ values match well except at low σ values. This is a consequence of the 0.7 km s⁻¹ channel widths of the Effelsburg data, which are much larger than the RAMPS 0.2 km s⁻¹ channel widths. Thus, RAMPS velocity dispersions are more accurate at low σ . The RAMPS values for N_{tot} and $N_{tot,ba}$ are approximately twice those found by Wienen et al. (2012). This discrepancy is likely a result of different NH₃ model assumptions about T_{ex} . While I assumed $T_{ex} = T_{rot}$, Wienen et al. (2012) assumed $T_{ex} = T_{kin}$, which is always larger than T_{rot} (Walmsley & Ungerechts 1983). Consequently, the RAMPS model derived larger N_{tot} and $N_{tot,ba}$ to compensate for the lower T_{ex} . If T_{ex} is in fact larger than T_{rot} for the clumps detected by RAMPS, the NH₃ model employed by RAMPS will produce larger NH₃ column densities and higher NH₃ abundances than actually exist. Despite disparate assumptions and analyses, the pointed surveys and RAMPS yield consistent results.

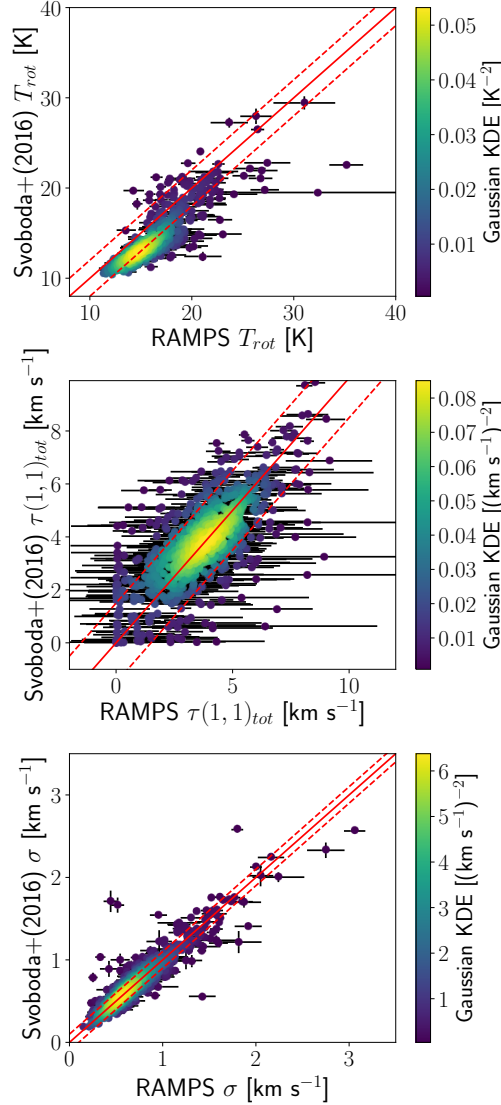


Fig. 2.29 Comparison of NH_3 derived properties from RAMPS data with the Svoboda et al. (2016) targeted follow-up observations of BGPS clumps. Top: The solid line represents $\text{RAMPS } T_{rot} = \text{Svoboda et al. (2016) } T_{rot}$ and the dashed lines represent $\text{RAMPS } T_{rot} = \text{Svoboda et al. (2016) } T_{rot} \pm 2 \text{ K}$. Middle: The solid line represents $\text{RAMPS } \tau(1,1)_{tot} = \text{Svoboda et al. (2016) } \tau(1,1)_{tot}$ and the dashed lines represent $\text{RAMPS } \tau(1,1)_{tot} = \text{Svoboda et al. (2016) } \tau(1,1)_{tot} \pm 1.5$. Bottom: The solid line represents $\text{RAMPS } \sigma = \text{Svoboda et al. (2016) } \sigma$ and the dashed lines represent $\text{RAMPS } \sigma = \text{Svoboda et al. (2016) } \sigma \pm 0.1 \text{ km s}^{-1}$.

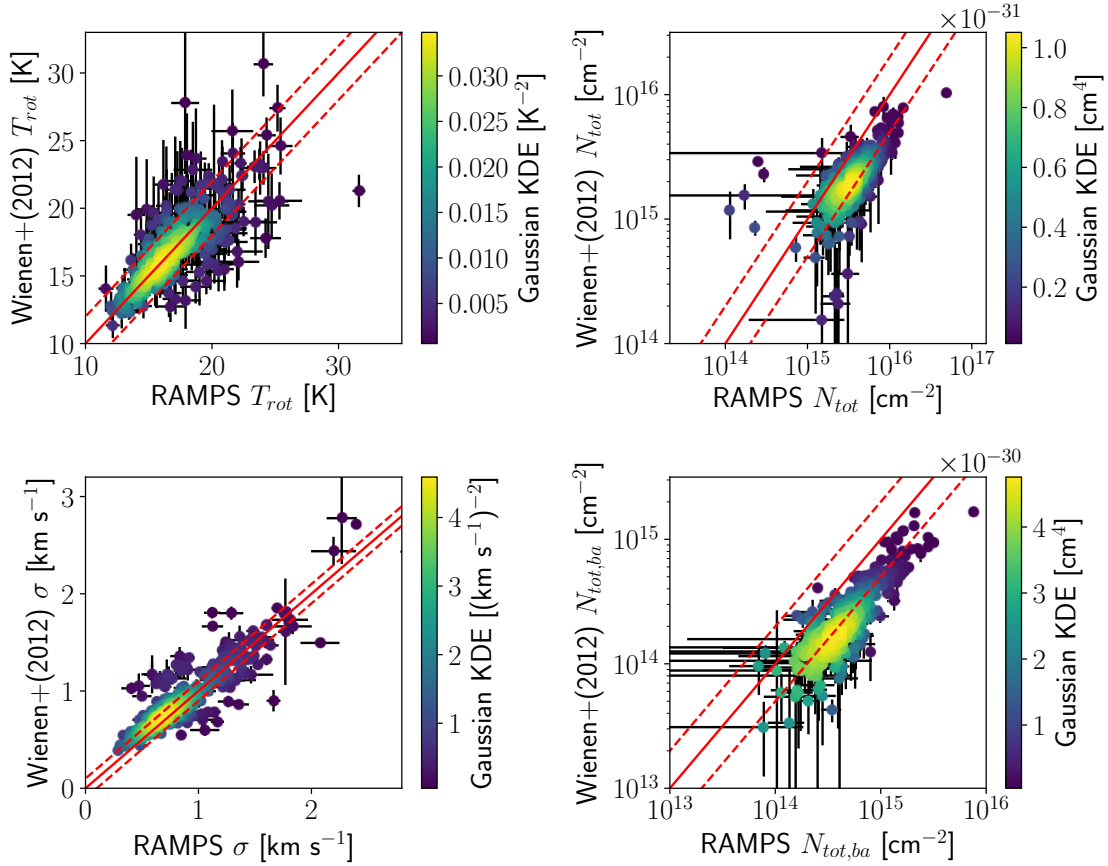


Fig. 2.30 Comparison of NH₃ derived properties from RAMPS data with the Wienen et al. (2012) targeted follow-up observations of ATLASGAL clumps. Top left: The solid line represents RAMPS $T_{rot} =$ Wienen et al. (2012) T_{rot} and the dashed lines represent RAMPS $T_{rot} =$ Wienen et al. (2012) $T_{rot} \pm 2$ K. Top right: The solid line represents RAMPS $N_{tot} =$ Wienen et al. (2012) N_{tot} and the dashed lines represent RAMPS $N_{tot} =$ Wienen et al. (2012) $2 \times N_{tot}$ and RAMPS $N_{tot} =$ Wienen et al. (2012) $\frac{1}{2} \times N_{tot}$. Bottom left: The solid line represents RAMPS $\sigma =$ Wienen et al. (2012) σ and the dashed lines represent RAMPS $\sigma =$ Wienen et al. (2012) $\sigma \pm 0.1$ km s^{-1} . Bottom right: The solid line represents RAMPS $N_{tot,ba} =$ Wienen et al. (2012) $N_{tot,ba}$ and the dashed lines represent RAMPS $N_{tot,ba} =$ Wienen et al. (2012) $2 \times N_{tot,ba}$ and RAMPS $N_{tot,ba} =$ Wienen et al. (2012) $\frac{1}{2} \times N_{tot,ba}$.

2.7 Conclusion

RAMPS is a survey of multiple molecular species and molecular transitions that covered 21.6 square degrees of the Galactic plane in the first Galactic quadrant. In this Chapter, I reported on the GBT observations and data reduction, the clump and H₂O maser identification methods, the derivation of gas properties from the RAMPS NH₃ data, and the derivation of dust properties from archival FIR dust continuum data. RAMPS is a significant improvement over previous large molecular line surveys owing to advancements in instrumentation on the GBT. Building on the excellent sensitivity and angular resolution of the GBT, the KFPA receiver array and the VEGAS spectrometer made a large *K*-band survey with unprecedented sensitivity possible. The KFPA's seven receivers mapped large areas in a relatively short amount of time, while VEGAS was able to observe simultaneously a large number of spectral lines over a wide frequency range. This combination gave RAMPS a distinct advantage in fast mapping at *K*-band frequencies.

An important consequence of the new instrumentation was the ability to map simultaneously the NH₃ inversion transitions, NH₃(1,1) through (5,5), and the 22.235 GHz H₂O maser line. Not only did the NH₃ inversion lines trace the dense molecular clumps where high-mass stars can form, but they also provided robust estimates of the gas temperature, column density, velocity dispersion, and LSR velocity. Among other things, the significant improvement in the detection of H₂O masers helped determine the presence of active star-formation. RAMPS is a leap forward in large mapping surveys of NH₃ and H₂O masers.

I presented integrated intensity maps of NH₃(1,1) and NH₃(2,2), H₂O positions, velocities, and brightness temperatures, as well as maps of T_{rot} , N_{tot} , $N_{tot,ba}$, σ , and V_{LSR} . I estimated distances using the Reid et al. (2016) maser parallax-based distance estimator. I also used other large archival datasets to estimate dust properties,

masses, luminosities, and evolutionary states for the RAMPs clumps. Comparisons between the RAMPs clump catalog and those of compatible dust continuum surveys showed that RAMPs recovered more cold clumps with low velocity dispersions, characteristics more frequently found in the quiescent clump population. Thus, RAMPs data can be used to better identify and characterize clumps in the earliest stages of star formation. Furthermore, comparisons with targeted NH₃ surveys show that, despite disparate assumptions and analyses, the values of T_{rot} , $N_{tot,ba}$, and σ agree among the surveys. Given that the RAMPs data importantly provide spatial information, these data will be crucial to answer open questions concerning spatial variations of the thermal, chemical, and kinematic properties of clumps at various evolutionary stages.

Chapter 3

The Early Dynamical Evolution of Molecular Clumps and Filaments

3.1 Introduction

3.1.1 Molecular Clump Kinematics

One of the most important open questions concerning high-mass star formation relates to their early evolution. In contrast to low-mass stars, the process by which high-mass stars acquire their final masses is not well understood. Because the typical distances to HMSFCs are large compared to clumps forming only low-mass stars, observations have yet to define a clear evolutionary sequence for high-mass star formation. The evolution of high-mass stars is particularly uncertain at the crucial early stages, since such sources are faint due to their low temperatures. Two of the prominent theories that seek to explain how high-mass protostars acquire their mass are turbulent core accretion (McKee & Tan 2003) and competitive accretion (Bonnell et al. 2001, 2004).

Turbulent core accretion posits that massive stars accrete primarily from gas that is gravitationally bound to their surrounding cores. In order for such cores to produce high-mass stars, their masses must be significantly greater than the thermal Jeans mass (Jeans 1928), which is $\sim 1 M_{\odot}$ at the temperatures and densities typical of quiescent molecular clumps. Turbulence offers a potential alternative to the thermal fragmentation scale. Turbulence in molecular clumps creates overdensities

with a range of masses. Some of these overdensities become gravitationally stable and are referred to as turbulent cores, while others are too turbulent compared to their masses and dissolve back into the clump. For such turbulent fragmentation, the spectrum of core masses sets the stellar initial mass function and the rarity of high-mass stars is a direct consequence of the scarcity of massive compact structures produced by turbulence. In this framework, massive prestellar cores are relatively long-lived structures (over at least several dynamical times, McKee & Tan 2003) that are supported by turbulence, but eventually collapse to form high-mass protostars.

In contrast, competitive accretion predicts that high-mass protostellar cores start their lives as low-mass ($\sim 1 M_{\odot}$) protostellar cores, which must accrete from their surrounding clumps to reach their final masses. The gravitational collapse of clumps is essential to provide a fresh supply of gas to their central regions. Competitive accretion predicts that such a collapse, and the subsequent cluster formation, occurs quickly, roughly on the dynamical time-scale (Bonnell et al. 2001). Low-mass protostars near the center of the collapsing clump sustain the high accretion rates needed to increase low-mass protostellar masses from $\sim 1 M_{\odot}$ to greater than $8 M_{\odot}$. Consequently, competitive accretion predicts that massive molecular clumps must undergo gravitational collapse to transition from the quiescent to the protostellar stage.

A common test of gravitational collapse is a virial analysis. The standard virial analysis assumes negligible magnetic fields and compares a clump's gravitational potential energy to its turbulent energy in order to assess the clump's gravitational stability. The virial mass of a clump is the mass that could be supported in equilibrium by a clump's turbulent energy and depends on a clump's velocity dispersion σ and radius R ($M_{vir} \propto \sigma^2 R$). The virial parameter, given by $\alpha = \frac{M_{vir}}{M_{clump}}$, compares a clump's mass to this threshold. Clumps with $\alpha < 1$ are subvirial and unstable to

collapse, clumps with $\alpha > 2$ are gravitationally unbound and will likely disperse, and clumps with $\alpha = 1 - 2$ are gravitationally bound and may become gravitationally unstable if perturbed (Kauffmann et al. 2013). Since competitive accretion requires that quiescent clumps collapse to provide the gas supply necessary to produce massive protostars, it predicts $\alpha \ll 2$ for clumps.

If the energy in magnetic fields is important, then magnetic fields can provide additional support against gravitational collapse (Strittmatter 1966). The critical mass for which magnetic fields can prevent collapse is given by $M_{B,crit} = 0.12 \left(\frac{\pi R^2 B_{avg}}{\sqrt{G}} \right)$, where B_{avg} is the average magnetic field strength and G is the gravitational constant (Bertoldi & McKee 1992). Thus, the critical mass for gravitational collapse that takes into account both turbulent and magnetic field energy is given by $M_{crit} = M_{vir} + M_{B,crit}$. Although many clumps do not have magnetic field measurements, Bertoldi & McKee (1992) argued that the magnetic energy and turbulent energy are in rough equipartition. Consequently, one can estimate the effect of both turbulence and magnetic fields on gravitational collapse by assuming that the combined turbulent and magnetic virial parameter is given by $\alpha_{turb+mag} = \frac{M_{vir} + M_{B,crit}}{M_{clump}} \approx 2\alpha$. If this relation is valid for high-mass star-forming clumps, then competitive accretion requires $\alpha \ll 1$ for massive quiescent clumps.

Larson (1981) compiled the sizes, masses, and velocity dispersions of a collection of molecular clouds taken from the literature (see Table 1 in Larson (1981) for references) in order to estimate the virial parameters of the molecular clouds. The resulting virial parameters had a mean of $\alpha = 5_{-3}^{+8}$, implying significant turbulent support against collapse. On the other hand, observations of clumps within molecular clouds have found that the more massive clumps are gravitationally stable or collapsing ($\alpha \lesssim 1$), while the less massive clumps are gravitationally unbound or

confined by external pressure ($\alpha \gg 1$) (Blitz 1987; Loren 1989a,b; Herbertz et al. 1991; Nozawa et al. 1991).

More recent investigations of molecular clump virial states show that the choice of molecular tracer is important. Several surveys have performed single-pointing NH₃ observations of BGPS (Svoboda et al. 2016) and ATLASGAL (Wienen et al. 2012, 2018) sources. Svoboda et al. (2016) found a median value of $\alpha = 0.73 \pm 0.06$ for their starless candidate clumps and $\alpha = 0.68 \pm 0.03$ for their protostellar clumps. Likewise, Wienen et al. (2012) and Wienen et al. (2018) both found $\alpha \sim 0.5$ for their clump samples.

Although these results imply that many of the dense molecular clumps in early evolutionary states may gravitationally unstable, the derived value of the virial parameter depends on underlying assumptions. Targeted NH₃ surveys can only probe the velocity dispersions along a single direction, but NH₃ mapping observations from RAMPS and HOPS show that the velocity dispersion varies throughout clumps. Furthermore, Svoboda et al. (2016), Wienen et al. (2012), and Wienen et al. (2018) determined clump sizes from their respective dust continuum data. Given that dust continuum fluxes at mm and submm wavelengths have a nonlinear dependence on the dust temperature, the sizes derived from the dust continuum may be biased toward smaller values in the case of internal protostellar or stellar heating. In the worst case, an angularly resolved hot core that dominates the mm flux in a clump would result in an estimated size similar to the core scale ($\sim 0.05 - 0.1$ pc) rather than the clump scale ($\sim 0.5 - 1$ pc). A virial analysis that determines the sizes of clumps directly from their mass surface density (Σ) distributions is necessary to determine whether clumps are truly subvirial.

Optically thick molecular lines offer an additional method to test whether clumps are gravitationally bound. Collapse motions give rise to asymmetric profiles

in optically thick lines (Snell & Loren 1977). One manifestation of this asymmetry is that optically thick lines tend to have blueshifted V_{LSR} values compared to optically thin lines, which is referred to as a “blue asymmetry.” Besides infall motions, generating the asymmetry requires a line-of-sight gradient in T_{ex} , such that T_{ex} near the center of the clump is larger than in its outer regions. Such a T_{ex} gradient is relatively common (Rigby et al. 2019), since it can arise from internal heating (Guzmán et al. 2015) or by a transition from subthermal ($n < n_{crit}$) emission in the more diffuse clump envelope to thermal ($n > n_{crit}$) emission near the denser clump center (MacLaren et al. 1988; Beuther et al. 2002; Mueller et al. 2002).

Figure 3.1 illustrates two idealized cases that produce blue asymmetries. In case 1, the clump is heated internally by a protostellar or stellar source, so the interior gas temperature is higher than in the clump envelope ($T_{hot} > T_{cold}$). If the optically thick transition is thermalized to the gas temperature, then the T_{ex} of the hot gas is larger than that of the cold gas. The optically thick line emission from redshifted infalling gas on the near side of the clump emits from a $\tau = 1$ surface where $T_{ex} = T_{cold}$. Due to the presence of solely redshifted emission on the near side of the clump, the blueshifted line emission becomes optically thick ($\tau > 1$) on the far side of the clump near the interior. Consequently, the blueshifted emission has a higher excitation temperature ($T_{ex} = T_{hot}$) than the redshifted emission, resulting in a blueshifted line asymmetry.

In case 2, the gas is isothermal, but features a density gradient with the highest densities toward the clump center. The gas in the clump envelope has a density that is less than the critical density ($n < n_{crit}$) of the optically thick transition, resulting in subthermal emission with $T_{ex} < T_{gas}$. On the other hand, the gas in the clump interior has a higher density ($n > n_{crit}$), resulting in thermal emission with $T_{ex} = T_{gas}$. As in case 1, the optically thick emission on the near side of the

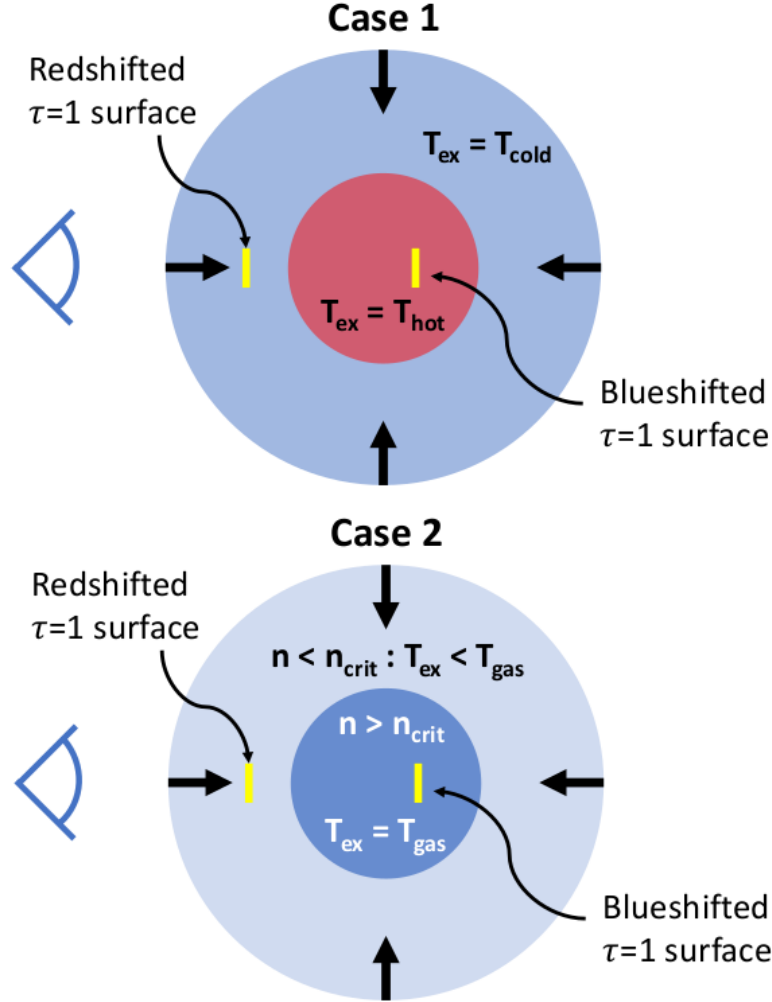


Fig. 3.1 Diagram displaying two idealized cases where gravitational infall causes blue asymmetric line profiles for optically thick transitions, where the observer is on the left. Case 1: Internal heating causes a gradient in T_{ex} . The line emission from the central region is thermalized to $T_{ex} = T_{hot}$, while the line emission from the envelope is thermalized to $T_{ex} = T_{cold}$. The redshifted emission becomes optically thick on the near side of the clump in a region where $T_{ex} = T_{cold}$. The blueshifted emission becomes optically thick on the far side of the clump in a region where $T_{ex} = T_{hot}$, resulting in more emission at blueshifted velocities. Case 2: The density profile of the clump is centrally condensed. The line emission from the central region is thermalized to $T_{ex} = T_{gas}$, while the line emission from the envelope is subthermal, with $T_{ex} < T_{gas}$. As in case 1, the blueshifted emission has a higher T_{ex} than the redshifted emission, resulting in a blue asymmetric line profile.

clump is redshifted, with a lower T_{ex} than the blueshifted emission on the far side of the clump. Thus, the resultant line from the optically thick transition displays a blueshifted line asymmetry.

Both of these cases describe idealized scenarios in which the infall rate is constant as a function of radius. In reality, more realistic velocity profiles will result in different $\tau = 1$ surfaces for emission at different velocities. Consequently, the emission emerging from a clump with such a velocity profile will have a more complex line shape.

Theorists have undertaken radiative transfer models to predict line shapes for optically thick molecular line emission in the presence of realistic infall motions. For spherically symmetric infall motions, optically thick lines often show double peaked profiles, where the blueshifted peaks are brighter than the redshifted peaks (Walker et al. 1994; Myers et al. 1996; Rawlings & Yates 2001). Blue asymmetric double peaked line profiles have been observed toward molecular cores (Walker et al. 1986; Myers et al. 1995; Narayanan et al. 1998), suggesting that these sources are undergoing gravitational collapse.

Gravitational collapse motions associated with high-mass star-forming clumps may be more complicated than those at the core scale and in low-mass star-forming regions. Filamentary structures and the associated asymmetrical gas flows are ubiquitous in high-mass star-forming regions (André et al. 2014), and the line emission from such sources may not provide as obvious of an infall signature as in the spherically symmetric case. Smith et al. (2012) performed radiative transfer modeling of optically thick lines from a massive filament and found that observational evidence of blue asymmetric line profiles strongly depends on viewing angle and often results in single peaked line profiles that are shifted blueward (Jackson et al. 2019). In addition, observations of blue asymmetric lines depend on the beam size, where observations

that probe smaller physical scales result in more significant blue asymmetries (Smith et al. 2013). Because high-mass star-forming clumps feature a range of inclination angles and distances, measurements of the blue asymmetry exhibit substantial scatter. Consequently, a large sample of measurements is necessary to detect a statistically significant shift in the velocities of optically thick lines compared to optically thin lines for an ensemble of sources.

3.1.2 Molecular Filament Kinematics

A study of clump kinematics provides information not only about the gravitational stability of clumps, but also about the possible flow motions along filaments. Such filamentary structures may play a role in transporting mass from the clump-scale to the core-scale (Balsara et al. 2001; Banerjee et al. 2006; Lu et al. 2018; Yuan et al. 2020), but their kinematic structure is not well understood. Although observers often attribute velocity gradients in molecular filaments to mass flows (e.g., Hacar & Tafalla 2011; Hacar et al. 2013; Kirk et al. 2013; Zernickel et al. 2013), projection effects and other forms of ordered motion, such as shear or rotation, can produce velocity gradients. Even in cases where a velocity gradient does indicate mass flow, the inferred direction of flow depends on the unknown filament orientation. Consequently, it is important to compare observations to theoretical predictions from simulated filaments, whose orientations and velocity structures are known.

Two recent hydrodynamical simulations, Smith et al. (2016) and Gómez & Vázquez-Semadeni (2014), make specific predictions about the relationship between velocity gradients along filaments and the positions of mass peaks where cores reside. Filaments in the Smith et al. (2016) simulation displayed the smallest velocity gradients near density peaks, indicating mass flow toward null points in the velocity gradient distribution. On the other hand, the Gómez & Vázquez-Semadeni (2014) filament simulation showed the largest velocity gradients at the density peaks, in-

dicating that the largest gravitational acceleration occurs near the density peaks. Because observed filaments have various orientations, a filament with a true velocity gradient of ∇V_{true} will have an observed velocity gradient (∇V_{obs}) in the range $-\nabla V_{true} < \nabla V_{obs} < +\nabla V_{true}$. Consequently, a large number of filaments must be analyzed to adequately test these theoretical predictions.

Several open questions remain concerning the early dynamical state of clumps and filaments. In particular, it is unclear if massive clumps undergo gravitational collapse to feed gas to their centers and if gas flows along filaments are important for transporting mass to cores. As of yet, the large samples, multiple datasets, and appropriate gas tracers necessary to accurately test these theoretical predictions have been too resource intensive to obtain. In this chapter, I will use RAMPS data, along with other large datasets, to test these open questions concerning the early evolution of molecular clumps and filaments. In Section 3.2, I test whether clumps are supported against gravitational collapse by turbulence using a virial analysis and a blue asymmetric line analysis. In Section 3.3, I test whether the velocity gradients within filaments are reproduced by simulations of gas flows onto cores. In Section 6, I conclude my analysis.

3.2 Gravitational Stability

In this section, I test whether the early evolution of clumps is associated with gravitational collapse, a central prediction of the theory of competitive accretion. In Section 3.2.1, I investigate the virial state of RAMPS clumps to determine if they are supported against gravitational collapse by turbulence. In Section 3.2.5, I perform a blue asymmetric line analysis to search for infall motions associated with gravitational collapse in the ensemble of clumps.

3.2.1 Virial Analysis

In this section, I perform a virial analysis to test whether molecular clumps are stable against gravitational collapse. In Section 3.2.2, I construct the sample of clumps used for the analysis. In Section 3.2.3, I calculate virial masses. In Section 3.2.4, I calculate virial parameters and compare results to theoretical predictions.

3.2.2 The Virial Analysis Subsample

Because the virial analysis is sensitive to the derived clump masses and radii, I removed sources for which accurate values of mass and radius could not be attained. The major limitation is the distance, which is needed to derive both masses and physical radii. The distance can be prone to large errors, since the near/far kinematic distance ambiguity results in two possible distances for most clumps. Consequently, I used the probabilities given by the Reid et al. (2016) distances to remove clumps with poorly constrained distances ($p < 75\%$). Although this reduced the size of the analysis sample from 2,680 to 1,195, it is necessary to avoid large systematic errors on the virial parameter.

Next, I removed clumps based on their angular sizes. Because observed sources are convolved with the telescope beam, the measured angular full width at half maximum (FWHM) diameters ($\theta_{obs,FWHM}$) for Gaussian sources are larger than their true values ($\theta_{src,FWHM}$) by $\theta_{obs,FWHM}^2 = \theta_{src,FWHM}^2 + \theta_{beam,FWHM}^2$, where $\theta_{beam,FWHM}$ is the FWHM beam size. In the case of non-Gaussian sources, this relation is approximate. On the other hand, the angular sizes determined from my clump-finding analysis represent the angular separations between the most distant pixels along the clump major axes (θ_{maj}) and minor axes (θ_{min}). Although these values represent the extent of the detected $\text{NH}_3(1,1)$ emission, these sizes suffer from a signal-to-noise bias, since clumps with higher signal-to-noise in their envelopes will have overesti-

mated θ_{maj} and θ_{min} values and clumps with lower signal-to-noise in their envelopes will have underestimated values. Furthermore, the NH₃ line intensity does not directly trace the gas column density, since it depends linearly on the gas temperature and on the NH₃ abundance ratio. Consequently, I determined the sizes for the virial analysis from the mass surface density maps.

For each clump, I found the peak surface density (Σ_{peak}) within the clump extent, which is defined by the extent of the NH₃(1,1) emission. I then defined a contour at $\Sigma = \frac{\Sigma_{peak}}{2}$, which has an interior solid angle of Ω_{src} . I calculated the effective half-width at half-maximum (HWHM) angular radius ($\theta_{HWHM,eff}$) within this contour as $\theta_{HWHM,eff} = \sqrt{\frac{\Omega_{src}}{\pi}}$. Out of the 1,195 clumps with well constrained distances, 48 feature multiple density peaks that are not enclosed by a common $\Sigma = \frac{\Sigma_{peak}}{2}$ contour. Given that the virial analysis assumes a single density condensation, I calculated $\theta_{HWHM,eff}$ for the density condensation containing Σ_{peak} . The deconvolved angular radius of a source is given by $\theta_{dec,HWHM}^2 = \theta_{obs,HWHM}^2 - \left(\frac{\theta_{beam,FWHM}}{2}\right)^2$. In order to exclude from the virial analysis sources with poorly determined deconvolved angular radii, I removed clumps with $\theta_{HWHM,eff} < 0.75 \times \theta_{beam,FWHM}$ from the virial analysis subsample. The final virial analysis subsample is comprised of 314 clumps with well defined masses and radii out of the full sample of 2,680 clumps. Table 3.1 lists a subsample of 11 clumps and their properties in Section 3.2.4. I provide the full sample of 314 clumps at OpenBU¹.

3.2.3 Calculating Virial Masses

The virial mass depends on a clump's density distribution and size. Molecular lines observations of giant molecular clouds (GMCs; Scoville & Solomon 1975; Solomon et al. 1979) and dust continuum observations of molecular clumps and

¹<https://open.bu.edu/handle/2144/43148>

cores in high-mass star-forming regions suggest that power-law radial density profiles ($\rho(r) \propto r^{-\gamma}$) are typical, with average power-law indices of $\gamma \sim 1.8$ (MacLaren et al. 1988; Beuther et al. 2002; Mueller et al. 2002; Garay et al. 2007). Because the Σ maps derived from the dust continuum data cannot accurately resolve density structures below the clump-scale (~ 1 pc), I assumed a power-law density index of $\gamma = 1.8$ for the virial analysis. Consequently, I calculated the virial masses for the analysis sample using the equation from MacLaren et al. (1988),

$$M_{vir} = 3 \left(\frac{5 - 2\gamma}{3 - \gamma} \right) \frac{\sigma^2 R}{G}, \quad (3.1)$$

where γ is the radial density profile power-law index, σ is the deconvolved 1D velocity dispersion, R is the physical radius of the clump, and G is the gravitational constant.

Similar to the angular convolution with the beam, the observed line widths were convolved with the channel width. Thus, the deconvolved velocity dispersion is given by $\sigma_{dec}^2 = \sigma_{obs}^2 - \frac{\Delta v_{chan}^2}{8\log(2)}$, where Δv_{chan} is the FWHM channel width. In addition, the RAMPS NH₃ observations provide σ throughout the clump, rather than at a single location like single-pointing surveys. I produced a single σ measurement for a given clump by determining the σ associated with the bulk of the turbulent energy. To do this, I weighted σ_{dec} by the square root of the mass surface density within the $\Sigma = \frac{\Sigma_{peak}}{2}$ contour. The energy-weighted σ is given by $\sigma_{wt} = \sqrt{\frac{\sum_i \sigma_i^2 \Sigma_i}{\sum_i \Sigma_i}}$, where σ_i is the deconvolved velocity dispersion of the i^{th} pixel and Σ_i is the mass surface density of the i^{th} pixel. Given that σ_{wt} was determined from the velocity dispersion throughout the clump region considered in the virial analysis, it should provide a more accurate assessment of a clump's turbulent energy than σ measured along a single line of sight in the clump.

I calculated the clump physical radii (R_{clump}) using the deconvolved angular FWHM diameters ($\theta_{dec,FWHM}$) and the adopted distances (d). The deconvolved

angular radii ($\theta_{R,dec}$) are half the respective $\theta_{dec,FWHM}$ values and the physical radii are given by $R_{clump} = d\theta_{R,dec}$, where $\theta_{R,dec}$ values are in units of radians.

Finally, I calculated the virial masses using Equation 3.1 and the derived velocity dispersions and physical radii. The resulting virial masses are given by $M_{vir} = 3.5 \frac{\sigma_{wt}^2 R_{clump}}{G}$. Figure 3.2 shows the distribution of M_{vir} for the virial analysis subsample.

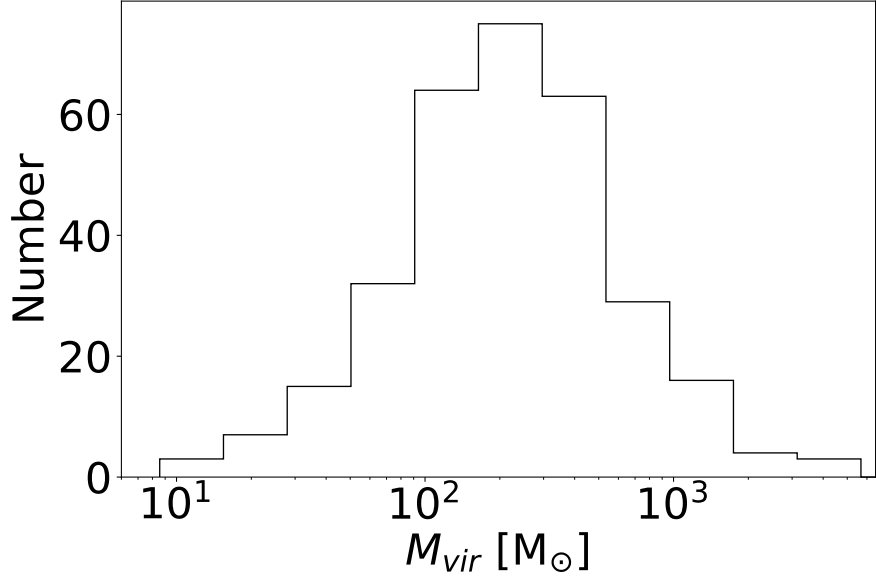


Fig. 3.2 Histogram of M_{vir} for the virial analysis subsample.

3.2.4 Virial Parameters

Next, I calculated the virial parameters using the virial masses and the clump masses determined within the respective $\Sigma = \frac{\Sigma_{peak}}{2}$ contours ($M_{clump,FWHM}$). If magnetic fields are negligible, a subvirial ($\alpha < 1$) α value implies gravitational collapse. A supervirial ($\alpha > 1$) α value implies that the clump is either gravitationally bound but stable against collapse ($\alpha = 1 - 2$) or gravitationally unbound ($\alpha > 2$). I investigated the evolution of α by splitting the analysis sample into quiescent, protostellar,

H II region, and PDR clump samples, which contain 48, 60, 136, and 70 clumps, respectively.

Table 3.1 lists the results of the virial analysis for the first 11 sources in the virial analysis sample. From left to right, the columns list the clump designations, FWHM radii, Σ -weighted velocity dispersions, FWHM masses, virial masses, virial parameters, and evolutionary states. I present these data for the full analysis sample at OpenBU².

Figure 3.3 displays M_{vir} vs. $M_{clump,FWHM}$ and histograms of α for these evolutionary samples. The virial analysis shows that the bulk of the clumps are subvirial, particular the massive clumps with $M > 260 M_\odot$ ³. Table 3.2 lists the fraction of subvirial clumps in each evolutionary category for high-mass and low-mass clumps. Competitive accretion predicts that massive quiescent clumps must eventually collapse to supply gas to the low-mass protostars in their centers, which are the precursors to the high-mass protostars in massive protostellar clumps. The results of my virial analysis support this prediction, since 100% of the massive quiescent clumps are subvirial. Even the lower mass quiescent clumps are generally subvirial, with 79% of the low-mass quiescent clumps having $\alpha < 1$. Including both low-mass and high-mass clumps, the quiescent sample has a median value of $\alpha \sim 0.4$. The protostellar subsample is even more subvirial, with a median value of $\alpha \sim 0.3$. This is true of the high-mass clumps, 97% of which are subvirial, and the low-mass clumps, 88% of which are subvirial. These results imply that the continuing collapse of protostellar clumps can maintain high accretion rates for the protostars near the clump centers.

Although the average α values for the H II region and PDR clump subsamples are larger than those of the quiescent and protostellar α averages, the bulk of these

²<https://open.bu.edu/handle/2144/43148>

³Assuming a 30% star formation efficiency and a Kroupa (2001) initial mass function, the most massive star produced by a $260 M_\odot$ clump is $8 M_\odot$ (Sanhueza et al. 2017).

Table 3.1. Virial Analysis Results

Clump Designation	R_{FWHM} (pc)	σ_{wt} (km s ⁻¹)	$M_{clump,FWHM}$ (M_\odot)	M_{vir} (M_\odot)	α	Evol. State
G10.566-0.026	0.81 ± 0.01	0.91 ± 0.02	3.7 ± 0.1 × 10 ²	5.4 ± 0.3 × 10 ²	1.45 ± 0.09	PDR
G10.615-0.031	0.78 ± 0.01	0.547 ± 0.009	6.5 ± 0.2 × 10 ²	1.90 ± 0.07 × 10 ²	0.29 ± 0.02	H
G10.682-0.033	0.38 ± 0.03	0.943 ± 0.005	3.7 ± 0.5 × 10 ²	2.7 ± 0.2 × 10 ²	0.7 ± 0.1	H
G10.701-0.100	0.66 ± 0.04	0.590 ± 0.005	2.8 ± 0.4 × 10 ²	1.9 ± 0.1 × 10 ²	0.7 ± 0.1	H
G10.724-0.330	0.46 ± 0.02	0.669 ± 0.004	6.1 ± 0.6 × 10 ²	1.67 ± 0.08 × 10 ²	0.27 ± 0.03	H
G10.978-0.363	0.95 ± 0.04	0.506 ± 0.002	1.0 ± 0.1 × 10 ³	1.98 ± 0.09 × 10 ²	0.19 ± 0.02	H
G12.030-0.031	1.06 ± 0.03	0.81 ± 0.01	1.03 ± 0.06 × 10 ³	5.7 ± 0.2 × 10 ²	0.55 ± 0.04	H
G12.377+0.005	0.8 ± 0.2	0.50 ± 0.01	3 ± 2 × 10 ²	1.6 ± 0.4 × 10 ²	0.5 ± 0.3	H
G12.670-0.206	0.72 ± 0.04	1.13 ± 0.03	9 ± 1 × 10 ¹	7.5 ± 0.6 × 10 ²	8.0 ± 1.0	PDR
G12.713-0.210	0.61 ± 0.03	1.00 ± 0.01	1.7 ± 0.2 × 10 ²	5.0 ± 0.3 × 10 ²	3.0 ± 0.4	H
G12.836-0.145	0.40 ± 0.03	0.61 ± 0.02	5.0 ± 0.7 × 10 ¹	1.2 ± 0.1 × 10 ²	2.4 ± 0.4	PDR

Table 3.2. Fraction of Collapsing Clumps

Sample	$\alpha < 1$	$\alpha < 0.5$
High-mass All	194/209 (93%)	145/209 (69%)
Low-mass All	70/105 (67%)	36/105 (34%)
High-mass Quiescent	24/24 (100%)	19/24 (79%)
Low-mass Quiescent	18/24 (75%)	10/24 (42%)
High-mass Protostellar	33/34 (97%)	30/34 (88%)
Low-mass Protostellar	23/26 (88%)	15/26 (58%)
High-mass H II Region	101/107 (94%)	70/107 (65%)
Low-mass H II Region	16/29 (59%)	5/29 (17%)
High-mass PDR	36/44 (82%)	26/44 (59%)
Low-mass PDR	13/26 (50%)	6/26 (23%)

Note. — If magnetic fields are negligible, then $\alpha < 1$ indicates collapse. If the magnetic field energy is in equipartition with the turbulent energy, then $\alpha < 0.5$ indicates collapse.

clumps are also subvirial. For the H II region clumps, 94% of the high-mass clumps and 59% of the low-mass clumps are subvirial. Thus, clump collapse may continue to drive accretion onto massive stars, even in the presence of significant radiation pressure (Krumholz et al. 2009).

The existence of low-mass clumps featuring H II regions may indicate that stellar feedback has altered the distribution of gas near the stellar source, making the present density more diffuse than it was previously. Alternatively, the H II regions visible in the MIR images may be unrelated sources that were erroneously associated with the clump.

For the PDR clumps, 82% of the high-mass clumps and 50% of the low-mass clumps are subvirial. Thus, even though the PDR clumps are irradiated by nearby

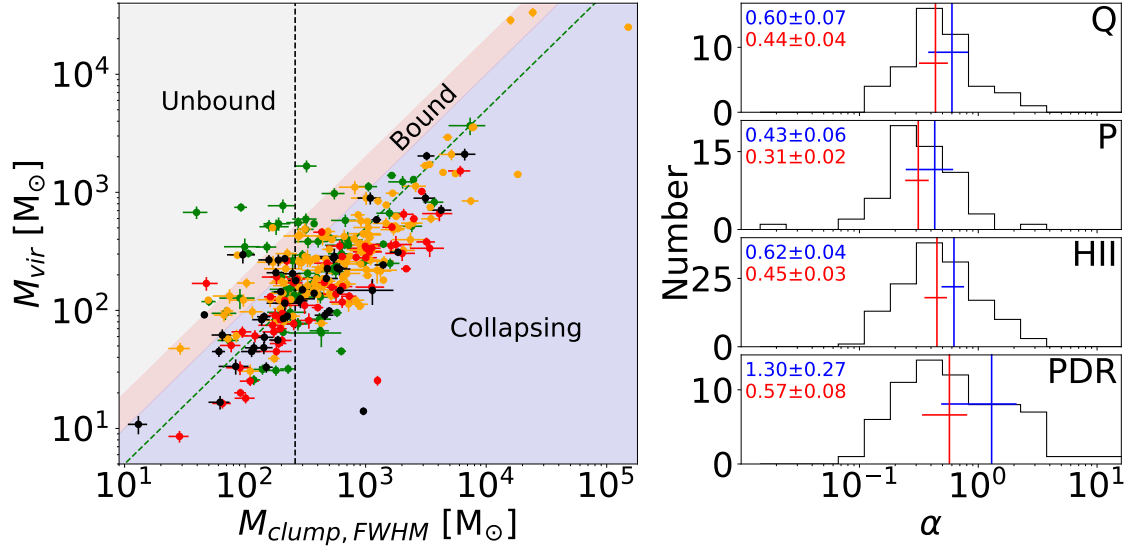


Fig. 3.3 Left: Symbol markers show M_{vir} vs. $M_{clump,FWHM}$ for the quiescent (black), protostellar (red), H II region (orange), and PDR (green) clumps. The shaded regions indicate clumps that are gravitationally unbound ($\alpha > 2$; gray), bound ($1 < \alpha < 2$; red), and collapsing ($\alpha < 1$; blue), assuming that the magnetic energy is negligible. The green dashed line indicates the boundary under which clumps are unstable to collapse if the magnetic energy is in equipartition with the turbulent energy. The black dashed line separates the high-mass ($M > 260 M_\odot$) and low-mass ($M < 260 M_\odot$) clumps. Right: From top to bottom, the panels show the distributions of α for the quiescent, protostellar, H II region, and PDR clumps. The vertical lines show the respective means (blue) and medians (red) for each distribution computed in linear space. The horizontal lines show three times the error on the respective values. The numerical values of the means (blue) and medians (red) are displayed in the upper left of each panel.

high-mass stars, their virial parameters suggest that some of the clumps in this subsample may undergo gravitational collapse.

My analysis up to now has neglected the effects of magnetic fields, which likely provide additional support against gravitational collapse (Strittmatter 1966). If the magnetic energy is comparable to the turbulent energy in molecular clumps (Crutcher 1999), then the critical virial parameter corresponding to gravitational instability is decreased by a factor of two Bertoldi & McKee (1992). In this case, clumps with

$\alpha < 0.5$ are gravitationally collapsing, those with $\alpha = 0.5 - 1$ are gravitationally bound, and those with $\alpha > 1$ are gravitationally unbound.

Table 3.2 also lists the fraction of clumps in each evolutionary category with $\alpha < 0.5$. Most of the massive quiescent and protostellar clumps also satisfy this more stringent requirement for collapse, with 79% and 88% having $\alpha < 0.5$, respectively. Thus, the presence of magnetic fields in equipartition with turbulence does not change my conclusions that massive clumps collapse during their early evolutionary stages. On the other hand, 42% and 58% of the low-mass quiescent and protostellar clumps, respectively, have $\alpha < 0.5$. Consequently, magnetic fields may be important in regulating the collapse of clumps that form low-mass stellar clusters.

Given the larger virial parameters associated with H II region and PDR clumps, more of these clumps could be supported by the inclusion of magnetic field energy. For H II region clumps, 65% of the high-mass clumps and 17% of the low-mass clumps have $\alpha < 0.5$. Likewise, 59% of the high-mass and 23% of the low-mass PDR clumps have $\alpha < 0.5$. Thus, the derived virial parameters suggest that magnetic fields, in addition to turbulence added by stellar feedback, could limit further collapse in many H II region and PDR clumps, particularly those with lower masses.

The α values derived by this virial analysis are similar to those found by Wienen et al. (2012) and Wienen et al. (2018). Wienen et al. (2012) found an average virial parameters of $\alpha = 0.21$ for sources with narrow line widths ($\sigma \lesssim 0.75 \text{ km s}^{-1}$) and $\alpha = 0.45$ for sources with broad line widths ($\sigma \gtrsim 0.75 \text{ km s}^{-1}$). Likewise, Wienen et al. (2018) found an average of $\alpha = 0.54$ for their full sample. The α values derived by my analysis and those of Wienen et al. (2012) and Wienen et al. (2018) are slightly smaller than the Svoboda et al. (2016) median values of $\alpha = 0.73$ for starless clumps and $\alpha = 0.68$ for protostellar clumps. As noted by Wienen et al. (2012), part of this discrepancy is likely the result of differing definitions of clump

radii. The BGPS clump sizes were defined by an “effective radius” (Rosolowsky et al. 2010) that is somewhat larger than the HWHM radii derived from the Σ analysis used here and from the ATLASGAL 870 μm dust continuum maps (Wienen et al. 2012). In addition, σ_{wt} used in my analysis is on average $\sim 5\%$ smaller than the σ values derived from the single pointing observations, though this corresponds to only a $\sim 10\%$ reduction in α . Regardless of these differences, the similar results returned by multiple analyses that utilized independent measurements, as well as disparate methods and assumptions, strengthens the argument that a significant portion of high-mass clumps are unstable to gravitational collapse.

On the other hand, there are two additional caveats for the virial analysis that must be kept in mind. The first caveat is the effect of the uncertain density distributions. Although massive molecular clumps and cores are centrally condensed, their measured power-law density indices span a range of γ from unity to 2.2 (e.g., van der Tak et al. 2000; Beuther et al. 2002; Mueller et al. 2002). If the clumps in my virial analysis subsample have shallower power-law density indices than the assumed $\gamma = 1.8$, then the derived virial parameters are underestimated. On the other hand, steeper power-law density indices would imply that the the derived virial parameters are overestimated. For the most extreme case of a uniform density ($\gamma = 0$), the virial parameters would be underestimated by $\sim 40\%$, while $\gamma = 1$ would correspond to a $\sim 30\%$ underestimation and $\gamma = 2.2$ would correspond to a $\sim 50\%$ overestimation. If the power-law density indices of the clumps span a range of values, but are not heavily skewed toward either extreme, the derived virial parameters would not be significantly skewed toward lower or higher values. Assuming this is the case, the uncertain density distributions should not substantially change the proportion of clumps that I have inferred are gravitationally unstable.

The second caveat is that the clump masses are likely more systematically uncertain than the error propagated from the errors on Σ and the distance. There is likely an error component associated with the dust properties, since dust composition, grain shapes, grain size distribution, icy mantle thickness, and ice composition are all uncertain quantities (Hildebrand 1983). Although the uncertain dust properties will add an additional source of error on the clump masses, my adopted value of the dust spectral index β and the dust opacity law were motivated by fits to the submm emission from massive clumps (Guzmán et al. 2015). Dust modeling by Ormel et al. (2011) implies that the submm β will only increase appreciably if dust coagulation produces very large ($\sim 100 \mu\text{m}$) grains, so these values are unlikely to be significantly discrepant in a systematic manner.

Despite these caveats, the results of my virial analysis imply that the majority of quiescent and protostellar clumps are gravitationally unstable to collapse. This finding supports the competitive accretion model of high-mass star formation, which predicts that massive clumps must collapse at early evolutionary stages to provide a large supply of gas to accreting protostars at the clump centers.

One argument against this result is that it produces much higher star-formation rates than are observed in our Galaxy (Zuckerman & Evans 1974). I can make a rough estimate of the star-formation rate implied by these results with a few assumptions. First, I assume that clumps with $\alpha < 0.5$ will collapse in a free-fall time (t_{ff}), which is given by $t_{ff} = \sqrt{\frac{3\pi}{32G\rho}}$, where ρ is the average mass density. An average number density of $n = 10^4 \text{ cm}^{-3}$ corresponds to $t_{ff} \approx 3 \times 10^5 \text{ yr}$ and an average number density of $n = 10^3 \text{ cm}^{-3}$ corresponds to $t_{ff} \approx 10^6 \text{ yr}$. Since the clumps with $\alpha < 0.5$ comprise 80% of the mass in the virial analysis subsample, I can further assume that 80% of the dense gas mass in the Galaxy will collapse in t_{ff} . Roman-Duval et al. (2016) estimated the very dense gas mass in the Galaxy from CS observations and

found $M_{dg} \sim 2.7 \times 10^7 M_\odot$. Given my assumptions, $M_{collapse} \sim 2.3 \times 10^7 M_\odot$ of dense gas will collapse in t_{ff} . The corresponding star formation rate is given by $\dot{M}_{SFR} = \epsilon \left(\frac{M_{collapse}}{t_{ff}} \right)$, where ϵ is the star formation efficiency. Assuming a standard star formation efficiency of $\epsilon = 0.3$ and an average number density of $n = 10^4 \text{ cm}^{-3}$, $\dot{M}_{SFR} \sim 23 M_\odot \text{ yr}^{-1}$. If $n = 10^3 \text{ cm}^{-3}$, this implies $\dot{M}_{SFR} \sim 7 M_\odot \text{ yr}^{-1}$. Estimates of the true star formation rate vary, but range between $0.7 - 5 M_\odot \text{ yr}^{-1}$ (Smith et al. 1978; Diehl et al. 2006; Misiriotis et al. 2006; Murray & Rahman 2010; Robitaille & Whitney 2010).

Given that my estimation of the star formation rate exceeds the observed rate, one or more of my assumptions must be incorrect. First, it is unclear what star formation efficiency is appropriate for this estimate. The star formation efficiency measured on Galactic scales is low, with an average of $\epsilon \sim 0.005$, while at the GMC scale the average star formation efficiency increases to $\epsilon \sim 0.08$ (Murray 2011). The average star formation efficiency is likely larger at the clump scale, but it is unclear whether $\epsilon = 0.3$ is an appropriate value for this sample of clumps.

My other assumption that may be incorrect is the significance of magnetic fields. Even in clumps where gravity dominates the turbulent and magnetic energy, the magnetic field may slow the collapse to larger timescales than t_{ff} (Krumholz & Federrath 2019). Furthermore, magnetic fields may be stronger than I have assumed in my analysis. Previous studies that found significantly subvirial clump populations have raised the possibility that strong magnetic fields may be required to prevent or slow collapse in the majority of clumps (Kauffmann et al. 2013).

Svoboda et al. (2016) reformulated Equations 6 and 16 from Kauffmann et al. (2013) to provide a limiting magnetic field strength required to support against collapse, $B \gtrsim 35 \mu\text{G} \left(\frac{2}{\alpha} - 1 \right) \left(\frac{\sigma}{1 \text{ km s}^{-1}} \right)^2 \left(\frac{1 \text{ pc}}{R} \right)$. The median magnetic field strength required to prevent the $\alpha < 0.5$ subsample from collapsing is $B \sim 0.15 \text{ mG}$, with the

most subvirial clumps requiring magnetic fields of $B \sim 1$ mG to prevent collapse. Curran & Chrysostomou (2007) performed submm imaging polarimetry observations toward a sample of 14 high-mass star-forming regions and measured their magnetic field strengths. They found magnetic field strengths of $B < 0.1$ mG up to $B = 5.7$ mG, with most of the sources in the $B = 0.2 - 0.4$ mG range. Likewise, Pillai et al. (2015) measured a magnetic field strength of $B \sim 0.25$ mG for the massive filament G11.11-0.12, which comprises a portion of the filament designated as G11.056-0.100 in the RAMPS catalog.

Although such magnetic field strengths are unlikely to halt gravitational collapse, since magnetic field energy can be lost through ambipolar diffusion (Zweibel 1988) or magnetic reconnection (Lazarian 2005), they would likely increase the collapse timescale to longer than t_{ff} . Thus, magnetic fields may play a crucial role in regulating star formation and limiting the star formation rate inferred from virial analyses to values nearer to those observed. Further magnetic field measurements for a large sample of clumps are necessary to determine the significance of magnetic support in high-mass star formation.

3.2.5 Blue Asymmetric Line Analysis

In this section, I search for infall motions toward molecular clumps using a blue asymmetric line analysis. In Section 3.2.5.1, I show that $^{13}\text{CO}(1-0)$ is optically thick toward dense molecular clumps and can be employed in a blue asymmetric line analysis. In Section 3.2.5.2, I describe the line fitting process. In Section 3.2.5.3, I determine line asymmetries and compare between evolutionary states. In Section 3.2.5.3, I compare to previous results.

3.2.5.1 $^{13}\text{CO}(1-0)$ as an Optically Thick Tracer of Dense Clumps

A blue asymmetric line analysis compares the velocities of an optically thick and an optically thin tracer to search for infall motions. Because the nonspherical density distributions and asymmetrical gas flows typical of high-mass star-forming regions cause this analysis to depend on viewing angle (Smith et al. 2012), a large number of spectra are needed to detect a significant trend. The Galactic Ring Survey (GRS; Jackson et al. 2006) is a survey of the $^{13}\text{CO}(1-0)$ transition in the Galactic longitude range $l = 18^\circ - 55.7^\circ$. GRS has a significant overlap with RAMPS, making it useful survey for a blue asymmetric line analysis. Although $^{13}\text{CO}(1-0)$ is not typically thought of as an optically thick tracer, it is almost certainly more optically thick than $\text{NH}_3(1,1)$ and can show signs of self absorption toward extremely high surface density ($\Sigma \gtrsim 1 \text{ g cm}^{-2}$) clumps (Lada & Wilking 1980).

I used RADEX (van der Tak et al. 2007), a non-LTE molecular radiative transfer code, to determine the expected optical depth at line center ($\tau(^{13}\text{CO}(1-0))_0$) for the gas properties typical of molecular clumps. The clumps in the RAMPS sample display a range of surface densities and temperatures, with typical values of $\Sigma = 0.01 - 1 \text{ g cm}^{-2}$ ($N(H_2) = 0.02 - 2 \times 10^{23} \text{ cm}^{-2}$) and $T_{kin} = 10 - 30 \text{ K}$. I assumed $n = 10^3 \text{ cm}^{-3}$, a lower density than typical clumps, but appropriate for $^{13}\text{CO}(1-0)$ since it is sensitive to more diffuse gas. I also assumed a typical ^{13}CO abundance of $\chi(^{13}\text{CO}) = 2 \times 10^{-6}$ (Dickman 1978) and modeled velocity dispersions of $\sigma = 0.5$ and 1 km s^{-1} . Although the temperature, density, and ^{13}CO abundance are unlikely to be constant throughout clumps, more complicated assumptions concerning the temperature, density, and ^{13}CO abundance distributions are not warranted by this proof of concept analysis.

Figure 3.4 shows the results of this analysis. Neglecting variations in the ^{13}CO abundance, the $^{13}\text{CO}(1-0)$ transition is optically thick ($\tau_0 \gtrsim 3$) over most of this parameter space, particularly for $T_{kin} = 10 - 20 \text{ K}$. Because the column densities

supplied to RADEX are beam-averaged values, the true ^{13}CO optical depths may be larger due to unresolved substructures. Given that most RAMPS clumps have $\text{NH}_3(1,1)$ optical depths of $\tau_0(\text{NH}_3(1,1)) = 0.5 - 2$, the $^{13}\text{CO}(1-0)$ transition will generally have much larger optical depths. Because the $\text{NH}_3(1,1)$ transition is an optically thin tracer and the $^{13}\text{CO}(1-0)$ transition is an optically thick tracer of dense clumps, $\text{NH}_3(1,1)$ and $^{13}\text{CO}(1-0)$ are suitable spectral lines to use for a blue asymmetry analysis

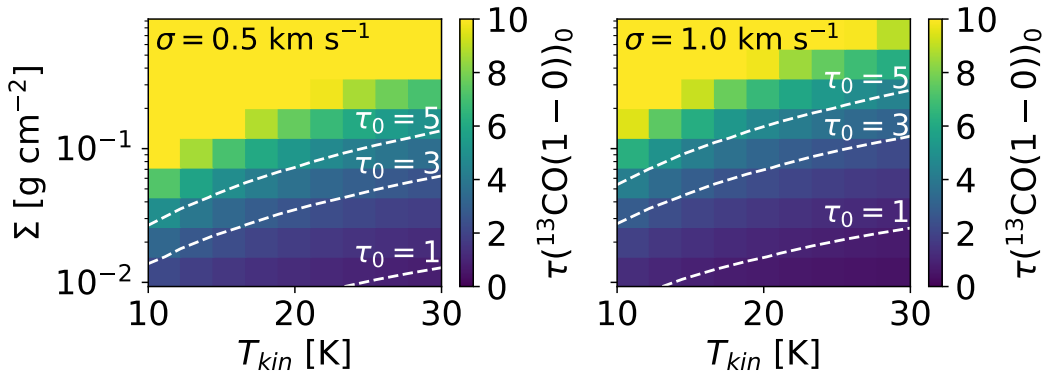


Fig. 3.4 RADEX $^{13}\text{CO}(1-0)$ optical depth at line center for a range of T_{kin} and Σ . Left: $\tau(^{13}\text{CO}(1-0))_0$ assuming $\sigma = 0.5 \text{ km s}^{-1}$. Right: $\tau(^{13}\text{CO}(1-0))_0$ assuming $\sigma = 1 \text{ km s}^{-1}$.

3.2.5.2 Line Fitting

In order to compare the velocities of the optically thin RAMPS $\text{NH}_3(1,1)$ emission and the optically thick GRS $^{13}\text{CO}(1-0)$ emission, I first regridded the RAMPS data along all three axes to match the GRS data. Next, I performed $\text{NH}_3(1,1)$ line fitting (Section 2.5.1.2) on the regridded data to determine the $\text{NH}_3(1,1)$ line center V_{LSR} . I performed a similar fitting on the $^{13}\text{CO}(1-0)$ data, modeling the $^{13}\text{CO}(1-0)$ line as a superposition of its two overlapping hyperfine lines. The hyperfine line at $V_{LSR} = v_0 - 0.044 \text{ km s}^{-1}$ has two thirds of the optical depth and the line at $v_0 + 0.089 \text{ km s}^{-1}$ has the remaining one third of the optical depth. As with the NH_3

line models, I modeled the $^{13}\text{CO}(1\text{-}0)$ optical depth profiles as overlapping Gaussian hyperfine lines with ratios equal to their respective statistical weights and produced the corresponding intensity profiles using Equation 2 from Appendix F.

I attempted to fit with an additional velocity component when there was significant ($> 3\sigma_{noise}$) emission in the residual. As was done for the $\text{NH}_3(1,1)$ fit routine, I accepted the fit with the greatest value of $\text{BIC} - 5 \times N_{comp}$, where BIC is the Bayesian information criterion and N_{comp} is the number of velocity components. I restricted the fit routine to a maximum of ten velocity components, which was sufficient to fit all significant velocity components in the vast majority of spectra. In total, 1,299 out of 2,680 RAMPS clumps had valid $^{13}\text{CO}(1\text{-}0)$ fits coincident with valid $\text{NH}_3(1,1)$ fits.

Figure 3.5 shows the best-fit velocities and velocity errors for every velocity component of the $^{13}\text{CO}(1\text{-}0)$ and $\text{NH}_3(1,1)$ fits. The median errors for both lines are much less than the channel width of 0.21 km s^{-1} . The velocity errors for the $^{13}\text{CO}(1\text{-}0)$ fits show a larger spread, but a smaller median value, than the $\text{NH}_3(1,1)$ fits. This is likely due to the fact that the $^{13}\text{CO}(1\text{-}0)$ lines tend to exhibit larger velocity dispersions than the $\text{NH}_3(1,1)$ lines, which result in larger velocity errors, as well as higher signal-to-noise ratios, which result in smaller velocity errors.

Fitting with the $^{13}\text{CO}(1\text{-}0)$ hyperfine model has two major differences compared to fitting with a pure Gaussian. First, the line intensity profile is determined by the optical depth profile, so models with high optical depth parameters produce flat-topped line profiles. Given that the surface densities and temperatures typical of RAMPS clumps can produce optically thick $^{13}\text{CO}(1\text{-}0)$ lines (Fig. 3.4), it is important to accurately model optically thick line profiles.

Second, the hyperfine lines have different optical depths, so the intensity-weighted velocity of the $^{13}\text{CO}(1\text{-}0)$ hyperfine lines changes with optical depth. On

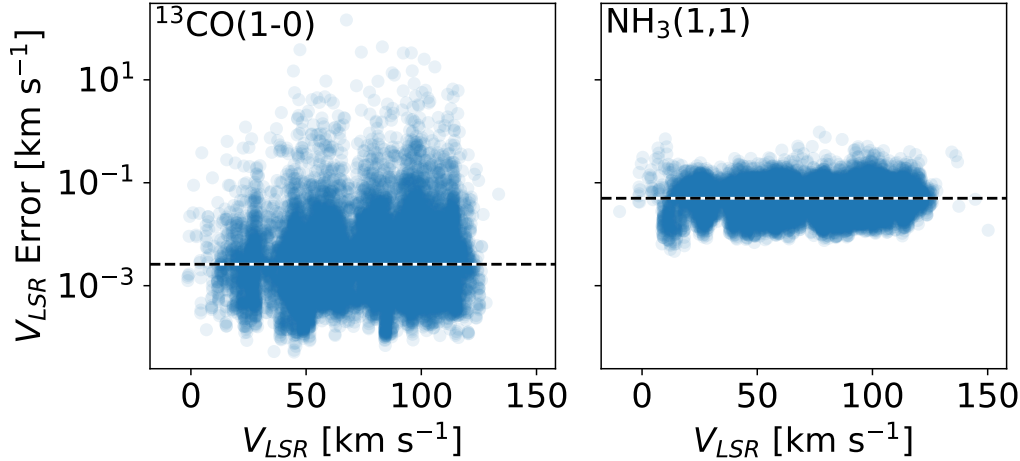


Fig. 3.5 Left: Error on line center V_{LSR} vs. V_{LSR} for the $^{13}\text{CO}(1-0)$ fits. The horizontal line shows the median velocity error of 0.003 km s^{-1} . Right: Error on V_{LSR} vs. V_{LSR} for the $\text{NH}_3(1,1)$ fits. The horizontal line shows the median velocity error of 0.05 km s^{-1} .

the other hand, the channel width of the GRS $^{13}\text{CO}(1-0)$ spectra is larger than the splitting of the hyperfine transitions, so the relative intensities of the $^{13}\text{CO}(1-0)$ hyperfine lines cannot be used to accurately determine the total optical depth of the $^{13}\text{CO}(1-0)$ line.

In principle, this inability could lead to systematic differences between the fit velocity and the true line velocity. To test this, I created a grid of synthetic $^{13}\text{CO}(1-0)$ spectra with a range of optical depths and velocity dispersions. I fit these synthetic spectra with a Gaussian line intensity model in order to determine whether the intensity-weighted line velocity differs significantly from the optical depth-weighted line velocity.

Figure 3.6 shows the results of this test. The velocity difference between the optical depth-weighted velocity (V_{true}) and the intensity-weighted Gaussian fit velocity (V_{fit}) is only significant for very narrow lines ($\sigma \leq 0.2 \text{ km s}^{-1}$). For larger velocity dispersions, the difference between these velocities is within $\pm 0.003 \text{ km s}^{-1}$. Given

that 99% of the $^{13}\text{CO}(1-0)$ fits used in the blue asymmetry analysis have velocity dispersions of $\sigma > 0.32 \text{ km s}^{-1}$ (white dashed line in Figure 3.6), the velocity errors due to the hyperfine splitting are small compared to the median $\text{NH}_3(1,1)$ fit velocity error and comparable to the median $^{13}\text{CO}(1-0)$ fit velocity error.

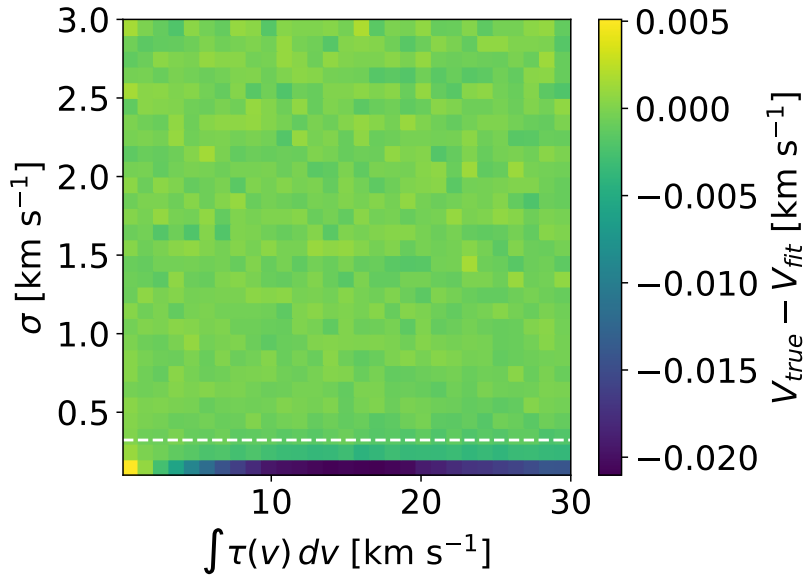


Fig. 3.6 Velocity difference between the optical depth-weighted velocity (V_{true}) and the intensity-weighted Gaussian fit velocity (V_{fit}) for synthetic $^{13}\text{CO}(1-0)$ with a range of velocity dispersions and total optical depths. The horizontal line marks $\sigma = 0.32 \text{ km s}^{-1}$, where 99% of the fits to the GRS $^{13}\text{CO}(1-0)$ data exhibit greater σ values.

Figure 3.7 shows several examples of the fits to the $\text{NH}_3(1,1)$ and $^{13}\text{CO}(1-0)$ spectra for a selection of RAMPS clumps. The fit results generally reproduce the data, to within the noise. In two cases (upper right and bottom middle panels), it is clear that the $^{13}\text{CO}(1-0)$ spectra have flatter peaks than pure Gaussians and are best fit by models with high optical depths at line center ($\tau(^{13}\text{CO}(1-0))_0 > 5$). Each panel also shows the velocity difference between $\text{NH}_3(1,1)$ and $^{13}\text{CO}(1-0)$ fits, $V_{diff} = V_{\text{NH}_3} - V_{^{13}\text{CO}}$. A variety of V_{diff} values are observed in the data.

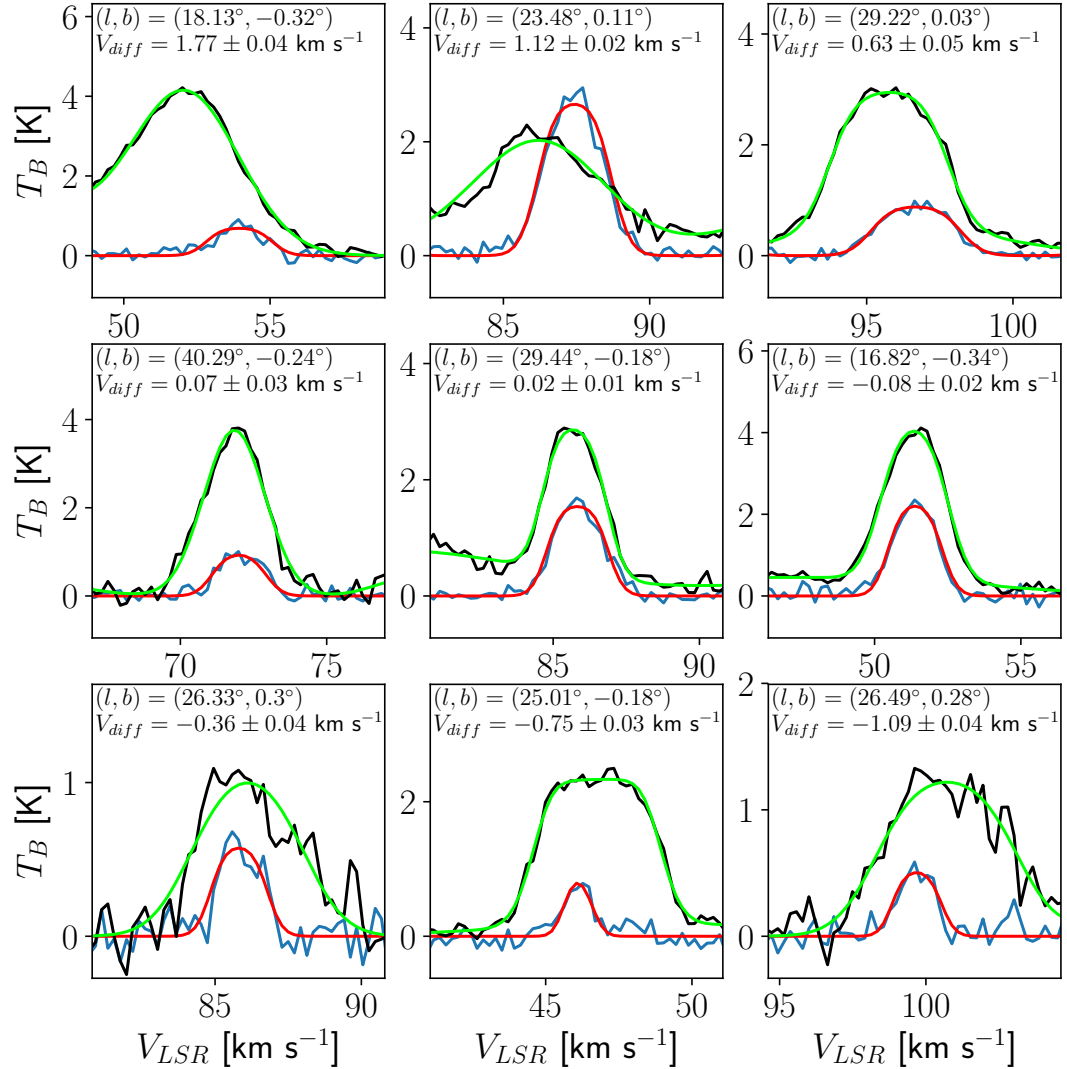


Fig. 3.7 Example fits to GRS and RAMPS spectra toward RAMPS clumps used in the blue asymmetry analysis. The NH₃(1,1) hyperfine satellite lines are outside the velocity bounds shown. The RAMPS NH₃(1,1) spectra are shown in blue, the NH₃(1,1) fits are shown in red, the GRS ¹³CO(1-0) spectra are shown in black, and the ¹³CO(1-0) fits are shown in green. The Galactic positions of the spectra and the velocity differences (V_{diff}) between the NH₃(1,1) and ¹³CO(1-0) fits are listed in the upper left of each panel.

3.2.5.3 Line Asymmetries

Next, I calculated V_{diff} for each pixel with a valid V_{NH_3} and $V_{^{13}\text{CO}}$ value. For each $\text{NH}_3(1,1)$ velocity component, I determined V_{diff} using the $^{13}\text{CO}(1-0)$ component that was closest in velocity. I excluded $\text{NH}_3(1,1)$ fits that featured multiple velocity components, since closely spaced lines can mimic asymmetries due to gravitational collapse, adding additional error to the data. I also excluded V_{diff} values with errors larger than the channel width (0.21 km s^{-1}) to reduce the error added by poor fit results.

Because the pixel size of the $^{13}\text{CO}(1-0)$ data cubes is approximately half the telescope beam width, the data are oversampled with respect to the angular resolution of the beam. To reduce the statistical effect of correlated V_{diff} values due to oversampling, I sampled V_{diff} values from every other pixel. Thus, each V_{diff} value used in my analysis was taken at least one GRS FWHM beam width ($46''$) away from every other value.

The remaining data are comprised of 4,286 independent V_{diff} measurements from 1,293 clumps. Next, I calculated clump-averaged V_{diff} values for the 712 clumps that feature multiple independent V_{diff} measurements. I propagated the individual errors on V_{diff} to determine the errors on the clump-averaged V_{diff} values.

Figure 3.8 shows the error on V_{diff} plotted against V_{diff} for each clump. The red line indicates significant red asymmetries ($V_{diff} < -3 \times V_{diff} \text{ Error}$) and the blue line indicates significant blue asymmetries ($V_{diff} > 3 \times V_{diff} \text{ Error}$). The distribution of V_{diff} values shows a slight excess of significantly blue asymmetric $^{13}\text{CO}(1-0)$ lines. Out of 1,293 clumps, 31% exhibit significant blue asymmetries and only 17% exhibit significant red asymmetries.

Figure 3.9 displays the distribution of V_{diff} values for all 1,293 clumps. The mean and median of the distribution are displayed in the upper left of the plot,

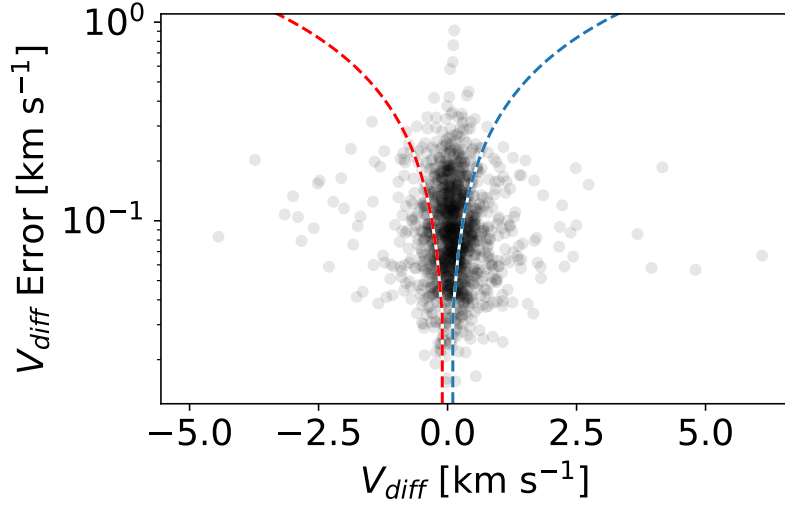


Fig. 3.8 Error on V_{diff} vs. V_{diff} for 1,293 clumps from the RAMPS sample. The red dashed line marks the significantly red asymmetric $^{13}\text{CO}(1\text{-}0)$ lines with $V_{diff} = -3 \times V_{diff}$ Error and the blue dashed line marks the significantly blue asymmetric $^{13}\text{CO}(1\text{-}0)$ lines with $V_{diff} = 3 \times V_{diff}$ Error.

with errors determined by bootstrap resampling. Both values indicate that the offset toward positive V_{diff} is significant ($\gtrsim 5\sigma_{err}$).

I also calculated the error on the mean of V_{diff} by propagating the fit uncertainty, which resulted in a mean of $V_{diff} = 0.108 \pm 0.004 \text{ km s}^{-1}$. Finally, I performed a two sample K-S test to compare the V_{diff} distribution to a Gaussian distribution centered at $V_{diff} = 0 \text{ km s}^{-1}$ with the same number of samples and the same standard deviation. The resulting K-S statistic is 0.16 and the p -value is 8.2×10^{-16} , indicating a very low likelihood that the V_{diff} distribution was drawn from a Gaussian distribution centered at $V_{diff} = 0 \text{ km s}^{-1}$.

The means, median, and K-S test all indicate a significant excess of blue asymmetric $^{13}\text{CO}(1\text{-}0)$ lines. These results suggest that gravitational infall motions are present in the RAMPS clump sample.

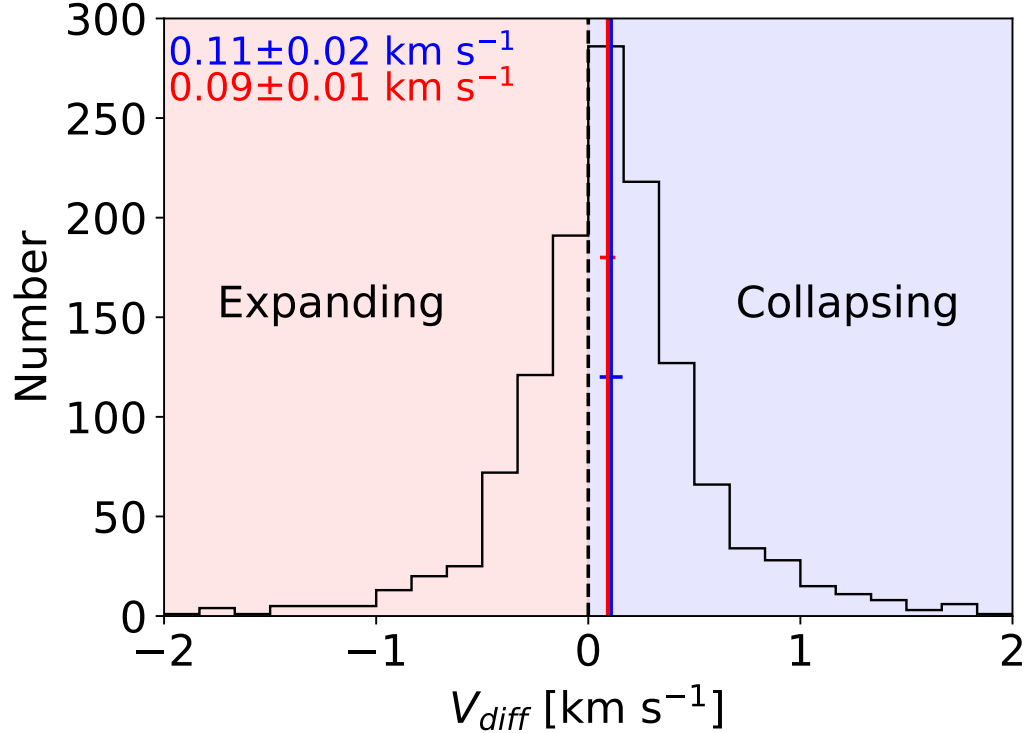


Fig. 3.9 Histogram of V_{diff} values for all 1,293 clumps, where the dashed black line marks $V_{diff} = 0 \text{ km s}^{-1}$, the blue vertical line marks the mean, and the red vertical line marks the median of the distribution. The solid horizontal lines signify three times the error on the respective values. The mean (blue) and median (red), with their respective 1σ errors, are displayed at the upper left. The red shaded region indicates $V_{diff} < 0 \text{ km s}^{-1}$, implying expansion motions, while the blue shaded region indicates $V_{diff} > 0 \text{ km s}^{-1}$, implying collapse motions.

Given that infall motions might be expected to evolve as clumps evolve, I separated the V_{diff} values shown in Figure 3.9 by evolutionary state. The resulting sample contained 131 quiescent clumps, 206 protostellar clumps, 467 H II region clumps, and 193 PDR clumps.

Figure 3.10 shows the V_{diff} distributions for each evolutionary state, with vertical lines indicating the means and medians for their respective distributions. The respective mean and median values are also displayed in the upper left of each panel.

The means and medians V_{diff} values of the quiescent and H II region clumps at least $3\sigma_{err}$ greater than $V_{diff} = 0 \text{ km s}^{-1}$, while these values for the protostellar and PDR clump samples are $< 3\sigma_{err}$ above $V_{diff} = 0 \text{ km s}^{-1}$. The quiescent sample exhibits the largest asymmetry, while the H II region clumps have the second largest asymmetry.

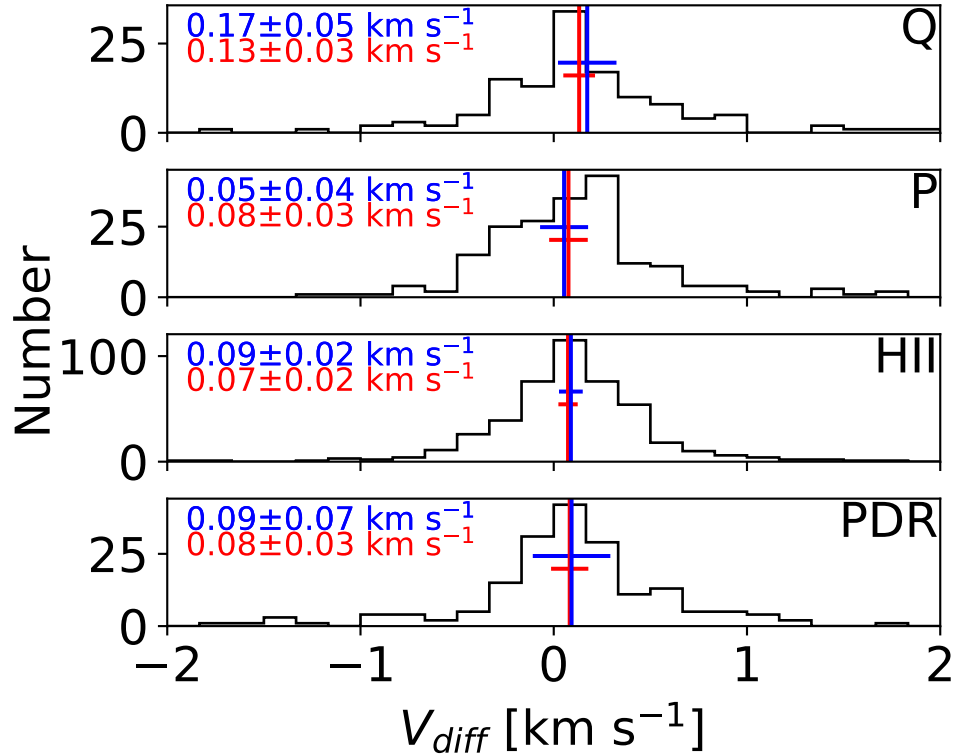


Fig. 3.10 Histograms of V_{diff} for massive ($M > 260 M_\odot$) clumps separated by evolutionary states, which are indicated in the top right of each panel. The vertical lines indicate the means (blue) and medians (red) of the distributions and the horizontal lines mark three times the respective errors. The mean and median values are also shown in upper left of each panel.

The significant blue asymmetry associated with quiescent clumps suggests that they are undergoing gravitational collapse, which is also implied by their low virial parameters. Both analyses, which used different datasets and methods, suggest that quiescent clumps are collapsing. These results provide additional support for a central

prediction of the competitive accretion theory, which relies on the collapse of clumps to form massive protostars. This also suggests either the presence of significant subthermal emission in the clump envelope or internal heating by low-mass protostars to produce a gradient in T_{ex} .

Given that the protostellar stage is associated with accretion, it is surprising that the protostellar clumps, which display MIR emission that suggests the presence of protostars, exhibit a less significant blue asymmetry than the H II region clumps. Furthermore, the contrast with the protostellar virial parameters, which had the lowest values compared to the other evolutionary subsamples, is puzzling. One possible explanation is the presence of protostellar outflows, which could alter the line center velocities and line shapes of the $^{13}\text{CO}(1-0)$ line. Alternatively, the less significant blue asymmetry may indicate variations in the infall velocities on the large scales traced by ^{13}CO or it may imply a contrast in the radiative transfer of the $^{13}\text{CO}(1-0)$ emission through protostellar clumps compared to the other evolutionary states.

Although H II regions are typically associated with expansion motions, the blue asymmetry measured toward clumps hosting H II regions is significant. The virial analysis found many subvirial H II region clumps, suggesting that collapse motions are plausible. In addition, the V_{diff} measurements were taken over the entire clumps, rather than solely toward the H II regions. Many clumps that host H II regions also contain cold, quiescent gas far from the exciting sources. The significant asymmetry of the H II region clump sample implies that sections of these clumps are undergoing collapse despite the presence of H II regions.

Unsurprisingly, the PDR clumps do not exhibit significant evidence of infall motions. This is likely a result of their close proximity to H II regions, which add heat, turbulence, and produce expansion motions in the surrounding gas, which makes detecting infall motions more difficult. Indeed, Figure 2.20 from Section 2.5.1.5

shows that PDR clumps exhibit larger velocity dispersions on average than the other evolutionary states, after the H II region clumps. In addition, PDR virial parameters are larger than those of the other evolutionary states, suggesting that infall motions may be less common toward these sources.

3.2.5.4 Comparison with Previous Results

Wienen et al. (2012) performed a similar comparison between NH₃(1,1) spectra and GRS ¹³CO spectra. They used NH₃(1,1) spectra from a single-pointing survey of ATLASGAL sources using the Effelsburg 100 m telescope. Of the 862 ATLASGAL sources detected in NH₃(1,1), 517 had a corresponding detection in the GRS ¹³CO(1-0) data. Their data exhibit a similar spread in V_{diff} values ($|V_{diff}| \lesssim 2 \text{ km s}^{-1}$), but a different distribution average. Using the published ¹³CO and NH₃(1,1) velocities from Wienen et al. (2012), I determined a mean of $V_{diff} = -0.308 \pm 0.005 \text{ km s}^{-1}$ by propagating fit uncertainties and $V_{diff} = -0.31 \pm 0.16 \text{ km s}^{-1}$ using bootstrap resampling. The large negative offset in the mean is in part due to a handful of sources with $V_{diff} < -10 \text{ km s}^{-1}$. In cases where the ¹³CO line is offset from the NH₃(1,1) line by several times its line width, the ¹³CO line is more likely associated with an unrelated source. Excluding sources with $|V_{diff}| > 5 \text{ km s}^{-1}$, the derived mean is $V_{diff} = -0.063 \pm 0.005 \text{ km s}^{-1}$ by propagating fit uncertainties and $V_{diff} = -0.06 \pm 0.03 \text{ km s}^{-1}$ using bootstrap resampling.

Although the Wienen et al. (2012) data exhibit a significantly different V_{diff} distribution, the cause of this discrepancy is unclear. To test whether differing samples may play a role, I compared the overlapping sources that had valid V_{diff} measurements both from my analysis and the analysis of Wienen et al. (2012). There were 316 Wienen et al. (2012) sources in common with my subsample. Excluding the sources with $|V_{diff}| > 5 \text{ km s}^{-1}$, the derived mean for the Wienen et al. (2012) subsample is $V_{diff} = 0.001 \pm 0.006 \text{ km s}^{-1}$ by propagating fit uncertainties and $V_{diff} = 0.00 \pm 0.04$

km s^{-1} using bootstrap resampling. On the other hand, the V_{diff} values derived from the RAMPS data exhibit a mean of $V_{diff} = 0.148 \pm 0.007 \text{ km s}^{-1}$ by propagating fit uncertainties and $V_{diff} = 0.15 \pm 0.03 \text{ km s}^{-1}$ using bootstrap resampling. Although the Wienen et al. (2012) subsample shows no significant offset from $V_{diff} = 0 \text{ km s}^{-1}$, the significant positive offset remains in the values derived from the RAMPS data. Consequently, the differing results may arise from differing line models. Whereas I modeled the $\text{NH}_3(1,1)$ magnetic hyperfine lines and the $^{13}\text{CO}(1-0)$ hyperfine lines, Wienen et al. (2012) modeled the $\text{NH}_3(1,1)$ satellite lines and the $^{13}\text{CO}(1-0)$ line as single Gaussians. Alternatively, the differing $\text{NH}_3(1,1)$ spectral resolution may be a factor in the disparate results. My analysis regredded the RAMPS data to the GRS spectral resolution of 0.21 km s^{-1} , while the Wienen et al. (2012) spectral resolution was $\sim 0.7 \text{ km s}^{-1}$.

Next, I compared the results from my full analysis sample to those of Jackson et al. (2019), who performed a blue asymmetry analysis using data from the Millimeter Astronomy Legacy Team 90 GHz Survey (MALT90; Jackson et al. 2013). MALT90 targeted multiple dense gas tracers including $\text{HCO}+(1-0)$, an optically thick tracer, and $\text{N}_2\text{H}+(1-0)$, an optically thin tracer. Jackson et al. (2019) investigated infall motions in MALT90 clumps by measuring the asymmetry parameter $A = \frac{I_{blue} - I_{red}}{I_{blue} + I_{red}}$, where I_{blue} and I_{red} are the $\text{HCO}+(1-0)$ integrated intensities blueward and redward, respectively, of the systemic velocity determined from $\text{N}_2\text{H}+(1-0)$. The asymmetry parameter is particularly advantageous for non-Gaussian lines, since the calculation of A makes few assumptions about optically thick line profiles.

Unfortunately, a direct comparison cannot be made with my analysis of the GRS data due to the underlying hyperfine structure of the $^{13}\text{CO}(1-0)$ line. Figure 3.11 shows A for a grid of synthetic $^{13}\text{CO}(1-0)$ lines that include the hyperfine splitting. Although the synthetic lines do not imply collapse, the underlying asym-

metry imposed by the hyperfine splitting results in a nonzero value of A . Because the $^{13}\text{CO}(1-0)$ transition's hyperfine structure results in a variable asymmetry parameter, the asymmetry parameter is not well suited for such an analysis using $^{13}\text{CO}(1-0)$ as the optically thick tracer. Consequently, I was able to perform only a qualitative comparison of the analyses.

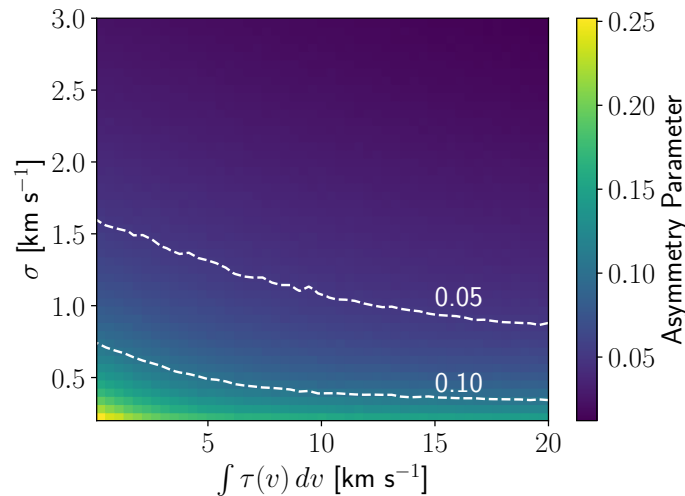


Fig. 3.11 Color shows the asymmetry parameter A for synthetic $^{13}\text{CO}(1-0)$ lines that include the hyperfine splitting. I modeled a grid of these lines with a range of velocity dispersions and integrated optical depths. The dashed lines show contours of constant A , with the values indicated above the lines.

Jackson et al. (2019) also investigated the variation of A with evolutionary state. Their evolutionary classifications were the same as those used for RAMPS, except they divided the H II region sample between compact and extended H II regions. Table 3.3 lists the mean and median V_{diff} values for my full sample and the evolutionary subsamples, as well as the corresponding A values from Jackson et al. (2019). Despite differing methods, our results are broadly consistent. Jackson et al. (2019) found that the mean A value was significantly above $A = 0$ for each of the evolutionary samples except for the PDR clumps. In addition, they found that the quiescent clumps exhibited a larger asymmetry than the protostellar clumps.

Table 3.3. Blue Asymmetry Comparison

Sample	This work (RAMPS) Mean V_{diff} (km s^{-1})	This work (RAMPS) Median V_{diff} (km s^{-1})	Jackson et al. (2019, MALT90) Mean A	Jackson et al. (2019, MALT90) Median A
All	0.11 ± 0.02	0.09 ± 0.01	0.08 ± 0.01	0.07 ± 0.01
Quiescent	0.17 ± 0.05	0.13 ± 0.03	0.13 ± 0.03	0.12 ± 0.04
Protostellar	0.05 ± 0.04	0.08 ± 0.03	0.11 ± 0.02	0.08 ± 0.02
CH II Region	0.14 ± 0.04	0.11 ± 0.05
H II Region	0.09 ± 0.02	0.07 ± 0.02	0.07 ± 0.02	0.05 ± 0.03
PDR	0.09 ± 0.07	0.08 ± 0.03	0.01 ± 0.03	0.00 ± 0.05

Jackson et al. (2019) found that the H II region sample had a lower mean and median A than the earlier evolutionary states. On the other hand, my analysis found that the H II region clumps had mean and median V_{diff} values that were greater than or similar to those of the protostellar sample. The larger asymmetry for the RAMPS H II region category may be due to the inclusion of compact H II regions, which Jackson et al. (2019) found had a more significant asymmetry than the extended H II region sample. In addition, here V_{diff} was measured throughout each clump, whereas Jackson et al. (2019) assessed the asymmetry parameter solely at the ATLASGAL emission peak. Consequently, the RAMPS analysis may be less sensitive to isolated outflow motions from a particular source within a clump. Given that disparate datasets and analysis methods have produced similar results, the global collapse of molecular clumps at early evolutionary stages is well supported. These data support competitive accretion's prediction that the global collapse of clumps is necessary to form high-mass protostars and stars.

3.3 Filament Kinematics

In this section, I investigate whether the kinematic structure of molecular filaments is consistent with gas flowing toward density peaks. In Section 3.3.1, I construct the sample of filaments I use for analysis. In Section 3.3.2, I determine filament “spine” paths along their long axes. In Section 3.3.3, I determine filament velocities and velocity gradients along their spines. In Section 3.3.4, I compare the results to predictions from simulations.

3.3.1 Filament Analysis Sample

Although there is no exact definition for a molecular filament, they are generally considered elongated structures with θ_{maj} much larger than θ_{min} . Consequently, I only included sources with $\frac{\theta_{maj}}{\theta_{min}} > 3$ in the filament analysis sample. Out of the 2,680 clumps in the full sample, 537 are filamentary clumps with $\frac{\theta_{maj}}{\theta_{min}} > 3$. In many cases, θ_{min} is not well resolved by the GBT beam, so $\frac{\theta_{maj}}{\theta_{min}}$ may be a lower limit for the deconvolved axial ratios. Next, I excluded filamentary clumps with short major axis angular diameters.

In Section 3.3.4, I compare the kinematics of RAMPS filaments to predictions from simulations by Gómez & Vázquez-Semadeni (2014) and Smith et al. (2016). These simulations predict differences in the velocity gradients measured at density peaks with those measured elsewhere in filaments. To test these theories requires at least two independent measurements of the velocity gradient within a filament, one of which is at the density peak. Thus, I required filaments have θ_{maj} values greater than four times the GBT beam width. This allowed for measurement of the velocity gradient at the density peak and an independent measurement two beam widths away. Of the 537 filamentary clumps, 284 meet this criterion.

Finally, I selected filaments from the full clump sample based on evolutionary state. If gas flows within filaments are important for accretion onto cores, then these flows would likely be particularly influential for quiescent and protostellar filaments. Furthermore, filaments that are near to, or host, H II regions, such as PDR and H II region filaments, may feature nongravitational flows due to high-mass stellar feedback. Consequently, I restricted my analysis to quiescent and protostellar filamentary clumps. Out of the 284 filamentary clumps with long angular diameters, 115 are in the quiescent or protostellar evolutionary stage.

Although the filament velocities are independent of distance, the derivation of the velocity gradient in physical units depends on the filament length, which depends on the distance. The inferred distances to some of the filaments in the analysis sample have low probabilities ($p_1 < 0.75$), so the magnitude of the derived velocity gradients will be more uncertain for these sources. On the other hand, the predictions from Gómez & Vázquez-Semadeni (2014) and Smith et al. (2016) compare velocity gradients within the same filament, so uncertainty in the velocity gradient magnitudes should not significantly affect this analysis. Consequently, I retained these sources in the filament analysis sample. Of the 115 filamentary clumps in the sample, 68 have $p_1 < 0.75$.

The sample contains 115 filamentary clumps that are suitable for this analysis. Of these, 66 are quiescent and 49 are protostellar. Table 3.4 lists the first 11 sources in the sample. From left to right, the columns list the filament designation, the major and minor angular diameters ($\theta_{maj} \times \theta_{min}$), the major and minor physical diameters ($D_{maj} \times D_{min}$), the minimum V_{LSR} (V_{min}), the maximum V_{LSR} (V_{max}), the most probable distance (d_1), the distance probability (p_1), and the evolutionary state. I present these data for the entire sample at OpenBU⁴.

⁴<https://open.bu.edu/handle/2144/43149>

Table 3.4. Filament Analysis Sample

Filament Designation	$\theta_{maj} \times \theta_{min}$ ($'' \times ''$)	$D_{maj} \times D_{min}$ (pc \times pc)	V_{min} (km s $^{-1}$)	V_{max} (km s $^{-1}$)	d_1 (kpc)	p_1	Evol. State
G10.377-0.051	164 \times 51	6.5 \times 2.0	68.0	70.5	8.2 \pm 0.1	0.68	Q
G10.417-0.023	141 \times 38	5.6 \times 1.5	67.2	69.3	8.2 \pm 0.1	0.69	Q
G11.010-0.392	150 \times 43	2.1 \times 0.6	28.7	30.6	2.9 \pm 0.2	0.67	Q
G11.056-0.100	1087 \times 108	15.0 \times 1.5	27.4	32.8	2.9 \pm 0.2	0.35	P
G11.104+0.119	211 \times 31	1.3 \times 0.2	11.5	14.0	1.3 \pm 0.1	0.26	P
G11.547+0.264	156 \times 42	2.2 \times 0.6	29.4	31.0	2.9 \pm 0.2	0.67	P
G12.114-0.028	146 \times 35	7.4 \times 1.8	111.1	112.1	10.5 \pm 0.3	0.75	Q
G12.266-0.141	192 \times 64	2.7 \times 0.9	33.1	34.3	2.9 \pm 0.3	0.39	P
G12.447-0.169	710 \times 78	10.1 \times 1.1	32.0	36.8	2.9 \pm 0.3	0.42	P
G12.507-0.090	181 \times 42	10.8 \times 2.5	19.7	21.2	12.4 \pm 0.3	0.35	Q
G12.737-0.335	337 \times 72	2.0 \times 0.4	10.6	12.7	1.3 \pm 0.1	0.40	P

3.3.2 Filament Spines

In order to analyze the velocity structure along a filament’s length, I first defined a path through cross section centers along the long axis of the filament. I will refer to this path as the filament’s “spine.”

I utilized the `medial_axis` function from the `skimage.morphology`⁵ package on a filament’s 2D label map to analyze the filament’s structure and determine its spine properties. The medial axis (Blum 1967) is defined as the locus of contiguous points that have the greatest distance from the edge of the filament. The medial distance of each pixel is the distance to the nearest edge and the medial axis traces the ridge of peak medial distance values through the filament.

Figure 3.12 shows an example of a medial axis analysis on a synthetic filament network. In the top panel, the white area represents the interior of the shape and the black region represents the background. The medial distance map in the bottom panel shows that the pixels farthest from the background region have the greatest medial distance. The medial axis traces the ridge of peak medial distance values across the shape. Figure 3.12 shows that the medial axis analysis reasonably identifies the filament network’s “skeleton,” or the pixels that trace the structure of the filament network.

Although the radial density distribution along a filament’s spine is not necessarily symmetric about the medial axis, the widths of low-mass (Arzoumanian et al. 2011) and high-mass (Hill et al. 2012; André et al. 2016) filaments are typically < 0.5 pc. Since these physical scales are not well resolved by the GBT beam at typical distances to massive molecular filaments ($d \gtrsim 3$ kpc), asymmetries in a filament’s radial density distribution do not strongly affect the identification of a filament’s structure. For such filaments, the medial axis provides a reasonable approximation

⁵<https://scikit-image.org/docs/dev/api/skimage.morphology.html>

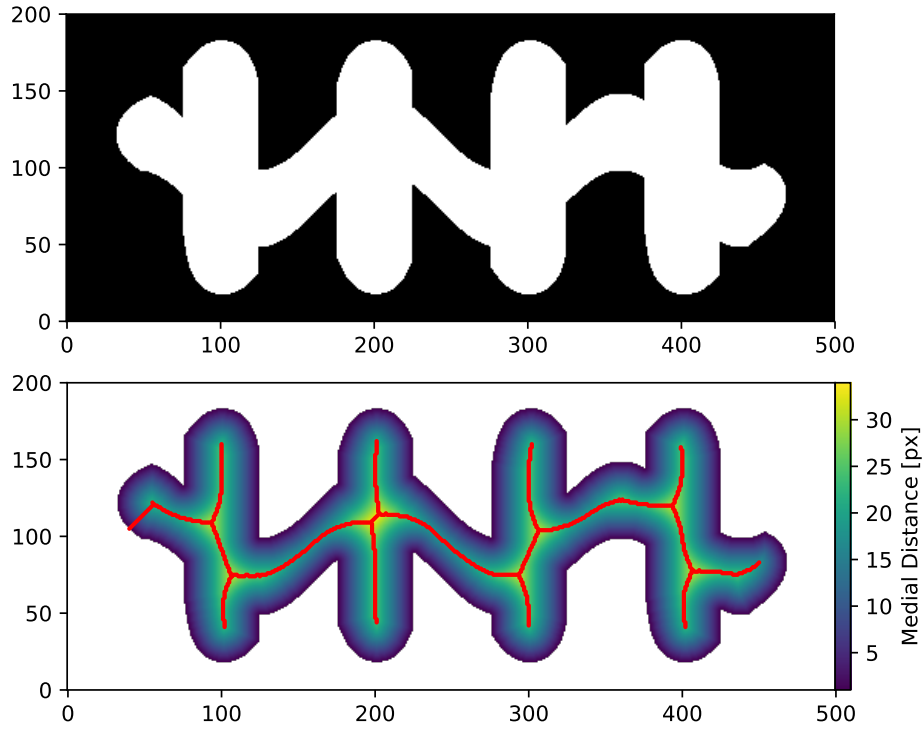


Fig. 3.12 Medial axis example. Top: The white pixels define a synthetic filament network and the black pixels define the background region. Bottom: Color shows the medial distance, which is the distance to the nearest background pixel. The red points mark the medial axis, which traces the ridge of peak medial distance values across the shape.

of the filament's skeleton and spine. Furthermore, methods that fit parametric functions to column density maps, such as Marchwinski et al. (2012), are not generally applicable to every filament shape. While many filament shapes and orientations have a one-to-one mapping between the “x” and “y” values of a filament's spine, this is not always the case. Given that a large sample of filaments will typically include filaments with various shapes and orientations, I opted for the nonparametric medial axis method of identifying a filament's spine.

Next, I performed a medial axis analysis on each of the filaments in the filament analysis subsample. I chose to perform the medial axis analysis on the 2D label

maps, since these maps define the outer boundary over which significant NH₃(1,1) emission was detected. For faint filaments, the clump-finding algorithm left the label maps with small holes caused by the signal-to-noise cutoff. The medial axis analysis assumed that any holes represented real voids in the filament structure, producing anomalous structures in the medial axis skeleton. In order to accurately trace filament structures, I filled holes with a size less than or equal to five pixels in the label maps prior to this analysis.

Panel A of Figure 3.13 shows the filament G11.056-0.100 and its medial axis skeleton displayed with colored symbol markers. The medial axis skeleton is a network of contiguous points within the filament. I defined the endpoints of this network as points that are on the edge of the filament that have only one neighboring point in the skeleton. I defined points with three or more neighboring points in the skeleton as vertices, which represent diverging pathways within the network. Panel A of Figure 3.13 indicates the network endpoints with blue markers and the vertices with green markers. The red markers show the skeleton segments, or “branches”, which I define as contiguous points that connect two vertices or a vertex and an endpoint.

Next, I pruned the medial axis skeleton to more easily identify the filament’s spine. I defined the filament spine’s endpoints as the two network endpoints with the greatest angular distance between them. I then pruned all branches that included an endpoint, excluding the two branches that included the filament spine’s endpoints. Panel B of Figure 3.13 shows the results of the pruning process, with the remaining branches, endpoints, and vertices indicated as in Panel A.

Finally, I defined the filament’s spine as the shortest path within the pruned skeleton that connected the two endpoints of the spine. To determine the shortest path, I used a Monte Carlo approach that performed random walks through the network. Possible spine paths were those that included both endpoints and only one

instance of each point in the path. I performed this random walk until the number of potential spine paths was equal to the square of the number of vertices in the pruned skeleton. I accepted the shortest of these possible spine paths as the filament spine. The red markers in Panel C of Figure 3.13 show the filament spine determined by this method.

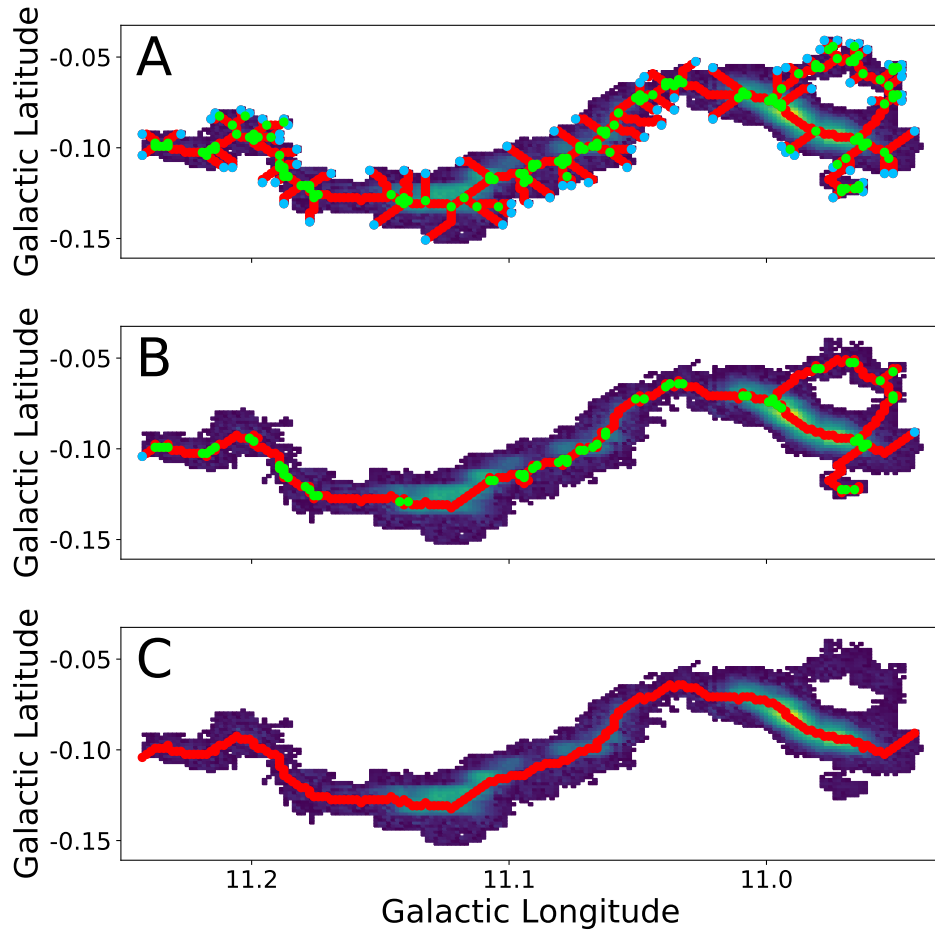


Fig. 3.13 Color shows the integrated intensity map of the filament G11.056-0.100. A: Red markers show the medial axis skeleton, green markers show the vertices, and blue markers show the endpoints. B: Red markers show the pruned skeleton, green and blue markers show the remaining vertices and endpoints, respectively. C: Red markers show the filament spine.

3.3.3 Filament Velocity Gradients

I used the spine paths and the NH₃(1,1) velocity maps to investigate gradients in the gas velocity with respect to position along filament spines (∇V_{LSR}). First, I removed spine points that were more closely spaced than half the FWHM telescope beam size to reduce correlation among velocity measurements. Next, I recorded the NH₃(1,1) fit velocities along the remaining spine points. The top panel of Figure 3.14 shows the position-velocity (*p-v*) distribution along the spine of G11.056-0.100.

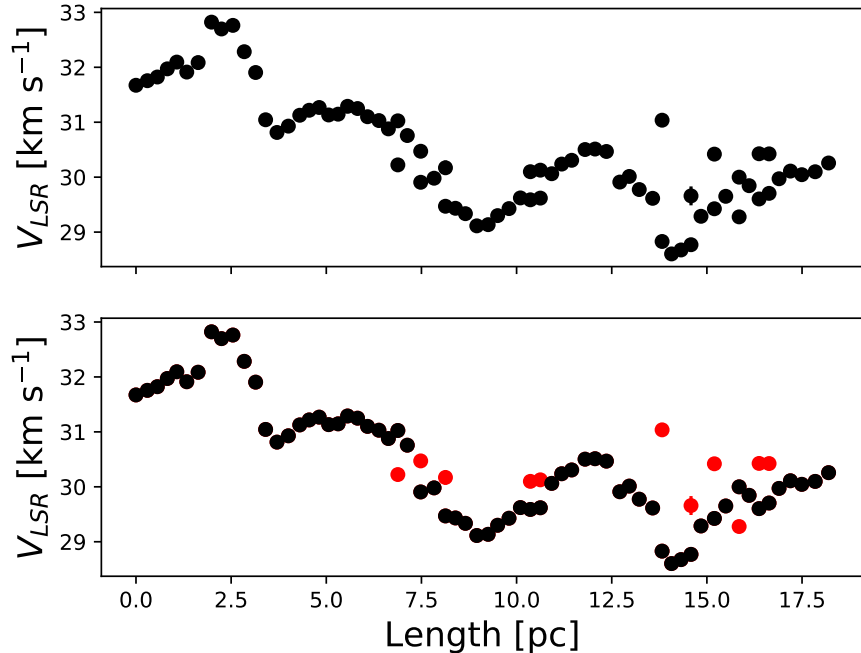


Fig. 3.14 The *p-v* distribution along the length of G11.056-0.100. Top: All NH₃(1,1) fit velocities are shown in black. Bottom: Points shown in red indicate velocity components that were removed for the velocity gradient analysis.

Some positions along the filament display more than one velocity component, which may signify the presence of overlapping subfilaments, outflows, or clumps at different distances. Because the velocity gradient calculation assumes only a single velocity component at each position, I removed one of the velocity components for

positions with two components. Simulations (Gómez & Vázquez-Semadeni 2014; Smith et al. 2016) and observations (Zernickel et al. 2013; Yuan et al. 2020) of velocity-coherent filaments imply a smoothly varying velocity structure ($\nabla V \lesssim 5 \text{ km s}^{-1} \text{ pc}^{-1}$; Smith et al. 2020). Consequently, I removed the velocity component that was further from the mean velocity of the two neighboring spine points. The bottom panel of Figure 3.14 shows the removed velocities with red markers.

Next, I performed a velocity gradient analysis using the `gradient` function from the `numpy` package on the discrete p - v distribution. For an interior position in the p - v distribution, the `gradient` function calculates ∇V_{LSR} as the slope between the velocity one step behind and one step forward of the considered position. If $V_{LSR}(x)$ is the velocity array in units of km s^{-1} , $p(x)$ is the position array in units of parsecs, and i is the location in the p - v array, then the gradient at the i^{th} location in the distribution is given by $\nabla V_{LSR}(i) = \frac{V_{LSR}(i+1) - V_{LSR}(i-1)}{p(i+1) - p(i-1)}$. This method is not possible for the left exterior point at $i = 0$ or the right exterior point at $i = i_{max}$, so the `gradient` function calculates the exterior gradients using the one-sided differences. For the left exterior point at $i = 0$, the velocity gradient is given by $\nabla V_{LSR}(0) = \frac{V_{LSR}(1) - V_{LSR}(0)}{p(1) - p(0)}$ and for the right exterior point at $i = i_{max}$, the velocity gradient is given by $\nabla V_{LSR}(i_{max}) = \frac{V_{LSR}(i_{max}) - V_{LSR}(i_{max}-1)}{p(i_{max}) - p(i_{max}-1)}$.

I calculated the error on the velocity gradient using a Monte Carlo approach. I assumed that the errors on the velocity measurements were Gaussian, such that many independent measurements of a velocity would result in a Gaussian distribution with a mean equal to the best-fit velocity and a standard deviation equal to the error on the best-fit velocity. For each velocity in a p - v distribution, I sampled 1,000 velocity values from a Gaussian distribution with a mean and standard deviation equal to the corresponding best-fit velocity and error, respectively. Next, I constructed 1,000 p - v distributions using the randomly sampled velocity values and used the `gradient`

function to calculate the corresponding velocity gradient distributions ($p\text{-}\nabla v$). Then, I calculated the mean and standard deviation of the 1,000 ∇V_{LSR} values at each position along the spine. I constructed the final $p\text{-}\nabla v$ distribution using these means and standard deviations as the values and errors on ∇V_{LSR} , respectively.

Figure 3.15 illustrates this method using synthetic data. The top panel shows synthetic velocity values with random errors (orange) and 1,000 $p\text{-}v$ distributions (blue) drawn from Gaussian distributions with means equal to the synthetic velocity values and standard deviations equal to the synthetic velocity errors. The bottom panel shows the 1,000 $p\text{-}\nabla v$ distributions (black) derived from the corresponding $p\text{-}v$ distributions in the top panel. The final $p\text{-}\nabla v$ distribution values and errors (green) are given by the means and standard deviations of the distributions shown in black.

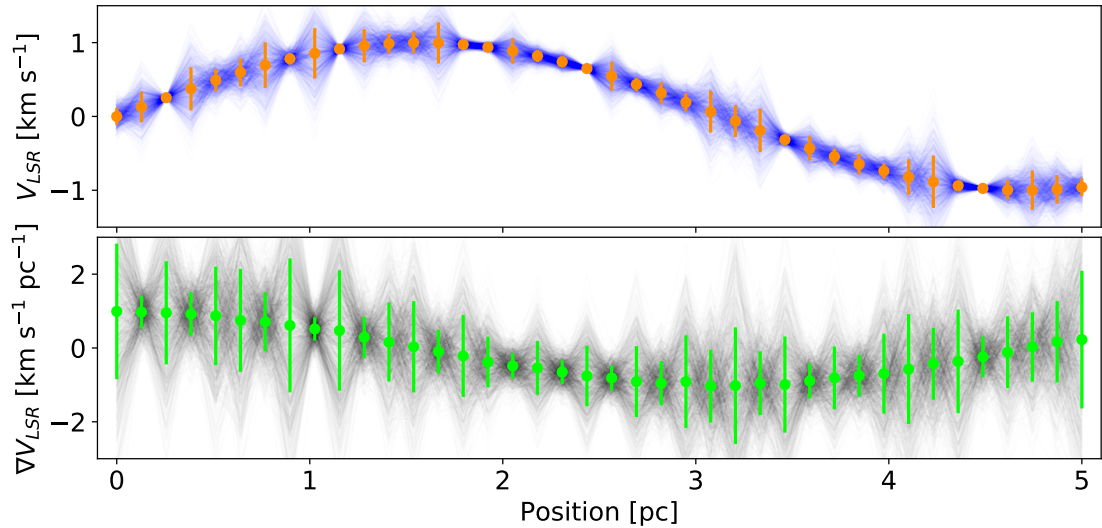


Fig. 3.15 Illustration of the Monte Carlo method to derive errors on ∇V_{LSR} . Top: Orange markers show synthetic velocity measurements with random errors. The blue lines show 1,000 $p\text{-}v$ distributions composed of velocities drawn from Gaussian distributions with means equal to the synthetic velocity values and standard deviations equal to the synthetic velocity error values. Bottom: Black lines show the 1,000 $p\text{-}\nabla v$ distributions derived from the corresponding $p\text{-}v$ distributions in the top panel. The green markers indicate the mean values of ∇V_{LSR} at each position and the error bars indicate the standard deviations of the ∇V_{LSR} values at each position.

Figure 3.16 shows an example of the p - v and p - ∇v distributions along the spine of G11.056-0.100. I derived the errors on the ∇V_{LSR} values using the method described in the previous paragraphs and illustrated in Figure 3.15. Because the p - v distribution has an oscillatory pattern, the p - ∇v distribution varies about $0 \text{ km s}^{-1} \text{ pc}^{-1}$.

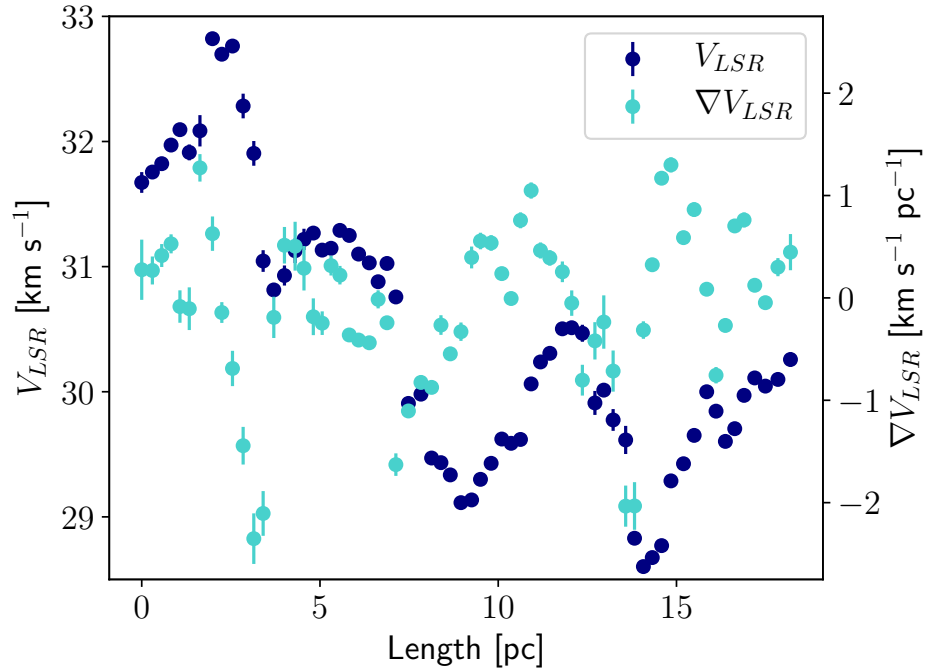


Fig. 3.16 The p - v (navy blue, left axis) and p - ∇v (turquoise, right axis) distributions along the spine of G11.056-0.100.

3.3.4 Comparison with Simulations

Filamentary structures are ubiquitous in star forming regions and may play an important role in moving mass from molecular clouds and clumps to core scales (Bal-sara et al. 2001; Banerjee et al. 2006; Kirk et al. 2013; Lu et al. 2018; Yuan et al. 2020). Because mass flows that accelerate along filaments produce velocity gradients, the kinematic structure of observed filaments can provide evidence for such

mass accretion. Unfortunately, gradients in the measured V_{LSR} can also be produced by twists in a filament, that change the line-of-sight velocity, or by shear motions. Consequently, the mere presence of a velocity gradient does not necessarily imply the existence of gravitational mass flows. Comparisons with simulations can help break this degeneracy, because unlike observed filaments, the 3D density and velocity structure of a simulated filament is known. Although current hydrodynamical simulations produce filamentary structures that are qualitatively similar to observed filaments, many predictions from such simulations have yet to be tested quantitatively. In particular, simulations by Smith et al. (2016) and Gómez & Vázquez-Semadeni (2014) make specific predictions about the relationship between a filament's velocity structure and the positions of mass peaks where cores reside.

Smith et al. (2016) simulated a turbulent, uniform density molecular cloud with a mass of $10^4 M_\odot$, a radius of 7 pc, and equal kinetic and gravitational energy. The turbulent cloud naturally evolved to form filamentary structures, which acquired more mass as the surrounding cloud collapsed. The larger, more massive filaments were composed of multiple velocity-coherent subfilaments, which can appear as separate velocity components along the line-of-sight. Smith et al. (2016) noted that the formation of overlapping subfilaments was reminiscent of observed filamentary networks in the L1495/B213 Taurus region (Hacar et al. 2013). Overlapping subfilaments are also apparent in the larger filaments detected by RAMPS (Fig. 3.14).

Smith et al. (2016) also investigated the p - v distribution along the spines of the simulated filaments, tracking the flow velocity and the one-dimensional velocity an observer would measure. Both the flow velocity and the observable velocity along the subfilament spines exhibited a spatially oscillating pattern about a roughly linear change in velocity as a function of position along the filament. Smith et al. (2016) found no correlation between the spatial oscillations in the velocity and density struc-

tures, so they attributed the spatial oscillations of the velocity to turbulence rather than to gravitational flow. On the other hand, they found that the linear pc-scale velocity gradient did indicate a net mass flow along the subfilament. They also found that mass tended to concentrate where the pc-scale velocity gradient changed signs, often occurring at the positions where subfilaments join. Thus, the Smith et al. (2016) simulation predicts that the peak density should be found where ∇V_{LSR} is nearly $0 \text{ km s}^{-1} \text{ pc}^{-1}$ and changes sign, while ∇V_{LSR} measured at a position away from the peak should be nonzero.

Gómez & Vázquez-Semadeni (2014) also investigated filament kinematics using a compressible hydrodynamical simulation, but with different initial conditions. The Gómez & Vázquez-Semadeni (2014) simulation started by colliding two warm, diffuse gas flows, a scenario that could be driven by kpc-scale instabilities (e.g., Elmegreen 1987; Kim et al. 2002) or turbulence (Heiles & Troland 2003) in the ISM. After the collision, the compressed gas in the resulting interface layer undergoes a phase change to a cold, dense state. The gas continues evolving under the influence of self-gravity and the turbulent velocity field generated by the collision. In their simulation, this turbulence created nonlinear density fluctuations that became unstable and fragmented into filamentary structures, which later fragmented to form cores. Gómez & Vázquez-Semadeni (2014) found that inflow motions occurred at every scale, with the large-scale flows feeding the collision interface layer, the interface layer feeding the filaments, and filaments feeding the cores. Consequently, their simulated filaments were not equilibrium structures, but rather long-lived flow features that moved gas from the cloud to the core scale.

The simulation produced two large filaments that had lengths of $\sim 15\text{pc}$ and dense gas ($n > 10^3 \text{ cm}^{-3}$) masses of $\sim 600 \text{ M}_\odot$. A closer inspection of the p - v distribution along the spines of these filaments revealed that subsections along their

long axes were separated in velocity by $1 - 2 \text{ km s}^{-1}$. The positions where these subsections met were associated with the largest velocity gradients and the highest column densities. Gómez & Vázquez-Semadeni (2014) claimed that these large velocity jumps between subsections were signatures of the global collapse of these filaments along their long axes. Smaller velocity jumps, signaling local collapse, were found at the positions of other density peaks in the filaments. Thus, the Gómez & Vázquez-Semadeni (2014) simulation predicts that ∇V_{LSR} will be largest at the peak column density position.

An inspection of the kinematic structure of RAMPS filaments revealed examples that match the predictions of each simulation. Figure 3.17 shows the kinematic and surface density structure of the filament G26.942+0.180. The left panel shows the velocity map with Σ contours overlaid. The spine of the filament is traced by symbol markers that are separated by at least half of the GBT FWHM beam width. The right panels show the $p-V_{LSR}$, $p-\nabla V_{LSR}$, and Σ distributions along the length of the filament, where the values in the distributions correspond to the positions of the symbol markers in the left panel. The filament exhibits two density peaks and the velocity varies by $\sim 1.5 \text{ km s}^{-1}$ across the length of the filament. The $p-\nabla V_{LSR}$ distribution across the density peaks shows a change in sign, with $\nabla V_{LSR} \sim 0 \text{ km s}^{-1} \text{ pc}^{-1}$ at the peaks. This is reminiscent of the Smith et al. (2016) simulation, which suggests that gas is flowing from the center and edges of the filament to the density peaks where the cores reside.

Figure 3.18 shows the kinematic and surface density structure of G28.517-0.145, where the data are displayed as in Figure 3.17. Like G26.942+0.180, G28.517-0.145 displays two density peaks along its spine. On the other hand, the $p-V_{LSR}$ distribution of G28.517-0.145 is different from that of G26.942+0.180. In contrast to G26.942+0.180, the $p-\nabla V_{LSR}$ distribution of G28.517-0.145 displays the largest

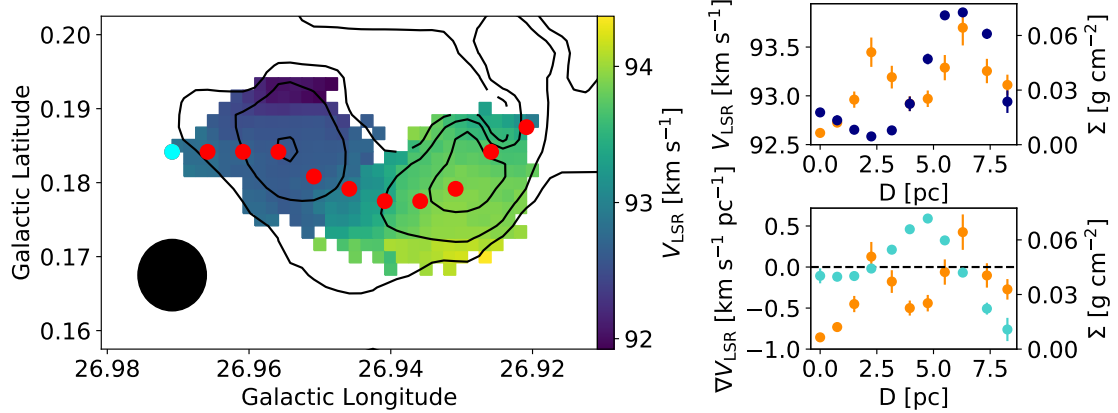


Fig. 3.17 Velocity and density structure of the filament G26.942+0.180. Left: Color shows the $\text{NH}_3(1,1)$ velocity map and contours mark surface densities of $\Sigma = 0.01, 0.025$, and 0.05 g cm^{-2} . Symbol markers indicate positions corresponding to the data points in the right panels, with the cyan symbol marking $D = 0 \text{ pc}$. The GBT beam size is shown in the lower left corner. Top right: $\text{NH}_3(1,1)$ V_{LSR} (navy blue) and Σ (orange) along the filament spine. Bottom right: $\text{NH}_3(1,1)$ ∇V_{LSR} (turquoise) and Σ (orange) along the filament spine. The dashed line marks $\nabla V_{LSR} = 0 \text{ km s}^{-1} \text{ pc}^{-1}$.

$|\nabla V_{LSR}|$ values near the density peaks. This is similar to the findings of Gómez & Vázquez-Semadeni (2014), who found that density peaks along their simulated filaments were preferentially associated with larger values of $|\nabla V_{LSR}|$. Although G28.517-0.145's p - ∇V_{LSR} distribution also exhibits larger $|\nabla V_{LSR}|$ values near the edge of the filament, the Gómez & Vázquez-Semadeni (2014) simulations do not preclude the presence of nonzero velocity gradients at other positions along the filament. Rather, the simulations predict that the density peaks be preferentially associated with larger values of $|\nabla V_{LSR}|$. These data may indicate that the increase in $|\nabla V_{LSR}|$ near the density peaks is a result of gravitational collapse along the filament spine.

Although both simulations can explain the kinematics of select filaments, it is unclear whether either simulation can account for the kinematic structure of the ensemble of star-forming filaments. Furthermore, nongravitational motions, like Galactic shear (Kim et al. 2002), and projection effects can produce velocity gradients that are unrelated to gravitationally accelerating flows in filaments.

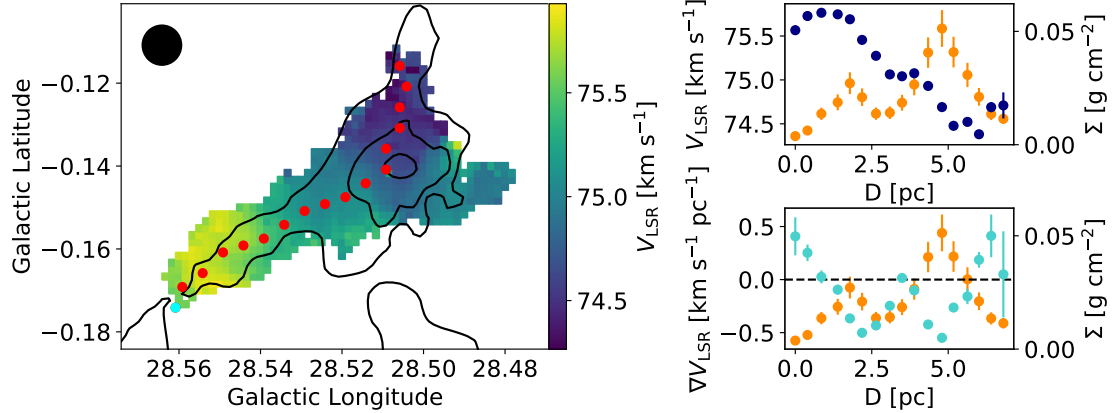


Fig. 3.18 Velocity and density structure of the filament G28.517-0.145. Left: Color shows the $\text{NH}_3(1,1)$ velocity map and contours mark surface densities of $\Sigma = 0.01, 0.03$, and 0.05 g cm^{-2} . Symbol markers indicate positions corresponding to the data points in the right panels, with the cyan symbol marking $D = 0 \text{ pc}$. The GBT beam size is shown in the upper left corner. Top right: $\text{NH}_3(1,1)$ V_{LSR} (navy blue) and Σ (orange) along the filament spine. Bottom right: $\text{NH}_3(1,1)$ ∇V_{LSR} (turquoise) and Σ (orange) along the filament spine. The dashed line marks $\nabla V_{LSR} = 0 \text{ km s}^{-1} \text{ pc}^{-1}$.

Galactic differential rotation can produce velocity gradients that are not due to filamentary accretion flows, but these velocity gradients are small compared to the observed values ($|\nabla V_{LSR}| < 0.05 \text{ km s}^{-1} \text{ pc}^{-1}$; Clemens 1985; Dib et al. 2012). Moreover, filaments that experience strong shear, either from the passage of a spiral arm shock or nearby supernovae, tend to be torn apart (Smith et al. 2020). Thus, these sources would not be recognized as filaments and included in my analysis sample.

Projection effects, where the filament is at some inclination angle with respect to the plane of the sky, will produce a measured velocity gradient that is reduced from the true value by a factor equal to the sine of the inclination angle (i) and can change sign about $i = 90^\circ$. For randomly oriented filaments, the spread in the observed ∇V_{LSR} values would be $-|\nabla V_{LSR, true}| \leq \nabla V_{LSR, obs} \leq |\nabla V_{LSR, true}|$. If the inclination angle is constant across the length of the filament, then any velocity gradients present will be scaled by the same factor, whereas a constant flow speed along a filament will not produce a velocity gradient at any inclination angle.

On the other hand, a change in the direction of a constant flow can mimic a velocity gradient caused by an accelerating flow. A filament whose long axis turns into or out of the plane of the sky will produce a gradient in the measured radial velocity, even if no velocity gradient exists along the direction of the actual filament’s long axis. Assuming that the filaments in the analysis sample do not feature such twists in a preferred direction with respect to the line-of-sight, the comparison between velocity gradients measured at the Σ peaks and those measured elsewhere in the filaments should not be biased. Because such projection effects tend to alter the measured velocity gradients from their true values, a large sample of filaments is necessary to quantitatively test the predictions of simulations.

To test these predictions, I constructed $p\text{-}\nabla v$ distributions for each of the filaments in the sample. I recorded the ∇V_{LSR} values at the sky-projected peak in the Σ distribution (∇V_{peak}), two FWHM beam widths away from the Σ peak (∇V_{off}), and at the Σ minimum (∇V_{min}) for each filament in the analysis sample. I compared the ∇V_{peak} and “off peak” ∇V_{off} values, since these ∇V_{LSR} values have a great enough distance between them to be independent measurements.

For some filaments, the “off peak” position falls on or near a local maximum in the Σ distribution. Consequently, I also compared the ∇V_{peak} and ∇V_{min} values, since these values are guaranteed to represent the velocity gradient away from any local maxima in the Σ distribution. Although this comparison may result in correlated ∇V_{LSR} values if the Σ minimum is only one beam width away from the Σ peak, this can only make the ∇V_{LSR} values at the Σ minimum more similar to those at the Σ peak. Given that both simulations predict different ∇V_{LSR} values at the Σ peak compared to those measured elsewhere, such correlations can only reduce the differences between these samples, rather than produce a false difference between these samples due to correlations.

Figure 3.19 displays ∇V_{peak} vs. ∇V_{off} and ∇V_{min} . The data exhibit significant scatter, with the majority of points clustering around $\nabla V_{peak} \sim 0 \text{ km s}^{-1} \text{ pc}^{-1}$, $\nabla V_{off} \sim 0 \text{ km s}^{-1} \text{ pc}^{-1}$, and $\nabla V_{min} \sim 0 \text{ km s}^{-1} \text{ pc}^{-1}$. The colored circles denote the approximate zones where these data would cluster in the case of the Gómez & Vázquez-Semadeni (2014) simulation (blue) and the Smith et al. (2016) simulation (red).

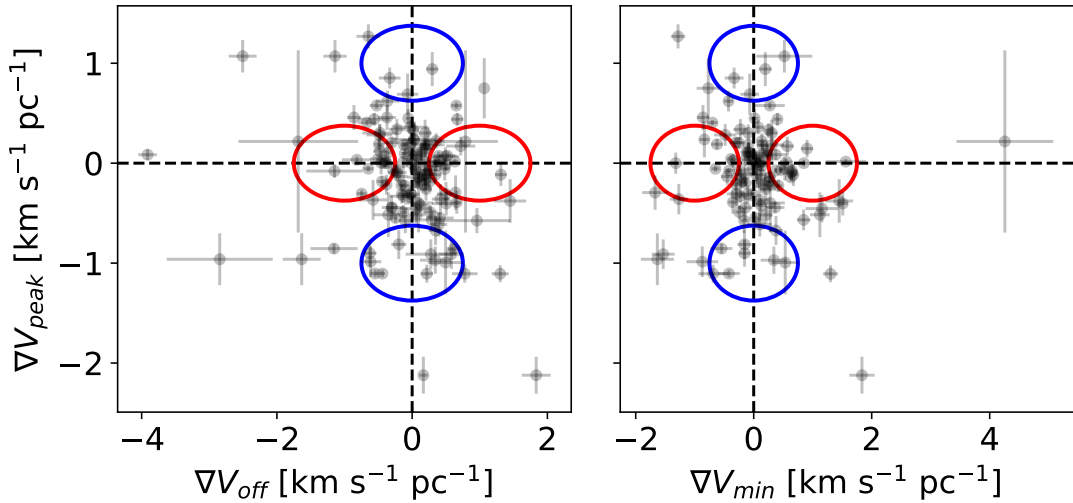


Fig. 3.19 Left: ∇V_{peak} vs. ∇V_{off} . The dashed lines mark $\nabla V_{peak} = 0 \text{ km s}^{-1} \text{ pc}^{-1}$ and $\nabla V_{off} = 0 \text{ km s}^{-1} \text{ pc}^{-1}$. The colored circles denote the approximate zones where these data would cluster in the case of the Gómez & Vázquez-Semadeni (2014) simulation (blue) and the Smith et al. (2016) simulation (red). Right: ∇V_{peak} vs. ∇V_{min} . The dashed lines mark $\nabla V_{peak} = 0 \text{ km s}^{-1} \text{ pc}^{-1}$ and $\nabla V_{min} = 0 \text{ km s}^{-1} \text{ pc}^{-1}$. The colored circles denote the approximate zones where these data would cluster in the case of the Gómez & Vázquez-Semadeni (2014) simulation (blue) and the Smith et al. (2016) simulation (red).

The Gómez & Vázquez-Semadeni (2014) simulation produced the largest absolute ∇V_{LSR} values at the Σ peaks ($|\nabla V_{peak}| \sim 0.5 - 3 \text{ km s}^{-1} \text{ pc}^{-1}$), with ∇V_{LSR} values closer to $0 \text{ km s}^{-1} \text{ pc}^{-1}$ elsewhere in the filaments. Given that projection effects will produce measured velocity gradients that are closer to $0 \text{ km s}^{-1} \text{ pc}^{-1}$, the measured velocity gradient values expected from this simulation may be closer

to $|\nabla V_{peak}| \sim 1 \text{ km s}^{-1} \text{ pc}^{-1}$. Thus, the Gómez & Vázquez-Semadeni (2014) simulation predicts that measured velocity gradients should cluster near the blue circles in Figure 3.19.

Conversely, the Smith et al. (2016) simulation produced filaments with $|\nabla V_{peak}| \sim 0 \text{ km s}^{-1} \text{ pc}^{-1}$ and nonzero velocity gradients of $|\nabla V_{LSR}| \sim 0.5 - 2 \text{ km s}^{-1} \text{ pc}^{-1}$ elsewhere in the filaments. Thus, the measured velocity gradient values from this simulation would cluster near the red circles in Figure 3.19.

Although some filaments exhibit velocity gradients that are similar to predictions from Gómez & Vázquez-Semadeni (2014) and Smith et al. (2016), the majority of the measured velocity gradients are clustered about $0 \text{ km s}^{-1} \text{ pc}^{-1}$, contrary to predictions by either simulation. The RAMPS data suggest that the filament kinematics produced by these simulations are not ubiquitous in real molecular filaments. Consequently, new models are needed to accurately reproduce the data.

3.4 Conclusions

In this Chapter, I have tested several predictions concerning the early evolution of molecular clumps and filaments. From my analysis, I have drawn the following conclusions:

1. The virial parameters of the quiescent and protostellar clumps in the RAMPS virial analysis sample are consistent with gravitational collapse even if the magnetic field energy is in equipartition with the turbulent energy. The corresponding star formation rate is in the range $\dot{M}_{SFR} = 7 - 23 \text{ } M_\odot \text{ yr}^{-1}$, roughly an order of magnitude greater than the range of published star formation rates for the Milky Way. Thus, magnetic field strengths of $B \sim 0.1 - 1 \text{ mG}$ may be required to slow the collapse of clumps with $\alpha < 0.5$. Nevertheless, these

findings support the competitive accretion model of high-mass star formation, which predicts $\alpha < 1$ at early evolutionary stages.

2. The blue asymmetry analysis implies that clumps feature significant infall motions, with the largest asymmetry in the quiescent stage. Such infall motions likely indicate gravitational collapse. This result further supports the central prediction of competitive accretion, which posits that quiescent clumps must undergo gravitational collapse to transition to the protostellar stage.
3. The filament analysis shows that velocity gradients along filament spines are ubiquitous, but not uniform. Comparisons between the velocity gradients at the density peaks with those measured elsewhere in the filaments are not reproduced by the filament simulations of Gómez & Vázquez-Semadeni (2014) or Smith et al. (2016).

Chapter 4

Protostellar and Stellar Feedback in Massive Molecular Clumps

4.1 Introduction

Protostellar and stellar feedback are thought to play a significant role in the formation of stars. Bipolar outflows and stellar winds are a source of kinetic energy that add turbulence to the surrounding gas. In addition, radiation from stars and protostars heats and changes the chemistry of the surrounding gas. Because such feedback occurs as protostellar and stellar sources continue accreting from their natal clumps (Kudritzki 2002), the changes to the gas properties of clumps can regulate star formation rates.

Some theories predict that massive stars cannot form without the presence of such feedback (Krumholz & McKee 2008). The theory of turbulent core accretion (McKee & Tan 2003) posits that massive stars originate from massive prestellar cores that are gravitationally supported by turbulence. While turbulent energy can support against gravitational collapse, turbulent cores can still become unstable to fragmentation on smaller scales. Fragmentation occurs when the mass of a parcel of gas exceeds the Jeans mass ($M_J \propto T^{\frac{3}{2}}\rho^{-\frac{1}{2}}$; Jeans 1928). One method to prevent fragmentation is to increase the gas temperature within the core. Krumholz et al. (2010) found that internal heating by an early generation of low-mass ($M \sim 1 M_{\odot}$) protostars could limit the fragmentation of massive ($M > 8 M_{\odot}$) prestellar cores and

allow the formation of massive protostars. Thus, Krumholz et al. (2010) predicts that the early formation of low-mass protostars is necessary to produce massive stars.

One of the other main theories of high-mass star formation, competitive accretion (Bonnell et al. 2001, 2004), also predicts that low-mass protostars must form prior to high-mass protostars within massive clumps. In this case, it is not feedback from low-mass protostars that enables the formation of massive protostars, but rather the low-mass protostars themselves become high-mass protostars through accretion. This “competitive” accretion also requires the formation of low-mass protostars prior to high-mass protostars.

Testing this prediction requires the detection of low-mass protostars in high-mass clumps prior to the formation of high-mass protostars. Detecting such embedded low-mass star formation is difficult, because low-mass protostars are much fainter than high-mass protostars (Kryukova et al. 2012) and the distances to typical high-mass star-forming clumps are large (Anderson & Bania 2009). Fortunately, H₂O masers offer a potential solution. Because H₂O masers are bright, with isotropic luminosities of $L_{\text{H}_2\text{O}} \sim 10^{-10} - 1 L_{\odot}$, and are excited by both low-mass (Furuya et al. 2001, 2003) and high-mass protostars (Palagi et al. 1993; Cyganowski et al. 2013), their presence can help identify low-mass protostars that are too faint to observe in the MIR.

RAMPS has the greatest point source sensitivity of any H₂O maser mapping survey to date. The average detection limit of 1.5 K corresponds to an isotropic H₂O maser luminosity of $L_{\text{H}_2\text{O}} = 4.7 \times 10^{-8} L_{\odot}$ at a distance of 3 kpc (Anglada et al. 1996). Given the correlation between $L_{\text{H}_2\text{O}}$ and protostellar bolometric luminosity (L_{bol}) (Furuya et al. 2003), the RAMPS H₂O maser catalog can be used to identify H₂O maser emission from low-mass protostars with $L_{\text{bol}} \gtrsim 10 L_{\odot}$ to the typical distances

of high-mass star-forming clumps. Consequently, the RAMPS H₂O maser data are suitable to test whether low-mass protostars form prior to high-mass protostars.

High-mass protostars and stars likely also have a significant effect on star formation because feedback from these sources is more extreme than their low-mass counterparts. Although low-mass protostars emit radiation and generate outflows, the bolometric luminosities of high-mass protostars and the momentum rates of their outflows are several orders of magnitude higher (Shepherd 2003). Feedback from massive protostars changes the thermal, chemical, and kinematic properties of the surrounding gas. The net effect of high-mass protostellar feedback on star formation is complicated and not well understood. On one hand, outflows can break up accretion flows and inject turbulence into clumps, which may help support clumps against gravitational collapse (Wang et al. 2010). Thus, kinematic feedback from high-mass protostars might inhibit further star formation and mass accretion. On the other hand, radiative feedback from high-mass protostars heats the surrounding gas, reducing fragmentation of accretion flows (Peters et al. 2010). Thus, radiative feedback from massive protostars could aid accretion. The effect of protostellar feedback on star formation will depend on the physical scales at which these feedback mechanisms are able to change the gas properties within clumps.

Once massive protostars reach the main sequence, their significant ionizing UV flux and radiation-driven winds can substantially alter the gas properties around them (Kudritzki 2002). Consequently, such feedback likely affects star formation within massive molecular clumps. Indeed, young stellar objects with circumstellar disks that form near massive stars can have their disks photoevaporated by UV radiation and carried off by stellar winds (Bally et al. 1995). These stellar winds also add substantial turbulent energy to the clump. In fact, strong feedback from massive stars may be required for theories of high-mass star formation that rely on

the gravitational collapse of clumps to form massive protostars (e.g., Bonnell et al. 2001, 2004; Vázquez-Semadeni et al. 2019).

If the entirety of all massive clumps were to collapse on the order of a free-fall time, the corresponding star formation rate would far exceed the observed values (Zuckerman & Evans 1974). If magnetic fields and turbulence do not slow the collapse of clumps significantly, then feedback from massive stars would be necessary to slow gravitational collapse and disperse some of the clump molecular gas before it can be accreted.

On the other hand, some star formation theories predict that the expansion of H II regions may trigger further star formation (Elmegreen 1998). The star-forming environments surrounding H II regions do in some cases exhibit geometries that are consistent with shock-triggered star formation (Zavagno et al. 2005; Kirsanova et al. 2008; Brand et al. 2011; Luisi et al. 2021), though in other cases the link between H II region shocks and nearby star formation is less clear (Deharveng et al. 2006). Whatever the effects on star formation, the size scales over which high-mass stars alter the properties of their surrounding gas are clearly import.

In order to determine the degree to which massive protostars and stars alter their surrounding gas properties, as well as the size scales on which these changes occur, mapping observations that can determine the gas temperatures, chemical abundances, and kinematics of molecular clumps that host high-mass protostars and stars are required. NH₃ mapping observations are an obvious choice for determining the gas properties of clumps, but previous NH₃ mapping surveys have either had poor angular resolution (Purcell et al. 2012) or observed a small sample of clumps (Urquhart et al. 2015). On the other hand, RAMPS data offer a sample of 383 protostellar clumps and 714 H II region clumps that were mapped at an angular resolution of $\sim 30''$. Thus, RAMPS is the best tool currently available to investigate the signif-

icance of massive protostellar and stellar feedback, as well as the size scales over which such feedback alters gas properties.

In Section 4.2, I test whether low-mass protostars form prior to high-mass protostars by searching for evidence of H₂O maser emission in massive quiescent clumps. In Section 4.3, I investigate the influence of high-mass protostellar and stellar feedback on the gas properties of protostellar and H II region clumps, particularly with respect to the physical size scales over which the gas properties have been modified.

4.2 The First Protostars in Massive Clumps

Krumholz et al. (2010) predicted that low-mass protostars must form prior to high-mass protostars in order to prevent Jeans fragmentation of massive turbulent cores. In addition, Bonnell et al. (2001) predicted that low-mass protostars are the precursors to high-mass protostars, requiring their presence prior to the protostellar clump stage as well. In this section, I test these theories by searching for H₂O masers, signals of star formation, within massive quiescent clumps. In Section 4.2.1, I assign H₂O masers to individual clumps and determine the evolutionary states with which they are associated. In Section 4.2.2, I discuss the H₂O masers associated with quiescent clumps. In Section 4.2.3, I describe the challenges of detecting H₂O masers associated with low-mass protostars in massive quiescent clumps and discuss future observations that could better test these theories.

4.2.1 Evolutionary States Associated with H₂O Masers

H₂O masers are excited by both low-mass and high-mass protostars. If an H₂O maser was found in a massive, quiescent clump, it would signal the presence of a low-mass protostar, since a high-mass protostar would be easily detectable in the MIR due to its much higher luminosity.

To test whether low-mass protostars can form in high-mass star-forming clumps prior to high-mass protostars, I searched for H₂O maser emission associated with massive quiescent clumps. I limited my search to H₂O masers that are associated with star-forming regions (SFRs), which I determined in Section 2.5.2.3. This reduced the likelihood that the SFR masers are associated with a molecular clump because of a chance alignment, since H₂O masers thought to be excited within SFRs typically have velocities near ($\lesssim 20 \text{ km s}^{-1}$) those of the associated molecular gas (Urquhart et al. 2011).

Next, I assigned the SFR masers to individual clumps in the RAMPS clump catalog. I assumed that a maser was excited within a particular clump if the maser position fell within half a beamwidth of the angular extent of the clump, defined by the extent of the 2D label map (Section 2.5.1.1), and the maser displayed emission within 20 km s⁻¹ of the NH₃ emission. Of the 351 SFR masers associated with molecular clumps, 3 masers are associated with quiescent clumps, 46 masers are associated with protostellar clumps, 222 masers are associated with H II region clumps, 17 masers are associated with PDR clumps, and 31 masers are associated with clumps in an unknown evolutionary state.

This leaves 33 SFR masers without corresponding clumps in the RAMPS catalog. Of these, 18 masers are associated with clumps that were detected by the clump-finding algorithm, but not included in the catalog. I chose to exclude these clumps from the catalog because they fell on the edge of the RAMPS observing region, so the RAMPS data could not provide accurate positions and gas properties. Nevertheless, the masers that are coincident with these sources fall within the adopted velocity limits and are likely physically associated with star formation. I inspected the MIR emission associated with these clumps and determined that 17

of these masers are associated with H II region clumps and the remaining maser is associated with a PDR clump.

Even accounting for these clumps, this still leaves 15 SFR masers unassociated with any clump that was detected by the clump-finding algorithm. In these cases, the NH₃ emission was not bright enough over a large enough angular area to be identified as a clump by the clump-finding algorithm. However, the NH₃ spectra indicate significant NH₃ emission within 20 km s⁻¹ of the H₂O maser emission, implying an association. I inspected the MIR emission toward these faint clumps and classified five as H II region clumps, two as PDR clumps, and eight as having an unknown evolutionary state.

Although the vast majority of the RAMPS masers are associated with H II region clumps, this does not necessarily imply that all of these masers are excited by H II region shocks. Clumps that host H II regions often feature sources of compact 24 μ m emission elsewhere in the clump, implying the presence of embedded high-mass protostars. Thus, some of these masers may be triggered by low- or high-mass protostars.

4.2.2 H₂O Masers Associated with Quiescent Clumps

My analysis of the clump evolutionary states associated with the SFR masers revealed three masers associated with quiescent clumps. Their designations in the RAMPS catalog are G11.010-0.392, G18.572-0.346, and G31.464+0.185 and their masses are $M_{clump} = 150 \pm 20$, 170 ± 30 , and $1060 \pm 220 M_{\odot}$, respectively. Only G31.464+0.185 has a mass greater than $260 M_{\odot}$, which is an approximate limiting mass for high-mass star formation (Sanhueza et al. 2017). Thus, G11.010-0.392 and G18.572-0.346 may not form massive protostars unless they acquire more mass from their surrounding molecular clouds prior to forming stars. On the other hand, G31.464+0.185 has sufficient mass to form stars with masses $> 8 M_{\odot}$. Thus, its

maser emission could be excited by a low-mass protostar prior to forming high-mass protostars, as predicted by the theories of turbulent core accretion and competitive accretion.

Next, I tested the probability that the H₂O maser coincident with G31.464+0.185 is not associated with the clump, but overlaps due to a chance alignment. I created 10^7 synthetic masers with random positions in the RAMPS survey region. I assigned velocities to these synthetic masers by randomly sampling from the V_{LSR} distribution of all detected RAMPS H₂O masers. Then, I searched for synthetic masers that overlapped with massive ($M_{clump} \geq 260 M_\odot$) quiescent clumps in the RAMPS data and had velocities within 20 km s⁻¹ of the clump's velocity. I found that 0.07% of the synthetic masers were associated with massive quiescent clumps by chance. Given that the full sample of RAMPS H₂O masers contains 707 sources, the expected number of “false positive” masers that are associated with massive quiescent clumps by chance is 0.5. Thus, there is a significant probability that the maser coincident with G31.464+0.185 is not physically associated with the clump.

Figure 4.1 displays the GLIMPSE and MIPSGAL MIR emission toward G31.464+0.185, with the mass surface density shown as contours and the position of the H₂O maser indicated by the cross. The clump exhibits a compact shape and is opaque at 8 μm. Furthermore, its dust temperature ($T_{dust} \sim 13$ K) and peak surface density ($\Sigma_{peak} \sim 0.09$ g cm⁻²) are similar to those of other quiescent clumps (Guzmán et al. 2015). In addition, it has a luminosity of $L_{bol} = 640 \pm 140 L_\odot$ and a light-to-mass ratio of $L_{bol}/M_{clump} = 0.6 \pm 0.2 \frac{L_\odot}{M_\odot}$, which is approximately equal to the median L_{bol}/M_{clump} for a sample of 933 quiescent ATLASGAL clumps (Urquhart et al. 2018). The MIR data show evidence of faint, compact 24 μm emission adjacent to the position of the H₂O maser. Given that the 24 μm emission is faint and the

clump's light-to-mass ratio is comparable to other quiescent clumps, the compact source may represent a low- or intermediate-mass protostar.

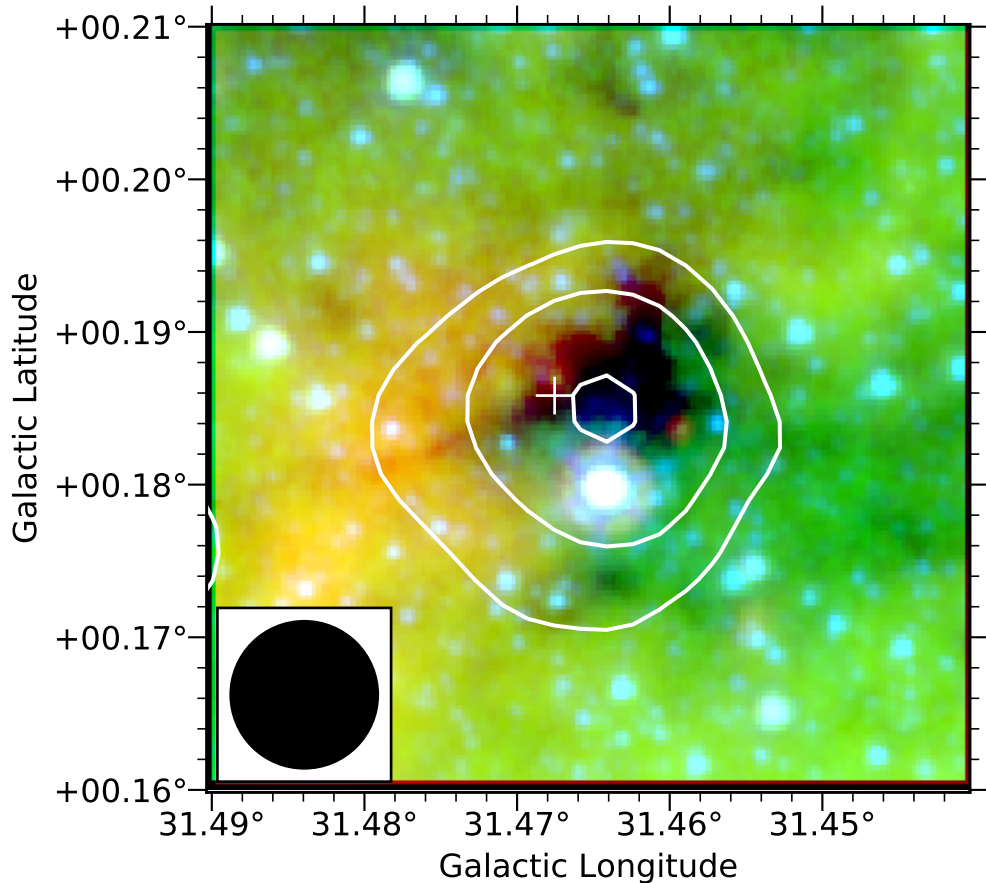


Fig. 4.1 Color shows the $3.6 \mu\text{m}$ (blue), $8 \mu\text{m}$ (green), and $24 \mu\text{m}$ (red) MIR emission toward G31.464+0.185. The contours indicate mass surface densities of $\Sigma = 0.02, 0.04$, and 0.08 g cm^{-2} . The cross marks the position of the H_2O maser and the black circle indicates the FWHM GBT beam size.

The isotropic H_2O maser luminosity (Equation 1.1) offers an additional method to estimate the mass and luminosity of the possible exciting source. The H_2O maser has an integrated line flux of $\int I_\nu dv \approx 2.4 \text{ Jy km s}^{-1}$, G31.464+0.185 has a distance of $d = 6.90 \pm 0.73 \text{ kpc}$ and a distance probability of $p = 0.73$. These values produce a luminosity of $L_{\text{H}_2\text{O}} = 2.6 \times 10^{-6} L_\odot$.

Furuya et al. (2003) observed a sample of H₂O masers associated with low-mass protostars ($L_{bol} < 100 L_\odot$) and found a correlation between L_{H_2O} and L_{bol} , but with a large spread in L_{H_2O} for a given L_{bol} value. The most luminous maser source associated with low-mass star formation in this sample has $L_{H_2O} \sim 2 \times 10^{-6} L_\odot$, similar to G31.464+0.185, and $L_{bol} \sim 40 L_\odot$. This luminosity is comparable to that of Class I protostars with envelope masses of $\sim 1 M_\odot$ (Bontemps et al. 2010). Thus, if the H₂O maser coincident with G31.464+0.185 is excited by star formation within the clump, the H₂O maser luminosity is consistent with excitation by a low-mass protostar.

4.2.3 Observational Challenges

Although I found only marginal evidence for low-mass protostars forming in massive quiescent clumps, my analysis was limited in its ability to answer this question. The main limitations of this analysis are threefold: H₂O masers excited by low-mass protostars are faint, certain shock geometries limit masering, and masers are highly time variable.

The luminosities of H₂O masers associated with low-mass protostars ($L_{H_2O} \sim 10^{-9} - 10^{-6}$; Furuya et al. 2003) are much lower than those associated with high-mass protostars ($L_{H_2O} \sim 10^{-7} - 10^{-1}$ Anglada et al. 1996). Although the RAMPS H₂O sensitivity limits detectable masers to $L_{H_2O} \gtrsim 5 \times 10^{-8} L_\odot$ at a distance of 3 kpc, $\sim 90\%$ of the clumps in the RAMPS sample have distances greater than 3 kpc. Furthermore, of the 111 quiescent clumps with $M_{clump} > 260 M_\odot$, only one of these massive quiescent clumps has a distance < 3 kpc. Consequently, more sensitive H₂O observations are required to detect low luminosity masers at the greater distances needed. Assuming an average low-mass protostellar H₂O maser luminosity of $L_{H_2O} = 10^{-8} L_\odot$, an H₂O maser velocity dispersion of $\sigma = 0.3 \text{ km s}^{-1}$, and a

distance of $d = 6$ kpc, the corresponding flux is $I_\nu = 12$ mJy, ~ 60 times lower than the RAMPS H₂O maser detection limit.

H₂O maser excitation requires high temperatures ($T \sim 400$ K) and column densities (Elitzur et al. 1989) to overpopulate the upper energy level, but these conditions alone will not produce a maser. Because the gas must be velocity-coherent with respect to the observer (Elitzur 1991), the detection of a maser depends on the shock geometry as much as the excitation conditions. Gas that is compressed by a shock pointed at the observer is unlikely to mase, while an outflow pointed in the plane of the sky can produce the high temperatures and high velocity-coherent column densities required. Assuming that outflows pointed $> 30^\circ$ out of the plane of the sky are unlikely to mase, randomly oriented outflows would yield masers in only half of the sources that produce the requisite excitation conditions. Thus, the requirement for a particular shock geometry severely limits the number of protostars that could produce detectable maser emission.

Finally, H₂O masers are extremely time variable. The luminosities of H₂O masers associated with low-mass protostars can vary above and below detection limits on month-long timescales, with brightness changes of two orders of magnitude possible over several months (Claussen et al. 1996). Claussen et al. (1996) found that the maser phase in low-mass embedded source spans only a third of the embedded phase. Thus, the population of potentially detectable masers is likely further reduced by two thirds.

Although considerations of shock geometry and time variability further limit the sample of detectable masers, an H₂O maser survey that targets a sufficiently large sample of massive quiescent clumps could determine whether low-mass protostars form prior to high-mass protostars. For the RAMPS sample, 43 massive quiescent clumps have distances less than 6 kpc. If unfavorable shock geometries and time

variability reduce the portion of detectable masers by a factor of six, this leaves ~ 7 massive quiescent clumps with H₂O masers that could be detected if they exist. Thus, an H₂O maser survey that targets the RAMPS massive quiescent clump sample with $d < 6$ kpc and achieves a flux sensitivity of 4 mJy could detect H₂O maser emission from low-mass protostars or place strong limits on their existence. Unfortunately, the integration time needed to complete such a survey would likely be prohibitive. To achieve a flux sensitivity of 4 mJy, an integration time of ~ 30 hours per source would be required, resulting in a total on source integration time of 1,290 hours.

4.3 Feedback from High-Mass Protostars and Stars

In this section, I examine the impact of high-mass protostellar and stellar feedback on molecular clumps. In Section 4.3.1, I investigate the effects of radiative and kinematic feedback from massive protostars by analyzing the distributions of enhanced gas temperature (T_{kin}), NH₃ abundance ($\chi(\text{NH}_3)$), and velocity dispersion (σ) in protostellar clumps. In Section 4.3.2, I perform a similar analysis on H II region clumps to determine the effects of radiative and kinematic feedback from massive stars.

4.3.1 High-Mass Protostellar Feedback

In this section, I investigate the size of the region within clumps altered by feedback from massive protostars by analyzing the angular distributions of T_{kin} , $\chi(\text{NH}_3)$, and σ to assess the influence of high-mass protostars on their surrounding gas. In Section 4.3.1.1, I create a subsample of protostellar clumps that is suitable for this analysis and determine the positions of the massive protostars the clumps host. In Section 4.3.1.2, I create 2D angular distributions of T_{kin} , $\chi(\text{NH}_3)$, and σ . In Section 4.3.1.3, I fit and analyze these distributions to determine the importance of

and size scales over which massive protostars alter the temperature, chemistry, and level of turbulence within their natal clumps.

4.3.1.1 The Protostellar Feedback Subsample

In order to examine the importance and extent of high-mass protostellar feedback, I first produced a subsample of protostellar clumps suitable for analysis. The main limiting factor for this analysis was the angular extent of the NH₃(2,2) emission, since significant NH₃(2,2) emission is required to determine gas temperatures and NH₃ abundances. To measure spatial variations in these quantities, the angular extent of the NH₃(2,2) emission must be resolved by the GBT telescope beam. Consequently, I restricted my analysis to protostellar clumps with successful PySpecKit fits of the NH₃(1,1) and (2,2) spectra covering at least 1.7 arcmin², resulting in a sample size of 29 protostellar clumps. This angular size ensures that the clumps in the sample are resolved by at least two beam widths, resulting in ≥ 6 independent measurements that are one FWHM beam width away from each other.

Next, I estimated the positions of the massive protostars that are the sources of protostellar feedback. Massive protostars heat the surrounding dust, which produces bright 24 μm emission. For each protostellar clump, I searched the MIPSGAL Point Source Catalog (Gutermuth & Heyer 2015) for 24 μm point sources located within the angular extent of the clump. In cases where multiple 24 μm sources are within a given clump, I adopted the position of the point source with the greatest 24 μm flux.

4.3.1.2 Protostellar Feedback Distributions of T_{kin} , $\chi(\text{NH}_3)$, and σ

After determining the position of the brightest 24 μm point source associated with each clump, I created distributions of T_{kin} , $\chi(\text{NH}_3)$, and σ as a function of Galactic longitude (l) and Galactic latitude (b). In Chapter 2, I derived σ values

both solely from fits to the NH₃(1,1) data and from simultaneous fits to the NH₃(1,1) and (2,2) data. Because NH₃(2,2) emission requires higher gas temperatures for excitation than NH₃(1,1) emission, the σ values derived from the simultaneous fits to the NH₃(1,1) and (2,2) spectra are more sensitive to the kinematics of hot gas than the σ values derived solely from the NH₃(1,1) spectra. Consequently, I chose to use the σ values derived from the simultaneous fits to the NH₃(1,1) and (2,2) spectra for this analysis.

Because the RAMPS maps are oversampled with respect to the angular resolution of the GBT, pairs of pixels that are separated by less than a beam width are not independent. To accurately model these data, I sampled pixels that are separated by one beam width in the T_{kin} , $\chi(\text{NH}_3)$, and σ maps. First, I fit the oversampled T_{kin} , $\chi(\text{NH}_3)$, and σ maps with 2D Gaussian models to estimate the positions of the distribution peaks. I sampled the pixels at the best-fit positions and every pixel in a grid with a one beam width spacing. Consequently, the T_{kin} , $\chi(\text{NH}_3)$, and σ values used to estimate the size scales of feedback are independent.

Finally, I restricted the angular extent of these distributions in order to estimate the physical extent of feedback associated with a single protostellar core within a clump. Therefore, I limited the angular extent of the distributions to three beam widths ($\sim 1.5'$) away from the position of the protostar to reduce the influence of feedback from other massive protostars within the same clump.

4.3.1.3 Protostellar Feedback Distribution Analysis

After producing the 2D angular distributions of independent T_{kin} , $\chi(\text{NH}_3)$, and σ values for each protostellar clump in the analysis subsample, I fit the distributions with 2D circular Gaussian models with constant offsets. Because feedback zones that are unresolved by the telescope beam will appear as beam-sized enhancements in the

gas properties, I restricted the minimum size of the Gaussian fits to the size of the beam.

Figure 4.2 shows example fits for the protostellar source G23.606-0.011. The panels in the left column of the figure show maps of T_{kin} , $\chi(\text{NH}_3)$, and σ with the position of the presumed protostar marked with a red circle and overlaid contours of constant Σ . The panels in the right column show the same maps overlaid with the best-fit FWHM sizes, the FWHM beam size, and the positions of the pixels used in the fit. Although the distributions of T_{kin} , $\chi(\text{NH}_3)$, and σ are unlikely to be reproduced exactly by a Gaussian model, the best-fit Gaussian models have produced reasonable estimates of the angular extents of the enhanced T_{kin} , $\chi(\text{NH}_3)$, and σ values.

The T_{kin} map exhibits a roughly symmetric T_{kin} angular extent with a peak temperature of $T_{kin} \sim 20$ K and a background temperature of $T_{kin} \sim 13$ K. The data and fit show that the enhanced temperature region is more extended than the angular extent of the beam, indicating that the region heated by feedback from the central protostar is resolved.

The map of $\chi(\text{NH}_3)$ exhibits an asymmetric distribution about the position of the 24 μm point source. The peak $\chi(\text{NH}_3)$ value is $\sim 5 \times 10^{-8}$, much higher than the background value of $\chi(\text{NH}_3) \sim 1 \times 10^{-8}$. While the $\chi(\text{NH}_3)$ values do display a peak, the distribution is not as clearly characterized by a 2D circular Gaussian model as is the T_{kin} distribution. Consequently, the fit is relatively poor, with $\chi^2_{red} \sim 20$.

The σ map displays a significantly extended region of enhanced σ values. The peak value is $\sigma \sim 1 \text{ km s}^{-1}$, a factor of ~ 3 greater than the background σ values. Although the 2D Gaussian fit appears to reproduce the large-scale σ enhancement relatively well, the peak σ values are offset from the best-fit position. Nevertheless, the enhanced σ values are clearly resolved compared to the size of the beam and

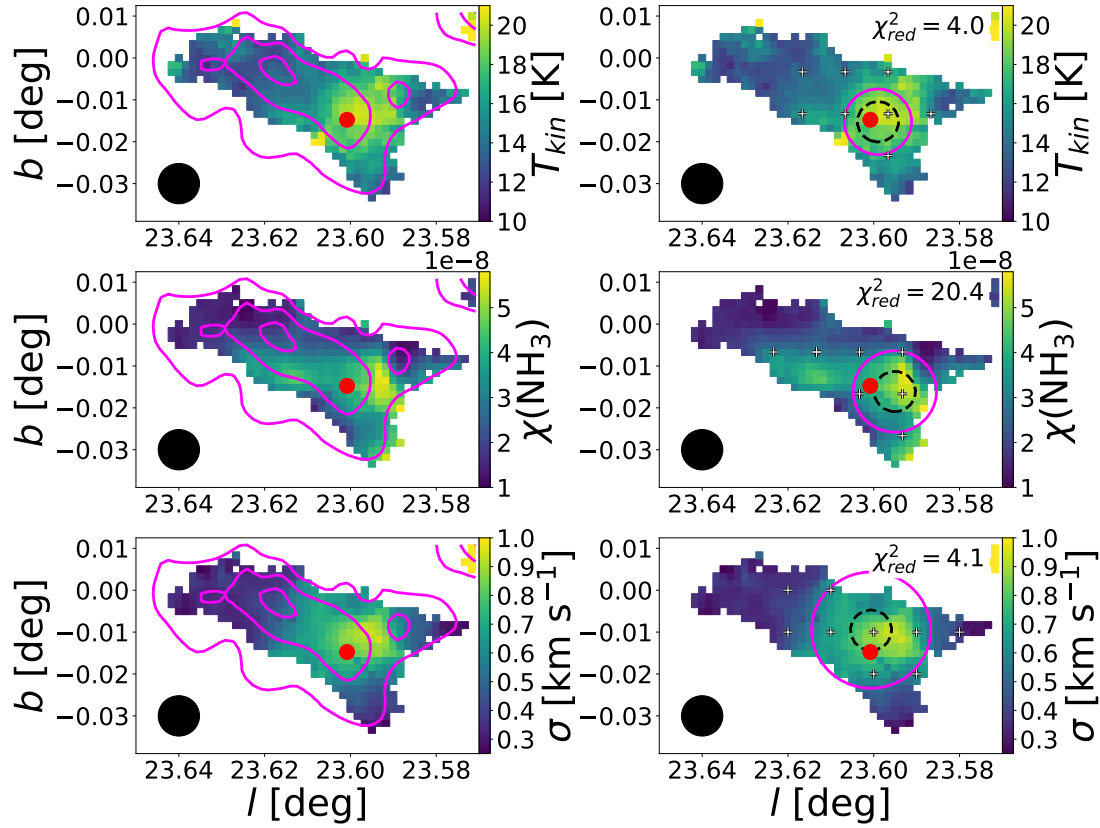


Fig. 4.2 Maps of T_{kin} (left), $\chi(\text{NH}_3)$ (middle), and σ (right) for the protostellar clump G23.606-0.011. The black circles in the lower left of each map indicate the FWHM beam size. The red circles show the location of the $24 \mu\text{m}$ point source. Left column: The magenta contours mark $\Sigma = 0.025, 0.075$, and 0.15 g cm^{-2} . Right column: The magenta circle shows the FWHM size of the best-fit 2D circular Gaussian model and the dashed black circle shows the FWHM beam size for comparison. White crosses show the positions of the independent pixels used in the fit. The corresponding reduced χ^2 (χ^2_{red}) values are shown in the upper right of each panel.

the size of the best-fit 2D Gaussian model has provided a reasonable estimate of the angular extent.

As demonstrated by the fit example in Figure 4.2, the 2D circular Gaussian model is sometimes overly simplistic compared to the maps of the gas properties. Consequently, some of the fit results have large error and are unreliable. Thus, I restricted further analysis to those fits where the errors on the Gaussian amplitudes, half width at half maximum (HWHM) angular sizes (θ_{HWHM}), and constant offsets were less than three times their respective parameter values. Only two T_{kin} fits, three $\chi(\text{NH}_3)$ fits, and five σ fits meet these criteria.

To get the physical size scales over which T_{kin} , $\chi(\text{NH}_3)$, and σ are enhanced, I multiplied the most probable clump distances (d_1) by the deconvolved HWHM angular sizes, which are given by $\theta_{HWHM,dec} = \sqrt{\theta_{HWHM}^2 - \theta_{beam,HWHM}^2}$. The HWHM radii are given by $R_{HWHM,1} = d_1 \theta_{HWHM,dec}$, where $\theta_{HWHM,dec}$ is in units of radians and d_1 is in units of parsecs. In some cases, the clump distances are poorly determined, with primary distance probabilities $p_1 < 0.75$. For these sources, I also determined $R_{HWHM,2}$ using the second most probable distance (d_2).

Figure 4.3 shows the 2D circular Gaussian best-fit amplitudes plotted against the HWHM physical radii for the fits to the T_{kin} , $\chi(\text{NH}_3)$, and σ distributions. The left column shows the $R_{HWHM,1}$ values and the right column shows the $R_{HWHM,2}$ values for the protostellar clumps with $p_1 < 0.75$. The fit amplitudes indicate the degree to which high-mass protostars change the properties of their surrounding gas and the physical radii provide the size scale over which these changes occur.

The fits to the T_{kin} distributions show that the massive protostars can heat the surrounding gas by ~ 8 K above the background temperature. The physical size scales over which this heating occurs are important because radiative feedback can heat accretion flows, reduce their fragmentation, and potentially aid further

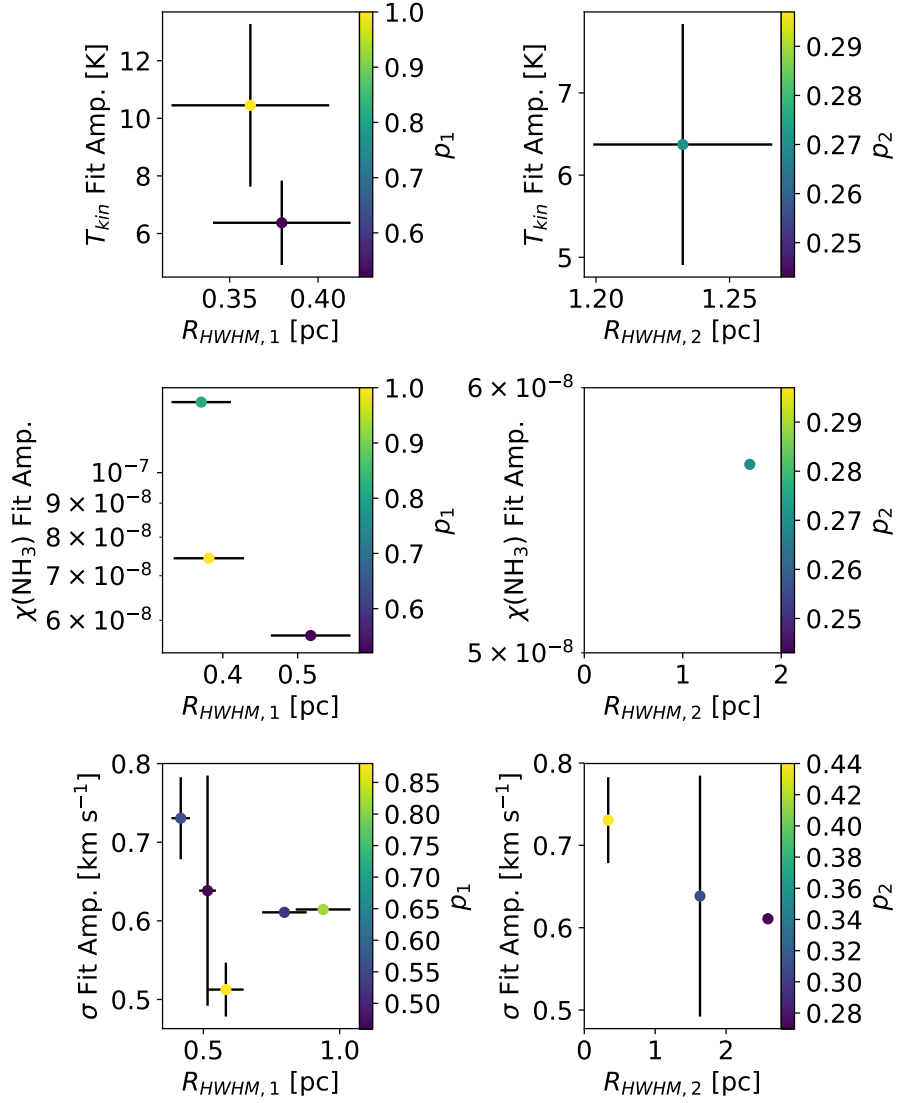


Fig. 4.3 Fit amplitudes plotted against R_{HWHM} for the 2D circular Gaussian fits to T_{kin} (top row), $\chi(\text{NH}_3)$ (middle row), and σ (bottom row) distributions of the protostellar clumps. The symbol colors indicate the probability of the distance assignments. The left column shows the $R_{HWHM,1}$ values assuming the most probable distance and the right column shows the $R_{HWHM,2}$ values using the second most probable distance for the clumps with $p_1 < 0.75$.

accretion onto massive protostars (Peters et al. 2010). The heated regions have sizes of $R_{HWHM,1} \sim 0.35 - 0.4$ pc. These results imply that radiative feedback from massive protostars can affect a region $\lesssim 0.5$ pc.

Gaches & Offner (2018) modeled the effect of radiative feedback from protoclusters, clusters dominated by protostars, of differing sizes on the temperature profile of their surrounding clump. They found that protostellar clusters containing more stars heat the clump to higher temperatures and over greater spatial extents. The protoclusters with $10^2 - 10^6$ protostars heat their surrounding clumps to visual extinctions of $A_V = 2 - 5$.

In order to determine the theoretical size scales for protostellar heating for the RAMPS protostellar clumps, I first estimated their gas densities. I assumed that the clumps were axisymmetric about their minor axes and used the average surface densities and the most probable distance d_1 to calculate their average number densities. The number densities have values of $n_1 \sim 4 \times 10^3$ and 6×10^3 cm $^{-3}$. Figure 4.4 shows $R_{HWHM,1}$ vs. n_1 and the dashed lines mark the values that correspond to $A_V = 2$ and 5. The measured $R_{HWHM,1}$ values derived from the T_{kin} distributions match the $A_V = 5$ line within two times the error on $R_{HWHM,1}$ and n_1 , suggesting that the protocluster luminosity model employed by Gaches & Offner (2018) may be a reasonable estimate of the true size scales of radiative feedback.

The second row of Figure 4.3 displays the fit amplitude for the $\chi(\text{NH}_3)$ distributions plotted against their R_{HWHM} values. The average increase above the background values is $\sim 8 \times 10^{-8}$, which corresponds to an average factor of ~ 7 increase in $\chi(\text{NH}_3)$. The $\chi(\text{NH}_3)$ values at the peak, which are given by the best-fit amplitudes added to the best-fit constant offsets, have a range of $\chi(\text{NH}_3) = 6.1 - 15 \times 10^{-8}$. The size scales of the $\chi(\text{NH}_3)$ enhanced regions are $R_{HWHM,1} \sim 0.4 - 0.5$ pc, similar

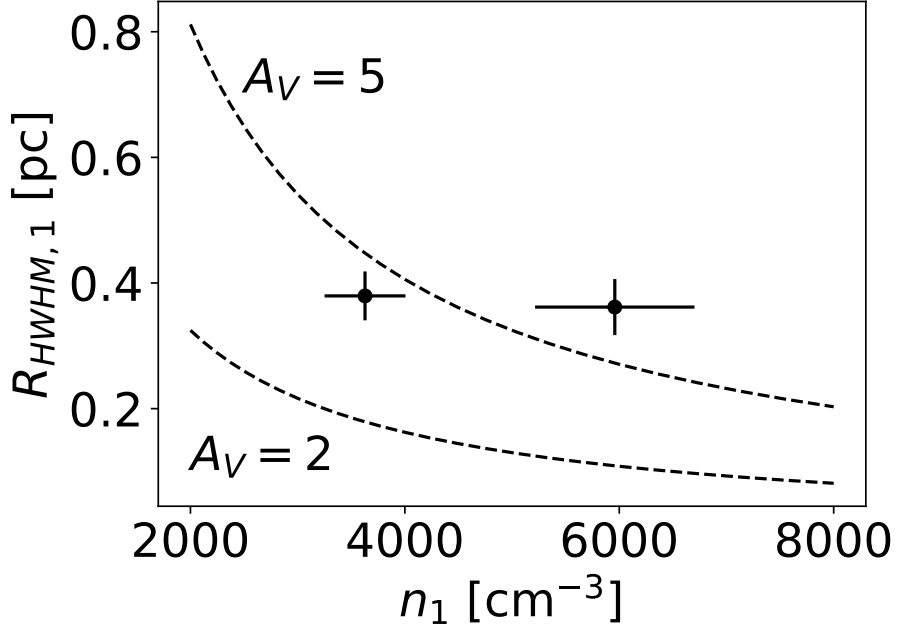


Fig. 4.4 R_{HWHM} vs. n assuming the most probable distance. The dashed lines mark the sizes and densities corresponding to $A_V = 2$ (lower) and 5 (upper).

to those of the T_{kin} enhanced regions. Next, I compared these values to theoretical predictions from chemical models.

Busquet et al. (2011) modeled the changes in chemical abundances in a massive protocluster in order to compare it to their molecular line data of the AFGL 5142 protocluster. After an initial phase of molecules freezing out onto dust grain mantles, they added a time-dependent heat source to represent radiative feedback by massive protostars. Prior to the protostellar feedback, the NH₃ abundance was $\chi(\text{NH}_3) = 4 \times 10^{-9}$, whereas the NH₃ abundance reached a peak of $\chi(\text{NH}_3) = 4 \times 10^{-8} \sim 10^5$ yr after the start of the feedback. Rodgers & Charnley (2001) also modeled the evolution of chemical abundances in hot protostellar cores. Their model produced high NH₃ abundances ($\chi(\text{NH}_3) > 10^{-7}$) in the cases of very hot gas ($T = 300$ K) and

NH_3 -rich ice on dust grain mantles. Thus, the highest $\chi(\text{NH}_3)$ value of 1.5×10^{-7} may be associated with particularly hot gas or NH_3 -rich icy mantles.

The third row of Figure 4.3 displays the fit amplitude for the σ distributions plotted against their R_{HWHM} values. The fit results indicate that massive protostars increase the velocity dispersion of the surrounding gas by $\sim 0.6 \text{ km s}^{-1}$ on average, which corresponds to a 250% increase over the background values. If massive protostars are able to increase the turbulence in nearby cores by the same factor, it would effectively increase the virial mass of such cores by a factor of ~ 6 , decreasing their ability to collapse. The size scales over which kinematic feedback occurs are $R_{HWHM,1} \lesssim 1 \text{ pc}$, similar to the values found for the extent of protostellar heating. Because kinematic and radiative feedback from high-mass protostars can affect clump properties over similar spatial scales, both of these effects will help determine the rate of accretion onto massive protostars in the presence of strong feedback.

The results of this analysis clearly show that feedback from massive protostars alters the temperature, chemistry, and kinematics of the surrounding gas. Such feedback occurs on scales of $R \sim 0.3 - 1 \text{ pc}$ and could alter the fragmentation (Peters et al. 2010), chemical abundances (Busquet et al. 2011), and turbulent support (Wang et al. 2010) of the gas within this radius. Consequently, theories of high-mass star formation must account for the effects of feedback from massive protostars on the formation and evolution of high-mass stellar clusters.

4.3.2 High-Mass Stellar Feedback

In Section 4.3.1, I demonstrated that feedback from high-mass protostars is common and alters clump properties on $< 1 \text{ pc}$ size scales. In this section, I continue my investigation of feedback into the later evolutionary stages. Once high-mass stars reach the main sequence, they form H II regions; thus, H II regions most often signal the presence of high-mass stars. Consequently, I investigate the distribution

of enhanced gas temperatures, NH_3 abundances, and velocity dispersions within H II region clumps. In Section 4.3.2.1, I create a subsample of H II region clumps that are suitable for this analysis and determine the positions of the high-mass stars they host. In Section 4.3.2.2, I create 2D angular distributions of T_{kin} , $\chi(\text{NH}_3)$, and σ . In Section 4.3.2.3, I fit and analyze these distributions to determine the significance of and size scales over which massive stars alter the temperature, chemistry, and level of turbulence within their natal clumps.

4.3.2.1 The Stellar Feedback Subsample

In order to determine the significance and extent of the radiative and kinematic feedback from massive stars, I performed the same spatial analysis on the H II region clumps as I did for the protostellar clumps. For this analysis, I also required clumps to have PySpecKit fit results covering at least 1.7 arcmin^2 . The resulting sample is comprised of 115 H II region clumps.

Next, I estimated the positions of the massive stars associated with the clumps in the H II region analysis sample. First, I searched the WISE Catalog of Galactic H II regions (Anderson et al. 2014) for H II regions or H II region candidates coincident with each clump. In some cases, there were multiple sources coincident with a single clump. Given that the UV radiation associated with massive stars causes fluorescent excitation of polycyclic aromatic hydrocarbons (PAHs) that are bright at $8 \mu\text{m}$ (Puget & Leger 1989), I adopted the position of the source with the greatest GLIMPSE $8 \mu\text{m}$ flux. In several cases, H II region clumps were not coincident with an Anderson et al. (2014) H II region or H II region candidate despite featuring bright compact or extended 8 and $24 \mu\text{m}$ emission. For these sources, I adopted the position of the peak GLIMPSE $8 \mu\text{m}$ flux within the bounds of the clump.

4.3.2.2 Stellar Feedback Distributions of T_{kin} , $\chi(\text{NH}_3)$, and σ

Using the same methods as in Section 4.3.1.2, I created 2D distributions of independent T_{kin} , $\chi(\text{NH}_3)$, and σ values within the H II region clumps. Similarly, I limited the angular extent of these distributions to three beam widths away from the H II region or H II region candidate to limit the inclusion of multiple high-mass stellar sources. Given the clustered nature of massive star formation (Lada et al. 1993; Zinnecker et al. 1993), some of these distributions feature multiple H II regions within the three beam width radius. Consequently, the feedback regions of some of these sources are not well modeled by a single Gaussian centered on the H II region with the greatest 8 μm flux.

4.3.2.3 Stellar Feedback Distribution Analysis

I fit the distributions of T_{kin} , $\chi(\text{NH}_3)$, and σ for each H II region clump in the analysis subsample with a 2D circular Gaussian model with a constant offset. Figure 4.5 shows example fits for the H II region clump G21.382-0.246. The panels in the left column of the figure show maps of T_{kin} , $\chi(\text{NH}_3)$, and σ with the position of the presumed protostar marked with a red circle and overlaid contours of constant Σ . The panels in the right column show the same maps overlaid with the best-fit FWHM sizes, the FWHM beam size, and the positions of the pixels used in the fit.

The T_{kin} map displays an angularly resolved temperature enhancement near the H II region, with a peak near the center of the H II region. The peak temperature is $T_{kin} \sim 25$ K, while the background temperature is $T_{kin} \sim 15$ K. Although the best-fit 2D Gaussian model fits the sampled pixels well, the best-fit position is shifted slightly toward lower Galactic latitudes than if all pixels were used in the fit.

The $\chi(\text{NH}_3)$ map also exhibits enhanced values that are angularly resolved. Like the T_{kin} fit, the best-fit position for the $\chi(\text{NH}_3)$ is shifted slightly toward lower

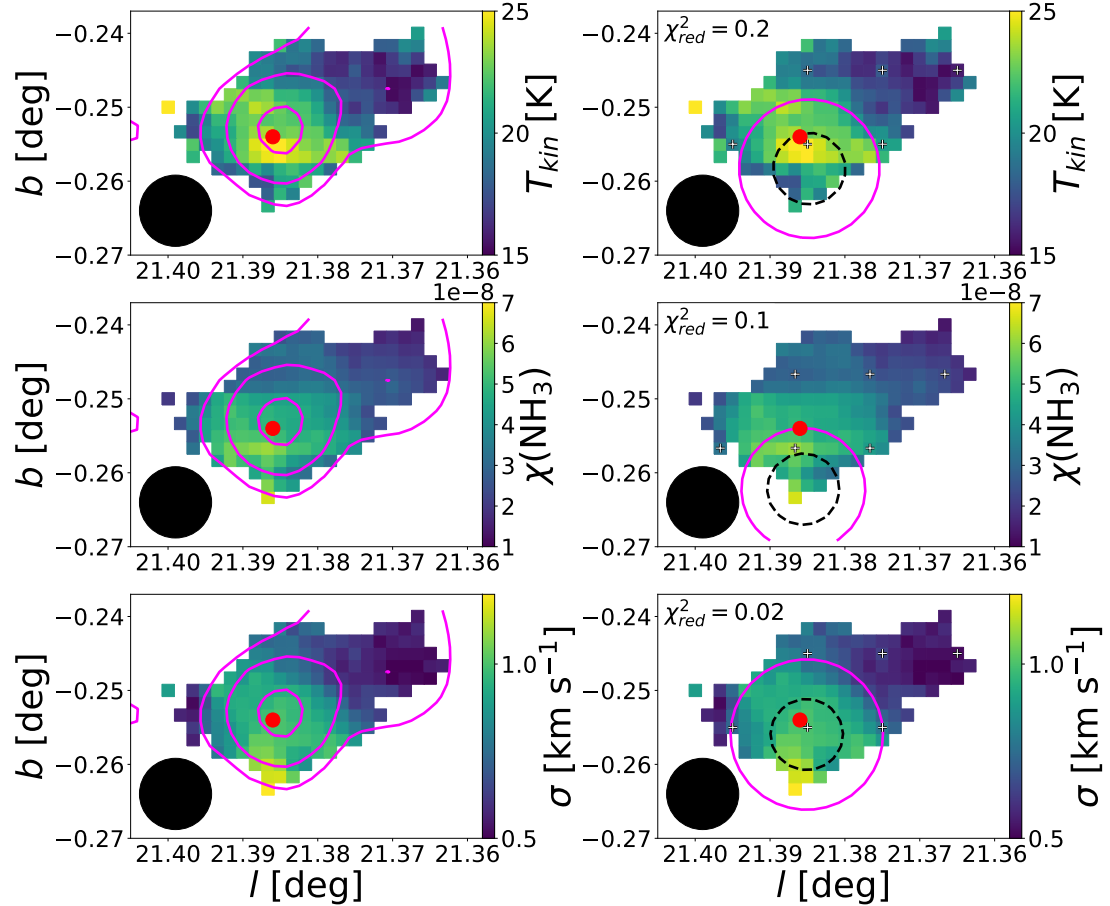


Fig. 4.5 Maps of T_{kin} (left), $\chi(\text{NH}_3)$ (middle), and σ (right) for the H II region clump G21.382-0.246. The black circles in the lower left of each map indicate the FWHM beam size. The red circles show the location of the H II region. Left column: The magenta contours mark $\Sigma = 0.025, 0.05$, and 0.1 g cm^{-2} . Right column: The magenta circle shows the FWHM size of the best-fit 2D circular Gaussian model and the dashed black circle shows the FWHM beam size for comparison. White crosses show the positions of the independent pixels used in the fit. The corresponding reduced χ^2 (χ^2_{red}) values are shown in the upper left of each panel.

Galactic latitudes than if all pixels were used in the fit. A visual comparison between the 2D $\chi(\text{NH}_3)$ map and the Gaussian fit suggests that the derived size scale is inaccurate. Consequently, I removed the $\chi(\text{NH}_3)$ fit for this source from further analysis.

The σ map also displays enhanced values that are well resolved by the beam. The peak σ value is more than double the background σ values, indicating a significant enhancement of the turbulent energy. The best-fit position of the 2D Gaussian model is closely aligned with the center of the H II region, implying that the source's stellar winds are the cause of the enhanced turbulence.

As in Section 4.3.1.3, I investigated the feedback size scales and change in gas properties for the analysis sample. I restricted this analysis to the fits where the errors on amplitudes, θ_{HWHM} , and constant offsets were less than three times their respective parameter values. Of the 115 H II region clumps in the sample, 11 T_{kin} fits, 18 $\chi(\text{NH}_3)$ fits, and 16 σ fits meet these criteria.

Figure 4.6 shows the 2D circular Gaussian best-fit amplitudes plotted against the HWHM physical radii for the fits to the T_{kin} , $\chi(\text{NH}_3)$, and σ distributions. The left column shows the $R_{HWHM,1}$ values and the right column shows the $R_{HWHM,2}$ values for the protostellar clumps with $p_1 < 0.75$. Many more H II regions feature successful 2D Gaussian fits than the protostellar sample, so the size scales of feedback and degree to which high-mass stars change the properties of their surrounding gas can be better determined.

The top row of Figure 4.6 displays the 2D circular Gaussian amplitudes plotted against $R_{HWHM,1}$ and $R_{HWHM,2}$ for the fits to the T_{kin} distributions. These fits show that the massive stars in this sample heat the surrounding gas by ~ 9 K above the background temperature on average. The physical size scales over which this heating occurs are important, since the UV radiation field of massive stars ionizes

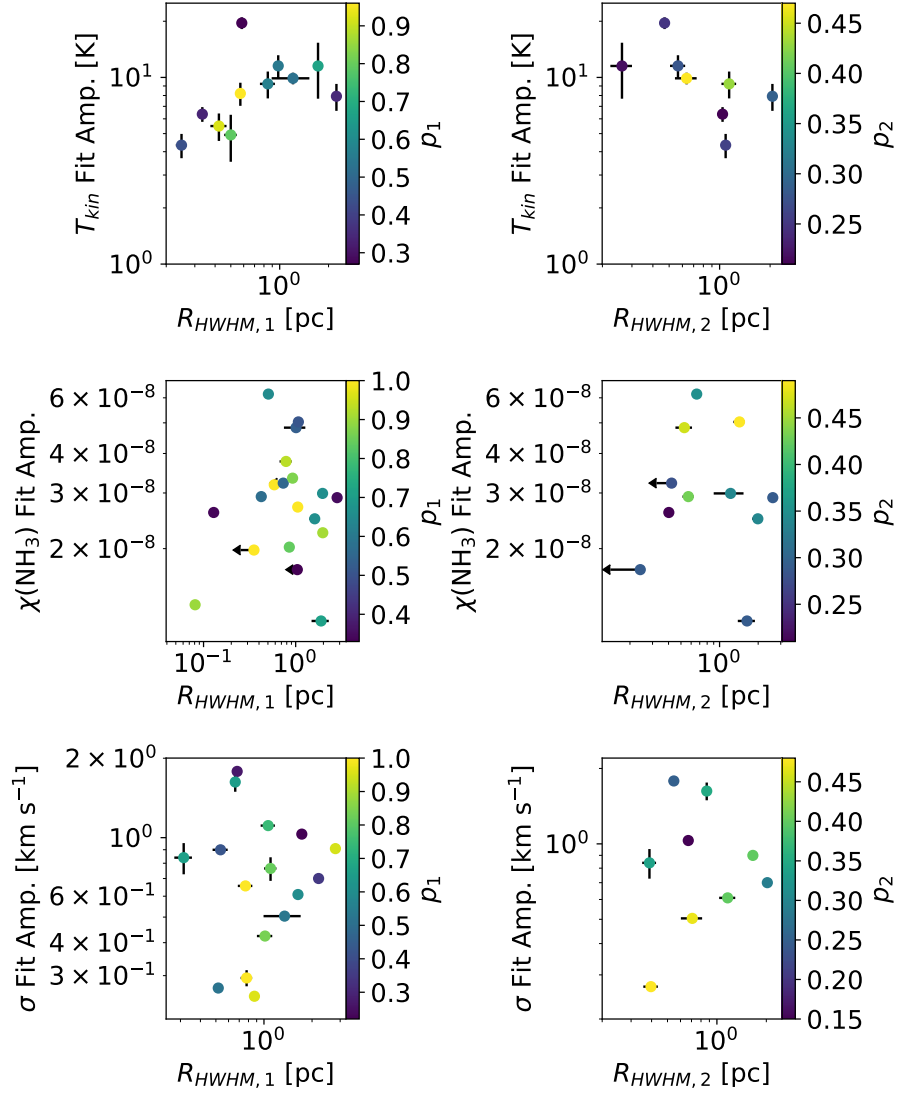


Fig. 4.6 Fit amplitudes plotted against R_{HWHM} for the 2D circular Gaussian fits to the T_{kin} (top row), $\chi(\text{NH}_3)$ (middle row), and σ (bottom row) distributions of the H II region clumps. The symbol colors indicate the probability of the distance assignments. The left column shows the $R_{HWHM,1}$ values assuming the most probable distance and the right column shows the $R_{HWHM,2}$ values for the clumps with $p_1 < 0.75$. The arrows indicate upper limits on $R_{HWHM,1}$ and $R_{HWHM,2}$.

the surrounding clump and can photoevaporate the circumstellar disks around young protostars (Meaburn 1988; O'dell & Wen 1994). The fits with resolved radii cover a range of $R_{HWHM} \sim 0.2 - 2$ pc, indicating that massive stars can heat and alter further star formation within clump-scale volumes of gas. Although these size scales are small compared to the range of observed H II regions sizes (Anderson et al. 2012; Tremblin et al. 2014), the stellar sources in this sample are still in an embedded phase and their H II regions have not expanded past the bounds of the clump.

The middle row of Figure 4.6 displays the 1D half-Gaussian amplitudes plotted against $R_{HWHM,1}$ and $R_{HWHM,2}$ for the fits to the $\chi(\text{NH}_3)$ distributions. The $\chi(\text{NH}_3)$ fits indicate that massive stars increase the NH_3 abundances of the surrounding gas by an average of 3×10^{-8} , which corresponds to a factor of ~ 3 increase over the background $\chi(\text{NH}_3)$ values. The size scales over which the massive stars in this sample increase $R_{HWHM,1} \sim 0.1 - 3$ pc.

The bottom row of Figure 4.6 displays the 1D half-Gaussian amplitudes plotted against R_{HWHM} for the σ distribution fits. These fit results indicate an average increase in the velocity dispersion of $\sim 0.8 \text{ km s}^{-1}$, which corresponds to a factor of ~ 2.5 increase above the background σ values and a factor of ~ 6 increase in the virial mass. The size scales over which the σ values are enhanced are in the range $R_{HWHM} \sim 0.3 - 3$ pc. Thus, massive stars significantly increase the turbulent support within their natal clumps over clump-scale radii.

The results of this analysis show that radiative and kinematic feedback from massive stars can alter the gas temperatures, chemical abundances, and turbulent velocity dispersions on the scale of clumps ($\sim 0.5 - 2$ pc). Consequently, their effect on star formation in massive clumps must be important. In addition to altering chemical abundances, the intense UV radiation from high-mass stars ionizes the surrounding gas. Even in the case of very dense gas, such as circumstellar disks around young

stars, the UV field ionizes these sources and the radiation-driven winds sweep the ionized gas away (Bally et al. 1995).

Given the significant turbulent energy input by the stellar winds, they may also inhibit further star formation within clumps. In fact, a collapsing clump with a virial parameter of $\alpha = 0.5$ would become gravitationally unbound if its virial mass were increased by a factor > 4 . Thus, feedback from massive stars may provide the mechanism necessary to halt star formation in theories involving the collapse of massive clumps, resulting in star formation rates that are similar to the observed values. On the other hand, some theories predict that the expansion of H II regions may actually trigger further star formation by compressing gas in a narrow shell (Elmegreen 1998). My analysis can only resolve gas structures at the clump scale (~ 1 pc), so it cannot test whether such dense shells are common and unstable to fragmentation. Nevertheless, this analysis shows that massive stellar feedback is an important factor whose effects must be included in all theories of massive star formation.

4.4 Conclusions

In this chapter I tested the importance of protostellar and stellar feedback in high-mass star formation. I have drawn the following conclusions from my analysis:

1. I searched for the presence of low-mass protostars in massive ($M_{clump} > 260 M_\odot$) quiescent clumps to test predictions from the theories of turbulent core accretion and competitive accretion. Although my search revealed a candidate clump that featured H₂O maser emission, a false positive test suggests an equal probability that the coincidence of the maser is due to a chance alignment with the clump. If the maser is excited by star formation in the clump, the maser luminosity of $L_{\text{H}_2\text{O}} = 2.6 \times 10^{-6} L_\odot$ is comparable to that expected from

excitation by a low-mass protostar. This analysis was limited by the small sample (one source) of nearby ($d < 3$ kpc) massive quiescent clumps. To better test this theories requires a flux sensitivity ~ 60 times better than the RAMPS observations in order to detect maser luminosities of $L_{\text{H}_2\text{O}} \sim 10^{-8} L_{\odot}$ at distances of 6 kpc.

2. My analysis of the protostellar clumps shows that radiative and kinematic feedback from high-mass protostars significantly alters the properties of the surrounding gas. In the immediate surroundings of high-mass protostars, I found enhanced values of T_{kin} (~ 8 K higher), $\chi(\text{NH}_3)$ ($\sim 8 \times 10^{-8}$ higher), and σ ($\sim 0.6 \text{ km s}^{-1}$ higher) over size scales of $\sim 0.3 - 1$ pc. This size scale is comparable to that predicted by the protocluster radiative feedback models of Gaches & Offner (2018). Simulations suggest that such heating could aid accretion onto massive protostars (Peters et al. 2010), while turbulence injected by outflows could inhibit further accretion (Wang et al. 2010). Given that both radiative and kinematic feedback affects gas properties on similar size scales, simulations including realistic treatments of both forms of feedback are required to investigate their combined effect on star formation.

3. My analysis of the H II region clumps shows that radiative and kinematic feedback from embedded high-mass stars alters the gas properties of clumps significantly over greater spatial scales than high-mass protostars. I found enhanced values of T_{kin} (~ 9 K higher), $\chi(\text{NH}_3)$ ($\sim 3 \times 10^{-8}$ higher), and σ ($\sim 0.8 \text{ km s}^{-1}$ higher) over size scales of $\sim 0.3 - 3$ pc. The strong UV field and radiation-driven winds can photoevaporate and sweep away the disks of nearby protostars (Bally et al. 1995). In addition, stellar winds from high-mass stars can add turbulent support and help slow or halt the gravitational collapse of clumps, which is predicted by theories that require the gravitational collapse

of clumps to form high-mass stars (e.g., Bonnell et al. 2001, 2004; Vázquez-Semadeni et al. 2019). The high-mass stars in this sample increased σ by a factor of ~ 2.5 above the background values on average. This level of increase suggests that a previously collapsing clump that forms a massive star can become gravitationally unbound as the H II region expands and adds turbulent energy to a larger portion of the clump. Thus, high-mass stars can significantly impact the evolution of their natal clumps and the stars and protostars that form near (~ 1 pc) them.

Chapter 5

External Feedback from the W41 Supernova Remnant

5.1 Introduction

In Chapter 4, I showed that internal feedback from evolving high-mass stars can change the gas properties of molecular clumps. In this Chapter, I will investigate whether external feedback from a nearby supernova remnant (SNR) can significantly change the gas properties, and potentially star-forming potential, of a dense molecular filament. High-mass stars end their lives as supernovae by releasing $\sim 10^{51}$ ergs of energy nearly instantaneously. The resulting shock waves can impact nearby molecular clouds (MCs), potentially accelerating, heating, and adding turbulence to the gas. While external feedback may help regulate star formation, the exact role such SNR shocks play is not yet well understood.

Previous efforts to investigate SNR-MC interactions analytically have demonstrated that SNR shocks can accelerate and heat MC gas, potentially destroying the cloud in the process (McKee & Cowie 1975; Heathcote & Brand 1983; McKee et al. 1987). Given the complex gas motions involved in shock interactions, researchers have also employed hydrodynamical simulations to better understand SNR-MC interactions. The results from such simulations differ, depending on assumptions, but show that shocks have the potential to disperse much of the gas in dense clouds (Sgro 1975; Xu & Stone 1995) or compress them to form denser structures (Wood-

ward 1976; Orlando et al. 2005). More recent 3D hydrodynamic simulations modeled the influence of SNe on the evolution of larger star-forming regions. These simulations find that the effects of these interactions on star formation depend sensitively on the relative positions of SNe and nearby MCs. Simulations by Smith et al. (2020) suggest that embedded and clustered SNe significantly inhibit the formation of stars, while simulations by Seifried et al. (2018) imply that turbulence injected by more distant SNe ($d \geq 25$ pc) is relatively short lived ($\sim 10^5$ yr). Because the influence of SNe on star formation has implications for galaxy evolution, observations of SNR-MC interactions are essential to test the differing theoretical predictions.

5.1.1 A Possible SNR-MC Interaction in G23.33-0.30

G23.33-0.30 (Hogge et al. 2019) is a dense molecular filament that exhibits the broadest molecular line widths detected in the RAMPs NH₃ data. Figure 5.1 displays RAMPs NH₃(1,1) through (4,4) spectra toward the same position in G23.33-0.30. The spectra show the uncommonly broad line emission associated with G23.33-0.30, which spans the velocity range $V_{LSR} = 55$ to 80 km s⁻¹. The NH₃(2,2) emission from G23.33-0.30, which does not feature bright hyperfine lines, exhibits peaks at $V_{LSR} \sim 60$ and 75 km s⁻¹. Both velocity components are broad, with full-width at half-maximum (FWHM) line widths $\Delta V_{FWHM} \sim 10$ km s⁻¹. Clumps with large line widths usually display bright mid-infrared (MIR) emission from massive protostars or H II regions. Thus, G23.33-0.30's lack of MIR emission is unique among clumps featuring broad NH₃ line widths.

The spectra also include emission from an unrelated background MC at $V_{LSR} = 102$ km s⁻¹. The emission from this source has a line width of $\Delta V_{FWHM} \sim 1.5$ km s⁻¹, which is within the typical range of NH₃ line widths for molecular clumps ($\Delta V_{FWHM} \sim 1 - 7$ km s⁻¹; Wienen et al. 2012; Svoboda et al. 2016; Wienen et al. 2018).

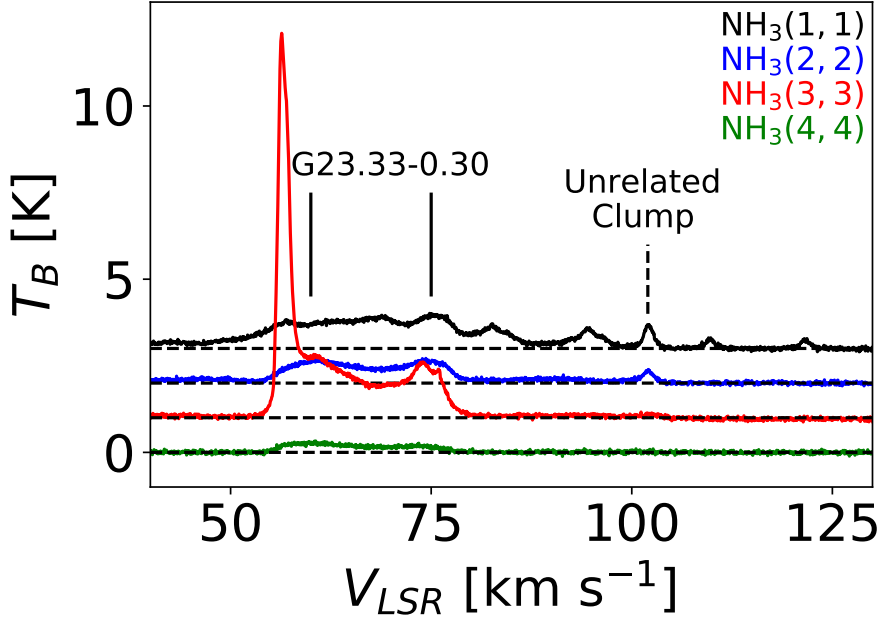


Fig. 5.1 RAMPS $\text{NH}_3(1,1)$ through $(4,4)$ spectra toward the peak of the narrow $\text{NH}_3(3,3)$ emission. The solid vertical lines mark the approximate velocities of two prominent peaks in the $\text{NH}_3(2,2)$ emission associated with G23.33-0.30. The dashed vertical line marks the velocity of a presumably unrelated clump at $V_{LSR} = 102 \text{ km s}^{-1}$.

The $\text{NH}_3(3,3)$ spectrum also displays a bright, narrow line component superposed on the broad component. Unlike the broad component, the bright, narrow line emission in the ortho ($K = 3n$) $\text{NH}_3(3,3)$ spectrum has no corresponding component in the para ($K \neq 3n$) transitions. Consequently, the narrow $\text{NH}_3(3,3)$ component was suspected of being a maser. The brightness temperature of the suspected $\text{NH}_3(3,3)$ maser measured from the GBT observations is $T_B \sim 10 \text{ K}$. To prove this emission is nonthermal, the measured brightness temperature, which is proportional to θ_{beam}^{-2} for a point source, must be much greater than the gas temperature. Because masers emit at such small spatial scales ($\sim 10^{-6} \text{ pc}$; Elitzur 1992), the single-dish observations lack the angular resolution necessary to determine a nonthermal brightness

temperature. Nevertheless, the narrow line width of this emission and its appearance solely in the $\text{NH}_3(3,3)$ spectrum suggests that it is from an $\text{NH}_3(3,3)$ maser.

Compared to other masing transitions, such as the 22 GHz $\text{H}_2\text{O}(6_{1,6} - 5_{2,3})$ transition, $\text{NH}_3(3,3)$ masers are exceedingly rare. Indeed, to my knowledge only 15 sources with $\text{NH}_3(3,3)$ masers have been discovered outside of the Galactic Center (Table 5.1). Although our understanding of $\text{NH}_3(3,3)$ maser excitation is incomplete, studies have found that they can be excited by shocks resulting from SNR-MC interactions (McEwen et al. 2016) or energetic outflows from high-mass protostars (Mangum & Wootten 1994; Kraemer & Jackson 1995; Zhang & Ho 1995). The majority of $\text{NH}_3(3,3)$ masers are faint, with fluxes of $\lesssim 1$ Jy. On the other hand, Walsh et al. (2011) measured a flux of 9.7 Jy for G23.33-0.30's maser candidate, while I measured a flux of ~ 5 Jy from the RAMPS data. Thus, if the emission from G23.33-0.30's maser candidate is genuinely nonthermal, it would be one of the brightest $\text{NH}_3(3,3)$ masers detected yet.

G23.33-0.30's broad NH_3 line emission is associated with a filamentary infrared dark cloud (IRDC) that resides within the giant molecular cloud (GMC) G23.0-0.4. G23.0-0.4 is a large ($\sim 84 \times 15$ pc), massive ($\sim 5 \times 10^5 \text{ M}_\odot$), and dense ($\sim 10^3 \text{ cm}^{-3}$) filamentary GMC (Su et al. 2015) that hosts multiple generations of high-mass star formation (Messineo et al. 2014). In particular, there are several nearby SNRs projected against G23.0-0.4, two of which, G22.7-0.2 (Su et al. 2014) and W41 (Frail et al. 2013; Su et al. 2015), may be interacting with the GMC.

Figure 5.2 shows the Multi-Array Galactic Plane Imaging Survey (MAGPI; Helfand et al. 2006) 20 cm continuum emission from W41 in color and the VLA Galactic Plane Survey (VGPS; Stil et al. 2006) 21 cm data as contours. W41 is an asymmetric shell-type supernova (Green 1991; Kassim 1992) suspected of interacting with the nearby GMC G23.0-0.4, which has a velocity near $V_{LSR} = 77 \text{ km s}^{-1}$ (Su

Table 5.1. Known NH₃(3,3) Masers

Source	Flux (Jy)	Reference
DR21(OH)	0.260	Mangum & Wootten (1994)
W51	0.230	Zhang & Ho (1995)
NGC 6334 V	0.114	Kraemer & Jackson (1995)
NGC 6334 I	0.482	Kraemer & Jackson (1995)
IRAS 20126+4104	0.079	Zhang et al. (1999)
G5.89-0.39	0.031	Hunter et al. (2008)
G20.08-0.14N	0.191	Galván-Madrid et al. (2009)
G23.33-0.30	9.7	Walsh et al. (2011)
G30.7206-00.0826	5	Urquhart et al. (2011)
G35.03+0.35	0.065	Brogan et al. (2011)
G28.34+0.06	0.03	Wang et al. (2012)
W51C	1.4	McEwen et al. (2016)
W44	0.07	McEwen et al. (2016)
G5.7-0.0	0.35	McEwen et al. (2016)
G1.4-0.1	0.58	McEwen et al. (2016)

et al. 2015). Frail et al. (2013) detected two 1720 MHz OH maser candidates, known to trace SNR-MC interactions (Wardle & Yusef-Zadeh 2002), coincident with W41’s central continuum peak. G23.33-0.30 is offset from the OH masers by $\sim 3'$ and sits at the edge of the central continuum peak.

W41 is also coincident with HESS J1834-087 (Aharonian et al. 2006; Albert et al. 2006), a source of TeV emission thought to be triggered by W41’s interaction with a GMC (Tian et al. 2007). Deep follow-up observations with H.E.S.S. revealed that the TeV emission is composed of a point-like source and an extended component (H. E. S. S. Collaboration et al. 2015). Although the pulsar candidate CXOU J183434.9-08444 (Misanovic et al. 2011) may account for the point-like component of the TeV emission, H. E. S. S. Collaboration et al. (2015) argued that the extended TeV emission is best explained by the SNR-MC interaction.

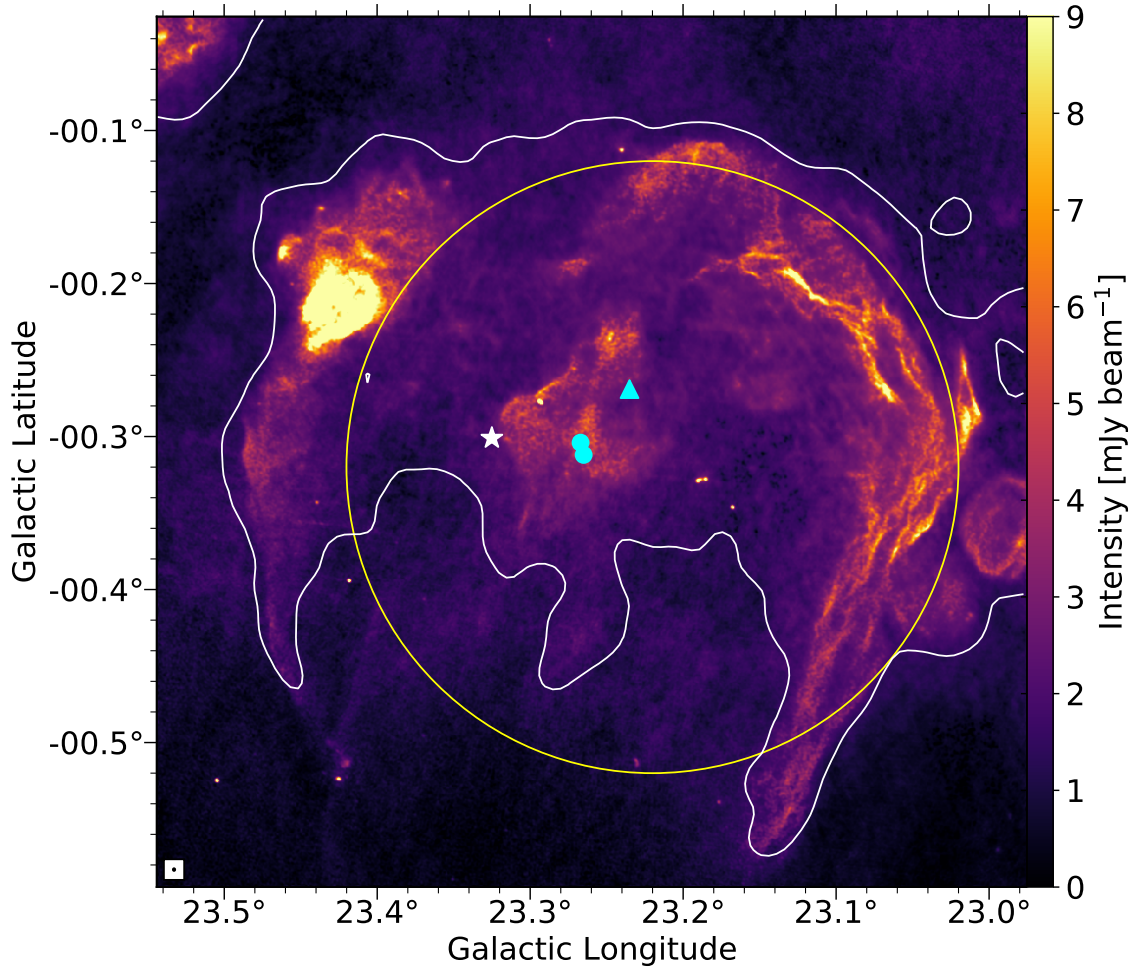


Fig. 5.2 Color shows the intensity of MAGPIS 20 cm continuum data. The white curves show the VGPS 21 cm continuum isointensity contour at 30 K. The white star shows the position of G23.33-0.30. The cyan circles coincident with the central 20 cm continuum peak indicate the positions of two 1720 MHz OH maser candidates, which have velocities near 75 km s^{-1} . The cyan triangle shows the position of the pulsar candidate CXOU J183434.9-08444. The large yellow circle displays the fitted position and FWHM size of the extended component of HESS J1834-087's TeV γ -ray emission. The MAGPIS beam size is shown in black in the lower left corner.

The MIR emission toward the W41 region traced by GLIMPSE and MIPSGAL is shown in Figure 5.3, displaying a rich and complicated star-forming complex. These data reveal filamentary IRDCs and several sources of bright MIR emission, but provide no kinematic information about the molecular gas near W41. In order to better understand the kinematics of the molecular gas in the W41 region, I analyzed the Galactic Ring Survey (GRS; Jackson et al. 2006) ^{13}CO (1-0) data. The GMC associated with G23.33-0.30 has a velocity of $V_{LSR} = 77 \text{ km s}^{-1}$.

If the broad emission in the GBT spectra represents gas that was blueshifted from the GMC velocity, then the component at $V_{LSR} = 60 \text{ km s}^{-1}$ would correspond to the most blueshifted velocity. Figure 5.4 shows the GRS ^{13}CO emission integrated over the velocity ranges $V_{LSR} = 59\text{--}61 \text{ km s}^{-1}$ (left panel) and $V_{LSR} = 76\text{--}78 \text{ km s}^{-1}$ (right panel), which are also indicated in the upper right corner of each panel. For reference, the MAGPIS 20 cm continuum is shown with contours and the position of G23.33-0.30 is shown with a star. The GMC emission crosses the extent of W41, but exhibits a deficit coincident with W41's central continuum peak. Conversely, the emission at $V_{LSR} = 60 \text{ km s}^{-1}$ peaks within the central continuum contour. The large scale gas kinematics provide additional support for the SNR-MC interaction scenario and suggest that the $V_{LSR} < 77 \text{ km s}^{-1}$ emission observed toward G23.33-0.30 may represent gas that was shock-accelerated as a result of this interaction.

On the other hand, G23.33-0.30's large peak H₂ column density of $N_{H_2} = 1.2 \times 10^{23} \text{ cm}^{-2}$ (Peretto et al. 2016) is similar to that of other high-mass IRDCs, which are thought to be the formation sites of high-mass stars and stellar clusters (Rathborne et al. 2006). Indeed, Figure 5.3 shows that the GMC G23.0-0.4 is coincident with many sources of MIR emission that are likely associated with massive protostars and H II regions. Although the Co-Ordinated Radio 'N' Infrared Survey for High-mass star formation (CORNISH; Hoare et al. 2012) did not detect an H II region

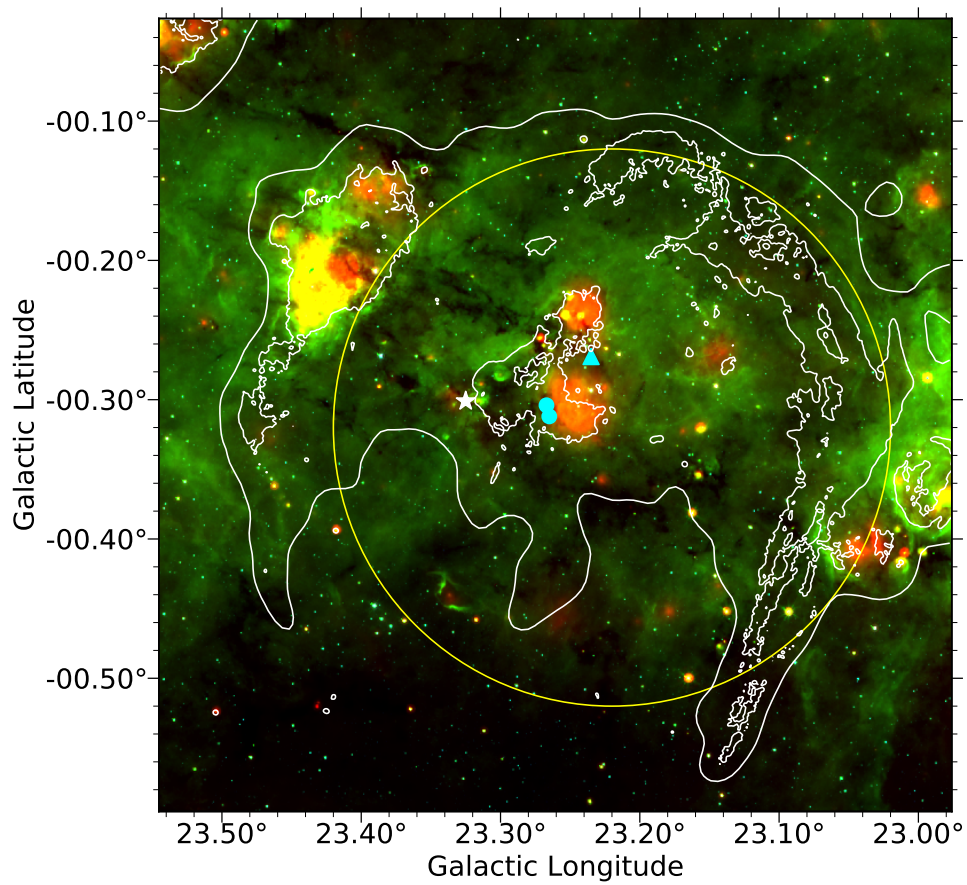


Fig. 5.3 Color shows the MIPSGAL 24 μm (red), GLIMPSE 8 μm (green) and 3.6 μm (blue) MIR data. For reference I show the MAGPIS 20 cm continuum data with contours at 3 mJy beam $^{-1}$, as well as the data overlaid in Figure 5.2.

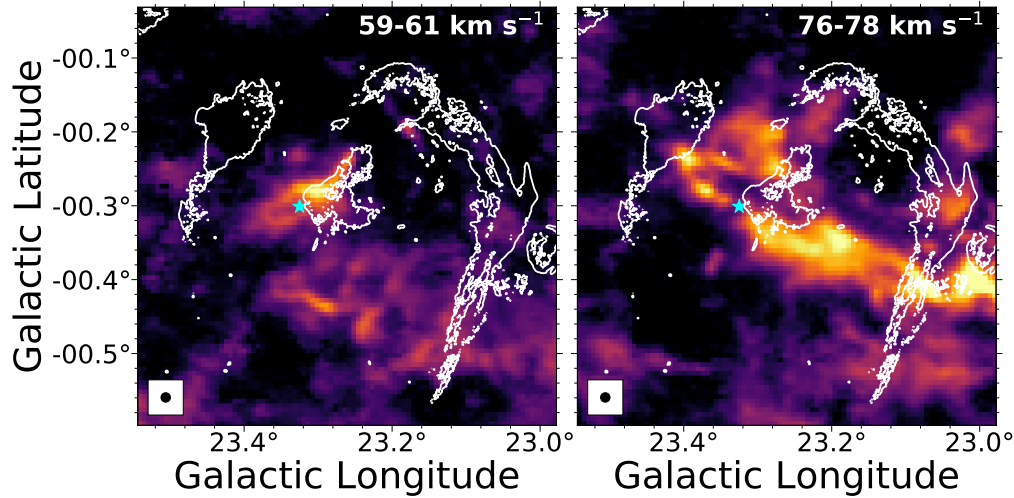


Fig. 5.4 GRS ^{13}CO emission integrated within two velocity ranges. White contours show the MAGPIS 20 cm continuum data at 3 mJy beam^{-1} and the cyan star shows the position of G23.33-0.30. The GRS beam size is shown in black in the lower left corner of each panel. Left: GRS ^{13}CO emission integrated between 59 and 61 km s^{-1} . Right: GRS ^{13}CO emission integrated between 76 and 78 km s^{-1} .

within G23.33-0.30, it could not rule out the presence of a deeply embedded massive protostar.

Considering that $\text{NH}_3(3,3)$ masers can also be excited by massive protostars, the currently available data cannot differentiate between the SNR-MC interaction and massive protostellar outflow scenarios. Consequently, both a SNR-MC interaction and protostellar outflows remain viable explanations for the $\text{NH}_3(3,3)$ maser candidate and G23.33-0.30's unusual kinematics.

New data are necessary to differentiate between these two scenarios. Specifically, I require data that probe the kinematics of dense ($\sim 10^4 \text{ cm}^{-3}$) gas at the $< 0.1 \text{ pc}$ scale. If the $\text{NH}_3(3,3)$ maser candidate and broad line widths are the result of protostellar outflows, then the turbulent line widths and maser emission should be localized to the area surrounding the protostellar core. On the other hand, evidence of extended turbulent line widths and a large-scale velocity gradient, or velocity dis-

continuity, would support the SNR-MC interaction scenario. In addition, transitions from a shock tracing molecule, such as SiO (Caselli et al. 1997), could help differentiate these scenarios by the distribution of shocked gas. SiO emission localized to a protostellar core or its outflow jets would support the outflow scenario, while extended SiO emission would provide additional evidence of a large-scale shock.

To confirm the suspected NH₃(3,3) maser emission, determine its excitation conditions, and investigate the nature of the broad NH₃ line widths, I have performed follow-up observations of G23.33-0.30 that probe the filament at the < 0.1 pc scale. In this Chapter, I describe these data and their analysis, which are also detailed in Hogge et al. (2019). I present Karl G. Jansky Very Large Array (VLA) observations of the NH₃(1,1) through (6,6) inversion lines, Atacama Compact Array (ACA) observations of SiO(5-4), CS(5-4), and 1.3 mm continuum, and Submillimeter Array¹ (SMA) observations of ¹³CO(2-1), C¹⁸O(2-1), and 1.3 mm continuum. In Section 5.2, I describe these observations and the reduction of the data. In Section 5.3, I present the results, in Section 5.4, I analyze the data, in Section 5.5, I discuss the analysis, and in Section 5.6, I provide my conclusions.

5.2 Observations and Data Reduction

I observed G23.33-0.30 using the VLA, operated by the National Radio Astronomy Observatory², the ACA, and the SMA. Table 5.2 provides a summary of the continuum and spectral line data analyzed in this work and Sections 5.2.1, 5.2.2, and 5.2.3 describe the calibration and reduction of these data. I also utilized archival data from several surveys, which are summarized in Table 5.3.

¹The Submillimeter Array is a joint project between the Smithsonian Astrophysical Observatory and the Academia Sinica Institute of Astronomy and Astrophysics, and is funded by the Smithsonian Institution and the Academia Sinica.

²The National Radio Astronomy Observatory (NRAO) is a facility of the National Science Foundation operated under cooperative agreement by Associated Universities, Inc.

Table 5.2. Observations

Telescope	Date	Transition	ν_0 (GHz)	θ_P (arcmin)	$\theta_{maj} \times \theta_{min}$ (arcsec)	ΔV_{BW} (km s $^{-1}$)	ΔV_{chan} (km s $^{-1}$)	σ_{noise} (mJy beam $^{-1}$)
SMA	2016 Jun 20	$^{13}\text{CO}(2-1)$	220.39868	0.8	4.1×2.2	345	0.17	82.5
—	—	$\text{C}^{18}\text{O}(2-1)$	219.56035	0.8	4.1×2.2	173	0.17	92.0
—	—	1.3 mm cont.	...	0.8	4.1×2.2	10435	...	1.1
VLA-A	2016 Oct 7	$\text{NH}_3(3,3)$	23.87013	1.9	0.13×0.09	50	0.39	8.1
VLA-D	2017 Apr 14	$\text{NH}_3(1,1)$	23.69450	1.9	3.8×2.7	51	0.40	1.6
—	—	$\text{NH}_3(2,2)$	23.72263	1.9	3.7×2.7	51	0.39	1.3
—	—	$\text{NH}_3(3,3)$	23.87013	1.9	3.7×2.7	50	0.39	0.6
—	—	$\text{NH}_3(4,4)$	24.13942	1.9	3.4×2.6	50	0.39	1.4
—	—	$\text{NH}_3(5,5)$	24.53299	1.8	3.4×2.6	49	0.38	1.1
—	—	$\text{NH}_3(6,6)$	25.05603	1.8	3.3×2.6	48	0.37	1.6
ACA	2017 Jul 10-13	$\text{SiO}(5-4)$	217.10498	0.8	7.2×4.5	689	0.34	20.2
—	—	1.3 mm cont.	...	0.8	6.6×4.0	5451	...	3.7
—	2017 Jul 8	$\text{CS}(5-4)$	244.93556	0.7	6.0×4.2	261	0.29	22.9
—	—	1.3 mm cont.	...	0.7	6.4×4.1	4984	...	4.3

Note. — ν_0 is the rest frequency of the spectral line, θ_P is the full width at half maximum (FWHM) size of the primary beam, $\theta_{maj} \times \theta_{min}$ is the FWHM size of the synthesized beam, ΔV_{BW} is the spectral bandwidth, and ΔV_{chan} is the spectral resolution.

Table 5.3. Archival Data

Survey	Telescope	Wavelength/Energy	Spatial Resolution	Reference
GLIMPSE	<i>Spitzer</i>	3.6 μm	< 2''	1, 2
GLIMPSE	<i>Spitzer</i>	8 μm	< 2''	1, 2
MIPSGAL	<i>Spitzer</i>	24 μm	6''	3
MAGPIS	VLA	20 cm	5.''4 \times 6.''2	4
VGPS	VLA	21 cm	1' \times 1'	5
GRS	FCRAO 14 m	$^{13}\text{CO}(1-0)$ - 2.7 mm	46''	6
H.E.S.S. Survey of Inner Galaxy	H.E.S.S.	0.1 – 100 TeV	$\sim 0^\circ 1$	7

Note. — References: (1) Benjamin et al. 2003; (2) Churchwell et al. 2009; (3) Carey et al. 2009; (4) Helfand et al. 2006; (5) Stil et al. 2006; (6) Jackson et al. 2006; (7) Aharonian et al. 2006.

5.2.1 VLA Observations

I observed G23.33-0.30 using the VLA in the D-array configuration for a seven hour track. I performed bandpass and flux calibration of the data using observations of J1331+305 (3C286) and I performed phase calibration using periodic observations of J1851+0035. The calibration and imaging of the data were performed using CASA³ 5.1.1-5 and I imaged the data using CASA’s `clean` algorithm with Briggs weighting and the robustness parameter set to 0.5. Because of the complex (l, b, v) structure of the thermal NH₃ emission, the cleaning process left some artifacts. These cleaning artifacts appeared as negative intensity features, but the maximum depth of these features was less than a few times the rms noise. Consequently, the cleaning artifacts did not significantly affect the analysis of these data.

G23.33-0.30 was also recently observed using the VLA in the A-array configuration (Killerby-Smith, private communication), which only detected NH₃(3,3) emission. The A-array observation used the same calibrators as the D-array, but the source used for bandpass and flux calibration was partially resolved by the A-array’s long baselines. Consequently, the fluxes measured from the A-array data are lower limits. The spectral band for the A-array observations was shifted to lower V_{LSR} compared to the D-array, so the D-array observations were able to detect emission up to $V_{LSR} = 90 \text{ km s}^{-1}$, while the A-array observations could only detect emission up to $V_{LSR} = 75 \text{ km s}^{-1}$. The A-array data were also reduced using CASA 5.1.1-5 and were imaged using CASA’s `clean` algorithm with natural weighting.

5.2.2 ACA Observations

I observed G23.33-0.30 with the ACA using three pointings and five 50 min execution blocks in two spectral setups. The first spectral setup was used to ob-

³<https://casa.nrao.edu/>

serve SiO(5-4) and was executed four times and the second spectral setup was used to observe CS(5-4) and was executed once. For both spectral setups, I performed bandpass calibration using observations of J1924-2914 and phase calibration using periodic observations of J1743-0350. For the first spectral setup, I performed flux calibration using observations of J1733-1304 and, for the second spectral setup, I used observations of J1751+0939. The ACA data were calibrated by the ALMA data reduction pipeline and imaged using CASA 4.7.2. I carried out imaging using CASA's `tclean` algorithm with Briggs weighting and the robustness parameter set to 0.5. Like the VLA NH₃ data, the SiO(5-4) and CS(5-4) emission exhibited a complex structure. Consequently, the cleaning of the ACA data also produced negative intensity features with a maximum depth of a few times the noise. Because these features were shallow, the cleaning artifacts did not significantly affect the analysis of these data.

5.2.3 SMA Observations

I observed G23.33-0.30 using the SMA for an eight hour track in the compact configuration. I performed bandpass calibration using observations of 3C454.3, flux calibration using observations of Neptune, and phase calibration using periodic observations of 1743-038. I calibrated the data using MIR⁴, an IDL-based data reduction software package, and converted the calibrated data to MIRIAD⁵ format for imaging using the `mir2miriad` procedure. I imaged the data with MIRIAD 4.3.8 using MIRIAD's `clean` algorithm with Briggs weighting and the robustness parameter set to 1.

⁴<https://www.cfa.harvard.edu/rtdc/SMAdata/process/mir/>

⁵<https://www.atnf.csiro.au/computing/software/miriad/>

5.3 Results

Figure 5.5 shows the $8 \mu\text{m}$ GLIMPSE image of G23.33-0.30 with the VLA NH₃(2,2) integrated intensity overlaid as contours. The thermal NH₃(2,2) emission traces the IRDC filament, while a gap in the $8 \mu\text{m}$ extinction ($l = 23.328^\circ$) corresponds to a local minimum in the NH₃(2,2) emission. The $\sim 3''$ spatial resolution of the D-array resolved the bright, narrow NH₃(3,3) line at $V_{LSR} \sim 56 \text{ km s}^{-1}$ detected by HOPS and RAMPS into two point-like sources, while also revealing another potential maser at $V_{LSR} \sim 76 \text{ km s}^{-1}$, $< 10''$ away from the other two sources. The VLA A-array observations of G23.33-0.30 (Killerby-Smith, private communication) resolved one of the maser candidates detected by the D-array into two sources. The positions of the four maser candidates are shown with symbol markers in Figure 5.5, which also displays the NH₃(2,2) and NH₃(3,3) spectra toward each source. The spectra show that the suspected NH₃(3,3) maser emission is much narrower and brighter than the thermal NH₃(2,2) and (3,3) emission. Three of the maser candidates have velocities near the peak of the narrowest NH₃(2,2) component at 56 km s^{-1} , while the faintest is found near a component peaking at 77 km s^{-1} .

Figure 5.6 illustrates the unusual kinematics in G23.33-0.30. The left panels show the NH₃(2,2), CS(5-4), and SiO(5-4) velocity first moment maps of the filament, with their respective integrated intensity contours overlaid, while the right panels show spectra taken across the width of the filament. The NH₃(2,2) and CS(5-4) data reveal a velocity discontinuity between a broad line component peaking at $V_{LSR} \sim 60 \text{ km s}^{-1}$ that is associated with the left edge of the filament and a narrower component at $V_{LSR} \sim 77 \text{ km s}^{-1}$ that is associated with the right side. The NH₃(2,2) data exhibit an additional narrow velocity component at $V_{LSR} \sim 56 \text{ km s}^{-1}$, peaking near the velocities of three of the maser candidates. The SiO(5-4) emission is extremely broad and peaks primarily at $V_{LSR} < 76 \text{ km s}^{-1}$.

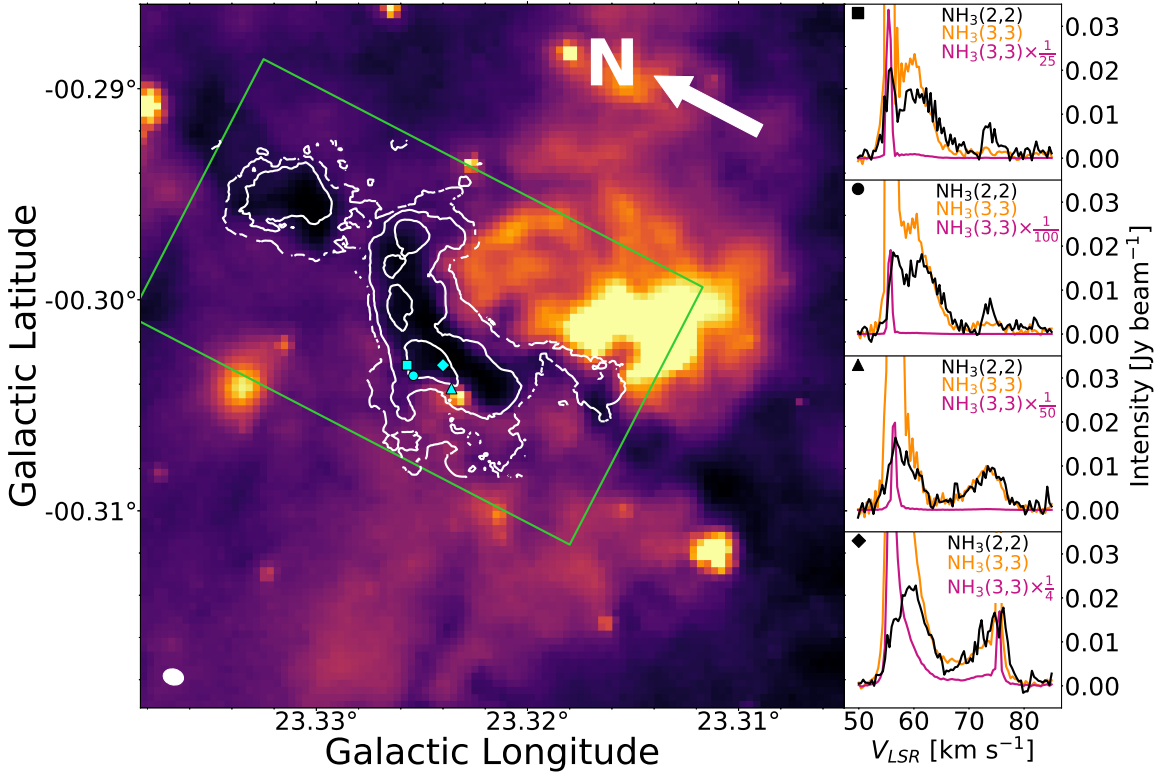


Fig. 5.5 Left: GLIMPSE 8 μm map of G23.33-0.30 with VLA $\text{NH}_3(2,2)$ integrated intensity contours overlaid at 10, 50, and 150 $\text{mJy beam}^{-1} \text{ km s}^{-1}$. The VLA D-array beam is shown in the lower left corner of the map and the arrow in the upper right corner points to the north celestial pole. The green rectangle shows the region used to make the position-velocity diagram in Figure 5.9. The symbol markers indicate the positions of the $\text{NH}_3(3,3)$ maser candidates. The thermal NH_3 emission traces an IRDC filament. Right: VLA D-array $\text{NH}_3(2,2)$ and $(3,3)$ spectra toward the four maser candidates, where the symbol markers in the upper left of each panel correspond to those in the GLIMPSE 8 μm map. The $\text{NH}_3(3,3)$ spectra are presented both at their true amplitude and scaled for comparison.

Due to the ACA's large spectral bandwidth, the ACA observations also detected emission near $V_{\text{LSR}} = 100 \text{ km s}^{-1}$. I do not show this emission in any figures, since it is associated with two background sources unrelated to G23.33-0.30. In addition, the spectra exhibit some regions of consecutive negative channels, which are the result of the cleaning artifacts described in Section 5.2.

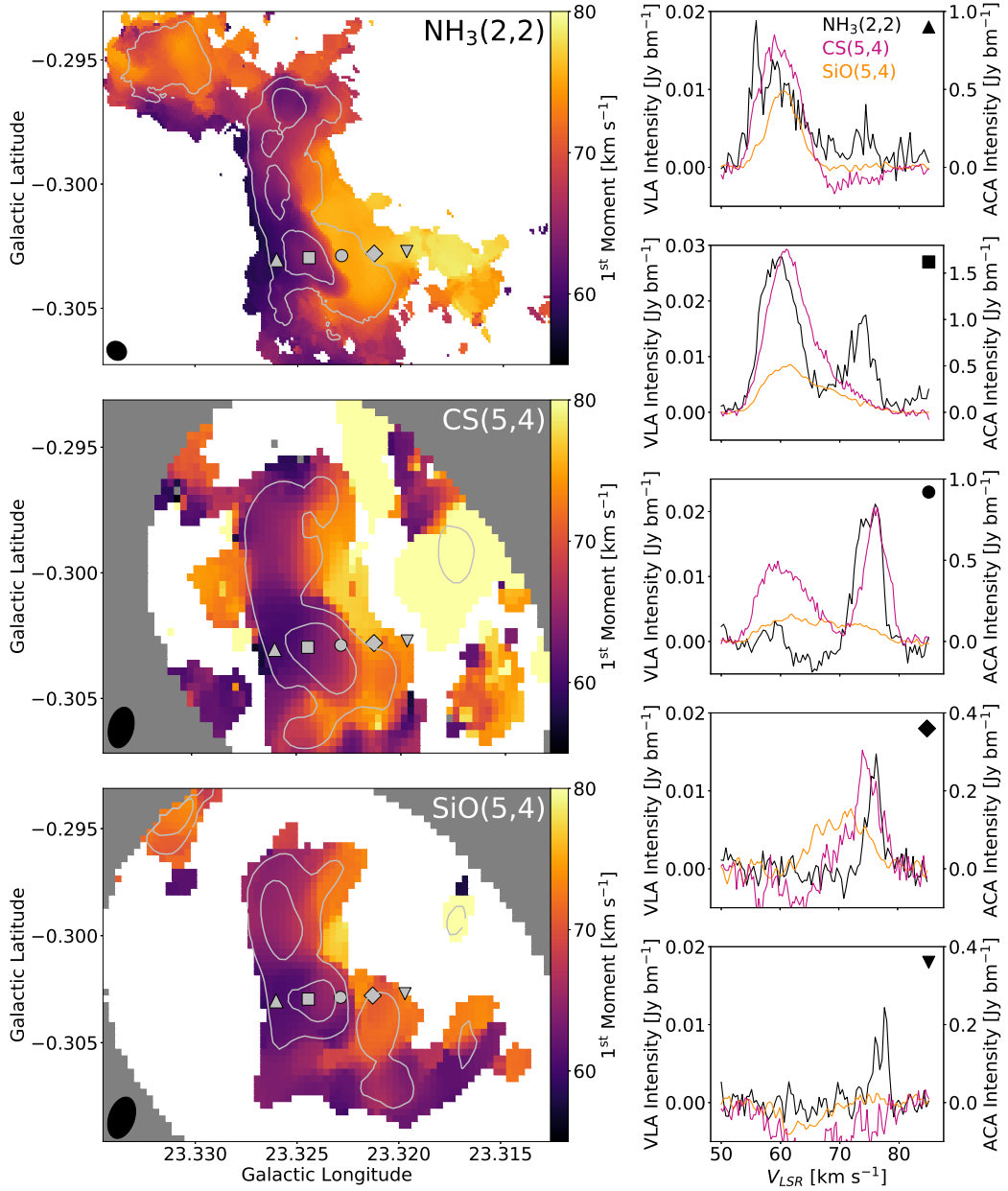


Fig. 5.6 Left: $\text{NH}_3(2,2)$ (top), $\text{CS}(5,4)$ (middle), and $\text{SiO}(5,4)$ (bottom) first moment maps overlaid with integrated intensity (moment 0) contours at 0.05 and 0.15, 2 and 8, and 1 and 4 Jy beam⁻¹ km s⁻¹, respectively. The symbols overlaid correspond to the locations of the spectra to the right. Right: $\text{NH}_3(2,2)$ (black), $\text{CS}(5,4)$ (magenta), and $\text{SiO}(5,4)$ (orange) spectra from the positions indicated by the symbol markers in the left panels. The left axis corresponds to the $\text{NH}_3(2,2)$ spectra, while the right axis corresponds to the $\text{CS}(5,4)$ and $\text{SiO}(5,4)$ spectra.

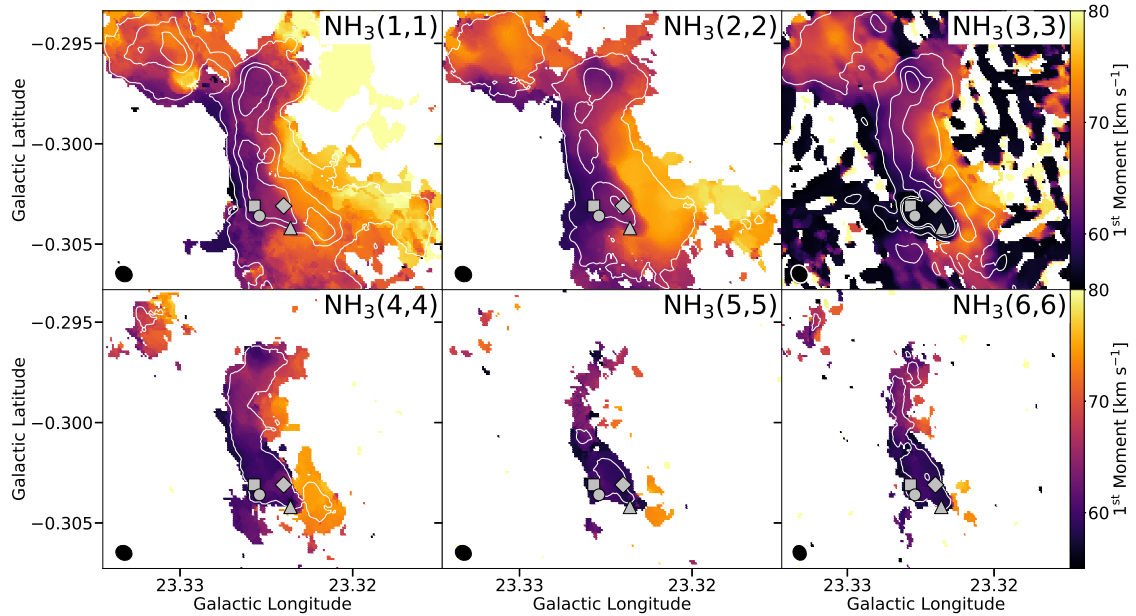


Fig. 5.7 $\text{NH}_3(1,1)$ (top left), $(2,2)$ (top middle), $(3,3)$ (top right), $(4,4)$ (bottom left), $(5,5)$ (bottom middle), and $(6,6)$ (bottom right) first moment maps overlaid with integrated intensity contours at 25 , 150 , and 250 mJy beam $^{-1}$ km s $^{-1}$. The silver symbol markers indicate the positions of the $\text{NH}_3(3,3)$ masers and the synthesized beam for each transition is shown in the lower left of the map.

G23.33-0.30 exhibits bright emission from all of the observed NH_3 inversion transitions. Figure 5.7 displays the $\text{NH}_3(1,1)$ through $(6,6)$ first moment maps with integrated intensity contours overlaid. The linear features in the $\text{NH}_3(3,3)$ map are a result of cleaning artifacts, not real emission. The emission from the higher energy transitions ($\text{NH}_3(4,4)$ through $(6,6)$) is strongest at lower V_{LSR} and displays similarly broad line widths as the 60 km s $^{-1}$ $\text{NH}_3(2,2)$ velocity component. The highest energy transition, $\text{NH}_3(6,6)$, features particularly bright emission compared to $\text{NH}_3(5,5)$, and even displays amplitude ratios of $\text{NH}_3(6,6)/(4,4) > 1$ near the peak of the $\text{NH}_3(6,6)$ emission. In contrast to the $\text{NH}_3(1,1)$ and $(2,2)$ data, the $\text{NH}_3(4,4)$ through $(6,6)$ emission peaks only at $V_{LSR} \leq 76$ km s $^{-1}$ and exhibits a velocity discontinuity between components peaking at $V_{LSR} \sim 59$ and 75 km s $^{-1}$.

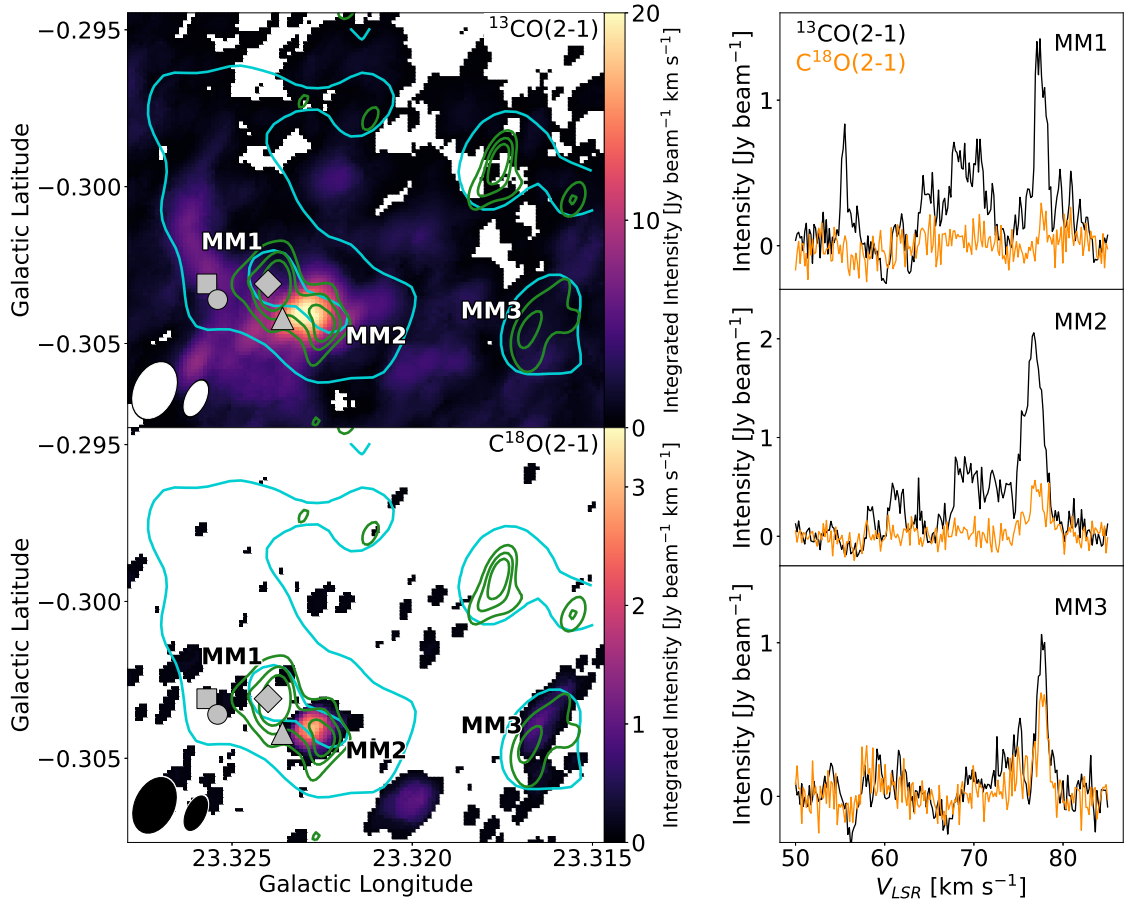


Fig. 5.8 Left: Color shows the SMA ^{13}CO (top) and C^{18}O (bottom) integrated intensity maps. Overlaid are 1.3 mm continuum contours from the ACA (cyan) at 4 and 30 mJy beam $^{-1}$ and the SMA (green) at 3.5, 7, and 10.5 mJy beam $^{-1}$. The lowest contours correspond to a 5σ detection in both cases. The silver symbol markers indicate the positions of the masers. The continuum data reveal three compact cores associated with the filament: MM1, MM2, and MM3. Right: SMA ^{13}CO (black) and C^{18}O (orange) spectra toward MM1, MM2, and MM3. The brightest line in each spectrum peaks at $V_{\text{LSR}} \sim 77$ km s $^{-1}$.

Figure 5.8 shows the SMA $^{13}\text{CO}(2\text{-}1)$, $\text{C}^{18}\text{O}(2\text{-}1)$, 1.3 mm continuum, and ACA 1.3 mm continuum data. Due to the ACA's superb *uv* coverage at shorter baselines, the continuum emission detected by the ACA traces the larger scale filament, while the SMA continuum observations are primarily sensitive to the compact continuum cores. Three of the continuum cores, MM1, MM2, and MM3, lie along the filament. Because the bright mm core west of the filament is coincident with emission near $V_{LSR} = 100 \text{ km s}^{-1}$, it is unlikely to be associated with G23.33-0.30. The SMA $^{13}\text{CO}(2\text{-}1)$ and $\text{C}^{18}\text{O}(2\text{-}1)$ emission peaks close to the location of MM2. The $^{13}\text{CO}(2\text{-}1)$ and $\text{C}^{18}\text{O}(2\text{-}1)$ spectra show that the velocity component at $V_{LSR} \sim 77 \text{ km s}^{-1}$ is brightest toward each of the cores associated with G23.33-0.30. There is also $^{13}\text{CO}(2\text{-}1)$ emission at lower V_{LSR} appearing mainly on the eastern edge of the filament in the range $V_{LSR} = 56 - 70 \text{ km s}^{-1}$.

Figure 5.9 displays the $\text{NH}_3(2,2)$ intensity integrated along lines of constant Right Ascension. Because the filament points roughly north to south, the figure shows the variation of the gas kinematics along G23.33-0.30's length. I have also overplotted the positions and velocities of the $\text{NH}_3(3,3)$ maser candidates and the positions of the continuum sources MM1, MM2, and MM3. While the vast majority of the emission is at $V_{LSR} < 78 \text{ km s}^{-1}$ and displays broad line widths, a small portion of the filament between MM2 and MM3 exhibits narrow line emission peaking at $V_{LSR} \sim 78 \text{ km s}^{-1}$. This narrow line emission corresponds to the southernmost section of the filament detected in $\text{NH}_3(2,2)$, but not $\text{SiO}(5\text{-}4)$. The gas north of this narrow line emission is at lower V_{LSR} and composed of two components: a narrow component at $V_{LSR} \sim 56 \text{ km s}^{-1}$, that is spatially and spectrally coincident with three of the $\text{NH}_3(3,3)$ maser candidates (Fig. 5.5), and a turbulent component peaking in the range $V_{LSR} = 60 - 76 \text{ km s}^{-1}$. The section of the filament associated with the $\text{NH}_3(3,3)$ maser candidate at $V_{LSR} = 76.4 \text{ km s}^{-1}$ is less turbulent and

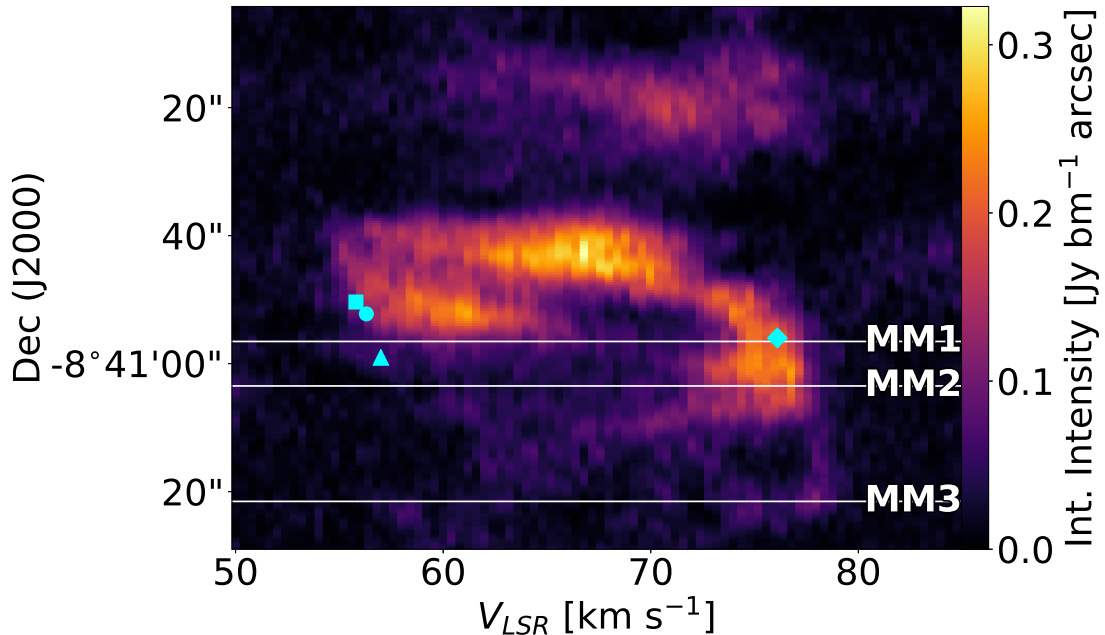


Fig. 5.9 Plot of Declination vs. V_{LSR} made from the $\text{NH}_3(2,2)$ intensity integrated over the Right Ascension axis. The region over which I performed the integration is shown with a green box in Figure 5.5. Because G23.33-0.30 is oriented roughly north to south, this displays the gas kinematics along the filament's length. The cyan symbol markers indicate the positions and velocities of the $\text{NH}_3(3,3)$ masers and the white horizontal lines mark the positions of the molecular cores MM1, MM2, and MM3.

less blueshifted than the northern part of the filament. Figure 5.9 also reveals slight deficits in emission in the range $67 < V_{LSR} < 75 \text{ km s}^{-1}$ at the positions of MM1 and MM2, while the NH_3 emission toward MM3 reveals a velocity discontinuity between components peaking at $V_{LSR} = 74 \text{ km s}^{-1}$ and $V_{LSR} = 78 \text{ km s}^{-1}$.

5.4 Analysis

5.4.1 $\text{NH}_3(3,3)$ Maser Emission

I determined the position and flux of each $\text{NH}_3(3,3)$ maser candidate by first fitting spectra to determine line amplitudes and then fitting these amplitude maps to estimate the positions. I used the Python Markov Chain Monte Carlo (MCMC)

Table 5.4. VLA NH₃(3,3) Maser Properties

	Maser 1	Maser 2	Maser 3	Maser 4
Symbol	○	△	□	◇
Array	A	A	A	D
<i>l</i> (deg)	23.325713	23.325393	23.323564	23.323966
<i>b</i> (deg)	-0.303063	-0.303566	-0.304137	-0.303085
<i>I</i> _ν (Jy)	1.312 ± 0.086	0.562 ± 0.049	0.453 ± 0.033	0.078 ± 0.001
<i>V</i> _{LSR} (km s ⁻¹)	56.319 ± 0.002	57.025 ± 0.007	55.754 ± 0.008	76.375 ± 0.003
σ (km s ⁻¹)	0.254 ± 0.003	0.242 ± 0.007	0.213 ± 0.005	0.187 ± 0.004
<i>T</i> _B (K)	171300 ± 11230	73380 ± 6398	59150 ± 4309	16.7 ± 0.2

fitting package `emcee` (Foreman-Mackey et al. 2013) to fit both the narrow line emission in the data cube and the resulting maps of the line amplitudes. I fit the narrow line emission with a Gaussian model and fit the amplitude maps with a model of the synthesized beam, since maser emission is expected to be unresolved. Table 5.4 presents the A-array fit results for the sources peaking at 56 – 57 km s⁻¹ and the D-array fit results for the source peaking at 76 km s⁻¹, as well as the symbol markers corresponding to each source shown in Figures 5.5, 5.7, 5.8, and 5.9. I list the best-fit values for each source’s Galactic coordinate position (*l, b*), flux (*I*_ν), LSR velocity (*V*_{LSR}), velocity dispersion (σ), and line brightness temperature (*T*_B).

Maser emission occurs in gas with a population inversion, with more molecules in the upper state of a transition than expected in LTE. Population inversions in the NH₃(3,3) transition are a result of collisions with H₂ molecules (Walmsley & Ungerechts 1983). The brightness temperature of a spectral line is given by $T_B = (T_{ex} - T_{bkg})(1 - e^{-\tau_\nu})$, where *T_{ex}* is the transition’s excitation temperature, *T_{bkg}* is the background temperature, and τ_ν is the optical depth at frequency ν . If the molecular transition is in LTE with gas at temperature *T_{gas}* and the background radiation is dominated by the Cosmic Microwave Background (CMB), then

$T_B \leq (T_{gas} - T_{CMB})$. On the other hand, a nonthermal population inversion produces negative values of τ_ν and T_{ex} , resulting in $T_B \gg T_{gas}$.

Given the low temperatures expected in G23.33-0.30 ($T_{gas} \ll 10^4$ K), the three masers detected by the A-array all exhibit $T_B \gg T_{gas}$, confirming their nonthermal nature. Because the source at $V_{LSR} = 76$ km s $^{-1}$ was outside of the velocity range of the A-array data, the D-array data provide the only measurement of its brightness temperature. This source is much fainter than the NH₃(3,3) masers at $V_{LSR} \sim 56-57$ km s $^{-1}$, exhibiting a D-array brightness temperature of only 17 K, which is comparable to temperatures of typical molecular clouds. Although the D-array brightness temperature cannot prove this source's nonthermal origin, it is approximately twice as bright as the peak thermal emission and exhibits a narrow line width, similar to those of the confirmed masers. Moreover, the NH₃(3,3) maser candidate has no corresponding velocity feature in any of the other NH₃ spectra. Consequently, I assume that the emission is nonthermal and will refer to this source as an NH₃(3,3) maser. Thus, G23.33-0.30 hosts four NH₃(3,3) masers: three associated with gas corresponding to the narrow NH₃(2,2) velocity component near 57 km s $^{-1}$, and a fourth associated with the asymmetric line emission peaking at 77 km s $^{-1}$.

5.4.2 Thermal NH₃ Emission

In addition to accelerating gas, shocks can heat and add turbulence to the entrained gas component. Using the NH₃ modeling methods described by Hogge et al. (2018), I employed a PySpecKit (Ginsburg & Mirocha 2011) LTE NH₃ model to investigate whether the gas properties in G23.33-0.30 indicate a shock. I first derived NH₃ rotational temperatures (T_{rot}), velocity dispersions (σ), and LSR velocities (V_{LSR}) from the NH₃(1,1) and (2,2) data cubes. In order to exclude emission that would be too faint to provide accurate derived quantities, I only fit pixels that had NH₃(2,2) integrated intensities greater than 10 mJy beam $^{-1}$ km s $^{-1}$. Figure 5.10

displays maps of the best-fit parameter values for the velocity component with the larger $\text{NH}_3(1,1)$ through $(2,2)$ integrated intensity. The maps are overlaid with the positions of the $\text{NH}_3(3,3)$ masers, which are expected to reside at the locations of shock fronts. Although the presence of broad, overlapping, and asymmetric line shapes did not allow for accurate fit results over the full map, it is clear that the gas at higher V_{LSR} is generally colder and has a lower velocity dispersion than that at lower V_{LSR} . The southernmost section of the filament, which has the largest measured V_{LSR} , was detected in $\text{NH}_3(2,2)$ but not $\text{SiO}(5-4)$. It also corresponds to the region that is coldest and has the lowest velocity dispersion, likely indicating that the gas in this portion of the filament is unshocked and that $V_{LSR} \sim 78 \text{ km s}^{-1}$ is the filament's pre-shock LSR velocity.

While the analysis of the $\text{NH}_3(1,1)$ and $(2,2)$ data implied only moderate heating of the turbulent component ($\Delta T \sim 30 - 40 \text{ K}$), the relatively bright emission from the higher energy transitions $\text{NH}_3(4,4)$ through $(6,6)$ indicates the presence of a hotter component to which the $\text{NH}_3(1,1)$ and $(2,2)$ amplitude ratio is insensitive. Consequently, I also performed fits using all of the observed para- NH_3 lines: $\text{NH}_3(1,1)$, $(2,2)$, $(4,4)$, and $(5,5)$. However, the best-fit models of the para- NH_3 lines often featured $\text{NH}_3(1,1)$ amplitudes that were smaller than those observed in the data and $\text{NH}_3(2,2)$ amplitudes larger than observed in the data. The fact that a single-temperature NH_3 model could not reproduce the para- NH_3 amplitudes suggests that there exists at least two temperature components. Thus, I performed fits using only $\text{NH}_3(4,4)$ and $(5,5)$ to better determine the temperature of the hotter component. The rotational temperatures based only on the $\text{NH}_3(4,4)$ and $(5,5)$ emission are $T_{rot}(4, 4; 5, 5) \sim 40 - 200 \text{ K}$, much higher than those derived from $\text{NH}_3(1,1)$ and $(2,2)$. Thus, the shock has deposited significant thermal ($T_{pre-shock} \sim 10 - 20$

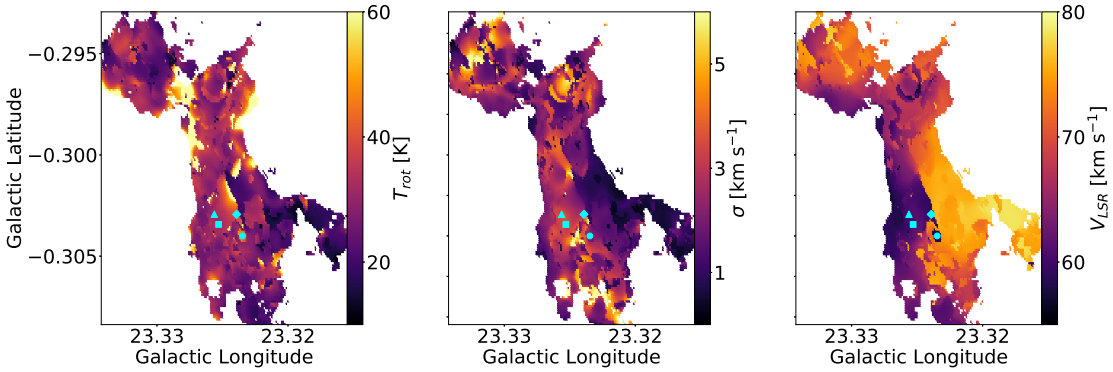


Fig. 5.10 Maps of the NH_3 model best-fit values of T_{rot} , σ , and V_{LSR} with the positions of the $\text{NH}_3(3,3)$ masers overlaid. The gas at the pre-shock velocity is cold and has a low velocity dispersion, while the turbulent component is hot and has $\sigma > 1 \text{ km s}^{-1}$.

K vs. $T_{\text{post-shock}} \sim 40 - 200 \text{ K}$) as well as turbulent ($\sigma_{\text{pre-shock}} < 1 \text{ km s}^{-1}$ vs. $\sigma_{\text{post-shock}} \sim 1 - 5 \text{ km s}^{-1}$) energy into the filament.

5.4.3 Virial Analysis

The SMA observations detected the 1.3 mm dust continuum emission from three compact sources associated with the filament, MM1, MM2, and MM3 (Fig. 5.8), which represent molecular cores embedded within G23.33-0.30. I used an MCMC routine to fit the positions and sizes of the cores. The compact continuum emission from these cores is superposed on more extended emission. Consequently, I modeled the SMA continuum emission as the superposition of two elliptical Gaussians convolved with the SMA synthesized beam and estimated their positions (l, b) and sizes ($R_1 \times R_2$). This analysis implies that MM1 and MM2 are at most barely resolved by the SMA synthesized beam, so their best-fit sizes are upper limits. Table 5.5 lists the fit results.

I performed a virial analysis of the cores to determine their dynamical stability. I determined the core masses (M_{core}), using the following equation from Hildebrand

(1983)

$$M_{core} = \mathbb{R} \frac{F_\nu D^2}{\kappa_\nu B_\nu(T)}, \quad (5.1)$$

where \mathbb{R} is the gas-to-dust mass ratio, F_ν is the source flux integrated within the FWHM boundary of the best-fit elliptical Gaussian, D is the distance to the source, κ_ν is the dust opacity, and $B_\nu(T_{dust})$ is the Planck function at the dust temperature T_{dust} . I assumed $\mathbb{R} = 100$ and $\kappa_{1.3 \text{ mm}} = 0.9 \text{ cm}^2 \text{ g}^{-1}$, which is the opacity expected for dust with thin ice mantles at a number density of 10^6 cm^{-3} (Ossenkopf & Henning 1994). Because the values of \mathbb{R} and $\kappa_{1.3 \text{ mm}}$ are uncertain, I assume a 30% uncertainty on the adopted values. I adopted a distance of $4.59^{+0.38}_{-0.33} \text{ kpc}$, the parallax distance to the high-mass star-forming region G23.01-0.41 that also resides within GMC 23.0-0.4 (Brunthaler et al. 2009). The dust temperature of G23.33-0.30 is in the range of $T_{dust} \sim 16 - 20 \text{ K}$, so I adopted $T_{dust} = 18 \pm 2 \text{ K}$. I measured F_ν within the FWHM boundary of the best-fit models. Next, I determined the virial masses of the cores using the method described in Section 3.2.3 and σ measured from the SMA $^{13}\text{CO}(2-1)$ spectra. Although I have only determined upper limits on the virial parameter for MM1 and MM2 due to the unresolved core radii, the upper limit radii are similar to the expected size of pre-stellar molecular cores (Ward-Thompson et al. 1999). Thus, the true virial parameters are unlikely to be much smaller than the upper limit estimates. My analysis indicates that all of the cores embedded within G23.33-0.30 have $\alpha \sim 1 - 2$, implying that they are all gravitationally bound if the turbulent energy dominates over the magnetic field energy. If magnetic fields are instead comparable to the turbulent energy, then MM2 and MM3 may be gravitationally unbound.

I also investigated the stability of the larger-scale filament by comparing G23.33-0.30's mass to the mass expected for a collapsing filament. I estimated G23.33-0.30's mass using the method described in Section 2.5.1.4.4. I calculated a gas mass of $M \sim 600 \text{ M}_\odot$ for the $\sim 3 \times 0.2 \text{ pc}$ portion of G23.33-0.30 visible in Figure 5.5, which

Table 5.5. Molecular Core Properties

	MM1	MM2	MM3
l (deg)	23.32384 ± 0.00002	23.32254 ± 0.00003	23.31680 ± 0.00003
b (deg)	-0.30314 ± 0.00001	-0.30459 ± 0.00002	-0.30465 ± 0.00002
R_1 (arcsec)	2.3 ± 0.1	2.3 ± 0.2	3.2 ± 0.3
R_2 (arcsec)	< 1.1	< 1.1	1.2 ± 0.1
R (pc)	< 0.036	< 0.035	0.044 ± 0.004
F_ν (mJy)	19.1 ± 0.2	13.9 ± 0.2	13.0 ± 0.3
M (M_\odot)	9.9 ± 4.7	7.2 ± 3.4	6.7 ± 3.2
$\sigma(^{13}\text{CO})$ (km s $^{-1}$)	0.57 ± 0.07	0.76 ± 0.02	0.43 ± 0.03
$\sigma(^{18}\text{O})$ (km s $^{-1}$)	...	0.83 ± 0.09	0.46 ± 0.06
M_{vir} (M_\odot)	< 9	< 17	6.5 ± 0.8
α	< 0.9	< 2.3	1.0 ± 0.5

corresponds to a linear mass density of $M/l \sim 200 M_\odot \text{ pc}^{-1}$. For a typical dense molecular clump (pc size scale), the minimum mass required to form an $8 M_\odot$ star is $\sim 260 M_\odot$ (Sanhueza et al. 2017), assuming a star formation efficiency of 30% and a Kroupa (2001) initial mass function. Although this places G23.33-0.30 in the category of potentially high-mass star-forming filaments, the filament’s highly blueshifted and turbulent gas make this less certain. The critical linear mass density above which a molecular filament is unstable to collapse is given by $(M/l)_{crit} = 466\sigma^2 M_\odot \text{ pc}^{-1}$ (Fiege & Pudritz 2000). Although the velocity dispersion varies throughout G23.33-0.30, a typical value is $\sigma \sim 2 \text{ km s}^{-1}$. This value provides a critical linear mass density of $(M/l)_{crit} \sim 2000 M_\odot \text{ pc}^{-1}$, a factor of ten larger than my estimate of G23.33-0.30’s linear mass density. The filament is not massive enough to collapse and is likely gravitationally unbound unless confined by external pressure.

5.5 Discussion

5.5.1 Evidence of a Large-Scale Shock

Although $\text{NH}_3(3,3)$ maser emission indicates shocked gas, the positions and velocities of the masers alone cannot distinguish between the protostellar outflow and SNR-MC interaction scenarios. On the other hand, the steep velocity gradient along the filament shown in Figure 5.9, which corresponds to an increase in temperature and velocity dispersion, implies a large-scale shock and greatly favors a SNR-MC interaction scenario. Moreover, the $\text{SiO}(5-4)$ emission, which traces shocked gas (Caselli et al. 1997), is extended throughout the filament (Fig. 5.6). While shocks from protostellar outflows could be consistent with the $\text{NH}_3(3,3)$ maser emission, the resulting SiO emission would be confined to narrow outflow jets emanating from the continuum cores. Since protostellar outflows cannot account for such extended SiO emission, it is more likely that a large-scale shock from a SNR is responsible.

Figure 5.11 shows plots of $T_{\text{rot}}(1,1; 2,2)$ and $\sigma(1,1; 2,2)$ vs. V_{LSR} and $T_{\text{rot}}(4,4; 5,5)$ and $\sigma(4,4; 5,5)$ vs. V_{LSR} . The $\text{NH}_3(4,4)$ and $(5,5)$ emission is clearly more sensitive to the hot gas component than the $\text{NH}_3(1,1)$ and $(2,2)$ emission. The plots of $T_{\text{rot}}(1,1; 2,2)$ and $\sigma(1,1; 2,2)$ vs. V_{LSR} show that the gas at the pre-shock velocity ($V_{\text{LSR}} = 77 - 78 \text{ km s}^{-1}$) is generally colder and has a lower velocity dispersion than the turbulent component at lower V_{LSR} , but the correlations among the parameters are not particularly tight. On the other hand, $T_{\text{rot}}(4,4; 5,5)$ and $\sigma(4,4; 5,5)$, which are sensitive to the shocked component, exhibit a more coherent relationship with V_{LSR} . The emission at $V_{\text{LSR}} < 60 \text{ km s}^{-1}$ displays positive correlations among $T_{\text{rot}}(4,4; 5,5)$, $\sigma(4,4; 5,5)$, and V_{LSR} , while the emission at $V_{\text{LSR}} > 60 \text{ km s}^{-1}$ displays negative correlations among these parameters. These trends are likely a signature of the impact that triggered the $\text{NH}_3(3,3)$ maser emission.

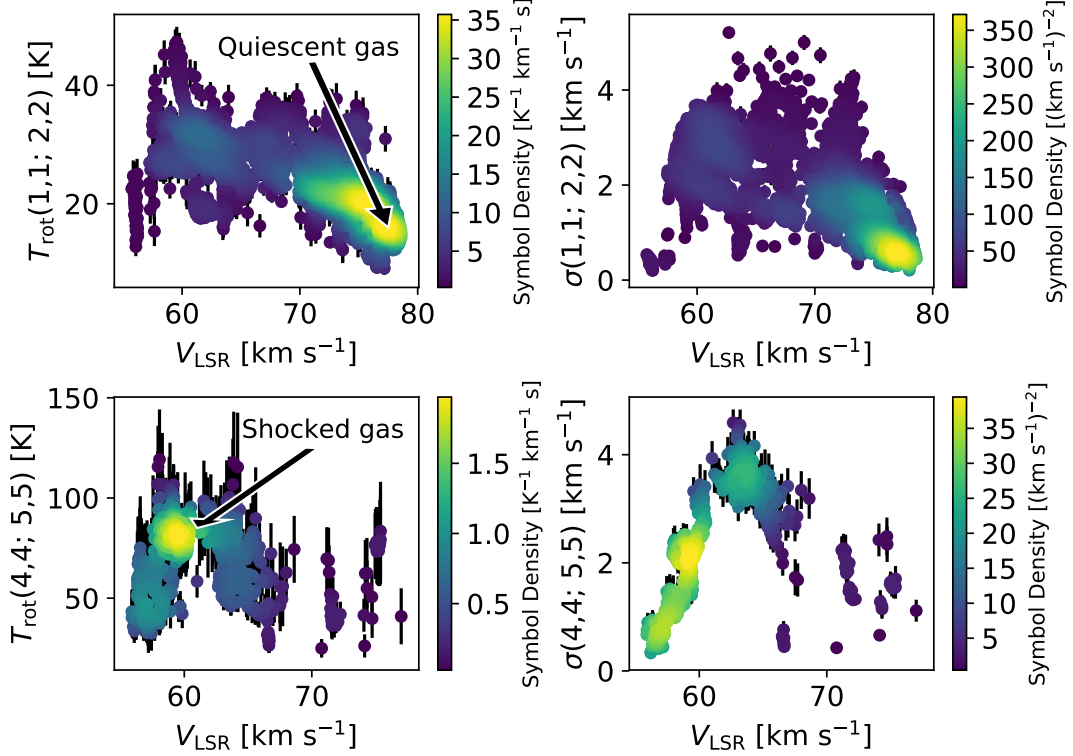


Fig. 5.11 Plots of the NH_3 model best-fit values of T_{rot} and σ vs. V_{LSR} , where the symbol color corresponds to the density of points given by the Gaussian kernel density estimator (KDE). The upper plots display the parameter values derived from the $\text{NH}_3(1,1)$ and $(2,2)$ spectra, while the lower plots show the values derived from the $\text{NH}_3(4,4)$ and $(5,5)$ spectra. I show only the fit results that have parameter errors below the 75th percentile and parameter values that are neither pegged to their maximum nor minimum values.

Figure 5.12 displays a cartoon to illustrate the shock interaction. Upon impacting the filament, the shock accelerates, heats, and adds turbulence to the gas. The velocity, temperature, and velocity dispersion of the pre-shock filament gas is $V_{\text{LSR}} \sim 77 \text{ km s}^{-1}$, $T \sim 10 \text{ K}$, and $\sigma \sim 0.5 \text{ km s}^{-1}$, respectively. The shock heats the gas to $T_{\text{shocked}} \sim 100 \text{ K}$ and increases its turbulent velocity dispersion to $\sigma_{\text{shocked}} \sim 4 \text{ km s}^{-1}$. After the passage of the shock, the gas is able to cool and dissipate its turbulence. Dense gas that is heated by a shock with a relatively low velocity ($V_{\text{shock}} \lesssim 100 \text{ km s}^{-1}$) cools quickly ($t_{\text{cool}} \lesssim 10 \text{ yr}$) (Pan et al. 2012). Turbulence dissipates on the

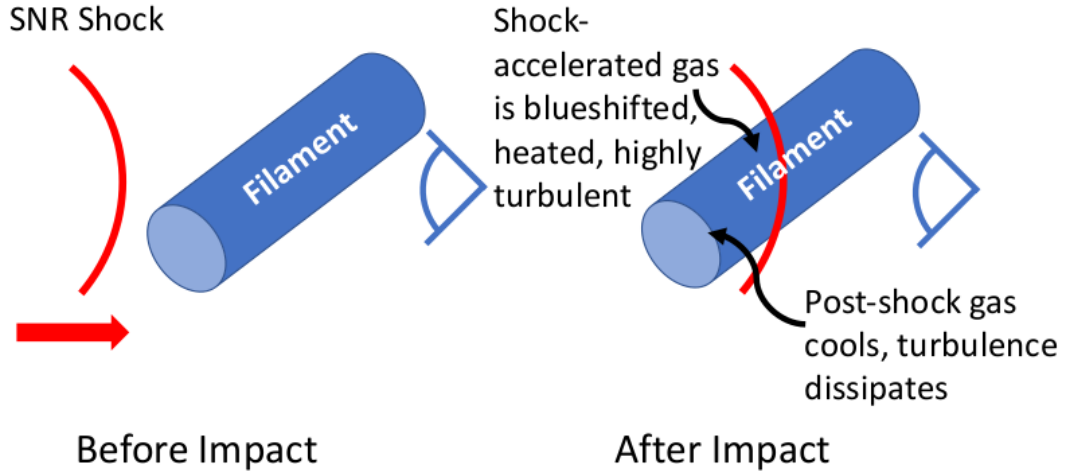


Fig. 5.12 Cartoon of the interaction between the shock wave and the filament G23.33-0.30, with the observer to the right. The shock wave blueshifts, heats, and adds turbulence to the filament gas. After the shock passes, the gas cools and its turbulence dissipates.

order of a crossing time $t_{cross} = \frac{L}{\sigma}$ (Goldreich & Kwan 1974), where L is the length scale of the cloud. The short axis of G23.33-0.30 has a width of $L \sim 0.2$ pc and the maximum post-shock velocity dispersions are $\sigma \sim 4 \text{ km s}^{-1}$, which results in a crossing time of $t_{cross} \sim 4 \times 10^4$ yr. The timescale for the shock to completely pass the filament depends on the orientation of the filament with respect to the plane of the shock, but likely occurs on timescales of $\sim 10^4 - 10^5$ yr. Thus, it is possible for the post-shock gas to cool and dissipate its turbulence before the shock passes the filament completely. This scenario is implied by Figure 5.11, which shows that the most blueshifted gas exhibits temperatures and velocity dispersions that are comparable to those of the quiescent pre-shock gas.

Assuming the maser at $V_{LSR} = 76.4 \text{ km s}^{-1}$ represents genuine nonthermal emission, it likely signals another shock front within the filament. This source is associated with gas at higher V_{LSR} and is much fainter than the other NH₃(3,3) masers. Figure 5.9 suggests that the maser, MM1, and MM2 are all associated with a section of the filament that exhibits values of T_{rot} , σ , and V_{LSR} that are

intermediate between the turbulent component and the pre-shock component. Given that this portion of the filament is situated between a highly shocked region and an unshocked region of the filament, I speculate that it is at an earlier stage of shock interaction than the hot, turbulent component.

The moderate temperature of this intermediate shocked component may in part explain the faintness of the maser at $V_{LSR} = 76.4 \text{ km s}^{-1}$. Figure 5.13 shows a non-LTE RADEX (van der Tak et al. 2007) plot of the expected $\text{NH}_3(3,3)$ optical depth ($\tau_{(3,3)}$) and brightness temperature ($T_B(3,3)$) as a function of the gas kinetic temperature (T_k) and number density (n) for the derived beam-averaged column density ($N_{\text{NH}_3} = 10^{15.5} \text{ cm}^{-2}$) and velocity dispersion ($\sigma = 1.7 \text{ km s}^{-1}$) of the intermediate shocked component. High brightness temperatures and negative optical depths, which indicate strong masering, are only achieved for higher temperatures. At low temperatures, the RADEX model predicts that the gas should either be weakly masering or non-masing. Given the low rotational temperature of the intermediate shocked component ($T_{\text{rot}}(1,1; 2,2) \sim 20 - 25 \text{ K}$), the lower $T_B(3,3)$ of the maser is expected. If the shock continues to heat this section of the filament, it is possible that the maser's brightness temperature will increase.

The large rotational temperatures of the hot, turbulent component demonstrate that the shock has heated the gas in the filament, but the $\text{NH}_3(4,4)$ and $(6,6)$ data also imply dust heating. NH_3 modeling by Faure et al. (2013) suggests that ortho- NH_3 ($K = 3n$) forms preferentially over para- NH_3 ($K \neq 3n$) on the surfaces of cold ($T < 30 \text{ K}$) dust grains. In addition, the ortho- NH_3 ground state is at a lower energy than the para- NH_3 ground state, resulting in a larger amount of energy needed to desorb para- NH_3 than ortho- NH_3 (Umemoto et al. 1999). Consequently, shocks that heat the icy mantles of cold dust grains release ortho-enhanced NH_3 into the gas phase and result in an ortho-to-para abundance ratio (OPR) larger than the

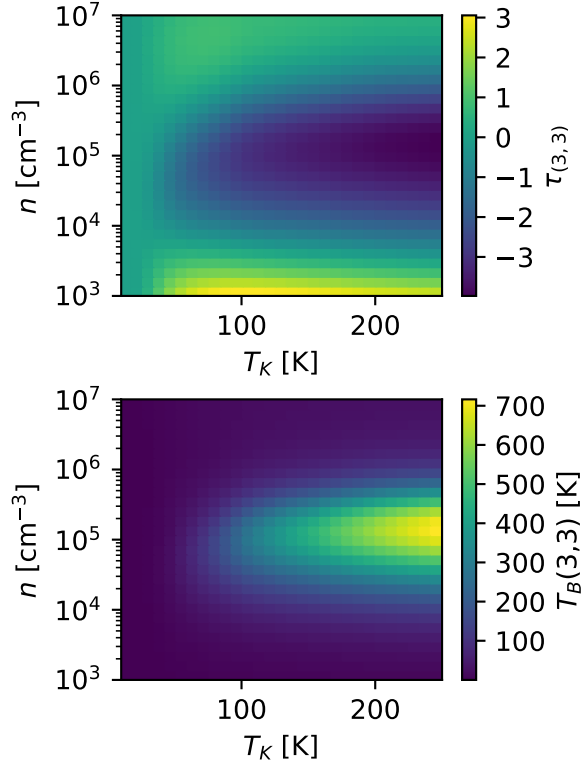


Fig. 5.13 Plot of the RADEX $\text{NH}_3(3,3)$ optical depth ($\tau_{(3,3)}$) (top) and brightness temperature ($T_B(3,3)$) (bottom) as a function of the kinetic temperature (T_k) and number density (n) for a column density of $N = 10^{15.5} \text{ cm}^{-2}$ and a velocity dispersion of $\sigma = 1.7 \text{ km s}^{-1}$.

statistical equilibrium value of $\text{OPR} = 1$. Enhanced OPRs have previously been observed by Umemoto et al. (1999) in the L1157 outflow and by de Wilt et al. (2017) toward SNR-MC interactions.

To confirm the presence of ortho-enhanced gas associated with G23.33-0.30, I fit the $\text{NH}_3(4,4)$ through $(6,6)$ spectra toward the peak of the $\text{NH}_3(6,6)$ emission. I calculated brightness temperature ratios of $\frac{T_B(5,5)}{T_B(4,4)} = 0.57 \pm 0.03$, $\frac{T_B(6,6)}{T_B(5,5)} = 2.71 \pm 0.13$, and $\frac{T_B(6,6)}{T_B(4,4)} = 1.54 \pm 0.06$. Figure 5.14 shows the $\text{NH}_3(4,4)$ through $(6,6)$ brightness temperature ratios predicted by RADEX for a range of temperatures and densities, assuming the column density ($N = 10^{15.5} \text{ cm}^{-2}$) and velocity dispersion ($\sigma = 1.75 \text{ km s}^{-1}$) measured from the $\text{NH}_3(4,4)$ and $(5,5)$ spectra and $\text{OPR} = 1$. The temperatures

and densities corresponding to the measured value of $\frac{T_B(5,5)}{T_B(4,4)}$ are indicated by the white lines overlaid on each plot. If the turbulent gas component had OPR=1, the lines would intersect the measured values of $\frac{T_B(6,6)}{T_B(5,5)}$ and $\frac{T_B(6,6)}{T_B(4,4)}$. However, the measured values for $\frac{T_B(6,6)}{T_B(5,5)}$ and $\frac{T_B(6,6)}{T_B(4,4)}$ correspond to temperatures that are more than double the temperature implied by the measured value of $\frac{T_B(5,5)}{T_B(4,4)}$. This discrepancy suggests that OPR > 1 for the turbulent gas component. Although masing in the NH₃(6,6) transition offers another possible explanation for the large ortho-to-para brightness ratios, the large velocity dispersion of the NH₃(6,6) line ($\sigma \sim 1.5 \text{ km s}^{-1}$) suggests thermal emission. Thus, G23.33-0.30 is associated with ortho-enhanced gas, implying that the shock has heated the filament's cold dust grains and sublimated NH₃ from their icy mantles.

5.5.2 W41's SNR-MC Interaction with GMC G23.0-0.4

Although molecular clouds can experience shocks due to protostellar jets or H II regions, supernova shocks deliver a stronger impulse over a much shorter time span. Supernovae release roughly 10^{51} ergs of energy nearly instantaneously, sending powerful shock waves over tens of parsecs. Despite the fact that only $\sim 5 - 10\%$ of the total energy is converted into kinetic energy in the shock (Walch & Naab 2015), the energy in a supernova shock can be sufficient to disrupt and disperse molecular clouds and cores. Using a simple $E_{\text{shock}} = \frac{1}{2}M_{\text{shocked}}\Delta V^2$ energy transfer analysis, the mass displaced by a SNR shock is approximately given by $M_{\text{shocked}} \sim \frac{2\Omega f_{\text{kin}} E_{SN}}{4\pi \Delta V^2}$, where Ω is the molecular cloud's solid angle at its distance from the supernova, f_{kin} is the kinetic efficiency of the SNR shock, E_{SN} is the total energy of the supernova, and ΔV is the change in velocity of the shocked gas. Assuming that $E_{SN} = 10^{51}$ ergs, $f_{\text{kin}} = 5\%$, $\Delta V = 10 \text{ km s}^{-1}$, and Ω is the solid angle of a spherical cloud with a radius of 0.5 pc radius at 5, 10, or 20 pc away from the supernova, the gas mass displaced by the shock is 130, 35, or 9 M_⊙, respectively.

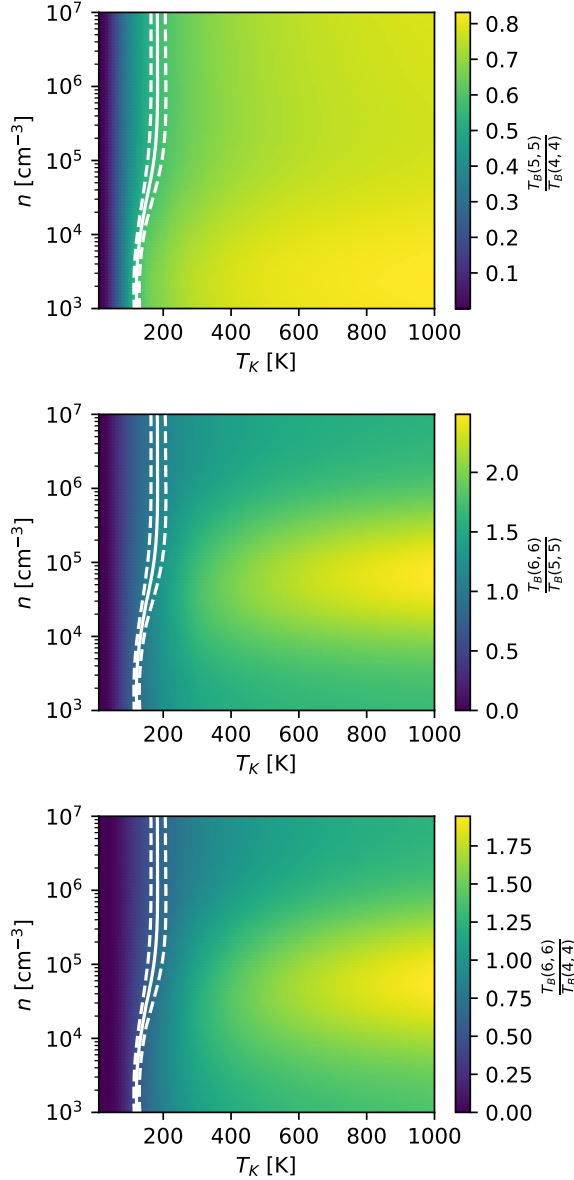


Fig. 5.14 Plot of RADEX brightness temperature ratios as a function of the kinetic temperature (T_k) and number density (n): $\frac{T_B(5,5)}{T_B(4,4)}$ (top), $\frac{T_B(6,6)}{T_B(5,5)}$ (middle), and $\frac{T_B(6,6)}{T_B(4,4)}$ (bottom). I assume a column density of $N = 10^{15.5} \text{ cm}^{-2}$ and a velocity dispersion of $\sigma = 1.75 \text{ km s}^{-1}$. The solid white line in each plot marks the temperatures and densities corresponding to the $\frac{T_B(5,5)}{T_B(4,4)} = 0.570 \pm 0.026$ measured towards the peak of the $\text{NH}_3(6,6)$ emission. The dashed lines mark the $1-\sigma$ uncertainties on the measured amplitude ratio.

Given the uncertainty in the shock properties, the mass in the shocked portion of G23.33-0.30 is comparable to the mass able to be displaced by a SNR shock, implying that a SNR is a plausible source for the shock that is accelerating the molecular filament gas. Considering the suggestions of a SNR-MC interaction between SNR W41 and GMC G23.0-0.4 (Frail et al. 2013), W41 is an attractive progenitor for the large-scale shock impacting G23.33-0.30. A SNR shock would likely supply enough energy to explain G23.33-0.30’s highly blueshifted emission, broad turbulent line widths, and increased temperature and velocity dispersion. Consequently, I speculate that the turbulent, blueshifted gas observed in G23.33-0.30 is the result of a large scale shock originating from the nearby SNR W41.

The VLA NH₃ data revealed three prominent velocity components: a narrow component at $V_{LSR} \sim 56 \text{ km s}^{-1}$ that appears to be associated with three of the NH₃(3,3) masers, a broad, turbulent component at $V_{LSR} \sim 60 \text{ km s}^{-1}$, and an asymmetric line peaked at $V_{LSR} \sim 77 \text{ km s}^{-1}$, which is associated with the NH₃(3,3) maser at $V_{LSR} \sim 76 \text{ km s}^{-1}$. I inspected the ¹³CO data for emission associated with these velocity components and created maps of the integrated intensity in 2 km s⁻¹ windows centered on these velocities. I also found another distinct ¹³CO(1-0) velocity component peaking at 81 – 82 km s⁻¹, which is spatially and spectrally adjacent to the other emission. Figure 5.15 shows the GRS ¹³CO(1-0) data integrated in the velocity ranges indicated in each panel, with the MAGPIS continuum overlaid for comparison. The lower velocity emission centered at 56 and 60 km s⁻¹ displays emission near the positions of W41’s central 20 cm continuum peak and G23.33-0.30. On the other hand, the emission at 77 km s⁻¹ clearly traces GMC G23.0-0.4, but exhibits a conspicuous deficit in emission where W41’s central continuum emission peaks. Finally, the 82 km s⁻¹ component traces a MC, seen as a collection of IRDC filaments

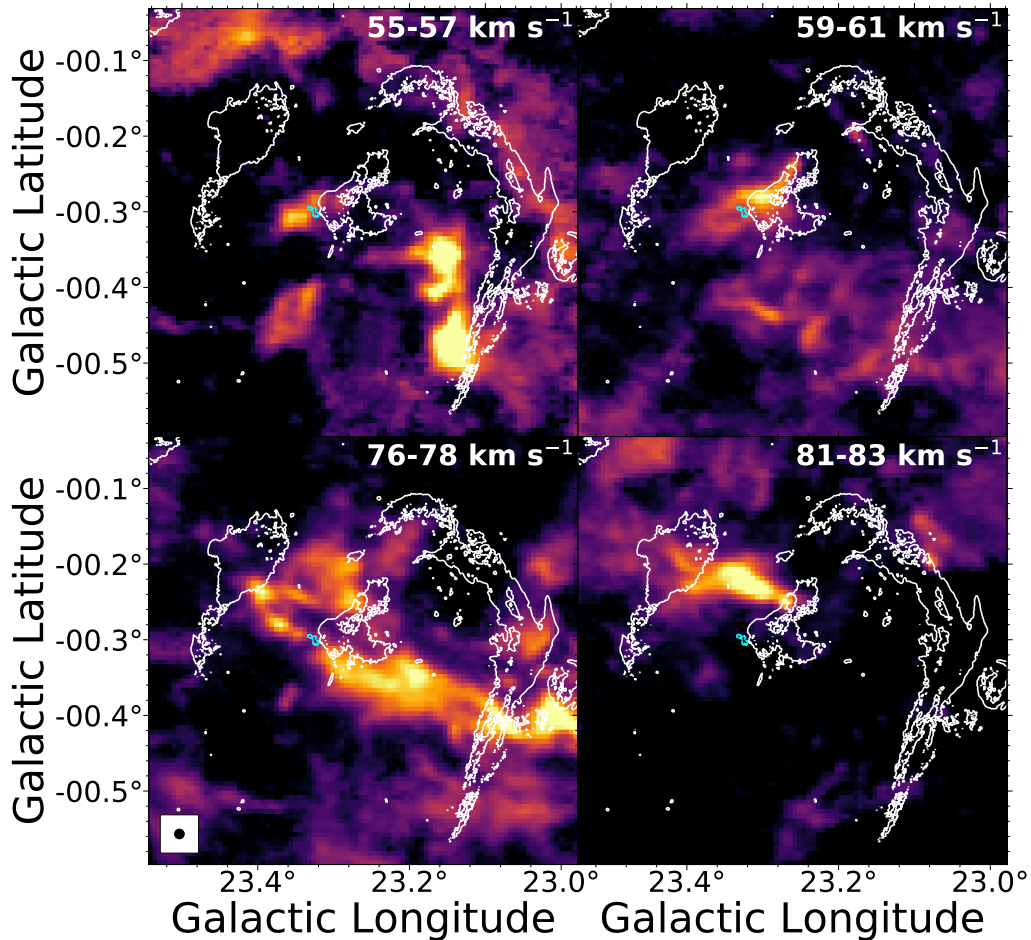


Fig. 5.15 Color shows the GRS $^{13}\text{CO}(1-0)$ integrated intensity over the ranges specified in each panel. I show the MAGPIS 20 cm continuum data with contours at 3 mJy beam $^{-1}$ for reference. The cyan contours show the VLA $\text{NH}_3(2,2)$ integrated intensity data from G23.33-0.30 at 50 mJy beam $^{-1}$ km s $^{-1}$. The GRS beam size is shown in black in the lower left corner of the bottom left panel.

in Figure 5.3, that could represent a background cloud or some other component of the GMC.

Tian et al. (2007) also noted the association between the lower velocity emission, W41's continuum, and HESS J1834-087, but they assumed that the emission represented a separate GMC with which W41 was interacting. If this were true, the emission from GMC G23.0-0.4 would likely be uncorrelated with the central 20 cm

continuum peak, rather than anti-correlated. Moreover, Figure 5.16 shows that the lower velocity emission at 56 and 60 km s⁻¹ and the GMC emission at 77 km s⁻¹ also appear to be anti-correlated. Figure 5.17 displays the ¹³CO intensity integrated over the range 59 – 61 km s⁻¹ plotted against the ¹³CO intensity integrated over the range 76 – 78 km s⁻¹. The panel also shows the Pearson *r* correlation coefficient value, which indicates that the data are strongly anti-correlated. In light of the agreement between the velocities of the 1720 MHz OH maser candidates and the GMC, as well as the apparent anti-correlation between the lower velocity emission and the GMC emission, I argue that these lower velocity components are associated with GMC G23.0-0.4 and the SNR-MC interaction.

Frail et al. (2013) also detected an OH absorption feature at 76 km s⁻¹, which places W41 within or behind G23.0-0.4. In addition, Leahy & Tian (2008) measured a maximum H I absorption velocity of 78 ± 2 km s⁻¹ toward W41, indicating that W41's progenitor may have formed within G23.0-0.4. The Reid et al. (2014) near kinematic distance for $V_{LSR} = 77$ km s⁻¹ toward G23.33-0.30 is $4.41^{+0.27}_{-0.26}$ kpc and the maser parallax distance to the nearby HMSFR G23.01-0.41 is $4.59^{+0.38}_{-0.33}$ kpc (Brunthaler et al. 2009). Considering that the GRS ¹³CO(1-0) data strongly imply that G23.01-0.41 and G23.33-0.30 both reside within GMC G23.0-0.4, I adopted the maser parallax distance for W41. W41's angular size of $\sim 0^\circ 5$ implies that the SNR has a physical diameter of ~ 40 pc. This size is in agreement with estimates from the Sedov relation (Sedov 1959), assuming a reasonable average density (~ 6 cm⁻³) and SNR age ($\sim 2 \times 10^5$ yr) (Tian et al. 2007).

Given that these data are consistent with an interaction between SNR W41 and GMC G23.0-0.4, I further speculate that the ¹³CO(1-0) emission with $V_{LSR} = 60 - 75$ km s⁻¹ (not shown) in the vicinity of the W41's central 20 cm continuum peak represents gas from G23.0-0.4 that has been shock-accelerated to its current velocity.

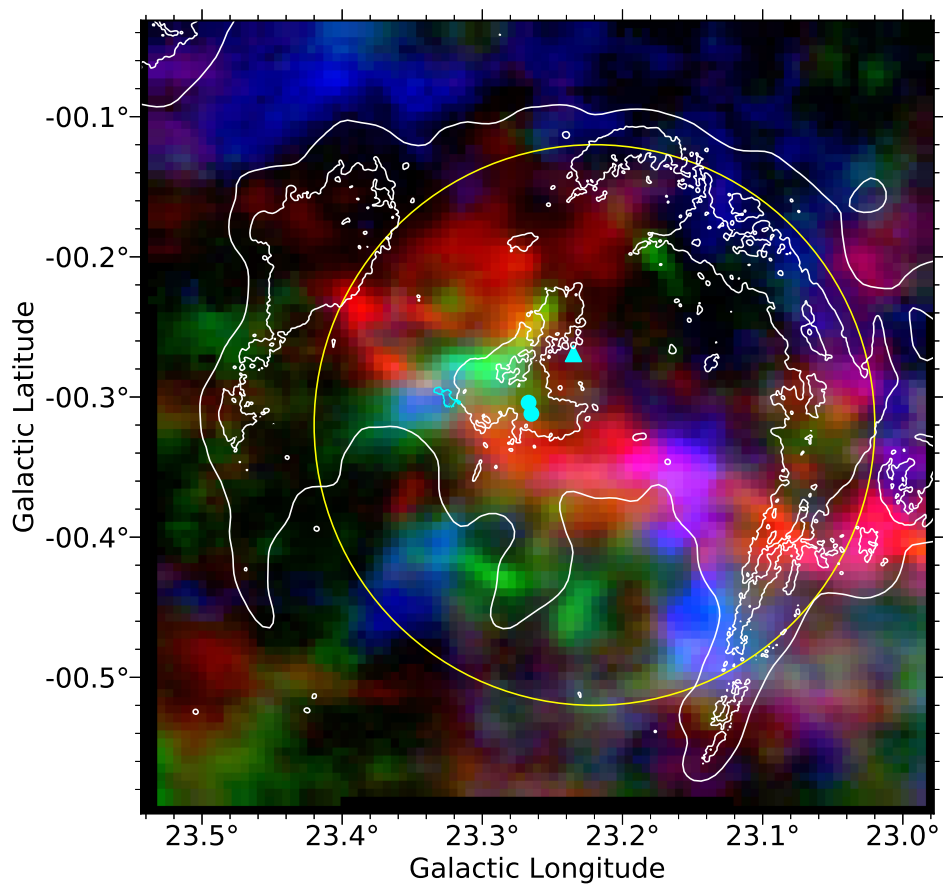


Fig. 5.16 Color shows the GRS ^{13}CO integrated intensity over the range $55 - 57 \text{ km s}^{-1}$ (blue), $59 - 61 \text{ km s}^{-1}$ (green), and $76 - 78 \text{ km s}^{-1}$ (red) for the same sky positions. Symbols and contours as in Figure 5.3.

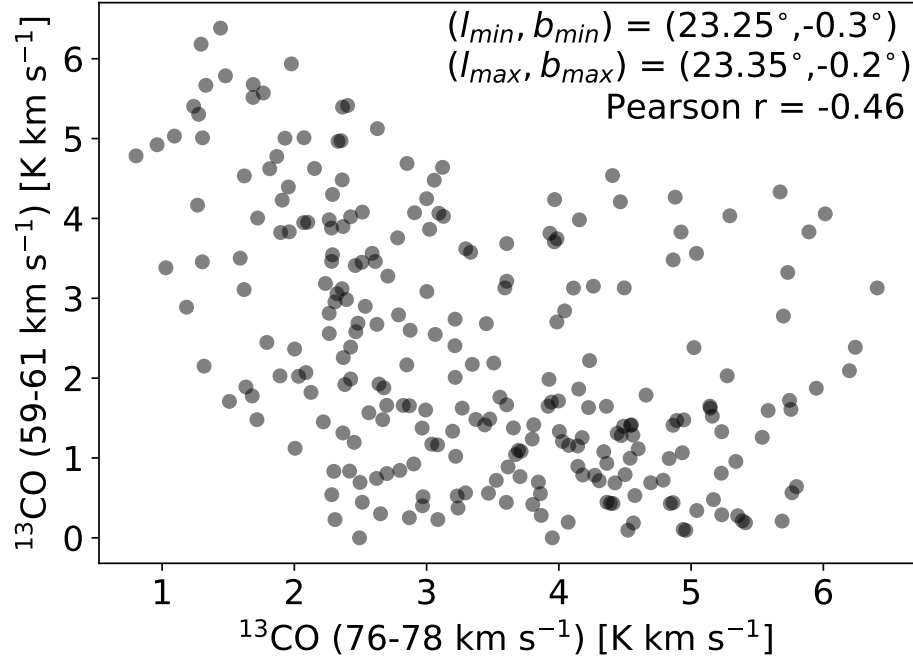


Fig. 5.17 GRS ^{13}CO intensity integrated over the range $59 - 61 \text{ km s}^{-1}$ plotted against the ^{13}CO intensity integrated over the range $76 - 78 \text{ km s}^{-1}$. The Galactic coordinates in the upper right corner indicate the extent of the data and the Pearson r correlation coefficient indicates the data are strongly anti-correlated.

Although CO molecules are dissociated in fast shocks, CO and its isotopologues can survive slower shocks ($v_{\text{shock}} \leq 25 \text{ km s}^{-1}$) impacting dense ($n \sim 10^3 - 10^5 \text{ cm}^{-3}$) gas (Hollenbach & McKee 1980). The $^{13}\text{CO}(1-0)$ component at $V_{\text{LSR}} = 56 \text{ km s}^{-1}$ seems to correspond to the gas component associated with the $\text{NH}_3(3,3)$ masers in G23.33-0.30. This gas component is moving with the largest velocity relative to G23.33-0.30, and may represent the first gas to be stripped from the filament and entrained in the shock front. The existence of unshocked gas within G23.33-0.30, as well as $^{13}\text{CO}(1-0)$ emission at the pre-shock velocity adjacent to the filament, implies that the interaction between SNR W41 and G23.33-0.30 is ongoing. This agrees with my interpretation of the interferometric data, which exhibits emission at $V_{\text{LSR}} = 77 - 78 \text{ km s}^{-1}$ (pre-shock gas), $V_{\text{LSR}} = 60 - 75 \text{ km s}^{-1}$ (turbulent,

shock-heated gas), and $V_{LSR} = 56 - 57 \text{ km s}^{-1}$ (post-shock gas entrained in shock front).

A caveat to this interpretation is that W41 lies near the plane of the Galaxy, so the line of sight towards the SNR is crowded with molecular clouds at various velocities, which could confuse my interpretation of the data. In addition, feedback from previous generations of high-mass stars can accelerate gas and create molecular gas structures that are physically close, but have different V_{LSR} . Thus, it is possible that the molecular gas with $V_{LSR} = 60 - 75 \text{ km s}^{-1}$ is not currently associated with the GMC, but is in fact a remnant of the larger GMC structure that is being impacted by the SNR shock from W41. On the other hand, it is difficult to imagine such a scenario producing the striking anti-correlation between the GMC velocity component and the $V_{LSR} = 60 \text{ km s}^{-1}$ velocity component. A SNR-MC interaction originating from W41 best explains the large turbulent line widths, heating, NH₃(3,3) masers, and blueshifted emission observed in G23.33-0.30.

An alternative explanation for G23.33-0.30's large turbulent line widths is energy added by nearby H II regions. Figure 5.18 shows a zoomed view of the MIR emission toward W41's central continuum peak. The overlaid circles show the positions and sizes of several nearby H II regions and candidate H II regions from the *WISE* Catalog of Galactic H II regions (Anderson et al. 2014). While it is clear that these H II regions cannot account for all of the 20 cm continuum emission toward W41's center, they likely contribute a portion of the emission. The red circles indicate H II regions that have known velocities from radio recombination lines (RRLs): G023.250-00.240 ($V_{LSR} = 76.3 \text{ km s}^{-1}$), G023.265-00.301a ($V_{LSR} = 73.1 \text{ km s}^{-1}$), and G023.295-00.280 ($V_{LSR} = 61.6 \text{ km s}^{-1}$). Although these velocities may indicate an association with the GMC or the 60 km s⁻¹ ¹³CO(1-0) component, it is unlikely that

these sources could account for the significant energy input implied by G23.33-0.30's large turbulent line widths given their angular separation from G23.33-0.30.

The source with the smallest angular separation from G23.33-0.30 is the candidate H II region G023.317-0.300. Although it lacks a reliable velocity from a RRL detection, its position behind G23.33-0.30 makes it an attractive alternative source for G23.33-0.30's turbulence. On the other hand, the interferometric data exhibit broad SiO(5-4) and CS(5-4) line emission peaking at $V_{LSR} = 97 \text{ km s}^{-1}$ near the center of the candidate H II region, potentially signifying its association with the background source HMSFR G23.44-0.18, which has a maser parallax distance of $5.88^{+1.37}_{-0.93} \text{ kpc}$. In addition, the velocity dispersion of G23.33-0.30's turbulent velocity component is $\sigma_{\text{shocked}} = 2 - 5 \text{ km s}^{-1}$, while the velocity dispersions measured towards H II regions in the RAMPS dataset (Hogge et al. 2018) rarely exceed $\sigma \sim 2 \text{ km s}^{-1}$. Thus, an H II region would need to input an unusually large amount of energy into G23.33-0.30 to reproduce the measured velocity dispersion. Furthermore, NH₃(3,3) masers have previously only been associated with SNR-MC interactions (McEwen et al. 2016) or energetic outflows from high-mass protostars (Mangum & Wootten 1994; Kraemer & Jackson 1995; Zhang & Ho 1995), so NH₃(3,3) maser emission resulting from an interaction with an H II region would also be unusual. Consequently, G23.33-0.30's high levels of turbulence are most likely the result of a SNR-MC interaction.

5.5.3 W41's Potential Impact Geometry

Figure 5.15 shows that the diameter of W41's shell is much larger than the radial extent of the GMC. If W41's interaction is ongoing and it exploded within G23.0-0.4, then W41's plane of sky diameter must be larger than its size along the line of sight. Dense molecular gas can slow or even stall the expansion of a SNR shock into a MC (Tatematsu et al. 1987). Given that MCs can exhibit asymmetric density profiles, core-collapse supernovae shell structures evolving in these environments can

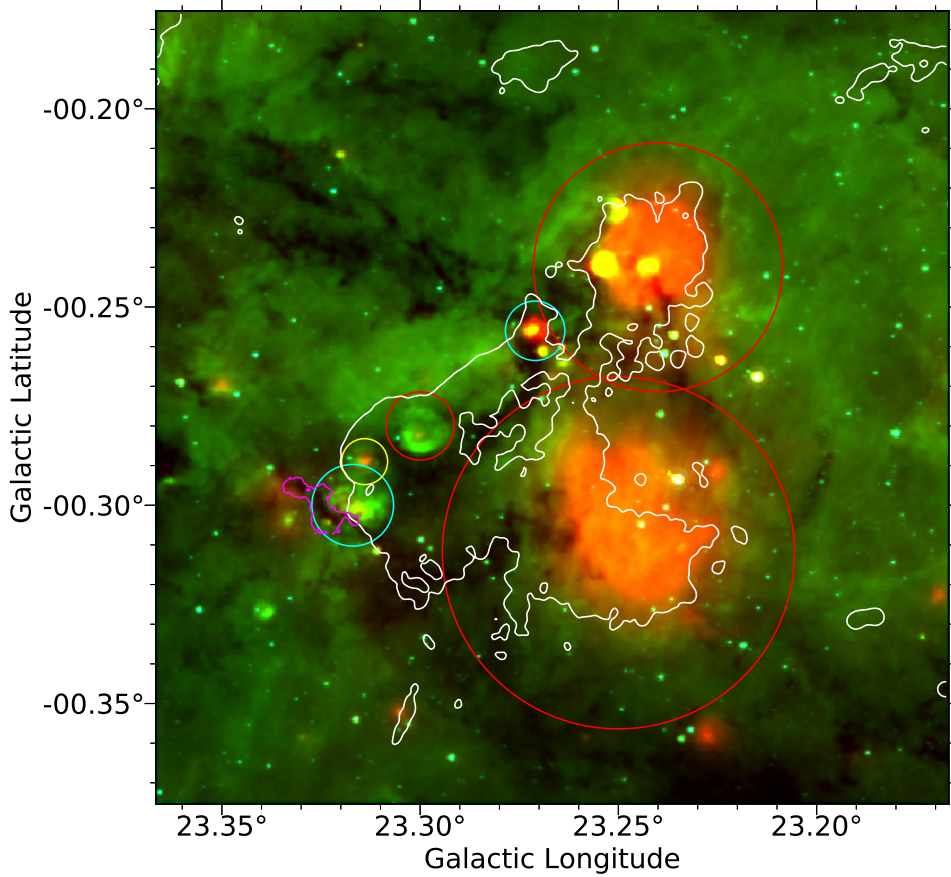


Fig. 5.18 Color shows the MIPSGAL 24 μm (red), GLIMPSE 8 μm (green) and 3.6 μm (blue) MIR data. The MAGPIS 20 cm continuum data are shown with white contours at 3 mJy beam $^{-1}$ and the magenta contours show the VLA NH₃(2,2) integrated intensity data of G23.33-0.30 at 50 mJy beam $^{-1}$ km s $^{-1}$. The circles show the nearby sources from the *WISE* HII Region Catalog. The red circles indicate known HII regions with RRL detections, the cyan circles indicate candidate HII regions that exhibit continue emission but lack RRL detections, and the yellow circle indicates a radio quiet candidate HII region, which exhibits the MIR characteristics of an HII region but lacks radio continuum and RRL emission.

also display asymmetries (Lopez et al. 2009). While this is plausible, W41’s expansion out of a dense, massive GMC would likely sweep up more molecular gas in its shell, whereas this signature is absent in the GRS data. On the other hand, early SNe expansion velocities are extreme ($v_{shock} > 1000 \text{ km s}^{-1}$) and decrease as the SNR expands (Taylor 1950; Sedov 1959). Thus, much of the molecular gas swept up by the fast shock may have been dissociated.

An alternative explanation is that W41’s progenitor formed within a MC ≤ 20 pc away from G23.0-0.4. The 82 km s^{-1} MC shown in Figure 5.15 could potentially be this cloud. The Reid et al. (2014) near kinematic distance for $V_{LSR} = 82 \text{ km s}^{-1}$ is $4.60^{+0.26}_{-0.27} \text{ kpc}$, consistent with the adopted distance to G23.33-0.30. Although Leahy & Tian (2008) measured a maximum H I absorption velocity of $78 \pm 2 \text{ km s}^{-1}$ toward W41, this may not preclude W41 from also being associated with a background MC. If W41 expanded out of this background MC, the shock may have blueshifted much of the foreground molecular gas that was previously associated with the background MC, confusing the interpretation. Hence, the uncertainty in the origin point of W41’s expansion leaves the impact geometry ambiguous.

I have searched for redshifted gas corresponding to the back side of the expanding supernova shell within G23.0-0.4 to help differentiate between these two scenarios. I detected CS emission peaking at $V_{LSR} = 98$ and 103 km s^{-1} and SiO emission peaking at $V_{LSR} = 96 \text{ km s}^{-1}$ near G23.33-0.30, but it is unclear whether this emission is associated with G23.0-0.4 or the interaction. Thus, I examined the GRS ^{13}CO data for signatures of a redshifted component potentially associated with the higher V_{LSR} gas. Although I found emission spanning $V_{LSR} = 93 - 106 \text{ km s}^{-1}$ toward the left half of W41, I am hesitant to associate this emission with the back side of the W41 shell due to the presence of two background sources. One of these background sources is HMSFR G23.44-0.18, which has a maser parallax distance of

$5.88^{+1.37}_{-0.93}$ kpc and $V_{LSR} = 97 \pm 3$ km s $^{-1}$, placing it in the Norma spiral arm near the end of the long bar (Brunthaler et al. 2009; Reid et al. 2014). The second background source is the H II region G23.42-0.21, which seems to contribute much of the continuum emission near W41’s left edge (Fig. 5.3). G23.42-0.21 has a recombination line velocity of 103 km s $^{-1}$ and a maximum H I absorption velocity of 106 km s $^{-1}$; hence, Leahy & Tian (2008) argued that the absorption velocity was significantly higher than the recombination velocity and that G23.42-0.21 must be assigned to the far distance of ~ 9.9 kpc.

Figures 5.19 and 5.20 display two potential interaction geometries: W41 embedded within the GMC and W41 behind the GMC, respectively. The shocked gas in G23.33-0.30 is blueshifted, indicating W41 must be behind G23.33-0.30, but the details of the interaction geometry depend on their positions relative to the GMC. Given G23.33-0.30’s large column density, its apparent position along the spine of G23.0-0.4, and the necessarily high-mass nature of W41’s progenitor, it is plausible that both G23.33-0.30 and W41’s progenitor formed near the dense central regions of their natal MCs. Figure 5.19 shows that if W41 were embedded in G23.0-0.4, then the most blueshifted emission associated with G23.33-0.30 would be found at the northernmost section of the filament. On the other hand, Figure 5.20 suggests that if W41 was behind the GMC, then the most blueshifted emission would occur nearer to the center of the filament.

Although the gas kinematics shown in Figure 5.9 seem to favor the latter scenario, this model is likely too simplistic to account for the complex shock propagation through an inhomogeneous medium. Indeed, neither of these explanations account for the fact that the eastern edge of the filament is more blueshifted than the western edge. If G23.33-0.30 is closer to the edge of the GMC than assumed, the shock could sweep past the bottom edge of the filament more quickly due to the decreased

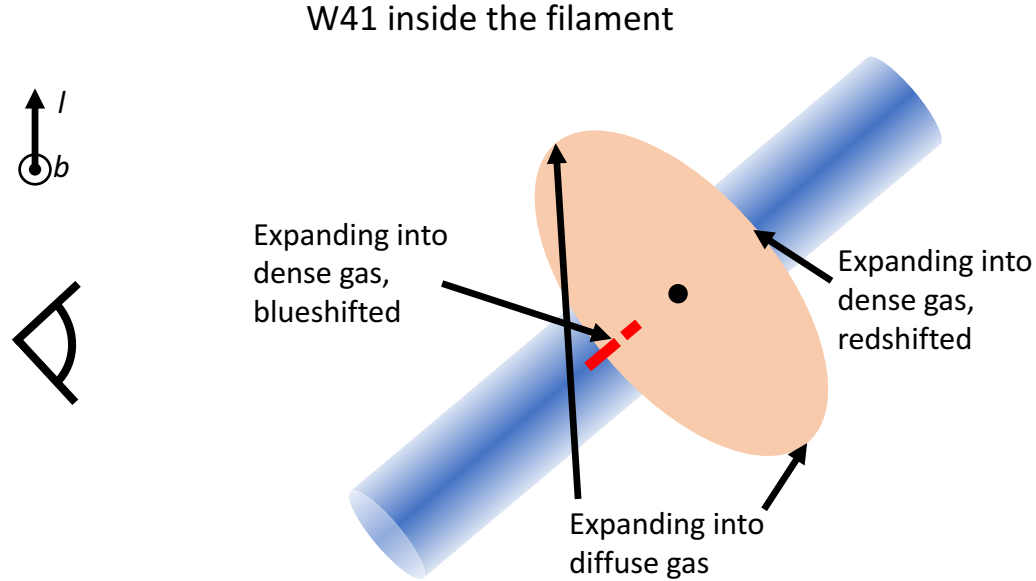


Fig. 5.19 Illustration of top-down view of the scenario in which W41 formed near the center of GMC G23.0-0.4. The figure shows the GMC represented as a blue cylinder, W41's shock bubble as a peach ellipse, G23.33-0.30 as red line segments, and the position of W41's progenitor as a black circle. The filament is rotated in the plane of the Galaxy, such that it roughly matches the orientation of the Reid et al. (2014) Scutum arm, in which the GMC may reside (Brunthaler et al. 2009). Although this model does not depend on the exact orientation of the GMC, some degree of rotation would be required in order to detect blueshifted emission at the location of G23.33-0.30.

density on the outskirts of the GMC. Another alternative is that projection effects are confusing my interpretation of the filament's velocity structure. Regardless of the uncertain impact geometry, W41's association with G23.33-0.30's blueshifted gas component and large velocity dispersions is well founded.

5.5.4 Possible Negative Feedback from SNR W41

Although shocks from supernovae may drive much of the turbulence in the ISM (Padoan et al. 2016), the influence of these shocks on star formation is an open question. Simulations of shock-cloud interactions that include dense substructures demonstrate that the more diffuse molecular gas is efficiently stripped from MCs,

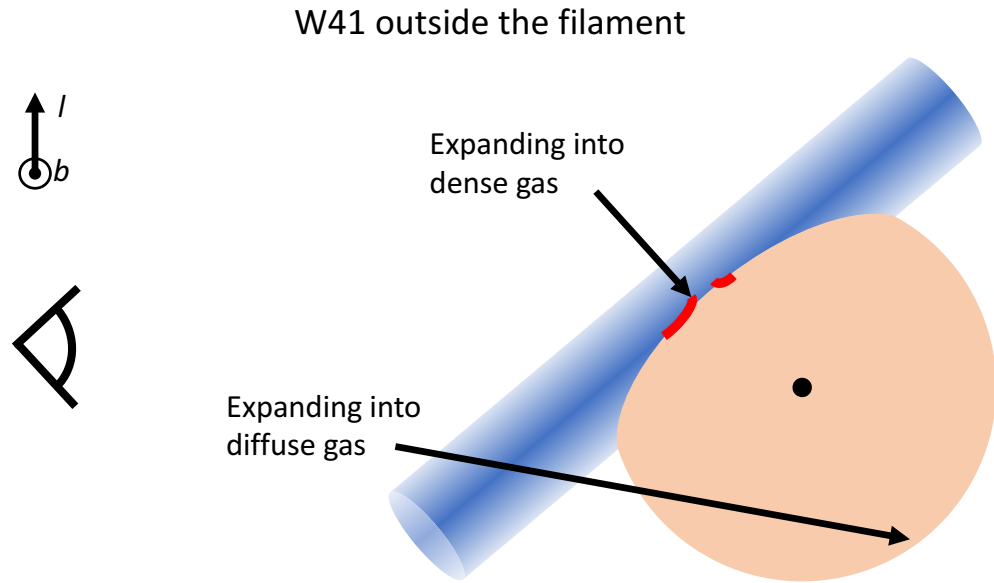


Fig. 5.20 Illustration of top-down view of the scenario in which W41 formed behind GMC G23.0-0.4. The meaning of the shapes is given in the caption of Figure 5.19.

while such an impact forms a bow shock around a sufficiently dense molecular core (Patnaude & Fesen 2005). It is possible that the emission deficits in Figure 5.9 at lower V_{LSR} represent a wake formed behind the cores, which would suggest that some dense gas associated with the cores will remain relatively unperturbed by the passage of the shock.

The virial analysis for the molecular cores suggests that they are gravitationally bound unless the magnetic field energy is comparable to the turbulent energy. On the other hand, the filament's linear mass density is a factor of ten below the critical linear mass density for collapse, suggesting that it may be gravitationally unbound. It is unclear whether the turbulence in the filament will cause it to disperse or dissipate. Magnetohydrodynamical simulations by Seifried et al. (2018) found that MCs that are a moderate distance ($D \sim 25$ pc) from SNe exhibit increased turbulent velocity dispersions by up to a few 1 km s^{-1} , but that the turbulence dissipates within a few 100 kyr. Indeed, the most blueshifted gas in Figure 5.11 exhibits velocity dispersions

comparable to the quiescent gas, implying that turbulence has dissipated from some of the post-shock gas while the shock interaction is ongoing. SNe that are close to a MC likely have a more significant impact on its star-forming potential. Smith et al. (2020) investigated the impact of SNe on star formation using a galactic-scale hydrodynamical simulation. In the first simulation, which they refer to as “potential dominated,” they randomly distributed SNe and found that they did not significantly inhibit further star formation. The second simulation, referred to as the “feedback dominated” case, more realistically clustered SNe within star-forming regions. In this case the clustered feedback from SNe had a substantial impact on further star formation.

The authors more closely investigated two “feedback dominated” and two “potential dominated” star-forming complexes and found that the “feedback dominated” complexes produced shorter, less massive filaments. These filaments also had lower mass to length ratios, half of which were below the critical value for gravitational fragmentation. One of the “feedback dominated” complexes experienced only external SNe, while the second featured four embedded SNe that exploded over 4 Myr. In the case of only external feedback, the filament velocity gradients were similar to, or smaller than, the filaments in the “potential dominated” complexes. On the other hand, the complex with embedded SNe featured filaments with large velocity gradients up to $30 \text{ km s}^{-1} \text{ pc}^{-1}$. The filaments with the largest velocity gradients were rapidly destroyed by shear. G23.33-0.30’s $\sim 20 \text{ km s}^{-1} \text{ pc}^{-1}$ velocity gradient is more consistent with the simulation featuring embedded SNe, which may indicate that W41’s progenitor was embedded within the GMC.

Although G23.33-0.30 has sufficient mass to produce high-mass stars and contains cores that may be gravitationally bound, it is unlikely that the filament will form massive stars. Assuming a $\sim 30\%$ star formation efficiency at the core scale, to

form massive protostars the cores would need to roughly triple their masses, which would require significant accretion from the filament. My analysis of filament kinematics in Chapter 3 suggests that gas flows within filaments may move filament gas onto cores or may form higher density regions that fragment into cores. On the other hand, the extreme turbulence within G23.33-0.30 is abnormal compared to other filaments that I investigated. G23.33-0.30’s mass per length is $\sim \frac{1}{10}$ the critical linear mass density for collapse, implying that the filament is gravitationally unbound. In addition, the large velocity gradient across the filament suggests that the shock is shearing the filament apart. If the shock interaction can strip away much of the filament gas surrounding the cores, the cores can only form low- and intermediate-mass stars. Consequently, W41’s interaction has likely inhibited star formation within G23.33-0.30, and possibly elsewhere in the GMC, by removing a reservoir of gas that could have been accreted by the cores.

5.6 Conclusion

G23.33-0.30 is a massive IRDC filament that exhibits broad molecular line widths and narrow $\text{NH}_3(3,3)$ line emission. I have imaged the filament using the VLA ($\text{NH}_3(1,1)$ through $(6,6)$), the SMA (^{13}CO , C^{18}O , 1.3 mm continuum), and the ACA ($\text{SiO}(5-4)$, $\text{CS}(5-4)$, 1.3 mm continuum) and I have drawn the following conclusions from the data:

1. I have confirmed the nonthermal nature of three $\text{NH}_3(3,3)$ masers that peak near $V_{LSR} = 56 \text{ km s}^{-1}$ and discovered a fourth $\text{NH}_3(3,3)$ maser at $V_{LSR} = 76 \text{ km s}^{-1}$.
2. The ACA observations revealed broad $\text{SiO}(5-4)$ emission throughout the filament, indicating the presence of a highly turbulent and extended shocked gas

component. The widespread nature of the SiO emission indicates a shock acting on scales larger than a protostellar outflow.

3. The NH₃ emission displays a velocity gradient along the length of the filament, with a significant portion of the filament apparently blueshifted by $\sim 10 - 17$ km s⁻¹ with respect to the rest of the filament. G23.33-0.30 also exhibits a velocity discontinuity across the width of the filament, which separates the shocked, turbulent component from the pre-shock component.
4. The LTE NH₃ model fitting has shown that the shocked component is hotter, more turbulent, and blueshifted compared to the pre-shock component. The correlation among T_{rot} , σ , and V_{LSR} implies that the shock is simultaneously accelerating, heating, and injecting turbulent energy into the shocked filament gas. The increased ortho-NH₃ abundance inferred from the large $\frac{T_B(6,6)}{T_B(5,5)}$ and $\frac{T_B(6,6)}{T_B(4,4)}$ brightness temperature ratios also implies dust heating.
5. G23.33-0.30 resides within the GMC G23.0-0.4, which previous authors have speculated is undergoing a SNR-MC interaction with W41. The interferometric data and the GRS ¹³CO data provide additional evidence of this interaction, which suggests that W41's shock is the common cause for the observed gas kinematics on large and small scales.
6. Although W41's impact geometry remains ambiguous, its interaction with G23.33-0.30 and its plane-of-sky diameter imply that it is at a distance of $d \leq 20$ pc from G23.33-0.30. Large-scale simulations suggest that SNe explosions can reduce the star-forming potential of nearby MCs.
7. The SMA 1.3 mm continuum data revealed dust cores embedded within G23.33-0.30. Although G23.33-0.30 appears to have sufficient mass ($M \sim 600 M_{\odot}$) to form a high-mass star, the observed gas kinematics suggest that the filament is

presently being displaced, and potentially dispersed, by the SNR shock. The virial analysis suggests that the cores may be gravitationally bound ($\alpha \sim 1-2$), but the removal of the filament's mass reservoir will likely prevent G23.33-0.30 from forming massive stars. Thus, the data are consistent with negative feedback from the SNR.

Chapter 6

Summary and Conclusions

In this dissertation, I have described the acquisition and analysis of new and archival datasets, which I used to answer some of the open questions in high-mass star formation. In Section 6.1, I summarize each Chapter. In Section 6.2, I address the open questions I sought to answer. In Section 6.3, I conclude my dissertation.

6.1 Chapter Summaries

In Section 6.1.1, I summarize Chapter 1 and restate the open questions addressed by my dissertation. In Section 6.1.2, I summarize Chapter 2. In Section 6.1.3, I summarize Chapter 3. In Section 6.1.4, I summarize Chapter 4. In Section 6.1.5, I summarize Chapter 5.

6.1.1 Chapter 1 Summary

In Chapter 1, I presented several open questions concerning how massive molecular clumps evolve as massive stars evolve within them. For reference, the questions are:

1. *What are the dynamical states of the youngest clumps?* 1.1 Are quiescent clumps in a state of gravitational collapse or are they supported by turbulence? 1.2 Are the velocity gradients observed in molecular filaments reproduced by simulations of gas flowing to dense cores?

2. *How does feedback begin and does it regulate the evolution of molecular clumps?* 2.1 Does protostellar feedback begin with low-mass protostars, prior to the formation of high-mass protostars? 2.2 Does radiative and kinematic feedback from high-mass protostars and massive MS stars change the thermal, chemical, and kinematic properties of their host clumps? 2.3 What are the physical sizes of the regions affected by such feedback?

3. *Can external feedback from SNe influence the evolution of nearby molecular clumps?* 3.1 Can supernova shocks inject turbulence into dense molecular filaments and their embedded cores? 3.2 Can interactions between SNe and dense filaments stimulate or inhibit the future formation of stars?

I described previous observational surveys of high-mass star-forming clumps, primarily focusing on mid-infrared (MIR) and far-infrared (FIR) observations, which trace dust emission and absorption, and radio molecular line observations, which trace the molecular gas that comprises molecular clumps. Despite the advantages offered by previous surveys, their shortcomings necessitate new data to help answer the outlined questions. To answer these questions requires a large sample of clumps at various evolutionary stages with measurements of their gas temperatures, velocity dispersions, and velocities at the ~ 1 pc scale. The Radio Ammonia Mid-Plane Survey (RAMPS) is a molecular line survey designed to provide these data.

6.1.2 Chapter 2 Summary

In Chapter 2, I described the RAMPS observations, the reduction, and the analysis of the $\text{NH}_3(1,1)$, $(2,2)$, and $\text{H}_2\text{O}(6_{1,6} - 5_{2,3})$ molecular line data. I used the NH_3 data to detect 2,680 molecular clumps and derive their gas properties and distances. I used archival FIR data to derive these clumps' dust temperatures, masses, and luminosities. I used archival MIR data to estimate these clumps' evolutionary states. I also analyzed the $\text{H}_2\text{O}(6_{1,6} - 5_{2,3})$ maser line data to detect 707 masers and

I investigated their radiative and kinematic properties, as well as their associated source.

RAMPS improves upon HOPS, the previous large NH₃ and H₂O mapping survey, due to the GBT’s better angular resolution and sensitivity. Thus, the RAMPS data have provided maps of the gas properties of many more clumps resolved at the ~ 1 pc scale and detected more H₂O masers per square degree. In addition, the RAMPS data are more sensitive to quiescent clumps than the submm and mm surveys like ATLASGAL and BGPS. Consequently, the RAMPS data are necessary to answer the open questions outlined above.

6.1.3 Chapter 3 Summary

In Chapter 3, I investigated the early dynamical evolution of molecular clumps and filaments. In particular, I analyzed data from RAMPS and archival datasets to test whether clumps at early stages of their evolution are supported by turbulence against gravitational collapse and whether the velocity gradients observed in molecular filaments are reproduced by hydrodynamical simulations. My virial analysis showed that young clumps are not supported against gravitational collapse by turbulence. Furthermore, magnetic fields can only prevent gravitational collapse if the magnetic energy is much larger than the turbulent energy. Given that I also found the largest blue asymmetry for the quiescent clumps, gravitational collapse motions are present at the earliest stages of high-mass star formation. Finally, my filament analysis showed that nonuniform velocity gradients in molecular filaments are common, but they are not well reproduced by current simulations.

6.1.4 Chapter 4 Summary

In Chapter 4, I tested whether low-mass protostars form first in massive clumps and I determined the size scales over which feedback from massive protostars and

stars heats, adds turbulence to, and alters the chemistry of molecular clumps. I tested whether low-mass protostars reside in massive quiescent clumps by searching for the presence of H₂O masers associated with star formation. Although I found a massive, quiescent clump coincident with a H₂O maser, there is an equal probability of a chance alignment between the maser and clump. Consequently, this question cannot be answered by these data. I determined the size scales over which feedback affects molecular clumps through spatial fitting of the RAMPS gas property maps. I found that massive protostars and stars significantly increase the temperature, velocity dispersion, and NH₃ abundance on scales of 0.3 – 1 pc and 0.3 – 3 pc, respectively.

6.1.5 Chapter 5 Summary

In Chapter 5, I investigated whether supernova feedback alters the gas properties of dense molecular gas and whether it affects star formation. My analysis has shown that the W41 supernova remnant shock has accelerated, heated, and added turbulence to the dense molecular filament G23.33-0.30. Although the molecular cores within G23.33-0.30 may remain gravitationally bound, the filament gas is highly turbulent and gravitationally unbound. Given that the supernova shock is removing gas that may have been accreted by the molecular cores, the shock interaction is inhibiting the formation of massive stars within G23.33-0.30.

6.2 Open Questions

In this Section, I address the three open questions and the related subquestions that I reiterated in Section 6.1.1.

6.2.1 What are the dynamical states of the youngest clumps?

To help answer this broader question, I also sought to answer two more specific questions in Chapter 3: *Are quiescent clumps in a state of gravitational collapse or*

are they supported by turbulence? Are the velocity gradients observed in molecular filaments reproduced by simulations of gas flowing to dense cores?

The virial analysis showed that quiescent clumps are not supported against gravitational collapse by turbulence. Furthermore, the significant blue asymmetry of the quiescent clump population indicates that collapse motions are present. Thus, quiescent clumps are not supported by turbulence, but are in a state of gravitational collapse.

For the kinematics of filaments, the observed filaments display a diverse assortment of nonuniform velocity gradients that are likely explained in part by gas flowing along filaments. Some simulations predict that such gas flows are accreting onto dense cores embedded within filaments. My analysis showed that these simulations do not accurately reproduce the observed velocity gradients along molecular filaments.

From these analyses, the most common dynamical state of the youngest clumps is gravitational collapse. Filamentary gas flows may play some role in accretion onto dense clumps and cores, but simulations must account for the diversity in the observed parsec-scale velocity gradients.

6.2.2 How does feedback begin and does it regulate the evolution of molecular clumps?

To help answer this broader question, I also sought to answer three more specific questions in Chapter 4: *Does protostellar feedback begin with low-mass protostars, prior to the formation of high-mass protostars? Does radiative and kinematic feedback from high-mass protostars and massive main sequence (MS) stars change the thermal, chemical, and kinematic properties of their host clumps? What are the physical sizes of the regions affected by such feedback?*

Although I found one candidate low-mass protostar in a massive molecular clump, a false-positive analysis indicates an equal likelihood that the candidate is not genuine. Thus, my analysis was not able to answer whether protostellar feedback begins with low-mass protostars, prior to the formation of high-mass protostars.

My analysis of the temperature, NH_3 abundance, and velocity dispersion maps showed that feedback from high-mass protostars and massive MS stars does significantly change the thermal, chemical, and kinematic properties of their host clumps. In some cases, the regions affected by such feedback are resolved by the RAMPS observations and have physical size scales of 0.3 – 3 pc.

Although my analysis cannot answer how feedback begins, it shows that protostellar and stellar feedback does regulate the evolution of molecular clumps. In particular, the turbulence injected by high-mass protostars and MS stars provides additional turbulent support, which can slow, or even halt, the gravitational collapse of molecular clumps.

6.2.3 Can external feedback from SNe influence the evolution of nearby molecular clumps?

To help answer this broader question, I also sought to answer two more specific questions in Chapter 5: *Can supernova shocks inject turbulence into dense molecular filaments and their embedded cores? Can interactions between SNe and dense filaments stimulate or inhibit the future formation of stars?*

My analysis of G23.33-0.30's gas properties showed that the shock-accelerated gas is hotter and more turbulent than the pre-shock gas, demonstrating that the supernova shock has injected turbulence into the dense molecular filament. On the other hand, the SMA $^{13}\text{CO}(2-1)$ velocity dispersions toward the molecular cores are similar to the $\text{NH}_3(1,1)$ velocity dispersion of the pre-shock gas, suggesting that the supernova shock has not injected turbulence into the molecular cores.

My analysis of the gravitational stability of the molecular filament and cores suggests that the cores may remain gravitationally bound, but that the filament is gravitationally unbound. Consequently, the removal of potentially accretable gas will inhibit the formation of massive stars within G23.33-0.30.

My analysis proves that external feedback from SNe can influence the evolution of nearby molecular clumps by adding thermal and turbulent energy to the gas. In particular, the turbulence added by supernova shocks may play an important role in dispersing dense gas structures and inhibiting star formation.

6.3 Conclusions

My analysis suggests that high-mass star formation is an extremely dynamic process. At the early evolutionary stages, gravitational collapse and filamentary flows in clumps help determine accretion rates. Once protostars and stars form, their radiative and kinematic feedback begins to change the gas properties of the surrounding gas. Because these sources are often still accreting, such changes could alter their own evolution, as well as the evolution of other nearby accreting sources. Feedback from external sources, such as supernovae, can also impact star formation in molecular clumps by removing potentially accretable gas from these systems, thereby inhibiting the formation of more massive stars.

Thus, high-mass star formation is a highly complex process where the evolution of molecular clumps is affected by large-scale gravitational, turbulent, and magnetic forces, as well as feedback from high-mass protostars, stars, and supernovae. To make further progress, large surveys of massive molecular clumps observed at smaller spatial scales are required to connect the gas properties on large and small scales, as well as provide the statistics necessary to adequately test high-mass star formation theories and simulations.

Appendices

A NH₃ Physics

The NH₃ molecule has a pyramidal symmetric top structure, with the nitrogen atom forming the top of the pyramid and the three hydrogen atoms forming the base. The rotational state of the NH₃ molecule is described by the rotational quantum number J and its projection along the molecular axis K . The dipole selection rules are $\Delta K = 0$ and $\Delta J = 0, \pm 1$, while collisional transitions and much slower radiative transitions (Oka et al. 1971) are allowed that follow $\delta k = \pm 3$ ($K = |k|$) selection rules. The individual spins of the hydrogen atoms also play a role in the NH₃ rotational state, since such collisional and radiative transitions cannot change the spins of the hydrogen atoms. Consequently, two species of NH₃ exist, para-NH₃ ($K \neq 3n$, hydrogen spins unaligned) and ortho-NH₃ ($K = 3n$, hydrogen spins aligned), which cannot mix except on long timescales ($\sim 10^6$ years) (Cheung et al. 1969a).

Because the $\Delta J = 1$ transitions in the far-infrared occur on short timescales (10–10² s), NH₃ in typical interstellar conditions is usually found in the lowest J state ($J = K$) within a given K -ladder (states with the same value of K). Thus, the most commonly observed NH₃ transitions are the $\Delta J = 0, \Delta K = 0$ “inversion transitions,” which result from the splitting of each $K > 0$ rotational state by the potential barrier that impedes the nitrogen nucleus from moving through the plane of the hydrogen atoms to the other side of the molecule. Figure A.1 shows the rotational energy level

diagram from Figure 1 of Ho & Townes (1983), which includes the inversion splitting of the $K > 0$ states.

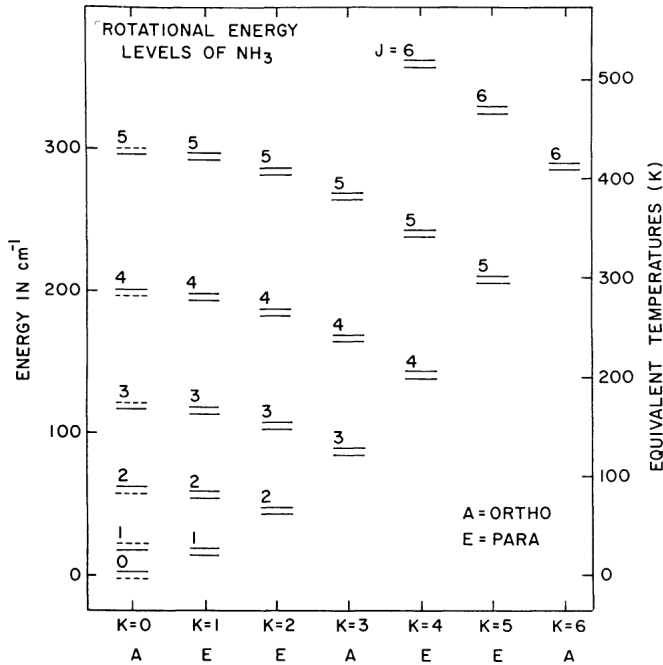


Fig. A.1 The NH_3 rotational energy level diagram from Ho & Townes (1983). Each $K > 0$ state is split into an inversion doublet due to the quantum tunneling of the nitrogen atom through the potential barrier of the hydrogen atoms.

The radiative selection rules for the NH_3 rotational states cause the population levels in each K -ladder to be largely determined by collisions. Consequently, in local thermodynamic equilibrium (LTE) the $J = K$ inversion line amplitudes are sensitive to the gas temperature. Specifically, the line brightness ratios of the various $J = K$ transitions provide the NH_3 rotational temperature (T_{rot}), the temperature at which LTE excitation matches the observed ratio of the rotational level populations. Because the NH_3 inversion transitions are closely spaced in frequency, but have a wide range in energy levels, a single spectral setup can be used to observe multiple lines that are sensitive to different temperature regimes.

On top of the inversion splitting, each state in the inversion doublet is additionally split by both nuclear quadrupole and magnetic hyperfine interactions. The nuclear quadrupole splitting is a result of the interaction between the nitrogen atom's electric quadrupole moment with the electric field of the hydrogen atoms. The nitrogen atom's spin ($I_N = 1$) results in three possible orientations and a three-fold splitting for each state in the inversion doublet. Transitions between these states produce five hyperfine lines, with the central line having the greatest intensity. Further splitting occurs due to the magnetic spin interactions among the hydrogen atoms and the nitrogen atom. The magnetic hyperfine splitting produces 18 hyperfine lines in the $\text{NH}_3(1,1)$ transition, but these are so closely spaced in frequency that they are often at least partially blended together. Thus, most observations of $\text{NH}_3(1,1)$ show only five obvious hyperfine lines.

The hyperfine splitting of the NH_3 inversion lines offers an additional diagnostic advantage. The ratios of the optical depths in the various hyperfine lines are proportional to the ratios of their quantum statistical weights, which are constant and known. Thus, the ratio of the hyperfine lines allows for the calculation of line optical depths (τ) and NH_3 column densities (N_{tot}). The $\text{NH}_3(1,1)$ transition displays particularly bright hyperfine lines, allowing for an accurate measure of the hyperfine amplitudes, and consequently, the $\text{NH}_3(1,1)$ optical depth ($\tau(1,1)_0$).

B Baseline Fitting

Before fitting for a baseline, I attempted to mask any lines present in the spectra, since these would influence the baseline fit if left unmasked. To automate this masking procedure, I masked groups of spectral channels that had a larger-than-average standard deviation, since these channels likely contained spectral lines. For each channel, I calculated the standard deviation of the nearest 40 channels, which I

will refer to as a channel’s “local standard deviation.” I then masked channels that had a local standard deviation larger than 1.5 times the median of the local standard deviations of all channels in the spectrum. Channels with a large local standard deviation were likely the result of a spectral line. On the other hand, a slowly varying baseline shape would result in channels with a local standard deviation closer to the average. This method reliably masked the majority of lines but was prone to miss broad line wings. To mitigate this, I also masked channels that were within 10 channels of a masked channel. Next, I fit spectra for a polynomial baseline of up to second order, where the order is chosen such that the fit results in the smallest reduced χ^2 . I then subtracted the baseline function from the original spectrum and smoothed the baseline-subtracted spectrum as described above.

After subtracting a baseline, I tested the quality of the fit by comparing an estimate of the “true noise” in a spectrum, i.e., the error on a channel value due to random Gaussian noise, to the rms in the line-free regions of the spectrum. These values should be equal for spectra that have no residual baseline shape; otherwise, the observed rms will be larger. To estimate the true noise, I calculated the noise using the average channel-to-channel difference. I refer to the channel-to-channel noise as σ_{diff} , where $\sigma_{\text{diff}} = \sqrt{\frac{1}{2(N-1)} \sum_{i=0}^{N-1} (T_i - T_{i+1})^2}$, where T_i is the brightness temperature of the i^{th} channel and N is the number of channels in a spectrum. While the rms is influenced by both the true noise and any baseline present in the spectrum, σ_{diff} is relatively unaffected by the presence of both a signal and a baseline, as long as they are slowly varying compared to the channel spacing (Rathborne et al. 2016). Thus, if the rms and σ_{diff} of the line-free portion of a spectrum are very different, there is likely a significant residual baseline present.

To test this, I simulated 10^5 synthetic spectra with 15,384 channels, the size of the unsmoothed RAMPS spectra after cropping. The synthetic spectra consisted

of random Gaussian noise with a known standard deviation. I then smoothed and resampled the spectra to match the real data since the H₂O data were smoothed and resampled with a seven-channel filter and the NH₃ data were smoothed and resampled with an 11-channel filter. The resulting spectra had 2,198 and 1,399 independent channels, respectively. Next, I calculated the relative difference (R) between the rms and σ_{diff} , given by $R = 1 - \frac{\sigma_{\text{diff}}}{\text{rms}}$, for each synthetic spectrum. Figure B.1 shows two histograms of the distribution of R corresponding to the different filter widths. The histograms have a mean of $\mu_R \sim 0$ and standard deviations of $\sigma_R \sim 0.01$ or 1%. Thus, σ_{diff} is a reliable estimator of the true rms for Gaussian noise.

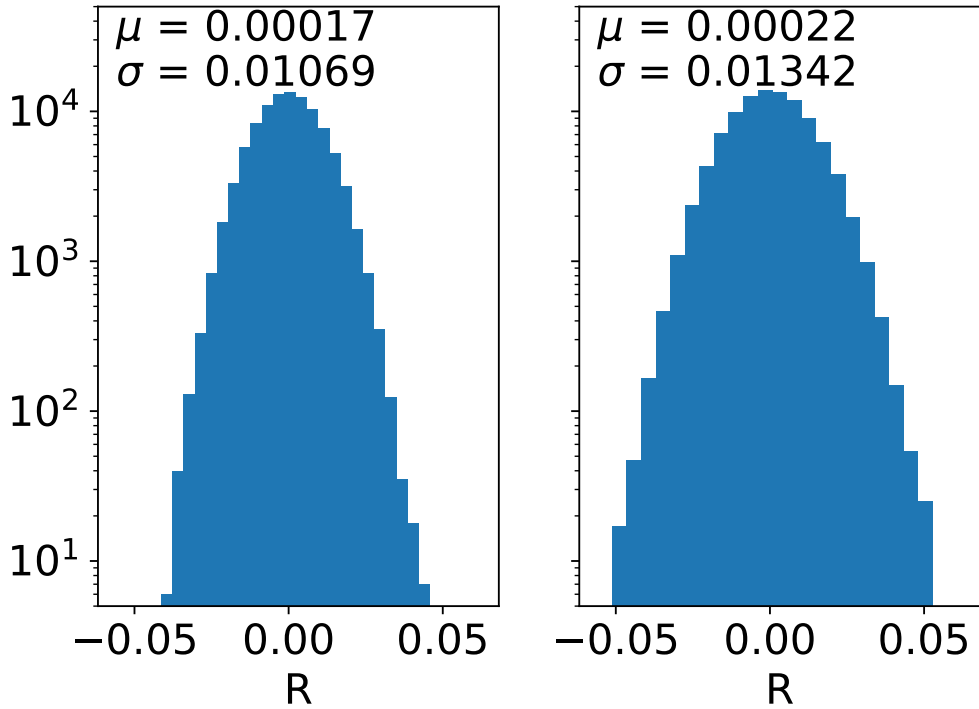


Fig. B.1 Histograms of the relative difference R between the rms and σ_{diff} for 10^5 synthetic spectra of Gaussian noise. Listed in each panel are the mean (μ) and standard deviation (σ) of each distribution. Left: Distribution of R for the synthetic spectra smoothed with a median filter width of seven channels. Right: Distribution of R for the synthetic spectra smoothed with a median filter width of 11 channels.

Next, I added a Gaussian signal to each synthetic spectrum to determine how σ_{diff} changes in the presence of signal. I gave the Gaussian signals uniform random values for both their line widths and S/Ns, where the line widths ranged from 0 to 10 channels and the S/Ns ranged from 0 to 100. For each synthetic spectrum of noise plus signal, I calculated R and binned the values as a function of the amplitude and standard deviation of the synthetic signal, which is shown in Figure B.2. As can be seen from Figure B.2, R remains small unless the signals have large signal-to-noise ratios and very narrow line widths. RAMPS NH₃ data have S/N < 100 and $\sigma > 1$ channel, so σ_{diff} is a reliable estimate of the noise when NH₃ signal is present. On the other hand, H₂O masers in the RAMPS dataset can have S/N > 1000 and line widths of $\sigma \sim 2$ channels, which adds a large source of error to σ_{diff} . Hence, bright, narrow lines must be masked in order for σ_{diff} to accurately represent the true noise in a spectrum.

Because bright lines add error to this estimate of the true noise, I masked each spectrum before comparing the rms to σ_{diff} . As a first estimate of the true noise, I calculated σ_{diff} for the unmasked spectrum. I then masked channels with an intensity greater than $3\sigma_{\text{diff}}$, as well as channels that were within 10 channels of a masked channel. Because bright H₂O masers add a large source of error to σ_{diff} , I also measured σ_{diff} for the masked spectrum, which does not include very bright lines. I then used this more accurate measurement of σ_{diff} to perform another round of masking channels with an intensity greater than $3\sigma_{\text{diff}}$, as well as channels that were within 10 channels of a masked channel. I then calculated R for this masked spectrum and used this value of R as a measure of the quality of the baseline fit. I also recorded the rms of the spectra, which I used as my estimate of the noise for later analysis.

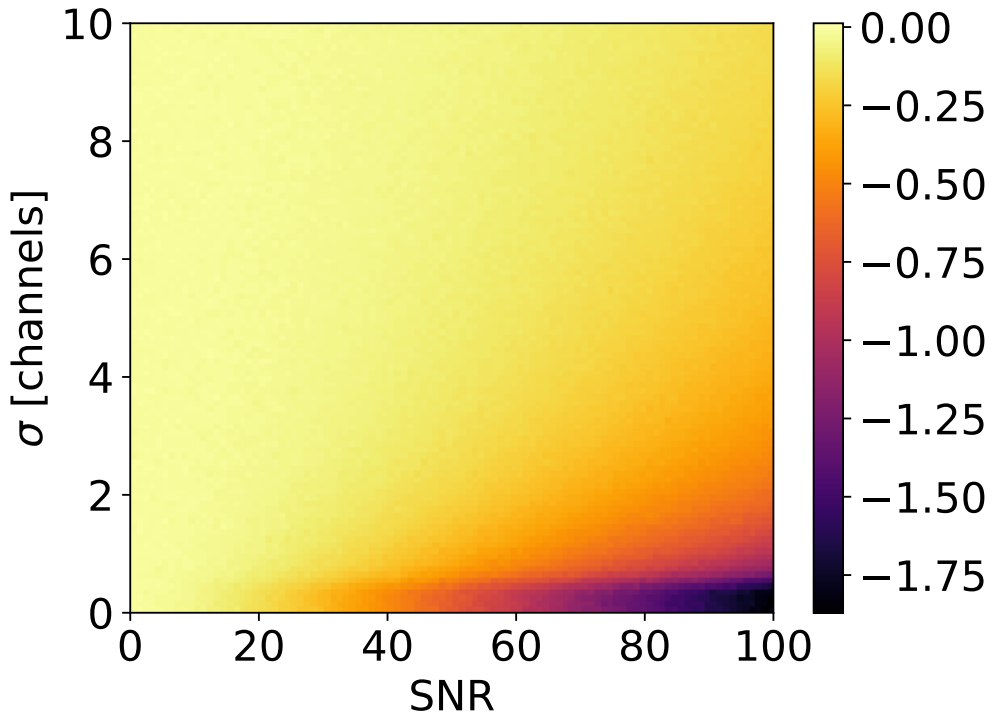


Fig. B.2 Color corresponds to the relative difference R between the rms and σ_{diff} for 10^5 synthetic spectra with Gaussian signals of varying width and amplitude. R values are binned according to the dispersion of the signal σ and the S/N to show the effect on σ_{diff} caused by the presence of signal.

Figure B.3 shows a few examples of RAMPS $\text{NH}_3(1,1)$ spectra and their associated values of R , which demonstrates that a poor baseline fit generally results in a larger value of R . A poor baseline fit can occur for spectra in which the spectral mask did not exclude all of the signal, as well as for spectra with a baseline shape more complicated than a second order polynomial. While the spectral mask was reliable for the majority of NH_3 lines in the RAMPS dataset, some lines were broader than typical NH_3 lines and were not well masked. To better fit spectra of this class, I attempted a second fit on spectra with $R > 3\sigma_R$ using a slightly different mask. To mask broader lines more effectively, I employed the same masking technique as

for the initial fit, but this time used a 120-channel, rather than 40-channel, window to calculate the array of local standard deviations. Due to the larger window size, this mask was more sensitive to broader spectral features, and so it more successfully masked broad lines. I performed another baseline fit using this masked spectrum and once again calculated R . If the spectrum is well fit by the second fit, R will likely be low, but if there is a residual baseline shape more complicated than second order, R will still be large. Low-amplitude signal that was not well masked may also increase the measured value of R . In either case, a poor fit has the potential to alter line amplitude ratios, which would change the parameter values calculated from future fits to the data. To mitigate this potential problem, if a spectrum had $R > 3\sigma_R$ after the second fit, I performed a third, more conservative fit. I used the mask from the second fit and forced a zeroth-order baseline fit, which is less likely to drastically change the line amplitude ratios.

In Figure B.4, I show histograms of R for all of the baseline fits of the NH₃(1,1), NH₃(2,2), and H₂O spectra. The distributions show a Gaussian component centered at $R \sim 0$, with long, shallow tails out to larger values of R . The Gaussian portions of each distribution match well the distributions found for synthetic Gaussian noise. The long tails in the distributions represent the poor baseline fits that were fit with a zeroth-order baseline. The vertical magenta line corresponds to $R = 3\sigma_R$, which shows the approximate threshold between good and bad baselines expected from the analysis of the synthetic data. Significantly bad baselines are rare in this dataset, with the percent of spectra with $R > 3\sigma_R$ for the NH₃(1,1), NH₃(2,2), and H₂O data equal to 3.5%, 2.1%, and 1.7%, respectively.

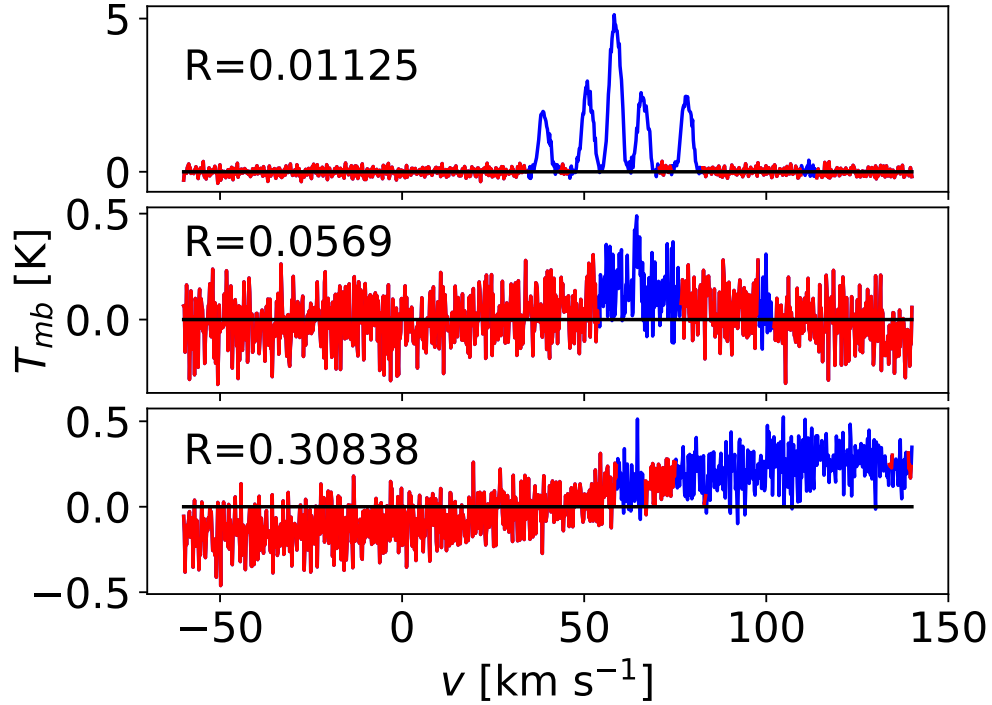


Fig. B.3 Examples of RAMPs $\text{NH}_3(1,1)$ spectra and their associated values of R . Masked channels are shown in blue, unmasked channels in red, and a fiducial line is set at $T_{mb} = 0$ K.

C Noise Maps

Figures C.1–C.10 show the $\text{NH}_3(1,1)$ noise maps not shown in Section 2.4. Figures C.11–C.21 and Figures C.22–C.31 show the $\text{NH}_3(2,2)$ and H_2O noise maps, respectively, for the full survey.

D Integrated Intensity Maps

Figures D.1–D.10 show the $\text{NH}_3(1,1)$ integrated intensity maps not shown in Section 2.4. Figures D.11–D.20 show the $\text{NH}_3(2,2)$ integrated intensity maps for all fields with detectable $\text{NH}_3(2,2)$ emission. I did not display the $\text{NH}_3(2,2)$ integrated

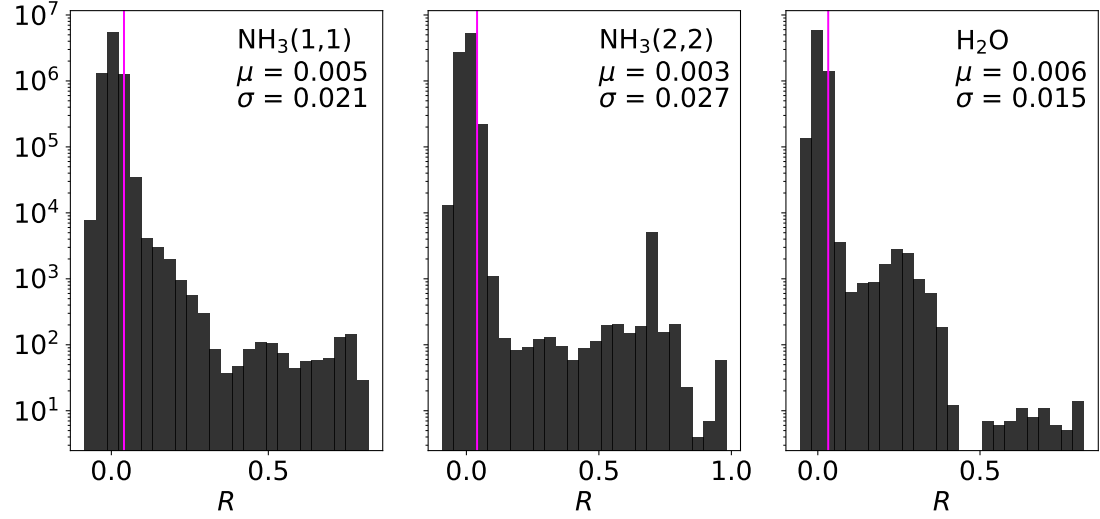


Fig. B.4 Histograms of R for all RAMPS $\text{NH}_3(1,1)$, $\text{NH}_3(2,2)$, and H_2O spectra, separated by line. The magenta lines show the $R = 3\sigma_R$ threshold used to restrict the complexity of the baseline fits.

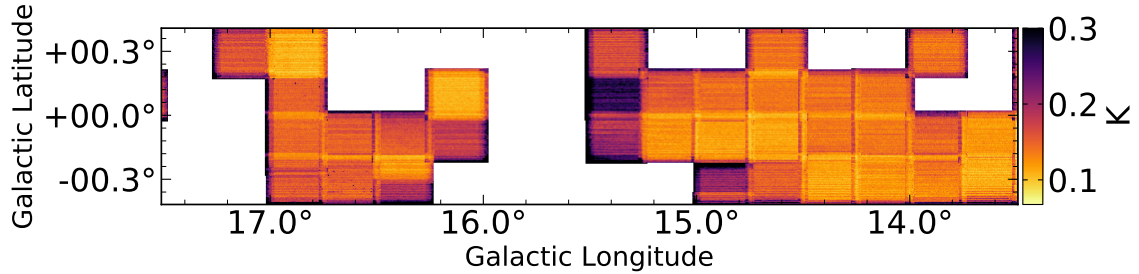


Fig. C.1 $\text{NH}_3(1,1)$ rms noise map for fields L14 through L17.

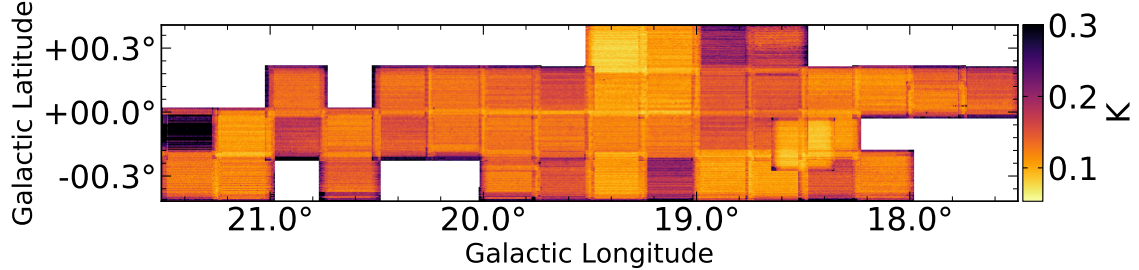


Fig. C.2 $\text{NH}_3(1,1)$ rms noise map for fields L18 through L21.

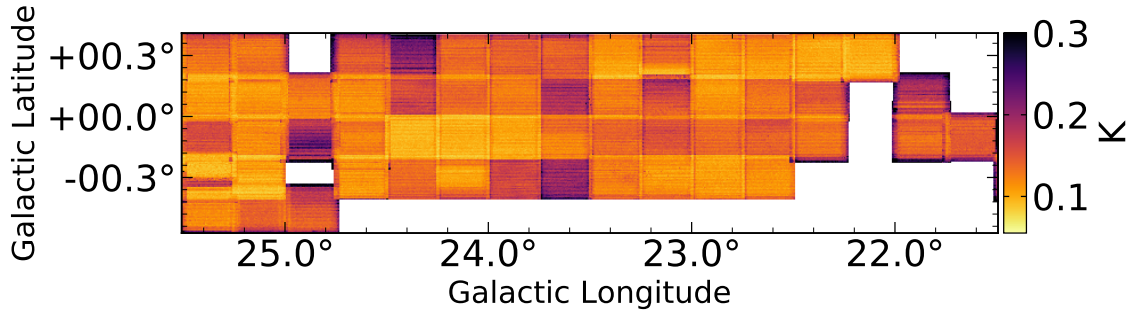


Fig. C.3 $\text{NH}_3(1,1)$ rms noise map for fields L22 through L25.

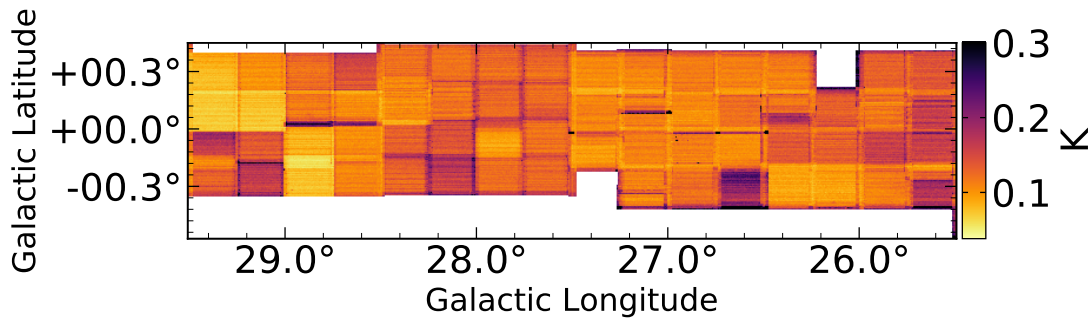


Fig. C.4 $\text{NH}_3(1,1)$ rms noise map for fields L26 through L29.

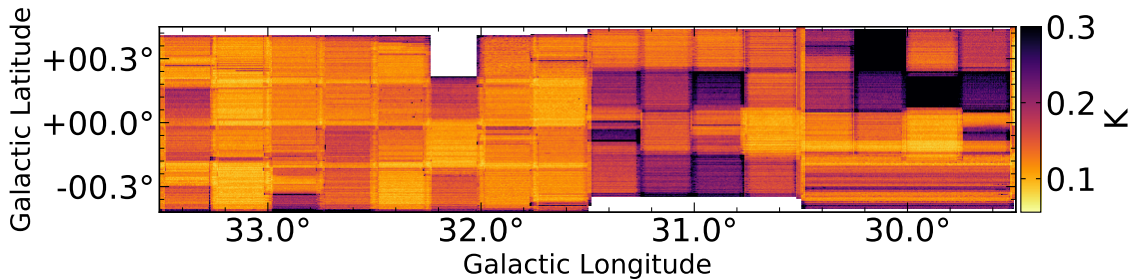


Fig. C.5 $\text{NH}_3(1,1)$ rms noise map for fields L30 through L33.

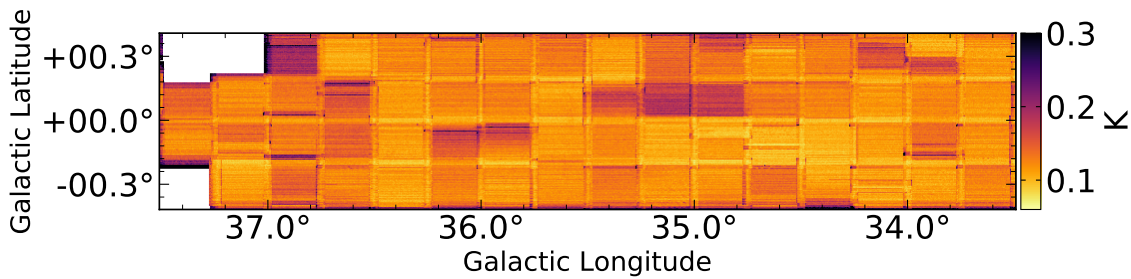


Fig. C.6 $\text{NH}_3(1,1)$ rms noise map for fields L34 through L37.

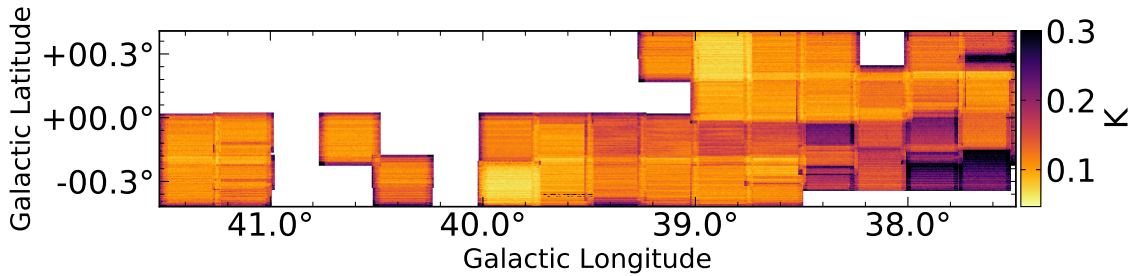


Fig. C.7 $\text{NH}_3(1,1)$ rms noise map for fields L38 through L41.

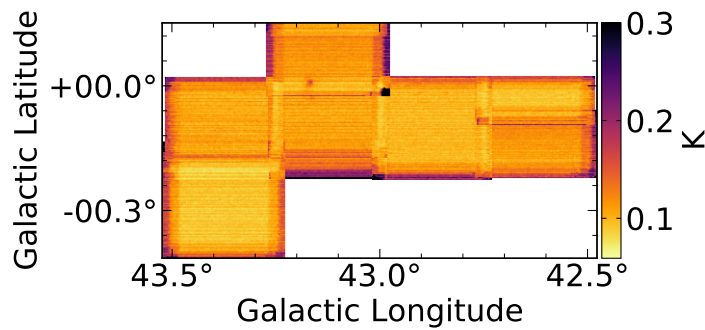


Fig. C.8 $\text{NH}_3(1,1)$ rms noise map for field L43.

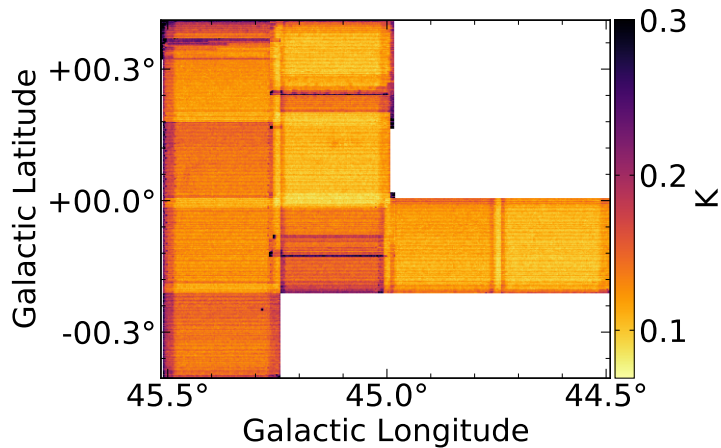


Fig. C.9 $\text{NH}_3(1,1)$ rms noise map for field L45.

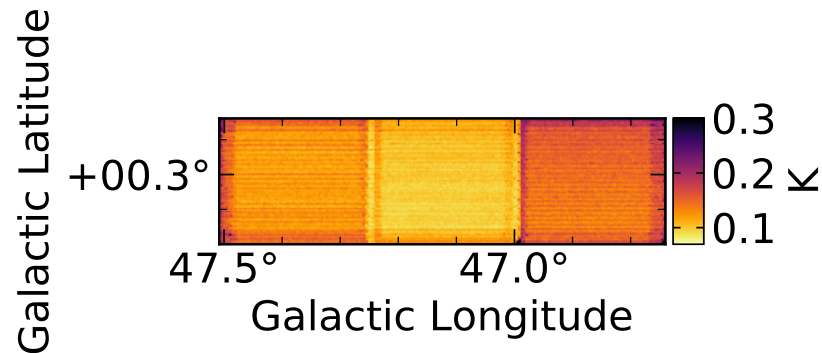


Fig. C.10 $\text{NH}_3(1,1)$ rms noise map for field L47.

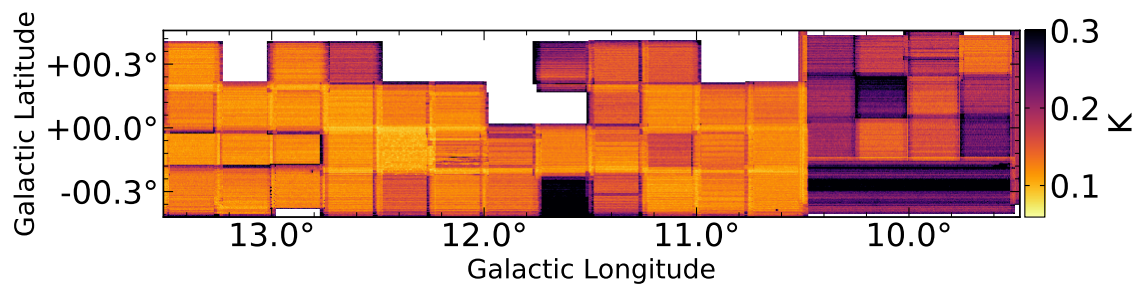


Fig. C.11 $\text{NH}_3(2,2)$ rms noise map for fields L10 through L13.

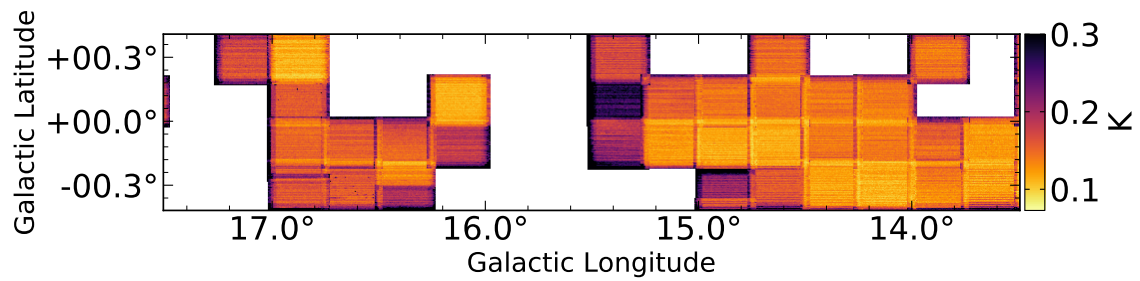


Fig. C.12 $\text{NH}_3(2,2)$ rms noise map for fields L14 through L17.

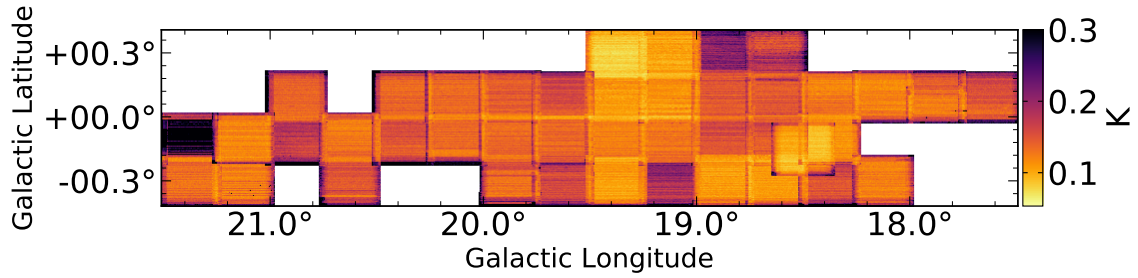


Fig. C.13 $\text{NH}_3(2,2)$ rms noise map for fields L18 through L21.

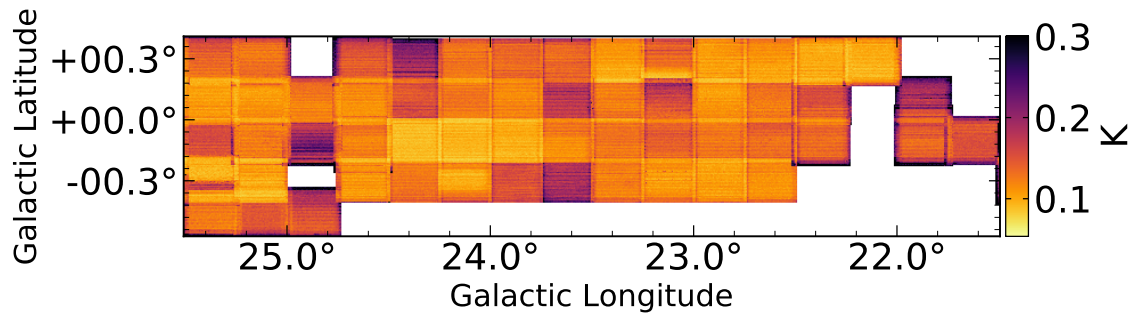


Fig. C.14 $\text{NH}_3(2,2)$ rms noise map for fields L22 through L25.

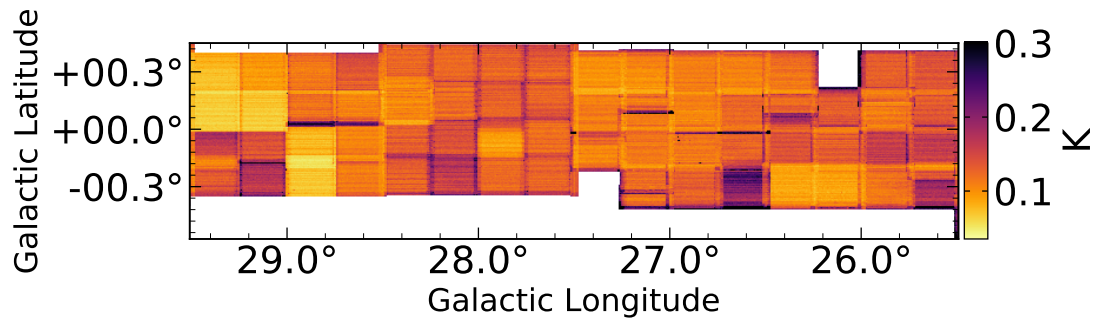


Fig. C.15 $\text{NH}_3(2,2)$ rms noise map for fields L26 through L29.

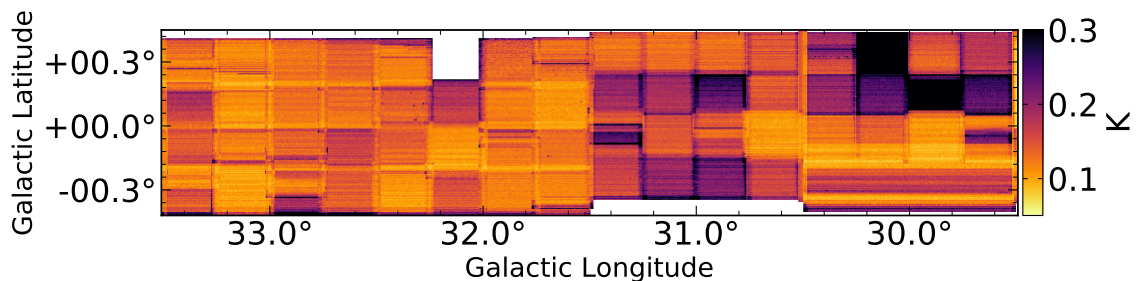


Fig. C.16 $\text{NH}_3(2,2)$ rms noise map for fields L30 through L33.

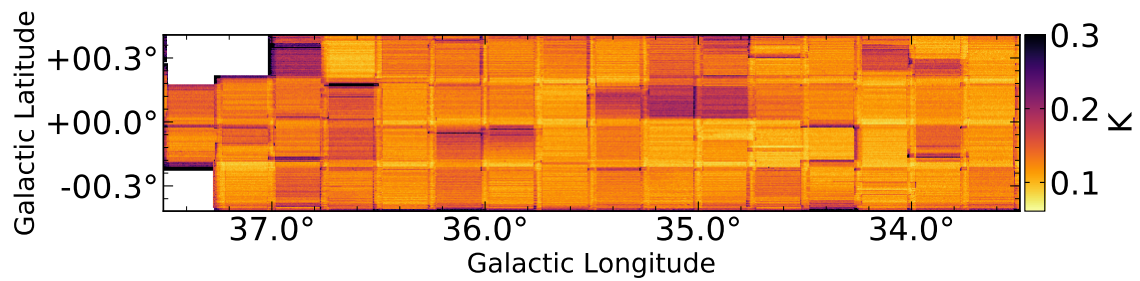


Fig. C.17 $\text{NH}_3(2,2)$ rms noise map for fields L34 through L37.

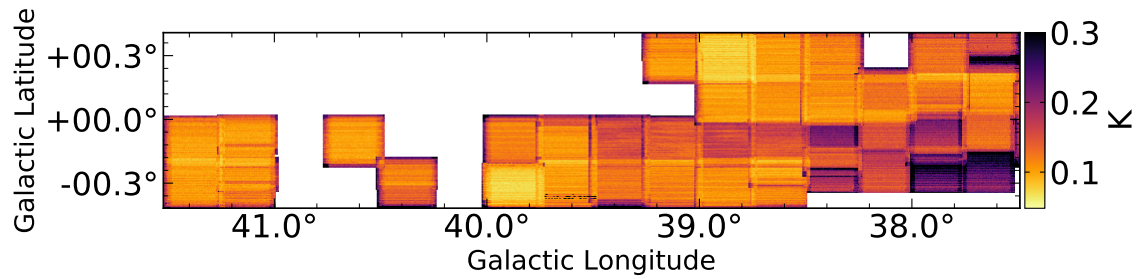


Fig. C.18 $\text{NH}_3(2,2)$ rms noise map for fields L38 through L41.

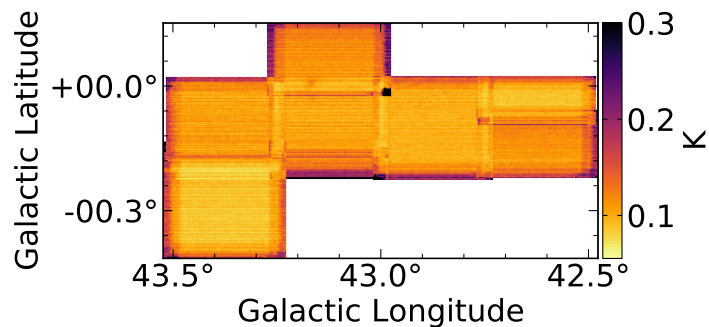


Fig. C.19 $\text{NH}_3(2,2)$ rms noise map for field L43.

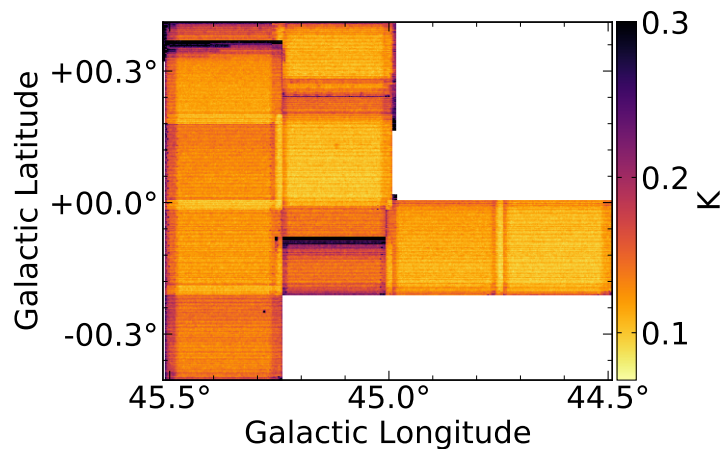


Fig. C.20 $\text{NH}_3(2,2)$ rms noise map for field L45.

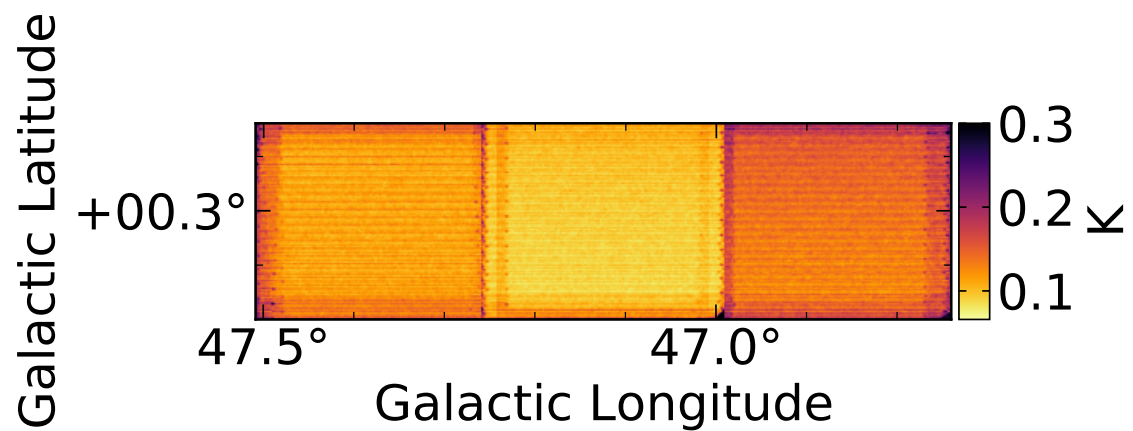


Fig. C.21 $\text{NH}_3(2,2)$ rms noise map for field L47.

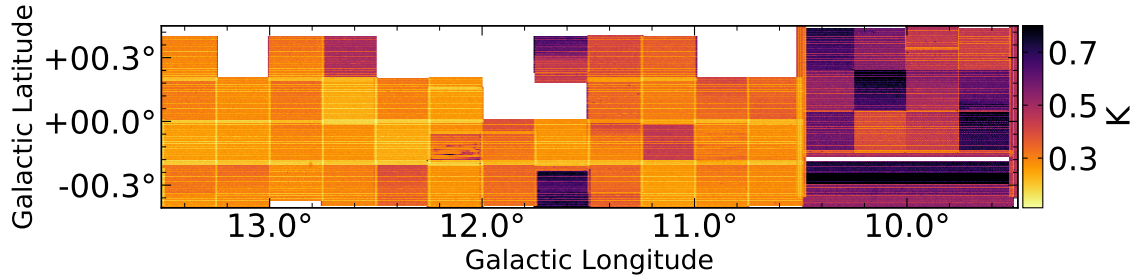


Fig. C.22 H₂O rms noise map for fields L10 through L13.

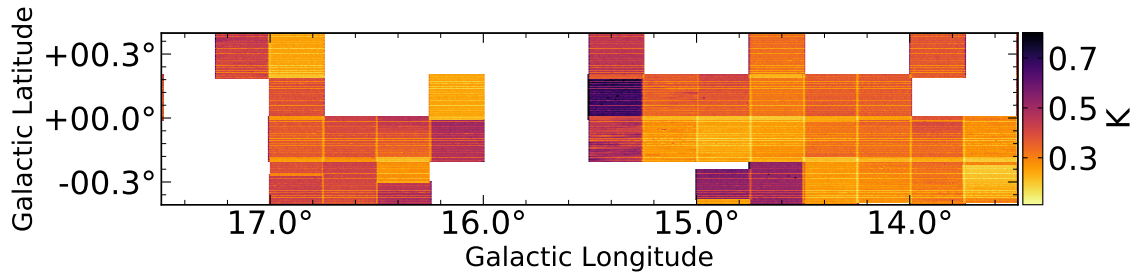


Fig. C.23 H₂O rms noise map for fields L14 through L17.

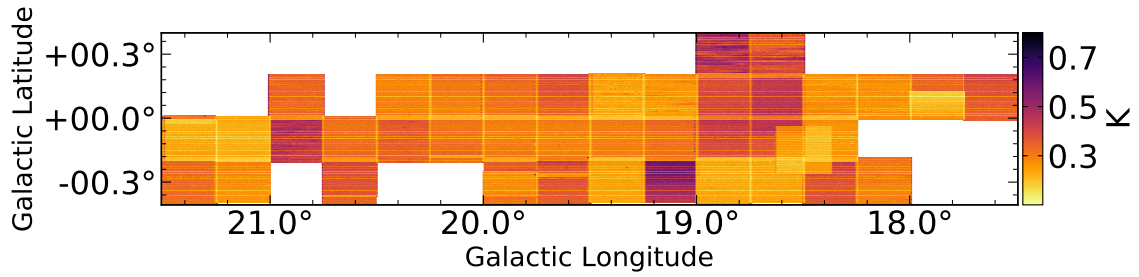


Fig. C.24 H₂O rms noise map for fields L18 through L21.

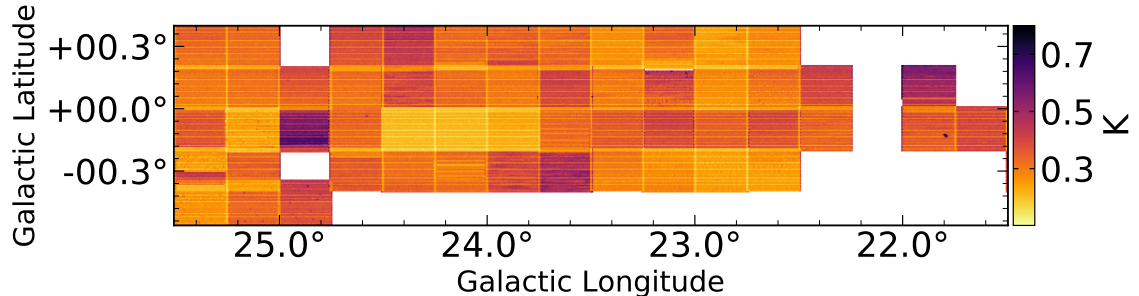


Fig. C.25 H₂O rms noise map for fields L22 through L25.

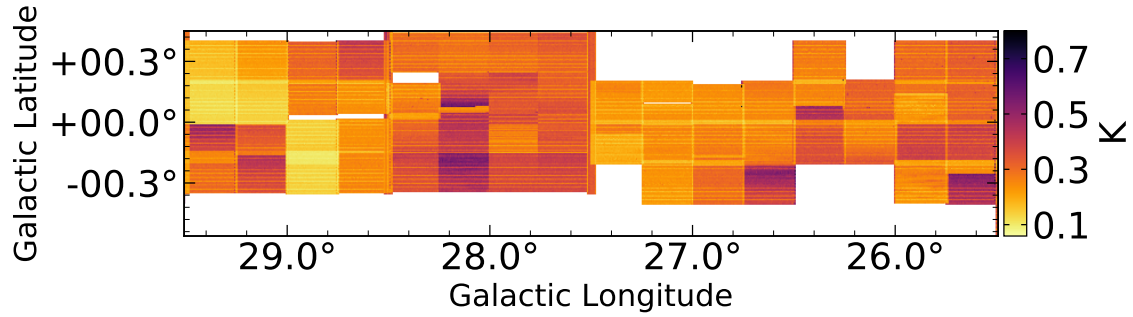


Fig. C.26 H₂O rms noise map for fields L26 through L29.

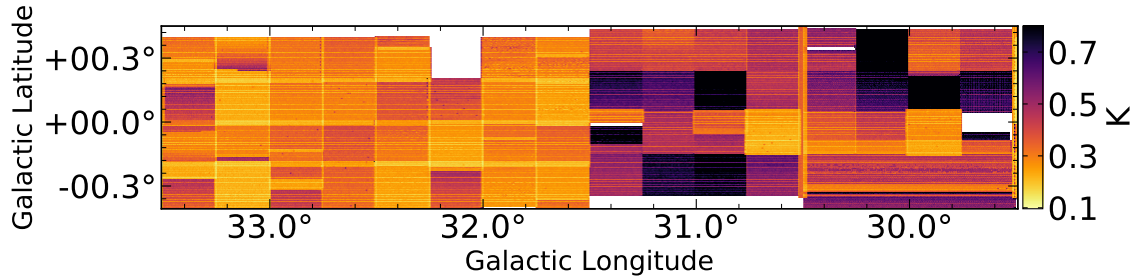


Fig. C.27 H₂O rms noise map for fields L30 through L33.

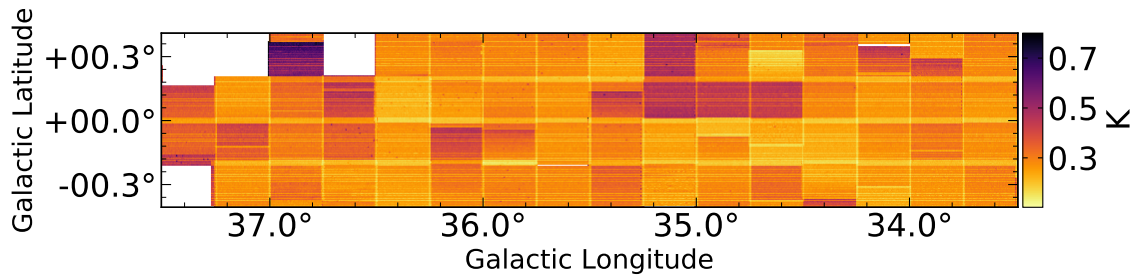


Fig. C.28 H₂O rms noise map for fields L34 through L37.

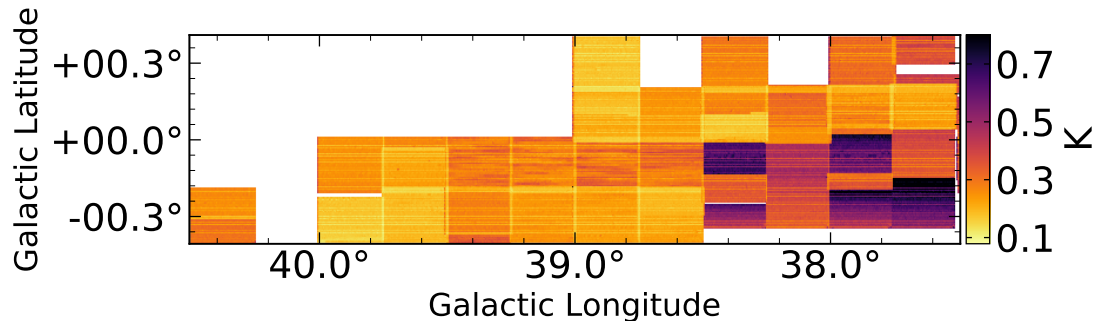


Fig. C.29 H₂O rms noise map for fields L38 through L40.

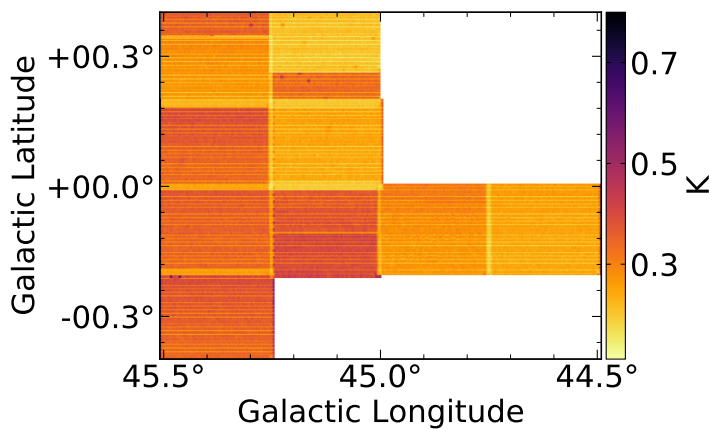


Fig. C.30 H₂O rms noise map for field L45.

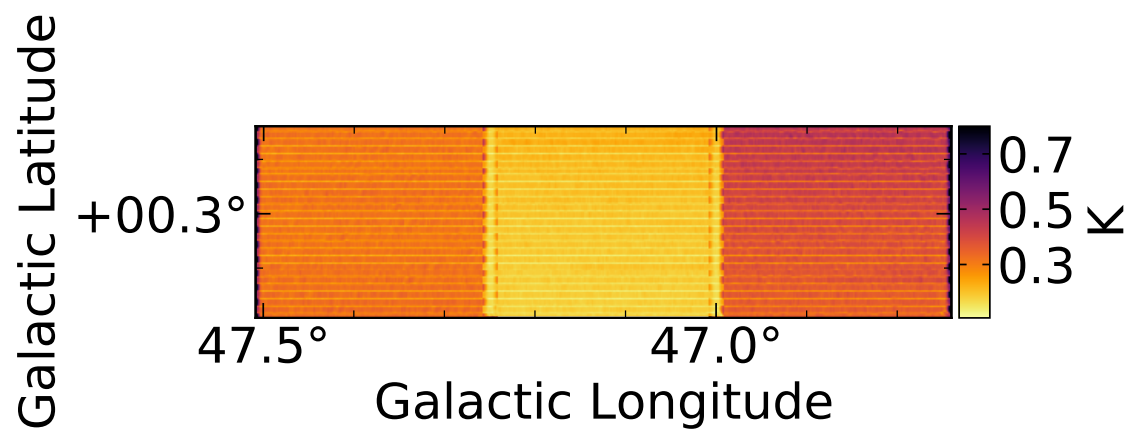


Fig. C.31 H₂O rms noise map for field L47.

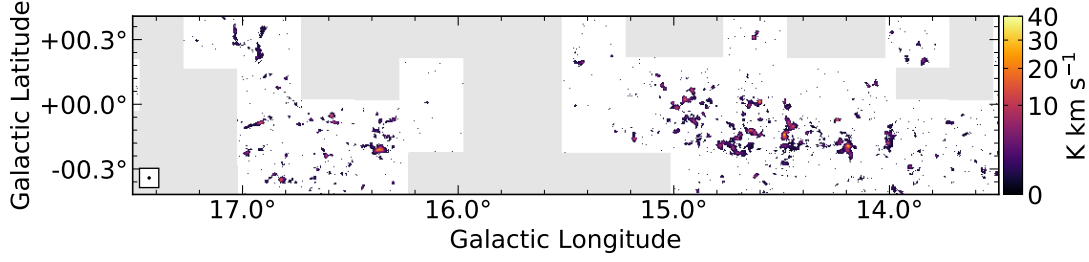


Fig. D.1 NH₃(1,1) integrated intensity map for fields L14 through L17. The GBT beam size is shown in the lower left.

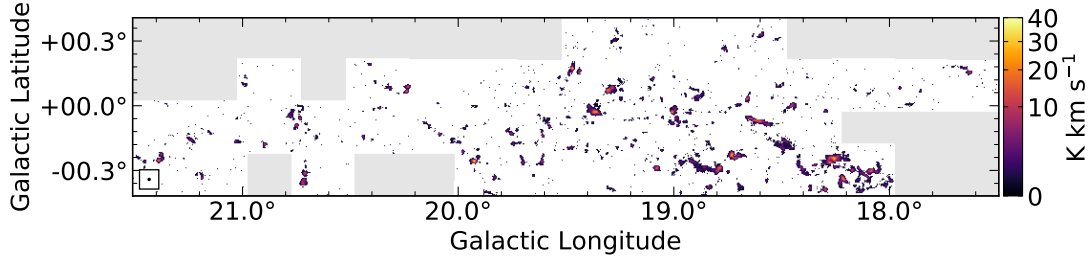


Fig. D.2 NH₃(1,1) integrated intensity map for fields L18 through L21. The GBT beam size is shown in the lower left.

intensity map for field L47, because there was no significant detection of NH₃(2,2) in this field.

E First Velocity Moment Maps

Figures D.1-D.10 show the NH₃(1,1) first velocity moment maps not shown in Section 2.4.

F NH₃ Line Modeling

In Appendix A, I described how the hyperfine splitting of the NH₃ inversion transitions allows one to calculate the optical depth of a line by comparing the statistical weights of the hyperfine transitions to the hyperfine line amplitudes. Although the NH₃(1,1) transition is split into 18 magnetic hyperfine lines, the broad line widths

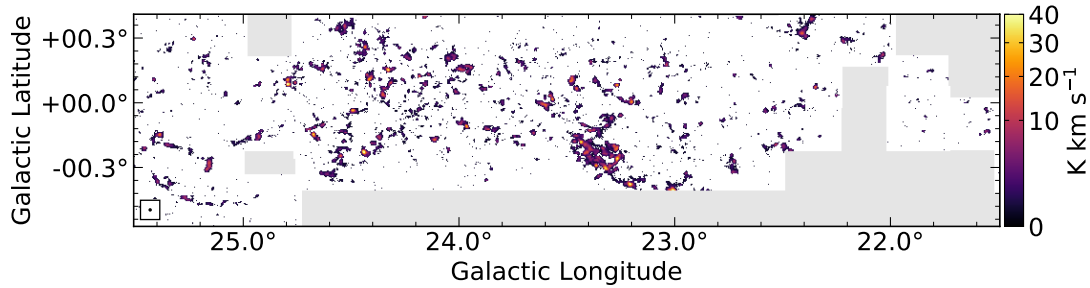


Fig. D.3 $\text{NH}_3(1,1)$ integrated intensity map for fields L22 through L25. The GBT beam size is shown in the lower left.

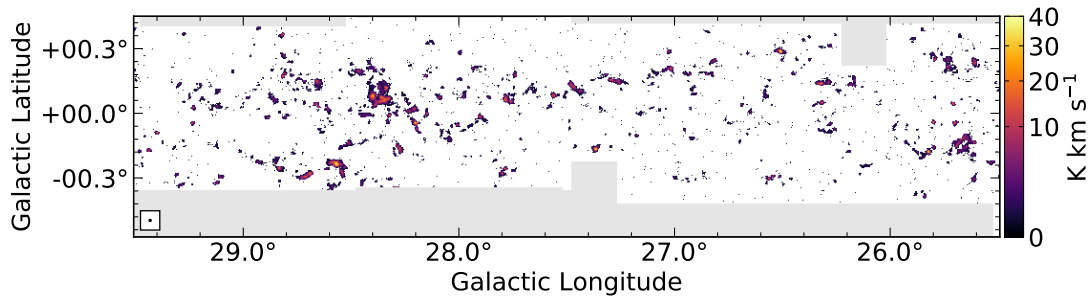


Fig. D.4 $\text{NH}_3(1,1)$ integrated intensity map for fields L26 through L29. The GBT beam size is shown in the lower left.

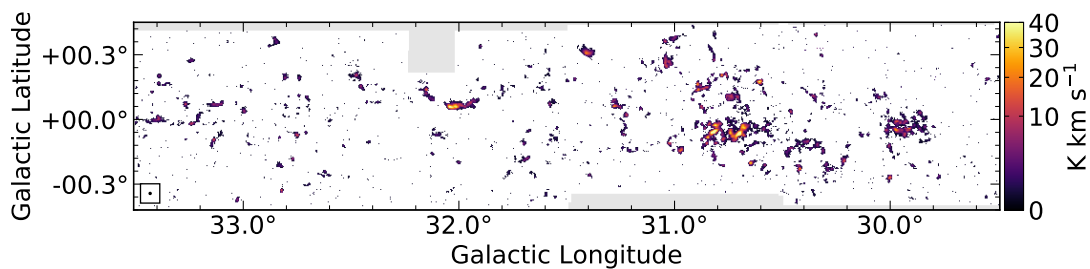


Fig. D.5 $\text{NH}_3(1,1)$ integrated intensity map for fields L30 through L33. The GBT beam size is shown in the lower left.

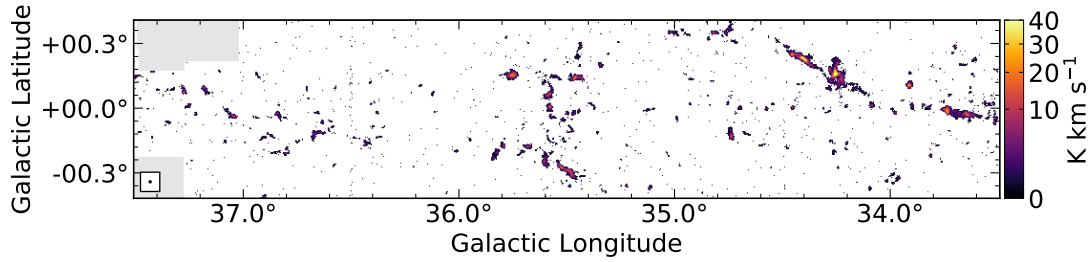


Fig. D.6 NH₃(1,1) integrated intensity map for fields L34 through L37. The GBT beam size is shown in the lower left.

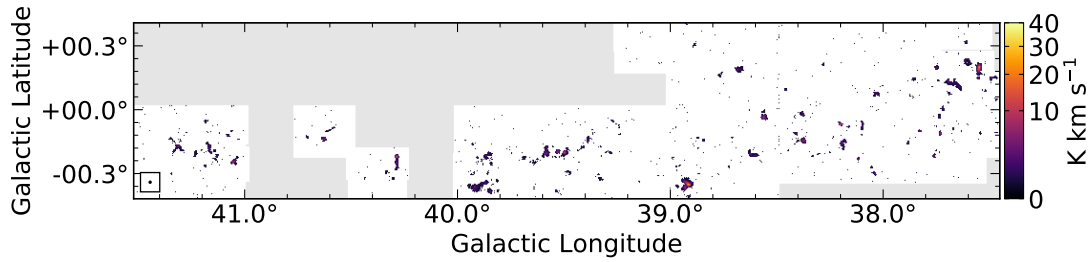


Fig. D.7 NH₃(1,1) integrated intensity map for fields L38 through L41. The GBT beam size is shown in the lower left.

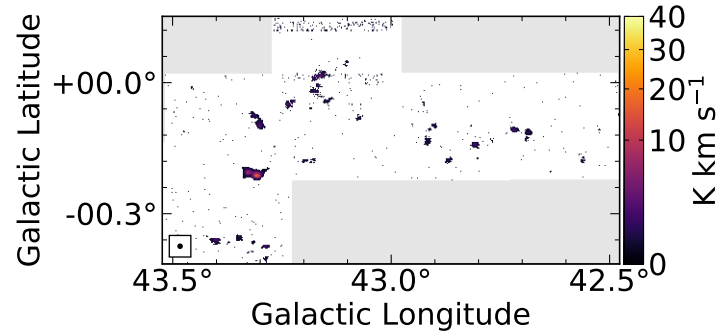


Fig. D.8 NH₃(1,1) integrated intensity map for field L43. The GBT beam size is shown in the lower left.

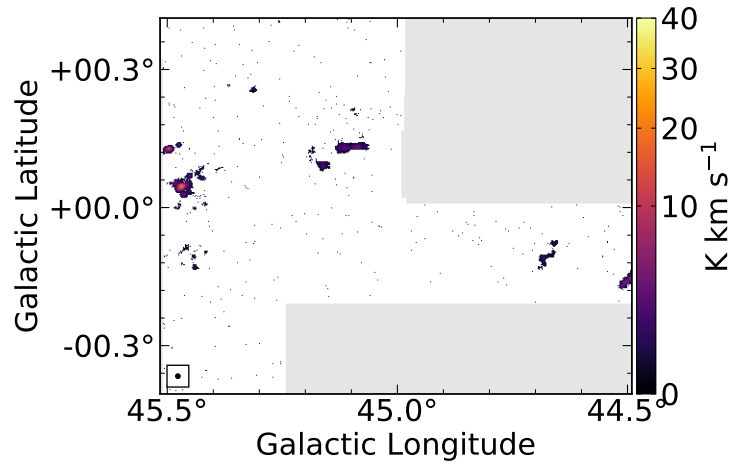


Fig. D.9 $\text{NH}_3(1,1)$ integrated intensity map for field L45. The GBT beam size is shown in the lower left.

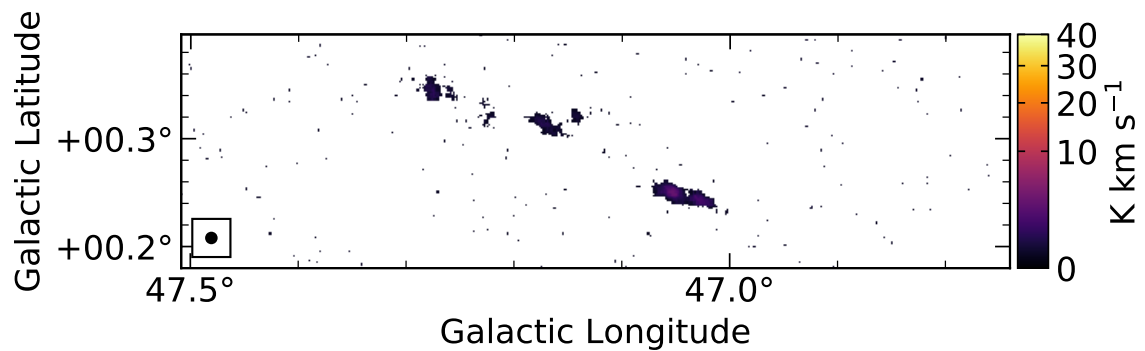


Fig. D.10 $\text{NH}_3(1,1)$ integrated intensity map for field L47. The GBT beam size is shown in the lower left.

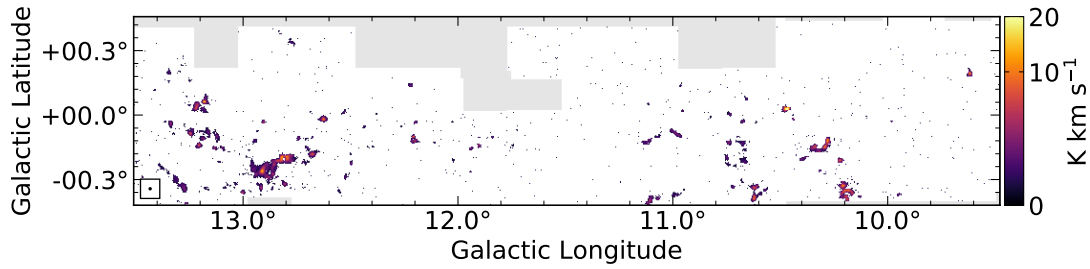


Fig. D.11 $\text{NH}_3(2,2)$ integrated intensity map for fields L10 through L13. The GBT beam size is shown in the lower left.

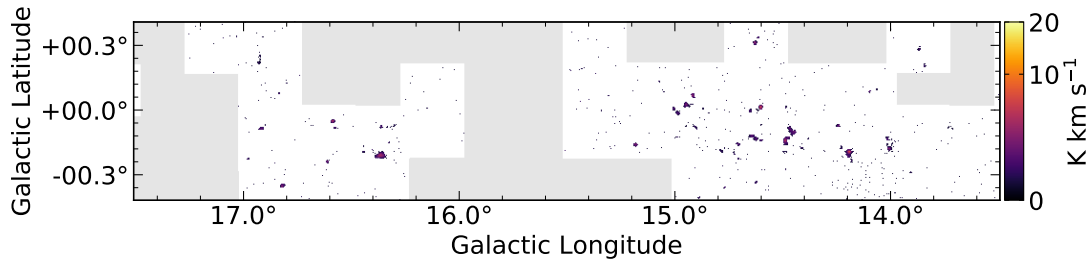


Fig. D.12 $\text{NH}_3(2,2)$ integrated intensity map for fields L14 through L17. The GBT beam size is shown in the lower left.

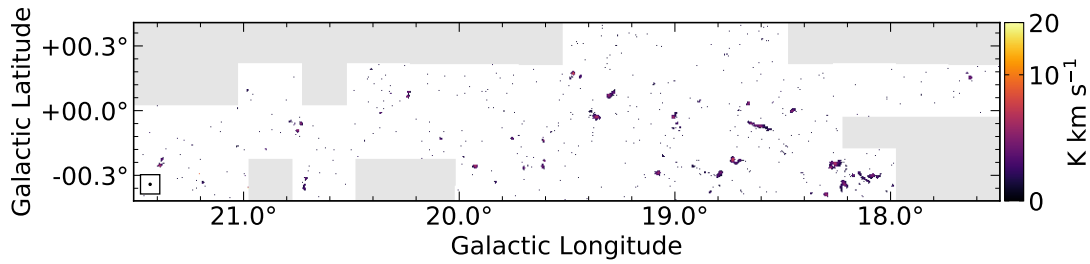


Fig. D.13 $\text{NH}_3(2,2)$ integrated intensity map for fields L18 through L21. The GBT beam size is shown in the lower left.

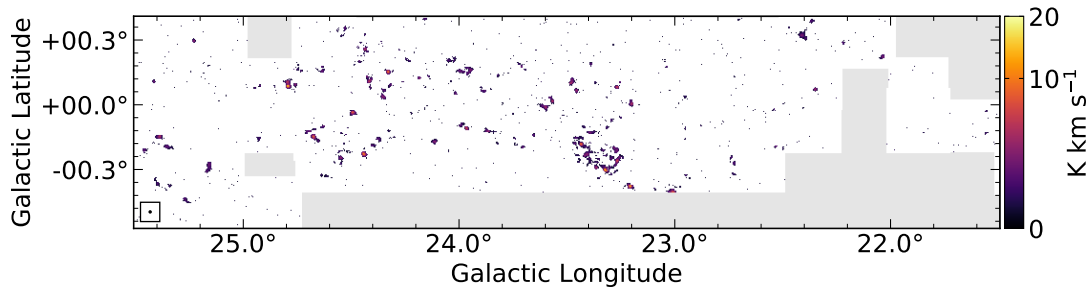


Fig. D.14 $\text{NH}_3(2,2)$ integrated intensity map for fields L22 through L25. The GBT beam size is shown in the lower left.

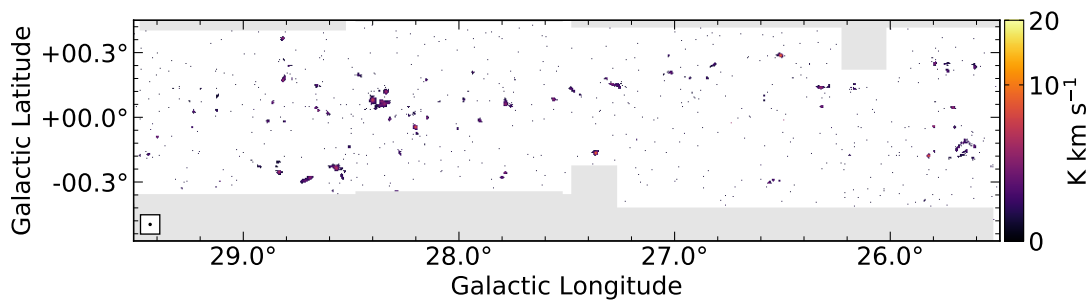


Fig. D.15 $\text{NH}_3(2,2)$ integrated intensity map for fields L26 through L29. The GBT beam size is shown in the lower left.

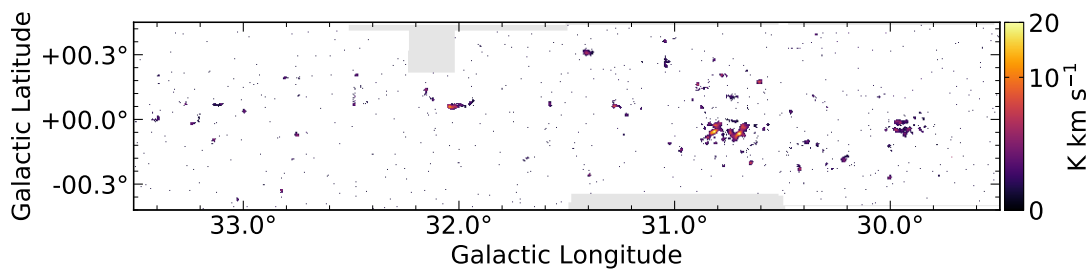


Fig. D.16 $\text{NH}_3(2,2)$ integrated intensity map for fields L30 through L33. The GBT beam size is shown in the lower left.

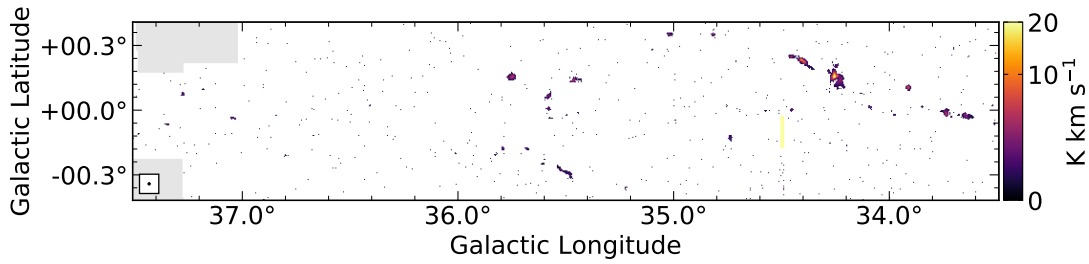


Fig. D.17 $\text{NH}_3(2,2)$ integrated intensity map for fields L34 through L37. The GBT beam size is shown in the lower left.

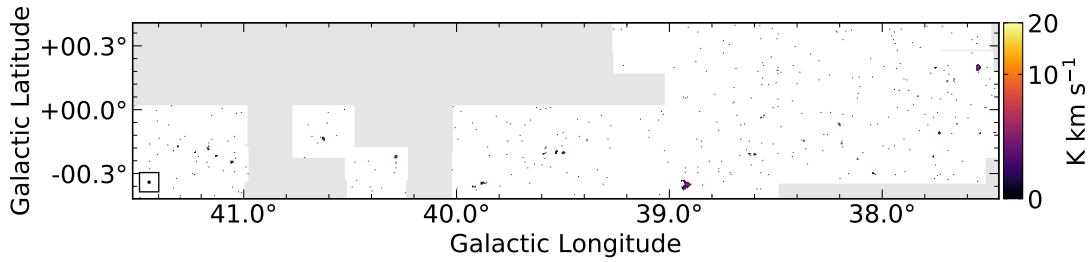


Fig. D.18 $\text{NH}_3(2,2)$ integrated intensity map for fields L38 through L41. The GBT beam size is shown in the lower left.

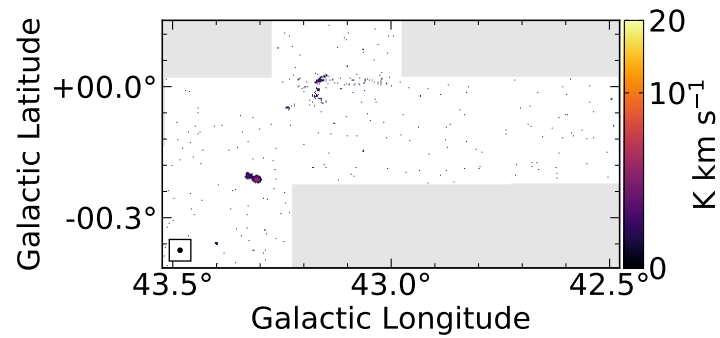


Fig. D.19 $\text{NH}_3(2,2)$ integrated intensity map for field L43. The GBT beam size is shown in the lower left.

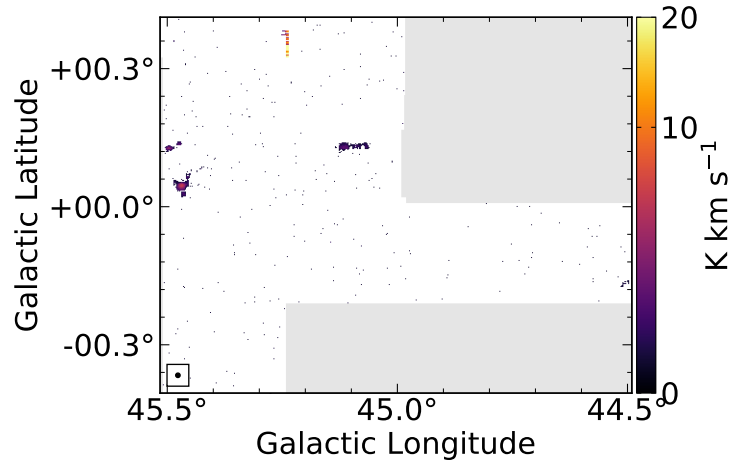


Fig. D.20 $\text{NH}_3(2,2)$ integrated intensity map for field L45. The GBT beam size is shown in the lower left.

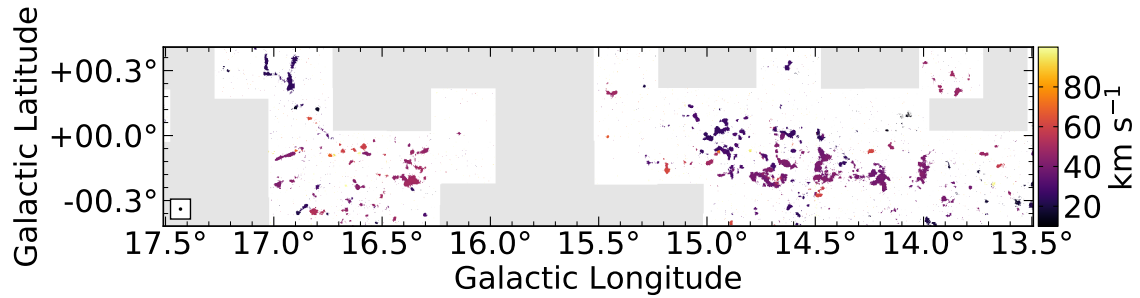


Fig. E.1 $\text{NH}_3(1,1)$ first moment map for fields L14 through L17. The GBT beam size is shown in the lower left.

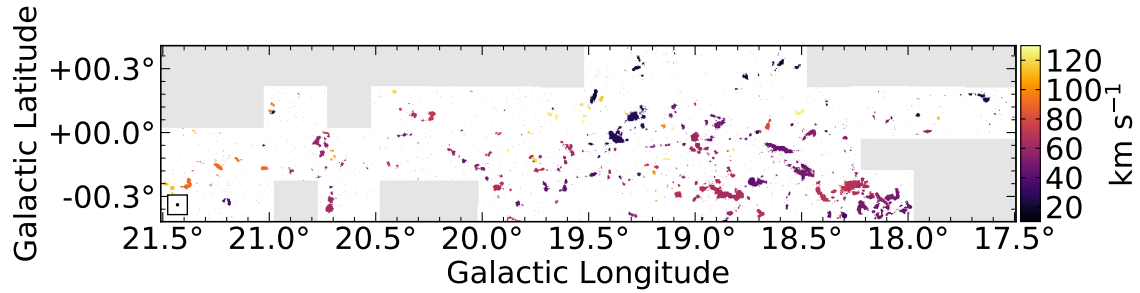


Fig. E.2 $\text{NH}_3(1,1)$ first moment map for fields L18 through L21. The GBT beam size is shown in the lower left.

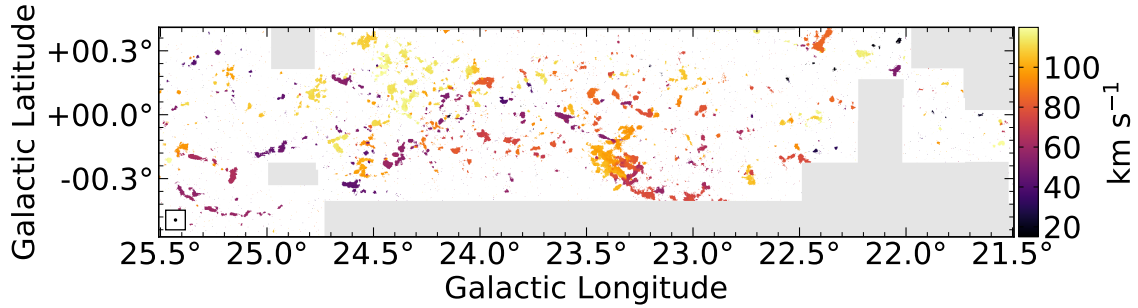


Fig. E.3 $\text{NH}_3(1,1)$ first moment map for fields L22 through L25. The GBT beam size is shown in the lower left.

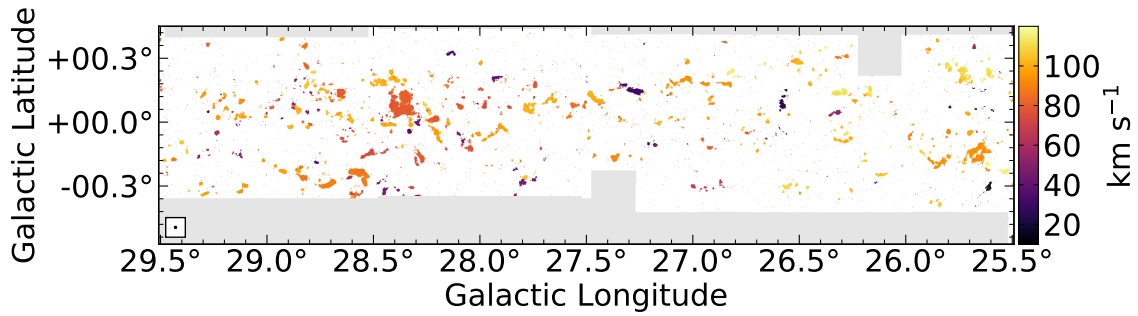


Fig. E.4 $\text{NH}_3(1,1)$ first moment map for fields L26 through L29. The GBT beam size is shown in the lower left.

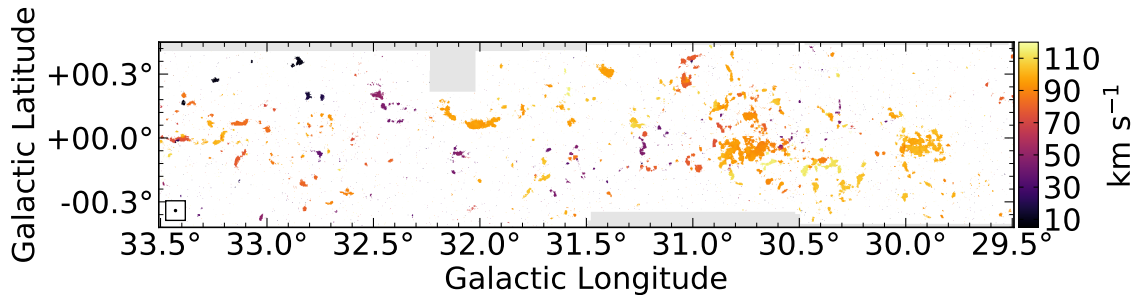


Fig. E.5 $\text{NH}_3(1,1)$ first moment map for fields L30 through L33. The GBT beam size is shown in the lower left.

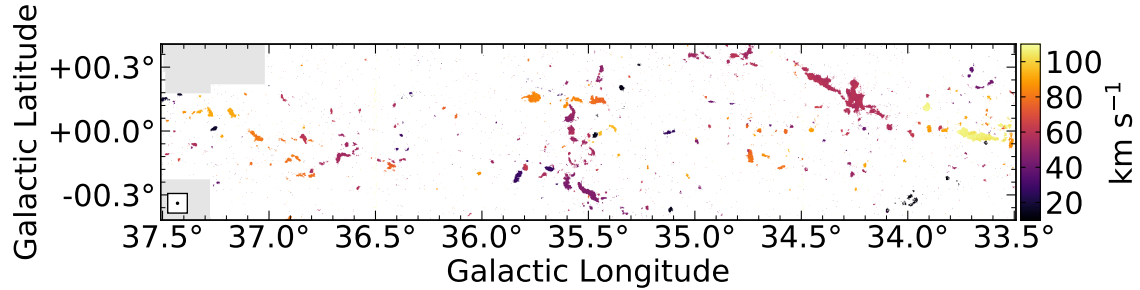


Fig. E.6 $\text{NH}_3(1,1)$ first moment map for fields L34 through L37. The GBT beam size is shown in the lower left.

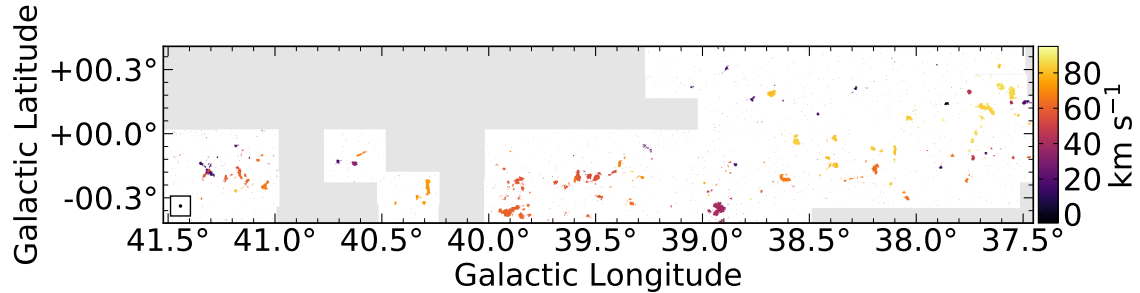


Fig. E.7 $\text{NH}_3(1,1)$ first moment map for fields L38 through L41. The GBT beam size is shown in the lower left.

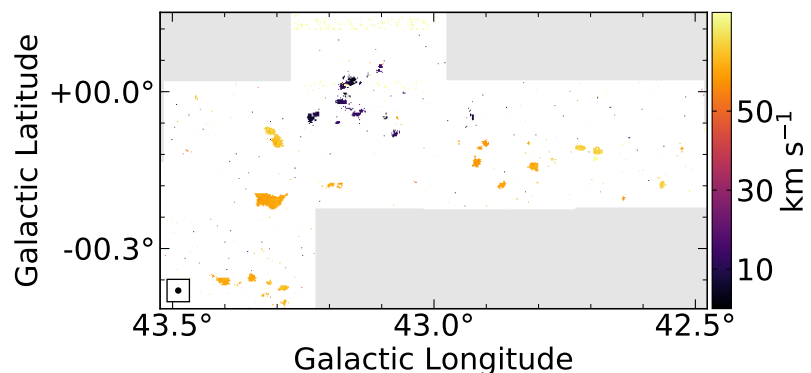


Fig. E.8 $\text{NH}_3(1,1)$ first moment map for field L43. The GBT beam size is shown in the lower left.

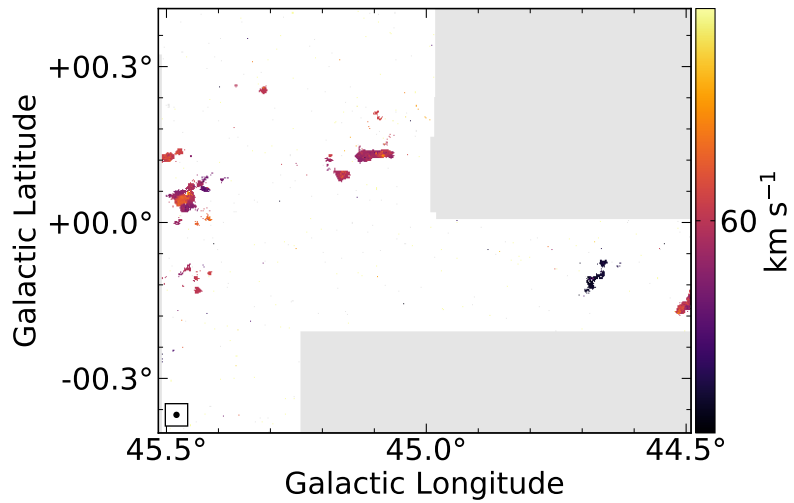


Fig. E.9 $\text{NH}_3(1,1)$ first moment map for field L45. The GBT beam size is shown in the lower left.

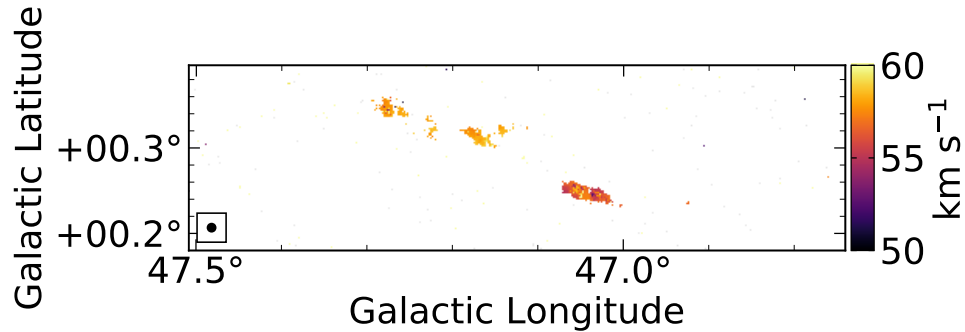


Fig. E.10 $\text{NH}_3(1,1)$ first moment map for field L47. The GBT beam size is shown in the lower left.

characteristic of the emission from typical molecular clumps often blend the closely spaced magnetic hyperfine lines. This is demonstrated by Figure F.1, which shows two model $\text{NH}_3(1,1)$ spectra, one with large line widths and one with narrow line widths. Thus, $\text{NH}_3(1,1)$ emission from molecular clumps usually displays only the prominent electric quadrupole hyperfine splitting, which splits the inversion transition into five hyperfine lines. Consequently, previous efforts to fit $\text{NH}_3(1,1)$ lines have often neglected the magnetic hyperfine lines in favor of solely fitting the five electric quadrupole hyperfine lines to derive gas properties (e.g., Longmore et al. 2017). In

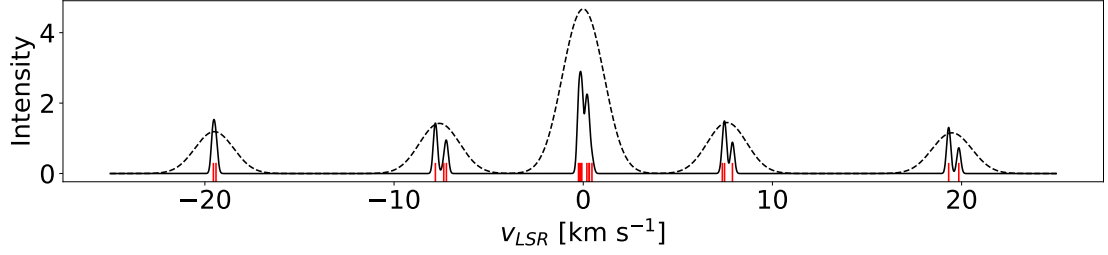


Fig. F.1 Model $\text{NH}_3(1,1)$ lines produced by PySpecKit. A model spectrum with narrow line widths is shown with a solid line, while a model spectrum with broad line widths is shown with a dashed line. The red vertical lines show the positions of the 18 magnetic hyperfine lines.

the absence of self-absorption or absorption, the central quadrupole line, usually referred to as the “main” line, is brighter than the other four electric quadrupole lines, which are referred to as “satellite” lines. In LTE, the ratio of the main line amplitude to the satellite line amplitudes is solely a function of the optical depth of the main line at line center ($\tau(1,1)_0$). A smaller ratio of the main line amplitude to the satellite line amplitudes corresponds to a larger optical depth. Thus, one determines $\tau(1,1)_0$ by solving the equation (Barrett et al. 1977),

$$\frac{\Delta T_B(\text{main})}{\Delta T_B(\text{satellite})} = \frac{1 - e^{-\tau(1,1)_0}}{1 - e^{-a\tau(1,1)_0}}, \quad (1)$$

where $\Delta T_B(\text{main})$ is the brightness temperature of the main line, $\Delta T_B(\text{satellite})$ is the brightness temperature of a satellite line, $\tau(1,1)_0$ is the optical depth of the main line at line center, and a is the ratio of the optical depth in the satellite line compared to optical depth in the main line. The value of a is a constant given by the quantum statistics of the hyperfine lines. For the two “inner” satellite lines, those closest in frequency to the main line, $a_{\text{inner}} \approx 0.28$. For the two “outer” satellite lines $a_{\text{outer}} \approx 0.22$.

The derivation of $\tau(1, 1)_0$ from the satellite line amplitudes is an approximation that assumes all of the magnetic hyperfine lines have the same frequencies as their corresponding electric quadrupole transitions. Although this approximation is valid for lines with large velocity dispersions, the magnetic hyperfine splitting becomes significant for narrow lines. To test this effect, I modeled the optical depth profiles of the magnetic hyperfine lines, adopting their frequencies and relative optical depths from the Lovas (2004) line list. I made the full NH₃(1,1) optical depth profile by superposing the individual Gaussian optical depth profiles of the magnetic hyperfine lines, each of which has a velocity dispersion of σ . I fit the optical depth profiles with five Gaussians at the velocities of the quadrupole transitions and compared the measured optical depth ratios (a_{meas}) to the quadrupole values (a_{quad}). Figure F.2 shows the relative difference between these values $\Delta a/a_{quad} = (a_{quad} - a_{meas})/a_{quad}$. At $\sigma \lesssim 0.5$ km s⁻¹ the quadrupole approximation of a used to determine NH₃(1,1) optical depths is different from the theoretical value by 5–20%. Because the thermal velocity dispersion of NH₃ is $\sigma_{therm} \sim 0.1$ km s⁻¹ at typical molecular clump temperatures, I fit the NH₃(1,1) spectra using the magnetic hyperfine model to provide more accurate estimates of $\tau(1, 1)_0$ and σ .

I fit RAMPS NH₃(1,1) spectra using the Python `optimize.curve_fit` function from the `scipy` library. The `curve_fit` function is a nonlinear least-squares method used to fit a function to data. As its input arguments, `curve_fit` takes a model function, data, initial parameters, and parameter boundaries. I used an NH₃(1,1) model that includes the 18 magnetic hyperfine lines, with frequencies and relative optical depths adopted from the Lovas (2004) line list. The line intensity profile is given by,

$$T_B(\nu) = (T_{ex} - T_{bkg})(1 - e^{-\tau(\nu)}), \quad (2)$$

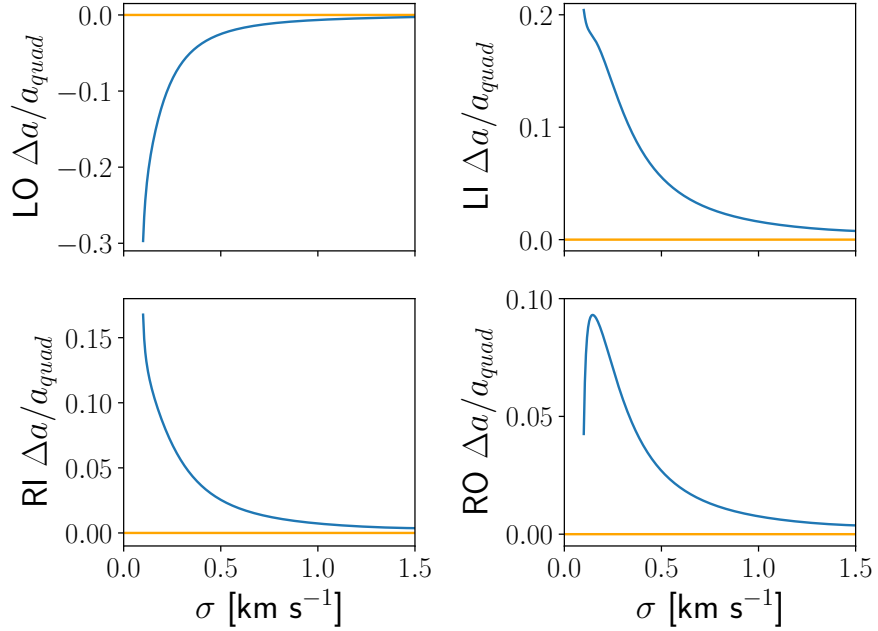


Fig. F.2 Relative difference between the quadrupole optical depth ratios (a_{quad}) and the measured ratios (a_{meas}) as a function of σ , where $\Delta a = a_{quad} - a_{meas}$. The panels show $\Delta a / a_{quad}$ for the left outer (top left), left inner (top right), right inner (bottom left), and right outer (bottom right) satellite lines.

where $T_B(\nu)$ is the intensity as a function of the frequency ν , T_{ex} is the excitation temperature of the transition, T_{bkg} is the temperature of the background radiation, and $\tau(\nu)$ is the optical depth profile as a function of ν . Equation 2 does not take into account beam dilution, the reduction of intensity due to unresolved emission. Consequently, the derived T_{ex} is often smaller than the gas temperature, indicating that unresolved emission is common. At the observed frequencies, the background radiation is typically dominated by the Cosmic Microwave Background (CMB), so $T_{bkg} = T_{CMB} = 2.73$ K. As described above, the optical depth profile is given by the superposition of the Gaussian optical depth profiles of each magnetic hyperfine line, each of which has a velocity dispersion of σ . The total optical depth of the $\text{NH}_3(1,1)$ line ($\tau(1,1)_{tot}$) is given by $\sum_{i=1}^{18} \tau_i(v)$, the sum of the optical depths for the

individual magnetic hyperfine lines. The $\text{NH}_3(1,1)$ V_{LSR} is set by the rest frequency of the unsplit line, which is equal to the optical depth-weighted velocity. Thus, the $\text{NH}_3(1,1)$ line model has four free parameters: T_{ex} , σ , V_{LSR} , and $\tau(1,1)_{tot}$. I initialized the fit parameters to reasonable values. I set $T_{ex,init} = 5$ K, $\sigma_{init} = 1$ km s^{-1} , $(\tau(1,1)_{tot})_{init} = 1$, and $v_{LSR,init}$ equal to the intensity-weighted velocity given by the 3D clump label. The T_{ex} , σ , V_{LSR} , and $\tau(1,1)_{tot}$ parameters were restricted to the range $2.73 - 50$ K, $0.05 - 10$ km s^{-1} , $-10 - 160$ km s^{-1} , and $0 - 50$, respectively.

Modeling the $\text{NH}_3(1,1)$ and $(2,2)$ simultaneously allows the estimation of the NH_3 rotational temperature and column density. I used an LTE NH_3 model, which assumes that $T_{ex} = T_{rot}$ for each transition. To create model spectra, the function uses the rotational temperature (T_{rot}), the total NH_3 column density (N_{tot}), the line width (σ), the velocity (V_{LSR}), the beam filling fraction (ϕ), and the ortho fraction as input parameters. The beam filling factor is a scaling factor between 0 and 1. If an emitting source contains no unresolved substructures, the beam filling factor equals 1. If the emitting source features emission on scales smaller than the telescope beam, the filling factor equals the solid angle of the emission divided by the solid angle of the beam. The ortho fraction is the fraction of NH_3 in ortho state. Ortho- NH_3 states are those with $K = 3n$, where n is an integer including 0, while para- NH_3 states have $K \neq 3n$.

With these input parameters, the code calculates the total optical depth within a given transition using the equation

$$\tau(J, K)_{tot} = \frac{N_{tot}g_u}{Q_{tot}} \frac{A_{ul}c^2}{8\pi\nu_0^2} \frac{c}{\sigma\nu_0\sqrt{2\pi}} \frac{1 - e^{\frac{-h\nu_0}{k_B T_{rot}}}}{1 + e^{\frac{-h\nu_0}{k_B T_{rot}}}}, \quad (3)$$

where $\tau(J, K)_{tot}$ is the total optical depth in the $\text{NH}_3(J, K)$ transition, g_u is the statistical weight of the upper state, A_{ul} is the Einstein A-coefficient of the transition, c is the speed of light, ν_0 is the rest frequency of the transition, h is Planck's constant,

k_B is the Boltzmann constant, and Q_{tot} is the molecular partition function, which is given by

$$Q_{tot} = \sum_{J \neq 3n} (2J + 1) e^{-h(J(J+1)B_{rot} + J^2(C_{rot} - B_{rot}))/k_B T_{rot}} \quad (4)$$

for para transitions and

$$Q_{tot} = \sum_{J=3n} 2(2J + 1) e^{-h(J(J+1)B_{rot} + J^2(C_{rot} - B_{rot}))/k_B T_{rot}} \quad (5)$$

for ortho transitions, where B_{rot} and C_{rot} are the NH₃ rotational constants. This formulation of $\tau(J, K)_{tot}$ can be derived from Equation 29 of Mangum & Shirley (2015) by relating the population in the upper state to the total population using the partition function and solving for $\tau(J, K)_{tot}$.

The code calculates $\tau(\nu)$, the optical depth profile of the magnetic hyperfine lines, using $\tau(J, K)_{tot}$, the known statistical weights, and Gaussian line profiles with a velocity dispersion of σ . I have also calculated and reported $\tau(1, 1)_0$, the NH₃(1,1) optical depth at the centroid of the main line. The code then creates the model spectrum using the equation

$$T_B(\nu) = \phi \frac{h\nu}{k_B} (1 - e^{-\tau(\nu)}) \left(\frac{1}{e^{\frac{h\nu}{k_B T_{rot}}} - 1} - \frac{1}{e^{\frac{h\nu}{k_B T_{bkg}}} - 1} \right), \quad (6)$$

where $T_{bkg} = T_{CMB}$. Although the original PySpecKit `ammonia_model` class does not include ϕ as a fit parameter, I have modified the fit routine to include it as a free parameter. This is a necessary step for fitting RAMPS NH₃ data, since many clumps feature emission that is unresolved by the GBT beam.

The fitting routine performs Levenberg–Marquardt least-squares minimization to find the best-fit parameters. I determined sensible starting values for T_{rot} , N_{tot} , and ϕ using an initial fit on a subset of the data. I found that reasonable starting values for T_{rot} , N_{tot} , and ϕ were 18 K, 10¹⁵ cm⁻², and 0.1, respectively. I used the

best-fit parameters from the preliminary fit to the NH₃(1,1) spectra as the initial values for σ and V_{LSR} . As with the preliminary fit, I chose to limit the parameter space. I allowed T_{rot} , N_{tot} , σ , V_{LSR} , and ϕ to vary within the ranges 5 – 100 K, $10^{12} – 10^{17}$ cm⁻², 0.05 – 10 km s⁻¹, –30 – 160 km s⁻¹, and 0 – 1, respectively. For the current analysis, I have fit only NH₃(1,1) and NH₃(2,2) spectra, both of which are para-NH₃ transitions that provide no information on the ortho transitions. Consequently, I fixed the ortho fraction parameter to its equilibrium value of 0.5, although deviations from this value have been observed (Umemoto et al. 1999).

List of Journal Abbreviations

A&A	Astronomy and Astrophysics
A&AS	Astronomy and Astrophysics Supplement Series
AJ	Astronomical Journal
ApJ	Astrophysical Journal
ApJS	Astrophysical Journal Supplement Series
ARA&A	Annual Review of Astronomy and Astrophysics
Bull. Astron. Inst. Netherlands	Bulletin of the Astronomical Institutes of the Netherlands
IEEE Proceedings	Institute of Electrical and Electronics Engineers Proceedings
MNRAS	Monthly Notices of the Royal Astronomical Society
PASA	Publications of the Astronomical Society of Australia
PASJ	Publications of the Astronomical Society of Japan
PASP	Publications of the Astronomical Society of the Pacific
Phys. Rev. Lett.	Physical Review Letters

References

- Aguirre, J. E., Ginsburg, A. G., Dunham, M. K., et al. 2011, ApJS, 192, 4
- Aharonian, F., Akhperjanian, A. G., Bazer-Bachi, A. R., et al. 2006, ApJ, 636, 777
- Albert, J., Aliu, E., Anderhub, H., et al. 2006, ApJ, 638, L101
- Anderson, L. D., & Bania, T. M. 2009, ApJ, 690, 706
- Anderson, L. D., Bania, T. M., Balser, D. S., et al. 2014, ApJS, 212, 1
- Anderson, L. D., Bania, T. M., Balser, D. S., & Rood, R. T. 2011, ApJS, 194, 32
- . 2012, ApJ, 754, 62
- André, P., Di Francesco, J., Ward-Thompson, D., et al. 2014, in Protostars and Planets VI, ed. H. Beuther, R. S. Klessen, C. P. Dullemond, & T. Henning, 27
- André, P., Men'shchikov, A., Bontemps, S., et al. 2010, A&A, 518, L102
- André, P., Revéret, V., Könyves, V., et al. 2016, A&A, 592, A54
- Anglada, G., Estalella, R., Pastor, J., Rodriguez, L. F., & Haschick, A. D. 1996, ApJ, 463, 205
- Aniano, G., Draine, B. T., Gordon, K. D., & Sandstrom, K. 2011, PASP, 123, 1218
- Anish Roshi, D., Bloss, M., Brandt, P., et al. 2012, arXiv e-prints, arXiv:1202.0938
- Ao, Y., Yang, J., Tatematsu, K., et al. 2018, AJ, 156, 210
- Arce, H. G., Shepherd, D., Gueth, F., et al. 2007, in Protostars and Planets V, ed. B. Reipurth, D. Jewitt, & K. Keil, 245
- Arthur, S. J., Henney, W. J., Mellem, G., de Colle, F., & Vázquez-Semadeni, E. 2011, MNRAS, 414, 1747

- Arzoumanian, D., André, P., Didelon, P., et al. 2011, A&A, 529, L6
- Bally, J., Devine, D., & Sutherland, R. 1995, in Revista Mexicana de Astronomia y Astrofisica Conference Series, Vol. 1, Revista Mexicana de Astronomia y Astrofisica Conference Series, ed. S. Lizano & J. M. Torrelles, 19
- Balsara, D., Ward-Thompson, D., & Crutcher, R. M. 2001, MNRAS, 327, 715
- Banerjee, R., Pudritz, R. E., & Anderson, D. W. 2006, MNRAS, 373, 1091
- Barrett, A. H., Ho, P. T. P., & Myers, P. C. 1977, ApJ, 211, L39
- Battersby, C., Bally, J., Ginsburg, A., et al. 2011, A&A, 535, A128
- Benjamin, R. A., Churchwell, E., Babler, B. L., et al. 2003, PASP, 115, 953
- Bertoldi, F., & McKee, C. F. 1992, ApJ, 395, 140
- Beuther, H., Schilke, P., Menten, K. M., et al. 2002, ApJ, 566, 945
- Bigiel, F., Leroy, A., Walter, F., et al. 2008, AJ, 136, 2846
- Billington, S. J., Urquhart, J. S., König, C., et al. 2020, MNRAS, 499, 2744
- Blitz, L. 1987, in NATO Advanced Study Institute (ASI) Series C, Vol. 210, Physical Processes in Interstellar Clouds, ed. G. E. Morfill & M. Scholer, 35–58
- Blum, H. 1967, in Models for the Perception of Speech and Visual Form, ed. W. Wathen-Dunn (Cambridge: MIT Press), 362–380
- Bonnell, I. A., & Bate, M. R. 2006, MNRAS, 370, 488
- Bonnell, I. A., Bate, M. R., Clarke, C. J., & Pringle, J. E. 2001, MNRAS, 323, 785
- Bonnell, I. A., Vine, S. G., & Bate, M. R. 2004, MNRAS, 349, 735
- Bontemps, S., André, P., Könyves, V., et al. 2010, A&A, 518, L85
- Bouhafs, N., Rist, C., Daniel, F., et al. 2017, MNRAS, 470, 2204
- Brand, J., Cesaroni, R., Comoretto, G., et al. 2003, A&A, 407, 573
- Brand, J., Massi, F., Zavagno, A., Deharveng, L., & Lefloch, B. 2011, A&A, 527, A62

- Breen, S. L., Caswell, J. L., Ellingsen, S. P., & Phillips, C. J. 2010, MNRAS, 406, 1487
- Brogan, C. L., Hunter, T. R., Cyganowski, C. J., et al. 2011, ApJ, 739, L16
- Brunthaler, A., Reid, M. J., Menten, K. M., et al. 2009, ApJ, 693, 424
- Busquet, G., Estalella, R., Zhang, Q., et al. 2011, A&A, 525, A141
- Carey, S. J., Noriega-Crespo, A., Mizuno, D. R., et al. 2009, PASP, 121, 76
- Caselli, P., Hartquist, T. W., & Havnes, O. 1997, A&A, 322, 296
- Caswell, J. L., & Breen, S. L. 2010, MNRAS, 407, 2599
- Chabrier, G. 2003, PASP, 115, 763
- Chambers, E. T., Jackson, J. M., Rathborne, J. M., & Simon, R. 2009, ApJS, 181, 360
- Cheung, A. C., Rank, D. M., Townes, C. H., Knowles, S. H., & Sullivan, W. T., I. 1969a, ApJ, 157, L13
- Cheung, A. C., Rank, D. M., Townes, C. H., Thornton, D. D., & Welch, W. J. 1968, Phys. Rev. Lett., 21, 1701
- . 1969b, Nature, 221, 626
- Churchwell, E., Babler, B. L., Meade, M. R., et al. 2009, PASP, 121, 213
- Claussen, M. J., Wilking, B. A., Benson, P. J., et al. 1996, ApJS, 106, 111
- Clemens, D. P. 1985, ApJ, 295, 422
- Clemens, D. P., Sanders, D. B., & Scoville, N. Z. 1988, ApJ, 327, 139
- Codella, C., Felli, M., & Natale, V. 1996, A&A, 311, 971
- Contreras, Y., Rathborne, J. M., Guzman, A., et al. 2017, MNRAS, 466, 340
- Crutcher, R. M. 1999, ApJ, 520, 706
- Csengeri, T., Urquhart, J. S., Schuller, F., et al. 2014, A&A, 565, A75
- Curran, R. L., & Chrysostomou, A. 2007, MNRAS, 382, 699
- Cyganowski, C. J., Koda, J., Rosolowsky, E., et al. 2013, ApJ, 764, 61
- Dame, T. M., Hartmann, D., & Thaddeus, P. 2001, ApJ, 547, 792

- de Wilt, P., Rowell, G., Walsh, A. J., et al. 2017, MNRAS, 468, 2093
- Deharveng, L., Lefloch, B., Massi, F., et al. 2006, A&A, 458, 191
- Dib, S., Helou, G., Moore, T. J. T., Urquhart, J. S., & Dariush, A. 2012, ApJ, 758, 125
- Dickman, R. L. 1978, ApJS, 37, 407
- Diehl, R., Halloin, H., Kretschmer, K., et al. 2006, Nature, 439, 45
- Draine, B. T. 1989, in Infrared Spectroscopy in Astronomy, ed. E. Böhm-Vitense (Paris, France: European Space Agency), 93
- Draine, B. T., & Li, A. 2001, ApJ, 551, 807
- Duarte-Cabral, A., & Dobbs, C. L. 2016, MNRAS, 458, 3667
- Dunham, M. K., Rosolowsky, E., Evans, Neal J., I., Cyganowski, C., & Urquhart, J. S. 2011, ApJ, 741, 110
- Elitzur, M. 1991, ApJ, 370, L45
- . 1992, ARA&A, 30, 75
- Elitzur, M., Hollenbach, D. J., & McKee, C. F. 1989, ApJ, 346, 983
- Elmegreen, B. G. 1987, ApJ, 312, 626
- Elmegreen, B. G. 1998, in Astronomical Society of the Pacific Conference Series, Vol. 148, Origins, ed. C. E. Woodward, J. M. Shull, & J. Thronson, Harley A., 150
- Evans, Neal J., I. 1999, ARA&A, 37, 311
- Faure, A., Hily-Blant, P., Le Gal, R., Rist, C., & Pineau des Forets, G. 2013, ApJ, 770, L2
- Fiege, J. D., & Pudritz, R. E. 2000, MNRAS, 311, 85
- Foreman-Mackey, D., Hogg, D. W., Lang, D., & Goodman, J. 2013, PASP, 125, 306
- Frail, D. A., Claussen, M. J., & Méhault, J. 2013, ApJ, 773, L19
- Furuya, R. S., Kitamura, Y., Wootten, A., Claussen, M. J., & Kawabe, R. 2003, ApJS, 144, 71

- Furuya, R. S., Kitamura, Y., Wootten, H. A., Claussen, M. J., & Kawabe, R. 2001, ApJ, 559, L143
- Gaches, B. A. L., & Offner, S. S. R. 2018, ApJ, 854, 156
- Galván-Madrid, R., Keto, E., Zhang, Q., et al. 2009, ApJ, 706, 1036
- Garay, G., Mardones, D., Brooks, K. J., Videla, L., & Contreras, Y. 2007, ApJ, 666, 309
- Ginsburg, A., & Mirocha, J. 2011, PySpecKit: Python Spectroscopic Toolkit v01.20, Astrophysics Source Code Library ascl:1109.001
- Goddi, C., & Moscadelli, L. 2006, A&A, 447, 577
- Goldreich, P., & Kwan, J. 1974, ApJ, 189, 441
- Goldsmith, P. F. 2001, ApJ, 557, 736
- Gómez, G. C., & Vázquez-Semadeni, E. 2014, ApJ, 791, 124
- Green, D. A. 1991, PASP, 103, 209
- Griffin, M. J., Abergel, A., Abreu, A., et al. 2010, A&A, 518, L3
- Gutermuth, R. A., & Heyer, M. 2015, AJ, 149, 64
- Guzmán, A. E., Sanhueza, P., Contreras, Y., et al. 2015, ApJ, 815, 130
- H. E. S. S. Collaboration, Abramowski, A., Aharonian, F., et al. 2015, A&A, 574, A27
- Hacar, A., & Tafalla, M. 2011, A&A, 533, A34
- Hacar, A., Tafalla, M., Kauffmann, J., & Kovács, A. 2013, A&A, 554, A55
- Hachisuka, K., Brunthaler, A., Menten, K. M., et al. 2009, ApJ, 696, 1981
- Healy, K. R., Hester, J. J., & Claussen, M. J. 2004, ApJ, 610, 835
- Heathcote, S. R., & Brand, P. W. J. L. 1983, MNRAS, 203, 67
- Heiles, C., & Troland, T. H. 2003, ApJ, 586, 1067
- Helfand, D. J., Becker, R. H., White, R. L., Fallon, A., & Tuttle, S. 2006, AJ, 131, 2525
- Henning, T., Linz, H., Krause, O., et al. 2010, A&A, 518, L95

- Herbertz, R., Ungerechts, H., & Winnewisser, G. 1991, A&A, 249, 483
- Herwig, F. 2005, ARA&A, 43, 435
- Hildebrand, R. H. 1983, QJRAS, 24, 267
- Hill, T., André, P., Arzoumanian, D., et al. 2012, A&A, 548, L6
- Ho, P. T. P., Martin, R. N., Myers, P. C., & Barrett, A. H. 1977, ApJ, 215, L29
- Ho, P. T. P., & Townes, C. H. 1983, ARA&A, 21, 239
- Hoare, M. G., Lumsden, S. L., Oudmaijer, R. D., et al. 2005, in Massive Star Birth: A Crossroads of Astrophysics, ed. R. Cesaroni, M. Felli, E. Churchwell, & M. Walmsley, Vol. 227, 370–375
- Hoare, M. G., Purcell, C. R., Churchwell, E. B., et al. 2012, PASP, 124, 939
- Hogge, T., Jackson, J., Stephens, I., et al. 2018, ApJS, 237, 27
- Hogge, T. G., Jackson, J. M., Allingham, D., et al. 2019, ApJ, 887, 79
- Hollenbach, D., & McKee, C. F. 1980, ApJ, 241, L47
- Honma, M., Bushimata, T., Choi, Y. K., et al. 2007, PASJ, 59, 889
- Honma, M., Nagayama, T., Ando, K., et al. 2012, PASJ, 64, 136
- Hunter, T. R., Brogan, C. L., Indebetouw, R., & Cyganowski, C. J. 2008, ApJ, 680, 1271
- Jackson, J. M., Rathborne, J. M., Shah, R. Y., et al. 2006, ApJS, 163, 145
- Jackson, J. M., Rathborne, J. M., Foster, J. B., et al. 2013, PASA, 30, e057
- Jackson, J. M., Whitaker, J. S., Rathborne, J. M., et al. 2019, ApJ, 870, 5
- Jeans, J. H. 1902, Philosophical Transactions of the Royal Society of London Series A, 199, 1
- . 1928, Astronomy and cosmogony (Cambridge, United Kingdom: Cambridge University Press)
- Juvela, M., & Ysard, N. 2012, A&A, 541, A33
- Kassim, N. E. 1992, AJ, 103, 943
- Kauffmann, J., Pillai, T., & Goldsmith, P. F. 2013, ApJ, 779, 185

- Kennicutt, Robert C., J. 1998, ARA&A, 36, 189
- Kennicutt, R. C. 2005, in Massive Star Birth: A Crossroads of Astrophysics, ed. R. Cesaroni, M. Felli, E. Churchwell, & M. Walmsley, Vol. 227, 3–11
- Kerton, C. R., Wolf-Chase, G., Arvidsson, K., Lintott, C. J., & Simpson, R. J. 2015, ApJ, 799, 153
- Kim, W.-T., Ostriker, E. C., & Stone, J. M. 2002, ApJ, 581, 1080
- Kirk, H., Myers, P. C., Bourke, T. L., et al. 2013, ApJ, 766, 115
- Kirsanova, M. S., Sobolev, A. M., Thomasson, M., et al. 2008, MNRAS, 388, 729
- Klassen, M., Pudritz, R. E., & Kirk, H. 2017, MNRAS, 465, 2254
- Kraemer, K. E., & Jackson, J. M. 1995, ApJ, 439, L9
- Kramer, C., Stutzki, J., Rohrig, R., & Corneliusen, U. 1998, A&A, 329, 249
- Kroupa, P. 2001, MNRAS, 322, 231
- Krumholz, M. R., Cunningham, A. J., Klein, R. I., & McKee, C. F. 2010, ApJ, 713, 1120
- Krumholz, M. R., & Federrath, C. 2019, Frontiers in Astronomy and Space Sciences, 6, 7
- Krumholz, M. R., Klein, R. I., & McKee, C. F. 2007, ApJ, 656, 959
- Krumholz, M. R., Klein, R. I., McKee, C. F., Offner, S. S. R., & Cunningham, A. J. 2009, Science, 323, 754
- Krumholz, M. R., & McKee, C. F. 2008, Nature, 451, 1082
- Kryukova, E., Megeath, S. T., Gutermuth, R. A., et al. 2012, AJ, 144, 31
- Kudritzki, R. P. 2002, ApJ, 577, 389
- Lada, C. J., & Wilking, B. A. 1980, ApJ, 238, 620
- Lada, E. A., Strom, K. M., & Myers, P. C. 1993, in Protostars and Planets III, ed. E. H. Levy & J. I. Lunine, 245
- Lagache, G., Abergel, A., Boulanger, F., & Puget, J. L. 1998, A&A, 333, 709
- Lampton, M., Margon, B., & Bowyer, S. 1976, ApJ, 208, 177

- Larson, R. B. 1981, MNRAS, 194, 809
- Larson, R. B., & Starrfield, S. 1971, A&A, 13, 190
- Lazarian, A. 2005, in American Institute of Physics Conference Series, Vol. 784, Magnetic Fields in the Universe: From Laboratory and Stars to Primordial Structures., ed. E. M. de Gouveia dal Pino, G. Lugones, & A. Lazarian, 42–53
- Leahy, D. A., & Tian, W. W. 2008, AJ, 135, 167
- Longmore, S. N., Walsh, A. J., Purcell, C. R., et al. 2017, MNRAS, 470, 1462
- Lopez, L. A., Ramirez-Ruiz, E., Badenes, C., et al. 2009, ApJ, 706, L106
- Loren, R. B. 1989a, ApJ, 338, 902
- . 1989b, ApJ, 338, 925
- Loren, R. B., Vanden Bout, P. A., & Davis, J. H. 1973, ApJ, 185, L67
- Lovas, F. J. 2004, Journal of Physical and Chemical Reference Data, 33, 177
- Lu, X., Zhang, Q., Liu, H. B., et al. 2018, ApJ, 855, 9
- Luisi, M., Anderson, L. D., Schneider, N., et al. 2021, Science Advances, 7, eabe9511
- MacLaren, I., Richardson, K. M., & Wolfendale, A. W. 1988, ApJ, 333, 821
- Mangum, J. G., & Shirley, Y. L. 2015, PASP, 127, 266
- Mangum, J. G., & Wootten, A. 1994, ApJ, 428, L33
- Marchwinski, R. C., Pavel, M. D., & Clemens, D. P. 2012, ApJ, 755, 130
- Masters, J., Garwood, B., Langston, G., & Shelton, A. 2011, in Astronomical Society of the Pacific Conference Series, Vol. 442, Astronomical Data Analysis Software and Systems XX, ed. I. N. Evans, A. Accomazzi, D. J. Mink, & A. H. Rots, 127
- Maxted, N. I., de Wilt, P., Rowell, G. P., et al. 2016, MNRAS, 462, 532
- McEwen, B. C., Pihlström, Y. M., & Sjouwerman, L. O. 2016, ApJ, 826, 189
- McKee, C. F., & Cowie, L. L. 1975, ApJ, 195, 715

- McKee, C. F., Hollenbach, D. J., Seab, G. C., & Tielens, A. G. G. M. 1987, ApJ, 318, 674
- McKee, C. F., & Tan, J. C. 2003, ApJ, 585, 850
- Meaburn, J. 1988, MNRAS, 233, 791
- Megeath, S. T., Wilson, T. L., & Corbin, M. R. 2005, ApJ, 622, L141
- Meidt, S. E., Leroy, A. K., Rosolowsky, E., et al. 2018, ApJ, 854, 100
- Men'shchikov, A., André, P., Didelon, P., et al. 2010, A&A, 518, L103
- Merello, M., Molinari, S., Rygl, K. L. J., et al. 2019, MNRAS, 483, 5355
- Messineo, M., Menten, K. M., Figer, D. F., et al. 2014, A&A, 569, A20
- Misanovic, Z., Kargaltsev, O., & Pavlov, G. G. 2011, ApJ, 735, 33
- Misiriotis, A., Xilouris, E. M., Papamastorakis, J., Boumis, P., & Goudis, C. D. 2006, A&A, 459, 113
- Molinari, S., Swinyard, B., Bally, J., et al. 2010a, A&A, 518, L100
- . 2010b, PASP, 122, 314
- Molinari, S., Schisano, E., Elia, D., et al. 2016, A&A, 591, A149
- Morgan, M., White, S., Lockman, J., et al. 2008, in Union Radio Scientifique Internationale XXIX General Assembly, J02p1
- Moscadelli, L., Cesaroni, R., & Rioja, M. J. 2005, A&A, 438, 889
- Moscadelli, L., Sanna, A., Goddi, C., et al. 2020, A&A, 635, A118
- Motte, F., Bontemps, S., & Louvet, F. 2018, ARA&A, 56, 41
- Mottram, J. C., Hoare, M. G., Lumsden, S. L., et al. 2007, A&A, 476, 1019
- Mueller, K. E., Shirley, Y. L., Evans, Neal J., I., & Jacobson, H. R. 2002, ApJS, 143, 469
- Murray, N. 2011, ApJ, 729, 133
- Murray, N., & Rahman, M. 2010, ApJ, 709, 424
- Myers, P. C., Bachiller, R., Caselli, P., et al. 1995, ApJ, 449, L65
- Myers, P. C., Mardones, D., Tafalla, M., Williams, J. P., & Wilner, D. J. 1996, ApJ, 465, L133

- Narayanan, G., Walker, C. K., & Buckley, H. D. 1998, ApJ, 496, 292
- Nozawa, S., Mizuno, A., Teshima, Y., Ogawa, H., & Fukui, Y. 1991, ApJS, 77, 647
- O'dell, C. R., & Wen, Z. 1994, ApJ, 436, 194
- Oká, T., Shimizu, F. O., Shimizu, T., & Watson, J. K. G. 1971, ApJ, 165, L15
- Oort, J. H., Kerr, F. J., & Westerhout, G. 1958, MNRAS, 118, 379
- Orlando, S., Peres, G., Reale, F., et al. 2005, A&A, 444, 505
- Ormel, C. W., Min, M., Tielens, A. G. G. M., Dominik, C., & Paszun, D. 2011, A&A, 532, A43
- Ossenkopf, V., & Henning, T. 1994, A&A, 291, 943
- Padoan, P., Pan, L., Haugbølle, T., & Nordlund, Å. 2016, ApJ, 822, 11
- Palagi, F., Cesaroni, R., Comoretto, G., Felli, M., & Natale, V. 1993, A&AS, 101, 153
- Pan, L., Desch, S. J., Scannapieco, E., & Timmes, F. X. 2012, ApJ, 756, 102
- Patnaude, D. J., & Fesen, R. A. 2005, ApJ, 633, 240
- Peretto, N., & Fuller, G. A. 2009, A&A, 505, 405
- Peretto, N., Lenfestey, C., Fuller, G. A., et al. 2016, A&A, 590, A72
- Peters, T., Klessen, R. S., Mac Low, M.-M., & Banerjee, R. 2010, ApJ, 725, 134
- Pillai, T., Kauffmann, J., Tan, J. C., et al. 2015, ApJ, 799, 74
- Pittard, J. M., & Parkin, E. R. 2016, MNRAS, 457, 4470
- Poglitsch, A., Waelkens, C., Geis, N., et al. 2010, A&A, 518, L2
- Prestage, R. M., Constantikes, K. T., Hunter, T. R., et al. 2009, IEEE Proceedings, 97, 1382
- Puget, J. L., & Leger, A. 1989, ARA&A, 27, 161
- Purcell, C. R., Longmore, S. N., Walsh, A. J., et al. 2012, MNRAS, 426, 1972

- Ramstedt, S., Schöier, F. L., & Olofsson, H. 2009, A&A, 499, 515
- Rathborne, J. M., Jackson, J. M., & Simon, R. 2006, ApJ, 641, 389
- Rathborne, J. M., Whitaker, J. S., Jackson, J. M., et al. 2016, PASA, 33, e030
- Rawlings, J. M. C., & Yates, J. A. 2001, MNRAS, 326, 1423
- Reach, W. T., Rho, J., & Jarrett, T. H. 2005, ApJ, 618, 297
- Reid, M. J., Dame, T. M., Menten, K. M., & Brunthaler, A. 2016, ApJ, 823, 77
- Reid, M. J., & Moran, J. M. 1981, ARA&A, 19, 231
- Reid, M. J., Menten, K. M., Zheng, X. W., et al. 2009, ApJ, 700, 137
- Reid, M. J., Menten, K. M., Brunthaler, A., et al. 2014, ApJ, 783, 130
- Rigby, A. J., Moore, T. J. T., Eden, D. J., et al. 2019, A&A, 632, A58
- Robitaille, T. P., & Whitney, B. A. 2010, ApJ, 710, L11
- Rodgers, S. D., & Charnley, S. B. 2001, ApJ, 546, 324
- Roman-Duval, J., Heyer, M., Brunt, C. M., et al. 2016, ApJ, 818, 144
- Rosolowsky, E., Dunham, M. K., Ginsburg, A., et al. 2010, ApJS, 188, 123
- Salpeter, E. E. 1955, ApJ, 121, 161
- Sanhueza, P., Jackson, J. M., Foster, J. B., et al. 2012, ApJ, 756, 60
- Sanhueza, P., Jackson, J. M., Zhang, Q., et al. 2017, ApJ, 841, 97
- Sault, R. J., Teuben, P. J., & Wright, M. C. H. 1995, in Astronomical Society of the Pacific Conference Series, Vol. 77, Astronomical Data Analysis Software and Systems IV, ed. R. A. Shaw, H. E. Payne, & J. J. E. Hayes, 433
- Schmidt, M. 1957, Bull. Astron. Inst. Netherlands, 13, 247
- Schuller, F., Menten, K. M., Contreras, Y., et al. 2009, A&A, 504, 415
- Schwartz, P. R., & Barrett, A. H. 1971, Contributions from the Kitt Peak National Observatory, 554, 95
- Schwartz, P. R., Harvey, P. M., & Barrett, A. H. 1974, ApJ, 187, 491

- Schwarz, G. 1978, Annals of Statistics, 6, 461
- Scott, D. W. 1992, Multivariate Density Estimation (New York, NY: Wiley)
- Scoville, N. Z., & Solomon, P. M. 1975, ApJ, 199, L105
- Sedov, L. I. 1959, Similarity and Dimensional Methods in Mechanics (New York, NY: Academic Press)
- Seifried, D., Walch, S., Haid, S., Girichidis, P., & Naab, T. 2018, ApJ, 855, 81
- Sellwood, J. A., & Sánchez, R. Z. 2010, MNRAS, 404, 1733
- Sgro, A. G. 1975, ApJ, 197, 621
- Shepherd, D. 2003, in Astronomical Society of the Pacific Conference Series, Vol. 287, Galactic Star Formation Across the Stellar Mass Spectrum, ed. J. M. De Buizer & N. S. van der Blieck, 333–344
- Shetty, R., Kauffmann, J., Schnee, S., & Goodman, A. A. 2009a, ApJ, 696, 676
- Shetty, R., Kauffmann, J., Schnee, S., Goodman, A. A., & Ercolano, B. 2009b, ApJ, 696, 2234
- Siringo, G., Kreysa, E., Kovács, A., et al. 2009, A&A, 497, 945
- Smith, L. F., Biermann, P., & Mezger, P. G. 1978, A&A, 66, 65
- Smith, R. J., Glover, S. C. O., Klessen, R. S., & Fuller, G. A. 2016, MNRAS, 455, 3640
- Smith, R. J., Shetty, R., Beuther, H., Klessen, R. S., & Bonnell, I. A. 2013, ApJ, 771, 24
- Smith, R. J., Shetty, R., Stutz, A. M., & Klessen, R. S. 2012, ApJ, 750, 64
- Smith, R. J., Treß, R. G., Sormani, M. C., et al. 2020, MNRAS, 492, 1594
- Snell, R. L., & Loren, R. B. 1977, ApJ, 211, 122
- Solomon, P. M., Scoville, N. Z., & Sanders, D. B. 1979, ApJ, 232, L89
- Spencer, J. H., Johnston, K. J., Moran, J. M., Reid, M. J., & Walker, R. C. 1979, ApJ, 230, 449
- Sridharan, T. K., Beuther, H., Saito, M., Wyrowski, F., & Schilke, P. 2005, ApJ, 634, L57

- Stil, J. M., Taylor, A. R., Dickey, J. M., et al. 2006, AJ, 132, 1158
- Strittmatter, P. A. 1966, MNRAS, 132, 359
- Stutzki, J., & Guesten, R. 1990, ApJ, 356, 513
- Su, Y., Yang, J., Zhou, X., Zhou, P., & Chen, Y. 2014, ApJ, 796, 122
- Su, Y., Zhang, S., Shao, X., & Yang, J. 2015, ApJ, 811, 134
- Svoboda, B. E., Shirley, Y. L., Battersby, C., et al. 2016, ApJ, 822, 59
- Sweitzer, J. S. 1978, ApJ, 225, 116
- Swift, J. J., Welch, W. J., & Di Francesco, J. 2005, ApJ, 620, 823
- Tatematsu, K., Fukui, Y., Nakano, M., et al. 1987, A&A, 184, 279
- Taylor, G. 1950, Proceedings of the Royal Society of London Series A, 201, 159
- Tian, W. W., Li, Z., Leahy, D. A., & Wang, Q. D. 2007, ApJ, 657, L25
- Tremblin, P., Anderson, L. D., Didelon, P., et al. 2014, A&A, 568, A4
- Umemoto, T., Mikami, H., Yamamoto, S., & Hirano, N. 1999, ApJ, 525, L105
- Urquhart, J. S., Hoare, M. G., Lumsden, S. L., Oudmaijer, R. D., & Moore, T. J. T. 2008, in Astronomical Society of the Pacific Conference Series, Vol. 387, Massive Star Formation: Observations Confront Theory, ed. H. Beuther, H. Linz, & T. Henning, 381
- Urquhart, J. S., Morgan, L. K., Figura, C. C., et al. 2011, MNRAS, 418, 1689
- Urquhart, J. S., Figura, C. C., Moore, T. J. T., et al. 2015, MNRAS, 452, 4029
- Urquhart, J. S., König, C., Giannetti, A., et al. 2018, MNRAS, 473, 1059
- van der Tak, F. F. S., Black, J. H., Schöier, F. L., Jansen, D. J., & van Dishoeck, E. F. 2007, A&A, 468, 627
- van der Tak, F. F. S., van Dishoeck, E. F., Evans, Neal J., I., & Blake, G. A. 2000, ApJ, 537, 283
- Vázquez-Semadeni, E., Palau, A., Ballesteros-Paredes, J., Gómez, G. C., & Zamora-Avilés, M. 2019, MNRAS, 490, 3061

- Voronkov, M. A., Caswell, J. L., Ellingsen, S. P., & Sobolev, A. M. 2010, MNRAS, 405, 2471
- Walch, S., & Naab, T. 2015, MNRAS, 451, 2757
- Walker, C. K., Lada, C. J., Young, E. T., Maloney, P. R., & Wilking, B. A. 1986, ApJ, 309, L47
- Walker, C. K., Narayanan, G., & Boss, A. P. 1994, ApJ, 431, 767
- Walmsley, C. M., & Ungerechts, H. 1983, A&A, 122, 164
- Walsh, A. J., Breen, S. L., Bains, I., & Vlemmings, W. H. T. 2009, MNRAS, 394, L70
- Walsh, A. J., Breen, S. L., Britton, T., et al. 2011, MNRAS, 416, 1764
- Wang, K., Zhang, Q., Wu, Y., Li, H.-b., & Zhang, H. 2012, ApJ, 745, L30
- Wang, P., Li, Z.-Y., Abel, T., & Nakamura, F. 2010, ApJ, 709, 27
- Ward-Thompson, D., Motte, F., & Andre, P. 1999, MNRAS, 305, 143
- Wardle, M., & Yusef-Zadeh, F. 2002, Science, 296, 2350
- Watson, C., Povich, M. S., Churchwell, E. B., et al. 2008, ApJ, 681, 1341
- Whitaker, J. S., Jackson, J. M., Rathborne, J. M., et al. 2017, AJ, 154, 140
- Wienen, M., Wyrowski, F., Menten, K. M., et al. 2018, A&A, 609, A125
- Wienen, M., Wyrowski, F., Schuller, F., et al. 2012, A&A, 544, A146
- Wienen, M., Wyrowski, F., Menten, K. M., et al. 2015, A&A, 579, A91
- Williams, J. P., de Geus, E. J., & Blitz, L. 1994, ApJ, 428, 693
- Wilson, T. L. 1972, A&A, 19, 354
- Wong, T., & Blitz, L. 2002, ApJ, 569, 157
- Woodward, P. R. 1976, ApJ, 207, 484
- Xu, J., & Stone, J. M. 1995, ApJ, 454, 172
- Xu, Y., Li, J. J., Reid, M. J., et al. 2013, ApJ, 769, 15
- Yoo, T. S. 2004, *Insight into Images: Principles and Practice for Segmentation, Registration, and Image Analysis* (Wellesley, MA: AK Peters Ltd)

- Yuan, L., Li, G.-X., Zhu, M., et al. 2020, A&A, 637, A67
- Yung, B. H. K., Nakashima, J.-i., Hsia, C.-H., & Imai, H. 2017, MNRAS, 465, 4482
- Zavagno, A., Deharveng, L., Brand, J., et al. 2005, in Massive Star Birth: A Crossroads of Astrophysics, ed. R. Cesaroni, M. Felli, E. Churchwell, & M. Walmsley, Vol. 227 (Cambridge, United Kingdom: Cambridge University Press), 346–351
- Zernickel, A., Schilke, P., & Smith, R. J. 2013, A&A, 554, L2
- Zhang, Q., & Ho, P. T. P. 1995, ApJ, 450, L63
- Zhang, Q., Hunter, T. R., Sridharan, T. K., & Cesaroni, R. 1999, ApJ, 527, L117
- Zinnecker, H., McCaughrean, M. J., & Wilking, B. A. 1993, in Protostars and Planets III, ed. E. H. Levy & J. I. Lunine, 429
- Zinnecker, H., & Yorke, H. W. 2007, ARA&A, 45, 481
- Zuckerman, B., & Evans, N. J., I. 1974, ApJ, 192, L149
- Zweibel, E. G. 1988, ApJ, 329, 384

Curriculum Vitae

